

INVESTIGATION, DESIGN, AND COMMERCIALIZATION OF  
ACTIVELY-ENHANCED SOLID-STATE GAS SENSOR ARRAYS

By

BRYAN MICHAEL BLACKBURN

A DISSERTATION PRESENTED TO THE GRADUATE SCHOOL  
OF THE UNIVERSITY OF FLORIDA IN PARTIAL FULFILLMENT  
OF THE REQUIREMENTS FOR THE DEGREE OF  
DOCTOR OF PHILOSOPHY

UNIVERSITY OF FLORIDA

2009

© 2009 Bryan Michael Blackburn

To my family and friends for always believing in me

## ACKNOWLEDGMENTS

I would like to thank my colleagues and mentors over my many years of study and personal growth. I would also like to thank my parents and grandparents for fostering in me from an early age a philosophy for continuous learning and improvement. This includes the pursuit of knowledge from all fronts: engineering, science, mathematics, business, religion, literature, and more. To my fiancée, Kaitlin, I am thankful for the many years of understanding and patience as I worked towards this and future goals. In and around the lab, I would like to thank Dr. Hee-Sung Yoon, Nick Vito, and Patrick Wanninkhof for helping me with various aspects of my work. For keeping me calm during times of high stress, I would like to thank Cynthia Kan. I would also like to thank my brother, Jeremy, for providing a constant source of healthy competition during our childhood. I would like to thank Dr. Scott Perry for many useful talks regarding surface science and the use of his equipment. Furthermore, I would like to thank his graduate student, Greg Dudder, for working with me on some of the surface science experiments and teaching me about photoelectron spectroscopy. I would also like to thank Dr. Juan Nino and Dr. Enrico Traversa for teaching me valuable concepts during my time as a graduate student. I would be remiss not to thank Dr. Toshi Nishida for serving as the initial source of inspiration while I was an undergraduate student in electrical engineering that lead me to pursue a doctorate degree; he has since continued to motivate me and I look forward to the possibility of working with him on projects in the future. Finally, I would like to thank my advisor Dr. Eric Wachsman and mentor P.N. ‘Vaidy’ Vaidyanathan for invaluable guidance and giving me the opportunity to prove myself as an engineer, scientist, and businessman.

## TABLE OF CONTENTS

	<u>page</u>
ACKNOWLEDGMENTS .....	4
LIST OF TABLES .....	10
LIST OF FIGURES .....	11
ABSTRACT.....	17
CHAPTER	
1 INTRODUCTION .....	19
1.1 Small, Robust, Low-Cost Selective Multifunctional Gas Sensors .....	19
1.1.1 Significance.....	19
1.1.1.1 Energy efficiency.....	19
1.1.1.2 Pollutant emissions.....	21
1.1.1.3 Process control.....	22
1.1.1.4 Noninvasive disease diagnostics and monitoring.....	23
1.1.2 Key Applications for Advanced Gas Sensor Technology .....	23
1.1.2.1 Energy production industry .....	24
1.1.2.2 Transportation, heavy equipment, and materials handling industries .....	26
1.1.2.3 Materials and chemical processing industries .....	28
1.1.2.4 Medical industry .....	29
1.1.2.5 Other important applications .....	31
1.1.3 General Requirements of Gas Sensors.....	32
1.1.3.1 Sensitivity .....	32
1.1.3.2 Selectivity .....	32
1.1.3.3 Response time.....	33
1.1.3.4 Repeatability, accuracy, and resolution.....	33
1.1.3.5 Signal-to-noise ratio .....	34
1.2 Research Objectives.....	34
1.2.1 Sensor Arrays for Detecting Multiple Gas Species .....	34
1.2.2 Thermal Enhancements.....	35
1.2.3 Electric-Field Enhancements .....	35
1.2.4 Surface Science Analysis.....	35
1.2.5 Improved R&D and Commercialization Efforts.....	36
2 BACKGROUND AND LITERATURE REVIEW .....	39
2.1 Gas Sensors.....	39
2.1.1 General Issues .....	40
2.1.2 Solid-State Gas Sensor Technology.....	41
2.1.2.1 Thermal sensors.....	41
2.1.2.2 Mass sensors .....	41

2.1.2.3	Optical sensors.....	41
2.1.2.4	Electrochemical sensors .....	41
2.1.3	Electrochemical Gas Sensor Theory .....	43
2.1.3.1	Principles of electronic and ionic conduction .....	43
2.1.3.2	Principles of solid-state electrochemistry.....	43
2.1.3.3	Electrochemical promotion .....	47
2.1.3.4	Semiconducting oxides.....	48
2.1.3.5	Mixed potential theory .....	50
2.1.3.6	Differential electrode equilibria theory .....	51
2.1.3.7	Electrolyte and gas sensing electrode materials .....	52
2.2	Related Work.....	54
2.2.1	Techniques for Studying Gas Sensor Mechanisms.....	54
2.2.1.1	Conductivity measurements .....	54
2.2.1.2	Controlled-potential techniques.....	55
2.2.1.3	Electrochemical impedance spectroscopy .....	55
2.2.1.4	Mass spectrometry.....	56
2.2.1.5	Kelvin probe work function measurements.....	56
2.2.1.6	Electron spectroscopic techniques.....	57
2.2.2	Electric-Field Effects in Surface Processes and Solid-State Devices.....	58
2.2.3	Other Important Electrolytes and Sensing Electrodes .....	59
3	DIFFERENTIAL ELECTRODE TEMPERATURE EFFECT .....	65
3.1	Introduction.....	65
3.2	Background.....	65
3.3	Experimental.....	67
3.3.1	Sample Preparation .....	68
3.3.2	Test Setup.....	69
3.3.3	Testing Procedures.....	69
3.3.4	3D Reconstruction of Sensing Electrodes with FIB/SEM.....	70
3.4	Results and Discussion .....	71
3.4.1	Proof of Concept.....	71
3.4.2	Changes in Sensitivity.....	72
3.4.3	Baseline Shifts .....	74
3.4.4	3D Reconstructions and Analysis .....	76
3.5	Conclusions.....	77
4	THERMALLY ENHANCED GAS SENSOR ARRAY .....	86
4.1	Introduction.....	86
4.2	Background.....	87
4.3	Experimental.....	88
4.3.1	Sample Preparation .....	89
4.3.2	Automated Experimental Setup .....	89
4.3.3	Experimental Procedure.....	90
4.4	Results and Discussion .....	90
4.4.1	NO <sub>x</sub> Gas Mixtures.....	91

4.4.1.1	NO <sub>2</sub> selectivity.....	91
4.4.1.2	Total NO <sub>x</sub> sensitivity .....	93
4.4.1.3	Possible explanations for sensing electrode-pair response.....	94
4.4.1.4	Determining NO and NO <sub>2</sub> concentrations .....	98
4.4.2	Other Gas Sensor Array Results .....	99
4.4.2.1	Effect of ambient temperature .....	100
4.4.2.2	Response time.....	101
4.4.2.3	Effect of total flow rate.....	101
4.4.2.4	Responses to other gases .....	102
4.5	Conclusions.....	102
<b>5</b>	<b>ELECTRIC-FIELD ENHANCEMENTS IN POTENTIOMETRIC GAS SENSORS AND OTHER SOLID-STATE IONIC DEVICES .....</b>	<b>110</b>
5.1	Introduction.....	110
5.2	Background.....	112
5.2.1	Electronic Theory of Catalysis and Chemisorption on Semiconductors .....	113
5.2.2	Related Work .....	113
5.3	Experimental.....	114
5.3.1	Sample Preparation .....	114
5.3.1.1	Planar sensor.....	114
5.3.1.2	Air-reference sample .....	115
5.3.1.3	TPD “capacitor-chip” sample.....	116
5.3.2	Experimental Setups .....	116
5.3.3	Testing Procedures.....	117
5.3.4	Electric-Field Simulations .....	118
5.4	Results and Discussion .....	120
5.4.1	Electric-Field Simulations .....	120
5.4.2	Field-Enhanced Sensor .....	122
5.4.2.1	Influence of electric-field shapes.....	123
5.4.2.2	Influence of electric-field magnitude .....	124
5.4.2.3	Influence of electric-field polarity .....	124
5.4.3	Air-Reference Results.....	125
5.4.4	“Capacitor-Chip” Results.....	128
5.4.5	Discussion .....	130
5.5	Conclusions.....	133
<b>6</b>	<b>DIRECT-WRITE RAPID PROTOTYPING .....</b>	<b>146</b>
6.1	Introduction.....	146
6.2	Background.....	148
6.3	Experimental.....	150
6.3.1	Ceramic Powders .....	151
6.3.2	Electrodes.....	151
6.3.3	Electrolytes .....	151
6.3.4	Direct-Write Machine Preparation.....	152
6.3.5	Initial Combinatorial Experiments.....	153

6.4	Results and Discussion .....	154
6.4.1	Powder Particle Size Analysis .....	155
6.4.2	Electrolyte Deposition .....	155
6.4.3	Electrode Deposition.....	156
6.4.4	Lines and Rastered Patterns .....	156
6.4.4.1	Line tests.....	156
6.4.4.2	Rastered patterns .....	157
6.4.4.3	Relationship between machine and material properties .....	157
6.4.5	Design and Performance Results .....	159
6.5	Conclusions.....	159
7	EXTENDED SURFACE SCIENCE STUDY OF SOLID-STATE GAS SENSORS BASED ON THE DIFFERENTIAL ELECTRODE EQUILIBRIA THEORY .....	169
7.1	Introduction.....	169
7.2	Background.....	171
7.2.1	Surface Science Techniques .....	171
7.2.1.1	Electron spectroscopy.....	171
7.2.1.2	Kelvin probe .....	171
7.2.2	Related Work .....	172
7.3	Experimental.....	174
7.3.1	Sample Preparation .....	174
7.3.2	UHV Test Setup.....	175
7.3.2.1	Photoemission spectrometer .....	175
7.3.2.2	Kelvin probe .....	175
7.3.3	Testing Procedures.....	176
7.3.3.1	Pretreatment.....	176
7.3.3.2	Surface science measurements .....	177
7.4	Results and Discussion .....	179
7.4.1	Photoelectron Spectra .....	179
7.4.1.1	Angle resolved photoelectron spectra .....	179
7.4.1.2	High resolution core-level XPS.....	180
7.4.1.3	Valence spectra.....	184
7.4.2	Contact Potential Difference.....	185
7.5	Conclusions.....	187
8	TOWARDS THE COMMERCIALIZATION OF MINIATURE SOLID-STATE POTENTIOMETRIC GAS SENSORS .....	197
8.1	Introduction.....	197
8.2	Background.....	198
8.3	Experimental.....	198
8.3.1	Fabrication of Rigid Substrate and Electrolyte Layer.....	199
8.3.1.1	Water-based tape casting .....	199
8.3.1.2	Tape shaping, lamination, trimming, and scoring .....	201
8.3.1.3	Deposition of YSZ electrolyte layer.....	202
8.3.2	Multilayer Deposition with Screen Printing .....	203

8.3.3	Wire Bonding for Packaging & Reliability Testing/Calibration .....	205
8.3.4	Multisensor Setup .....	207
8.4	Results and Discussion .....	208
8.4.1	Sensor Array Fabrication .....	208
8.4.1.1	Al <sub>2</sub> O <sub>3</sub> /YSZ.....	208
8.4.1.2	Automated screen printing .....	211
8.4.2	Wire Bonding.....	211
8.4.3	Sensor Testing.....	212
8.5	Conclusions and Future Work .....	213
8.5.1	Multisensor Testing in New Reactors.....	213
8.5.2	Further Miniaturization and New Designs.....	213
8.5.3	Expanded Materials Development for New Applications .....	214
9	CONCLUSIONS.....	225
<b>APPENDIX</b>		
A	MORE ON THE THERMALLY MODIFIED GAS SENSOR ARRAY.....	228
A.1	Heating Element Design .....	228
A.2	Surface Temperature Measurements .....	228
A.2	Finite Element Modeling of Thermal Distributions .....	229
B	MORE ON THE ELECTRIC-FIELD ENHANCED GAS SENSOR .....	231
C	PROGRAMMING .....	232
D	ADDITIONAL INFORMATION.....	233
D.1	Spray Coating .....	233
D.2	Pulsed Laser Deposition of La <sub>2</sub> CuO <sub>4</sub> .....	233
D.3	Multi-Sensor Reactor Design and Modeling .....	234
	LIST OF REFERENCES .....	237
	BIOGRAPHICAL SKETCH .....	256

## LIST OF TABLES

<u>Table</u>		<u>page</u>
1-1	Energy consumption data for the materials and chemical processing industries.....	38
2-1	Key electrolytes for gas sensors.....	64
2-2	Key sensing electrodes for gas sensors.....	64
3-1	Surface temperature measurements and heater power at three voltage setpoints.....	85
4-1	Typical NO <sub>x</sub> response times at 500 °C and 600 °C (at different heater setpoints, 300 ccm total flow rate).....	109
5-1	Field-bias schemes to investigate the effect of field shape, magnitude, and polarity.....	145
5-2	Summary of trends for field-bias schemes 1-4.....	145
6-1	Comparison of different “additive” direct-write fabrication methods to a more standard technique.....	168
7-1	Ex-situ pretreatments for surface science study.....	196
7-2	XPS peak positions for N 1s family.....	196
7-3	XPS peak positions for O 1s family.....	196
7-4	XPS peak positions for Cu 2p family.....	196
7-5	XPS peak positions for La 3d family.....	196
8-1	Densification of tapes during tape lamination.....	224
8-2	Film thickness dependence on spin coating parameters.....	224
8-3	YSZ film crack width dependence on heat treatment.....	224
A-1	Physical parameters used for thermal modeling.....	230

## LIST OF FIGURES

<u>Figure</u>		<u>page</u>
1-1	Trends in the number of publications involving fuel cells since 1955 .....	37
1-2	Relationship between fuel economy, air-to-fuel ratio, and pollutant emissions .....	37
2-1	Solid-state ‘thermal’ (catalyst) gas sensor .....	60
2-2	Solid-state ‘mass’ gas sensor .....	60
2-3	Conceptual representation of a solid-state ‘optical’ gas sensor .....	60
2-4	Solid-state ‘electrochemical’ (chemiresistive) gas sensor .....	60
2-5	Schematics of Lambda (oxygen) probe and an amperometric gas sensor .....	61
2-6	Relationship between Volta, surface, and Galvani potentials in a metal .....	61
2-7	Illustration of various reaction paths that can occur at the electrical conductor, electrolyte, and triple-phase-boundary in an electrochemical device .....	61
2-8	Current-potential curve from Butler-Volmer equation and Tafel plot .....	61
2-9	Formation of depleted surface layer during chemisorption of O <sub>2</sub> gas .....	62
2-10	Schematic showing barriers to conduction .....	62
2-11	Basic concept of mixed potential theory .....	62
2-12	Cubic-fluorite structure of yttria-stabilized zirconia (YSZ) solid electrolyte .....	62
2-13	La <sub>2</sub> CuO <sub>4</sub> crystal structure illustrating perovskite-type nature .....	63
3-1	Schematic of first-generation investigatory gas sensor array .....	78
3-2	Thermal model for first-generation investigatory gas sensor array .....	78
3-3	Schematic of second-generation investigatory array .....	78
3-4	La <sub>2</sub> CuO <sub>4</sub> -Pt sensor response to NO <sub>x</sub> as a function of heater voltage setpoint .....	79
3-5	Plots of steady-state sensor response versus gas concentration for Pt(3)-LCO(4) ...	79
3-6	NO sensor response from the LCO(4)-LCO(2) and Pt(3)-Pt(1) signals as a function of the difference in temperature between the electrodes of each electrode-pair .....	80

3-7	NO <sub>2</sub> sensor response from the LCO(4)-LCO(2) and Pt(3)-Pt(1) signals as a function of the difference in temperature between the electrodes of each electrode-pair .....	80
3-8	NO sensor response from the LCO(2)-Pt(3) and LCO(4)-Pt(1) signals as a function of the difference in temperature between the electrodes of each electrode-pair. ....	80
3-9	NO <sub>2</sub> sensor response from the LCO(2)-Pt(3) and LCO(4)-Pt(1) signals as a function of the difference in temperature between the electrodes of each electrode-pair .....	81
3-10	NO sensor response from the LCO(4)-Pt(3) and LCO(2)-Pt(1) signals as a function of the difference in temperature between the electrodes of each electrode-pair .....	81
3-11	NO <sub>2</sub> sensor response from the LCO(4)-Pt(3) and LCO(2)-Pt(1) signals as a function of the difference in temperature between the electrodes of each electrode-pair .....	81
3-12	Baseline shifts versus difference in temperature between the electrodes of each electrode-pair .....	82
3-13	3D reconstructions of two electrode materials made using images from FIB-SEM slices .....	83
3-14	Phase fraction and tortuosity as determined from 3D reconstruction of Pt/YSZ and LCO/YSZ .....	83
3-15	3D skeleton reconstruction of LCO and pore structure on YSZ.....	84
4-1	Schematic of second-generation gas sensor array .....	105
4-2	NO <sub>2</sub> sensor response at three different total heater power settings with an ambient temperature of 600 °C .....	105
4-3	Response to NO <sub>2</sub> gas steps with and without 200 ppm NO for the LCO(2)-Pt(1) electrode-pair and an ambient temperature of 600 °C .....	106
4-4	Response to NO gas steps with and without 200 ppm NO <sub>2</sub> for the LCO(2)-Pt(1) electrode-pair for an ambient temperature of 600 °C .....	106
4-5	Sensitivity versus total heater power for LCO(2)-Pt(1) electrode-pair with an ambient temperature of 600 °C .....	107
4-6	Sensitivity versus total heater power for LCO(2)-LCO(4) sensing electrode-pair with an ambient temperature of 600 °C .....	107

4-7	Total NO <sub>x</sub> sensitivity for LCO(2)-LCO(4) sensing electrode-pair when total heater power was ~81 mW with an ambient temperature of 600 °C. ....	108
5-1	Planar sensor and air-reference configurations.....	135
5-2	LCO capacitor-type chip used in TPD experiments .....	135
5-3	Test setup for air-reference with gas effluent measurements .....	136
5-4	2D contour and vector plots of electric-field shapes for bias schemes tested with the field-enhanced sensor.....	136
5-5	Geometry for numerical and analytical calculations of electric-field strength.....	137
5-6	Analytical results for the electric field in the z-direction along the central axis of a charged annulus and effect of superposition.....	137
5-7	Results of numerical analysis for the off-axis electric field of a ring of charge as a function of distance (z) from the plane of the ring along the central axis for field-biases of 1, 5, and 8 V .....	137
5-8	Results of numerical analysis for the off-axis electric field of a ring of charge as a function of distance (r) from the center of the ring along the radial direction .....	138
5-9	NO <sub>x</sub> sensor results for field-bias scheme 1 with positive polarity for several temperatures, showing the effect on sensitivity .....	138
5-10	NO <sub>x</sub> sensor results for field-bias scheme 1 with negative polarity, showing the effect of field-bias magnitude on sensitivity at 500 °C .....	139
5-11	NO <sub>x</sub> sensor results for field-bias scheme 2 with positive/negative polarities and multiple field-bias magnitudes, showing enhanced selectivity, at 500 °C .....	139
5-12	NO <sub>x</sub> sensor results for field-bias scheme 3 with negative polarities and multiple field-bias magnitudes, showing trends in sensitivity at 500 °C.....	140
5-13	NO <sub>x</sub> sensor results for field-bias scheme 4 with positive/negative polarities and multiple field-bias magnitudes, showing trends in sensitivity at 450 °C.....	140
5-14	Mass spectrometer measured NO <sub>x</sub> concentrations versus applied electric-field voltage during 650 ppm NO feed and 650 ppm NO <sub>2</sub> feed using air-reference sample .....	141
5-15	Mass spectrometer measured NO <sub>x</sub> concentrations and air-reference sample sensitivity versus applied electric-field voltage during 650 ppm NO feed and 650 ppm NO <sub>2</sub> feed .....	141
5-16	FIB-SEM reconstruction of bulk porous LCO used in air-reference sample .....	142

5-17	SEM image of LCO powder (scale-bar is 1 $\mu\text{m}$ ) .....	142
5-18	Measured NO and NO <sub>2</sub> desorption profiles for 1% NO/1% O <sub>2</sub> TPD at various electric-field biases across the capacitor-type chip.....	142
5-19	Measured NO and NO <sub>2</sub> desorption profiles for 1% NO <sub>2</sub> /1% O <sub>2</sub> TPD at various electric-field biases across the capacitor-type chip.....	143
5-20	Adsorbate concentration versus E-field bias for NO and NO <sub>2</sub> adsorption .....	143
5-21	Modeled field-strength for field-electrodes with +Q on top and bottom.....	144
6-1	Close up view of the nScript 3Dn 450 HP dual pump assemblies with fine ceramic tips in action .....	161
6-2	Pattern emulated during line tests with LCO.....	161
6-3	Typical particle-size distributions of powders used in this work .....	161
6-4	Comparison of spin-coated and nScript-deposited GDC electrolyte .....	162
6-5	Example of “3D” YSZ structure made with the rapid prototype system.....	163
6-6	Typical electrode microstructure for nScript deposited pastes .....	163
6-7	Effect of backing pressure and gantry speed on the linewidth and thickness during line tests with LCO deposited on YSZ.....	164
6-8	Cross-sections of circular LCO samples made during rastered pattern experiments .....	164
6-9	Examples of scaling and complex pattern capabilities of nScript-deposition technique .....	165
6-10	Direct-write fuel cell sealing and deposition of gas channels.....	165
6-11	One possible micro IT-SOFC stack configuration.....	166
6-12	Performance results for IT-SOFC consisting of rapid-prototyped LSCF cathode on top of a spin-coated GDC electrolyte film supported by a Ni-GDC anode .....	166
6-13	nScript deposited microheaters for future gas sensor arrays.....	167
7-1	Band model of a semiconductor showing the influence of surface adsorbates on the work function and basic circuit concept of a Kelvin probe .....	188
7-2	Depiction of the sample/platen in the UHV holder and the arrangement for angle resolved photoelectron measurements .....	188

7-3	O 1s photoelectron spectra at 15, 55, and 75° for O <sub>2</sub> , NO, and NO <sub>2</sub> pretreatments.....	189
7-4	Comparison of the O 1s spectrum before, during, and after in-situ heating to 250 °C .....	190
7-5	Comparison of the C 1s x-ray photoelectron spectra for O <sub>2</sub> , NO <sub>2</sub> , NO, and NO+Efield pretreatments with a takeoff angle of 55° .....	190
7-6	Comparison of the N 1s x-ray photoelectron spectra for O <sub>2</sub> , NO <sub>2</sub> , and NO+Efield pretreatments with a takeoff angle of 55° .....	191
7-7	Comparison of the O 1s x-ray photoelectron spectra for O <sub>2</sub> , NO <sub>2</sub> , NO, and NO+Efield pretreatments with a takeoff angle of 55° .....	191
7-8	Comparison of the Cu 2p x-ray photoelectron spectra for O <sub>2</sub> , NO <sub>2</sub> , NO, and NO+Efield pretreatments with a takeoff angle of 55° .....	192
7-9	Comparison of the La 3d x-ray photoelectron spectra for O <sub>2</sub> , NO <sub>2</sub> , NO, and NO+Efield pretreatments with a takeoff angle of 55° .....	192
7-10	Theoretical density of states for La <sub>2</sub> CuO <sub>4</sub> compared with experimental XPS valence spectra for O <sub>2</sub> , NO <sub>2</sub> , NO, and NO+Efield pretreatments.....	193
7-11	Difference spectra of valence structure.....	194
7-12	Comparison of the XPS and UPS valence spectra for the O <sub>2</sub> pretreatment.....	194
7-13	Comparison of the change in contact potential difference (i.e., work function) of La <sub>2</sub> CuO <sub>4</sub> and WO <sub>3</sub> to NO and NO <sub>2</sub> pretreatments .....	195
8-1	Multilayer ceramic processing for manufacture of the gas sensor arrays.....	215
8-2	A possible configuration for the small potentiometric gas sensor array (<1cm <sup>2</sup> ) ..	215
8-3	Illustration of the laminating process.....	215
8-4	SEM micrograph of laminated tape before and after trimming.....	216
8-5	Custom three-axis cutting/punching machine and sintered/scored alumina substrates before and after device separation.....	216
8-6	Illustration of screen designs allowing a degree of flexibility in the final sensor layout.....	217
8-7	Screen printing patterns used for the batch fabrication of the gas sensors .....	217
8-8	Facilities for scale-up multi-sensor testing .....	218

8-9	Cross-sectional and surface SEM images of a spin coated YSZ film on an Al <sub>2</sub> O <sub>3</sub> support.....	219
8-10	An example of a high magnification SEM micrograph showing improved YSZ films on Al <sub>2</sub> O <sub>3</sub> supports .....	220
8-11	Batch-processed La <sub>2</sub> CuO <sub>4</sub> sensing electrodes deposited with automated DEK screen printer.....	220
8-12	Wire bonding pads and resulting analysis of a Pt wire bonds to an Au pad.....	221
8-13	NO response of the La <sub>2</sub> CuO <sub>4</sub> -Pt electrode-pair on YSZ and Al <sub>2</sub> O <sub>3</sub> /YSZ substrates at 450 °C.....	221
8-14	NO <sub>x</sub> response of the La <sub>2</sub> CuO <sub>4</sub> -Pt electrode-pair on YSZ and Al <sub>2</sub> O <sub>3</sub> /YSZ substrates at 475 °C.....	222
8-15	NO <sub>2</sub> response of the La <sub>2</sub> CuO <sub>4</sub> -Pt electrode-pair on YSZ and Al <sub>2</sub> O <sub>3</sub> /YSZ substrates at 500 °C.....	222
8-16	NO <sub>2</sub> response of the La <sub>2</sub> CuO <sub>4</sub> -Pt electrode-pair on YSZ and Al <sub>2</sub> O <sub>3</sub> /YSZ substrates at 575 °C.....	222
8-17	NO response of the La <sub>2</sub> CuO <sub>4</sub> -Pt electrode-pair on YSZ and Al <sub>2</sub> O <sub>3</sub> /YSZ substrates at 575 °C.....	223
8-18	Two examples of packaging that may be used to house the advanced gas sensor technology.....	223
8-19	Rapid prototypes of gas sensor array features .....	223
D-1	XRD of the Pulsed-Laser-Deposited La <sub>2</sub> CuO <sub>4</sub> thin film .....	235
D-2	CFD simulation of multi-sensor reactor before adding the side and top hemispheres.....	235
D-3	CFD simulation of multi-sensor reactor after adding the side and top hemispheres.....	236

Abstract of Dissertation Presented to the Graduate School  
of the University of Florida in Partial Fulfillment of the  
Requirements for the Degree of Doctor of Philosophy

INVESTIGATION, DESIGN, AND COMMERCIALIZATION OF  
ACTIVELY-ENHANCED SOLID-STATE GAS SENSOR ARRAYS

By

Bryan Michael Blackburn

December 2009

Chair: Eric D. Wachsman

Major: Materials Science & Engineering

Low cost, high-performance gas sensors are needed for many applications in order to quantify (parts per billion, ppb, to parts per million, ppm) concentrations of individual species in complex gas mixtures. These devices must often function reliably over long periods of time (e.g., months to years) without any possibility for recalibration (i.e., they must be stable). Such gas sensors are significant for many applications and industries, including possible improvements in energy efficiency, pollutant emissions, process control, disease diagnostics, and more. This work involved the development of methods to “actively” enhance the performance of potentiometric gas sensors. Such devices, based on coupling two electrodes (either metals and/or semiconducting oxides) to a solid electrolyte, have been studied in one form or another for over 100 years; though only recently have breakthroughs provided insight into the development of solid-state gas sensors capable of selectively quantifying low levels of individual species of interest in complex gas mixtures. In this work, local modifications in temperature and the electric field about the sensing electrodes were explored to enhance device performance. This involved the fabrication and testing of many devices, including prototype multifunctional gas sensor arrays for selectively detecting multiple gas species (e.g., NO and NO<sub>2</sub>) in the presence of others. Electrical properties of the devices provided insight into the mechanisms behind the

“active” enhancements. Several surface science techniques were used to further investigate the sensing mechanisms of the devices and the “active” enhancement methods for the sensors and potentially other solid-state ionic devices. During the course of the work, materials were developed for use with a cutting-edge direct-write tool for rapid prototyping of solid-state ionic devices, including gas sensors and solid oxide fuel cells. Finally, R&D procedures were improved through automated experiments and fabrication; significant steps were taken towards future commercialization; and future research goals and methods were recommended.

## CHAPTER 1 INTRODUCTION

Gas sensors are devices that can be used to improve a manufacturing process, ensure the safety and health of humans and the environment, or to guarantee national security. While successful in certain fields, currently available methods for detecting multiple gases in complex mixtures are expensive, bulky, non-selective, or ill-suited for many applications.<sup>1</sup> However, a new type of electrochemical, potentiometric (voltage output) sensor offers a low-cost, robust alternative with significantly improved selectivity, stability, and more. This opens the possibility for gas sensors to be used in many significant applications and industries as discussed below, along with the research objectives of this work.

### **1.1 Small, Robust, Low-Cost Selective Multifunctional Gas Sensors**

#### **1.1.1 Significance**

High-performance gas sensors are needed for many applications in order to quantify the (parts per billion, ppb, to parts per million, ppm) levels of, often several, individual gas species. In many situations, these devices must function reliably over long periods of time (e.g., months to years) without any possibility for recalibration (i.e., they must be stable). The gas sensor research described herein involves improvements in sensitivity and selectivity, and other important features. Therefore, this work is significant for many applications and industries, including possible improvements in energy efficiency, pollutant emissions, process control, disease diagnostics, and more.

##### **1.1.1.1 Energy efficiency**

Worldwide dependence on fossil fuels has taken a toll on global economies in recent years. For instance, gas prices rose to \$4 per gallon in June 2008 as a result of record oil prices in January 2008.<sup>2</sup> With the link between commodities and GDP, the recent spikes in oil and

derived products have resulted in annual net oil imports exceeding \$800 billion, or about 2% of global GDP, with the import cost to some countries exceeding 15% of their national GDP.<sup>3-6</sup> Beyond the financial implications of such dependencies, the coupled relationship between economic, socio-economic, political, and cultural issues further complicates the problem. For example, this issue has led to increased strain on resources (e.g., biomass being used as an energy source instead of food) which may result in increased conflict amongst nations, as has happened in the past.<sup>2,7</sup>

Accordingly, improvements in energy efficiency are critical and have caused a shift in research and development efforts towards alternative energy and more efficient use of currently used power sources. For example, the number of fuel cell related journal articles and patents has increased considerably since the early 1990s (i.e., after the last oil crisis), with major increases in 2004, 2006, and 2008 as seen in Figure 1-1. Similar trends are observed for gas sensor research related to energy efficiency. There has also recently been a drive for ensuring a sustainable future in terms of materials, renewable resources, pollution, minimization of resource usage (e.g., energy efficiency), and many more areas.<sup>8-11</sup> The combined effort for a sustainable future stems from the complicated relationship between the globally significant issues mentioned above and the potential long-term harm to the environment, human health, and other relevant systems.

Fuel economy is a term sometimes used to describe the efficiency of a combustion process (e.g., miles per gallon for automobiles). In the United States and Europe, the fuel economy of automobiles is directly related to energy security and the cost of fuel because most oil is imported.<sup>12</sup> Furthermore, there is often a tradeoff between fuel economy and the emission of pollutants which can cause harm to the entire world. As such a balance must be made between the two in order to gain the best benefit from these processes. In order to accomplish this, there

is a need for advanced gas sensor technology to provide feedback as to the gas composition of, for example, combustion exhausts, which when coupled with other information about the system (e.g., pressure, temperature, and load requirements) can be used to make decisions about control parameters such as how to best mix fuel and air.

### **1.1.1.2 Pollutant emissions**

Pollution is responsible for negatively affecting the environment and health of humans, animals, and ecosystems around the world. Furthermore, these systems are linked to each other in many, often not obvious, ways, thereby increasing the importance of mitigating any chance for damage to any of them. Examples of main pollutants include inorganic (e.g., CO, NO<sub>x</sub>, CO<sub>2</sub>, SO<sub>x</sub>); volatile organic compounds and unburned hydrocarbons, or HCs, (e.g., Naphthalene, or C<sub>10</sub>H<sub>8</sub>, and other polycyclic compounds); and semi-volatile organic compounds (e.g., particulate matter).<sup>13-17</sup> These pollutants can come from such sources as stationary and mobile combustion processes, incinerators, or landfills. For example, CO and HCs form during incomplete combustion of fuels and are known or suspected of causing cancer or other serious health effects (e.g., lung damage). NO<sub>x</sub> forms during combustion at high temperatures can react with HCs in the presence of sunlight produce ground-level ozone, which is the major component of smog.<sup>12,14,18</sup> Smog can aggravate asthma attacks or other health related problems in children and the elderly. Furthermore, NO<sub>x</sub> and SO<sub>x</sub> react to form (e.g., acetic and formic) acid rain, which can damage soil (i.e., impacting agriculture) and important infrastructure (e.g., roads and bridges), buildings, and other man-made structures.<sup>14,16-18</sup> Also, NH<sub>3</sub> is toxic and CH<sub>4</sub> is a greenhouse gas that can be explosive or cause asphyxia. The issues described above were realized as early as the 1970s, when government formed the EPA and began issuing regulations to limit emissions and other pollutants.<sup>14,17,19</sup> This has been accomplished in many ways, such as with three-way catalytic converters (TWCCs) which are used to remove CO, HCs, and NO<sub>x</sub> from

automobile exhausts.<sup>18,20</sup> Another example is the use of stack scrubbers combined with selective catalytic reduction (SCR) in coal burning power plants to remove NO<sub>x</sub> and SO<sub>x</sub>.<sup>14,21</sup> However, the effectiveness of these techniques may change over time as the catalysts that make them work age or as the input or necessary output conditions change.

Pollution also comes from chemical manufacturing processes, which can release toxic substances such as benzene or vinyl chloride into the air; these have been associated with cancer, birth defects and long-term damage to the lungs, brain, and central nervous system.<sup>14</sup> Some researchers also believe that these gases are also (directly or indirectly) responsible for global climate change, which if left unchecked could lead to increased risk for forest fires, hurricanes, famine, and more harmful consequences.<sup>22,23</sup> The possibility of climate change has even been associated as a risk to U.S. national security due to food shortages, decreased quality and availability of fresh water, and disrupted access to energy supplies.<sup>22</sup> Even if only a few of these negative effects from pollution were to occur, there would be enough risk to warrant special technology to mitigate the potential damage. Since current technology is limited in its effectiveness in doing so, new innovations are needed.

### **1.1.1.3 Process control**

Process control is an important topic in almost all industries, but in particular for manufacturing. Many manufacturing processes involve the use of gases (e.g., plastic materials production) or the development of off-gassed species during various (e.g., aqueous) chemical reactions. In many cases it is desirable to know the concentration of the gases in order to optimize the process for improved yield or long-term stability, which could affect the quality of or cost to manufacture a chemical or material. Furthermore, due to increased competition, fluctuating demand, and other economic factors, there is a drive to utilize chemical process engineering for improvements in process safety, robustness, and flexibility.<sup>24-26</sup> Pressure,

temperature, and single component gas measurements are now commonly used in process control. With the measurement of multiple gas species, advanced process control algorithms can be used to achieve enhanced operation of complex chemical processes under optimum conditions. However, expensive analytical techniques are only currently available for process control, though they do not offer the manufacturing flexibility that the market demands.

#### **1.1.1.4 Noninvasive disease diagnostics and monitoring**

Current means for disease diagnostics and monitoring are time consuming, expensive, inconvenient/uncomfortable for patients, or not effective at early detection of disease. These methods include long-standing techniques such as ex-situ blood and urine lab analyses, which do not provide real-time data, have been used successfully to determine disease, but must be continuously administered in order to monitor its development. Other diagnostic tools (e.g., x-ray based computed tomography (CT) scans and positron emission tomography (PET)) emit radiation, which when repeated exposures occur can be harmful to the patient.<sup>27,28</sup> Many other non-radiation-emitting medical devices (e.g., optical coherence tomography) are being developed and/or improved to make them more intrusive than invasive.<sup>29</sup> However, the ultimate goal should be a non-invasive technology that can provide diagnostics and monitoring of many different diseases and disorders.

#### **1.1.2 Key Applications for Advanced Gas Sensor Technology**

Multi-gas sensing is needed in the energy production, automotive, chemical processing, and medical industries in order to improve energy efficiency, reduce emissions, increase product yield, and detect/monitor disease. However, available sensors are limited by:

- **Cost:** Unable to cost effectively detect and quantify multiple gases
- **Sensitivity:** Unable to accurately measure gases to desired levels
- **Selectivity:** Unable to distinguish between gases in complex mixtures
- **Durability:** They fail or need periodic recalibration due to interferents

- **Versatility:** Several sensors to detect multiple gases; speed too slow
- **Complexity:** They are difficult to manufacture, integrate, and use

The technology developed in this work improves the function of electrochemical gas sensors using novel material science principles and several patented methods for “actively” enhancing performance. This has the potential to advance sensor technology on the same six critical frontiers:

- **Cost:** Advanced materials, manufacturing, & designs drive down costs
- **Sensitivity:** Low concentration (ppb and ppm) gas quantification
- **Selectivity:** Accurate target gas measurement in complex mixtures
- **Durability:** Can function in harsh environments without degradation
- **Versatility:** Multifunctional materials for multi-gas sensing in a single product
- **Simplicity:** Sensor designs simplify manufacturing, integration, and use

There are many opportunities for commercializing this technology. Applications require sensors capable of detecting related gas species at ppb to ppm levels, in ambient room temperature and chemically/thermally harsh environments. These opportunities include:

- **Portable Sensing Equipment:** field tests or mobile platforms
- **Handheld Monitoring:** medical breath analysis or safety badges
- **Stationary Power Generation:** emissions monitoring for power plants
- **Remote Monitoring:** industrial process and manufacturing control
- **Fail Safe Detection:** sulfur levels in reformat feed stock for fuel cells
- **Other:** automotive; unmanned robotics; materials handling

There are likely many more applications, but for the sake of brevity, only a brief overview of key areas for such advanced gas sensor technology is discussed below.

### 1.1.2.1 Energy production industry

This industry includes stationary power generation (e.g., coal or gas turbine power plants) and technology for mobile power (e.g., diesel generator). Gas sensors utilized in these combustion processes are important in terms of potential for improved energy efficiency and reduced pollutant emissions. Combustion control includes two primary methods: operating point control (OPC) and active combustion control (ACC). ACC can be further broken into active

combustion enhancement (ACE) and active instability control (AIC). OPC is utilized for efficiency and pollutant emissions management, while ACE is used for optimizing performance and AIC is used to limit combustion oscillations.<sup>30</sup> AIC is primarily being explored as a means to reduce exhaust emissions in the lean premixed combustors of high-temperature gas turbines. The lean combustion mode reduces NO<sub>x</sub> emissions but creates instabilities such as pressure oscillations, which can progressively worsen as combustion conditions change to meet dynamic power output requirements. These instabilities can result in combustor failure due to damage from excessive heat, mechanical loads, and vibrations.<sup>30-32</sup> There is therefore a tradeoff between noise and emissions, but combustion efficiency can be controlled using the data from gas sensors measuring concentrations of CO, CO<sub>2</sub>, and other pollutants. In ACE there is no premixing which can lead to nonuniformity in gas turbine temperatures, resulting in increased emissions. Gas (and pressure and temperature) sensors can be used in an ACE mode with control algorithms to vary turbine parameters to create gas/pressure fluctuations that are out of phase with the instabilities, thereby enhancing mixing and reducing emission levels.<sup>30,32</sup> In OPC for gas turbines, stoichiometric (air-to-fuel ratio) conditions are slowly changed to stabilize the combustion flame, which also results in increased NO<sub>x</sub> emissions. As described above, one alternative to this is the use of lean premixed combustion, which is a mode susceptible to an increased amount of instability. In this case, control of the operating point results in a tradeoff between NO<sub>x</sub> and CO emissions and instability. OPC is simpler than the ACC methods, which involve a direct feedback loop; however, with the improvements in gas sensing technology the increased use of ACC methods presents the chance to further improve energy efficiency and reduce emissions.

Coal combustion is a nonlinear process dependent on the coal quality and operating conditions. Gas sensors can be used to monitor the coal quality, allowing system controls to then vary combustion parameters based on levels of contaminants and dilution.<sup>33</sup> Additionally, they may be used to develop improved maintenance strategies and faster, more accurate fault detection (e.g., from contaminants).<sup>33,34</sup> The OPC method can also be used to control coal combustion processes, but compared to use with gas turbines there is no need to worry about flame instability.

Currently available methods of high-temperature (400 – 1600 °C) gas detection in fossil energy power systems are limited in their bulkiness, cost, accuracy, repeatability, sensitivity, and speed. Such methods are also limited in that real-time, online measurements are not easily achieved due to compensation methods for interference sources (e.g., soot or H<sub>2</sub>O) and limitations due to application-based restrictions (e.g., high pressure). The gas sensor technology developed in this work is currently appropriate for use in the exhaust of coal and gas turbine systems. However, with additional materials development the technology can also be extended for use in turbine combustors (1000 – 1600 °C)

As alternative energy sources become more widespread in the future, use of advanced multi-gas sensors will also be useful in such systems as fuel cells, as will be described briefly in one of the sections below. Furthermore, the use of gas sensors with diesel generators is related to the use of diesel engines in transportation, heavy equipment, and materials handling as discussed below.

#### **1.1.2.2 Transportation, heavy equipment, and materials handling industries**

Multi-gas sensors will be useful in the transportation, heavy equipment, and materials handling industries. The transportation industry involves transport of people and cargo using vehicles such as automobiles, freight trucks and trains, and aircraft. As discussed above, for

vehicles using combustion engines there are tradeoffs between fuel efficiency and pollutant emissions. As shown in Figure 1-2, rich-burn combustion has improved performance at the expense of increased fuel consumption. Whereas lean-burn conditions result in lower performance, but with reduced fuel consumption and emissions. To further improve efficiency and reduce emissions, on-board diagnostic (OBD) systems adjust air-to-fuel ratios (AFR) to keep combustion near the stoichiometric point (SP), where reactions balance and TWCCs work best. When the AFR is below the SP, the engine runs “rich” and unburned fuel increases HC and CO pollutants. Above the SP, the automobile runs fuel “lean,” resulting in greater efficiency but more NO<sub>x</sub>. Currently, OBD systems utilize oxygen sensors before and after the TWCC to control the AFR and to monitor the efficiency of the TWCC.<sup>30</sup> Gas sensors currently used in automobiles only directly measure oxygen levels and make assumptions about the rest of the gas composition. Therefore, a major improvement of OBD systems will come with the introduction of gas sensor arrays to provide gas concentration data for multiple species. An advanced OBD system will then be able to actively switch between the combustion modes using closed-loop control to adjust engine parameters based on driving conditions and TWCC efficiency.

General materials handling vehicles (e.g., conveyers and cranes/hoists) and heavy equipment (e.g., pavers, earth movers/backhoes/bulldozers, and excavators) used in construction and mining are classified as using non-road diesel engines.<sup>35,36</sup> Some of the equipment, such as forklifts, can also be powered by propane, natural gas, or gasoline and can be improved as described above.<sup>35</sup> The EPA has mandated that these systems take advantage of advanced emissions control technologies, including the gas sensors developed in this work, between 2008 and 2014 in order to reduce pollutant emissions. Predicted environmental benefits include reduced NO<sub>x</sub> emissions of 738,000 tons annually, which could prevent more than 8,000

hospitalizations, 12,000 premature deaths, 15,000 heart attacks, and 1,000,000 lost work days each year.<sup>37</sup>

### **1.1.2.3 Materials and chemical processing industries**

Manufacturing industries depend on energy resources for fuel and power to convert raw materials into various products. This includes chemicals, petroleum refining, mining, glass, aluminum, steel, and metal casting industries. As shown in Table 1-1, these manufacturing activities account for a large percentage (>15% in 1998) of total US energy consumption.<sup>38</sup> More efficient manufacturing processes help lower production costs, increase productivity, and provide for a more sustainable future. One way to accomplish this is with the use of advanced gas sensor technology to measure both trace levels (e.g., contaminants or undesirable side reactions) and major components of gas mixtures or off-gassed substances during manufacturing processes. For example, in ethylene manufacturing the presence of  $\text{NH}_3$  or  $\text{C}_2\text{H}_2$  will destroy the catalyst in the polymerization reaction.<sup>39,40</sup> Identification and control of these contaminants can prevent downtime and cut production costs. As another example, consider bioprocessing (e.g., pharmaceutical manufacturing or wastewater treatment), where robust gas sensors could be useful in monitoring such processing steps as fermentation, which typically requires a sterile environment, sealed off from the ambient.<sup>41-46</sup> Other methods for monitoring fermentation processes, such as ultrasonic techniques or total biomass weight measurements, are insufficient as indicators or are prone to error due to effects from dispersed gas bubbles.<sup>41</sup> However, off-gassed ammonia, oxygen, ethanol, CO,  $\text{SO}_x$ ,  $\text{NO}_x$ , and other species can be measured to gain information about the progress of a biochemical process. On-line measurements using robust gas sensors is desirable as a way to control input parameters (e.g., nutrient levels) in batch processes where it can take hours to empty reaction vessels, during which time reactions continue and could result in undesirable byproducts. Currently, only off-line measurements using gas

chromatography are possible. Furthermore, the presence of other VOCs and ammonia derived compounds can interfere with such measurements.<sup>44</sup>

In addition to these applications, many chemical- and bioprocessing methods involve aqueous phase monitoring. In wastewater treatment, for example, this is challenging because of the hostile environment in which equipment may undergo fouling. Therefore, there is a need for robust, reliable on-line sensors for improved process control by removing the sensor from contact with the harsh wastewater. One such gas that can be monitored is off-gassed N<sub>2</sub>O which is released as stress response and can be related to the biological status of nitrifying bacteria.<sup>25</sup>

#### **1.1.2.4 Medical industry**

Breath analysis has been used as a diagnostic tool in medicine for centuries. The ancient Greeks and other cultures knew that the aroma (e.g., sweetness) of human breath can indicate certain diseases and ailments.<sup>47</sup> Human breath contains large amounts of H<sub>2</sub>O, CO<sub>2</sub>, N<sub>2</sub>, O<sub>2</sub> and trace (i.e., ppb to ppm) levels of other inorganic gases (e.g., CO and NO<sub>x</sub>) and approximately 200 volatile organic compounds (VOCs) common to all individuals; some of which can be used as status indicators for various biological functions. Breath analysis has been studied in the medical field to identify biomarkers for the diagnoses and monitoring of diseases involving the kidneys (e.g., uremia), liver (e.g., cirrhosis), and metabolic processes (e.g., diabetes); cancer (e.g., lung and breast cancer); neurological diseases (e.g., schizophrenia and bipolar disorder); and many other biological deficiencies.<sup>47-49</sup> There are also research efforts involving the use of breath analysis in medicinal compliance, monitoring implant rejection, toxicology, and identification of illegal drug use.<sup>50</sup> Compared to standard methods of medical diagnosis tools (e.g., blood work or PET scans), breath analysis is non-invasive, harmless, quick, and in many cases can be used to identify and monitor medical problems before any other symptoms are displayed.<sup>49</sup> Breath analysis may consist of gas measurement directly from exhaled breath or indirectly from

stored/concentrated samples. In clinical diagnosis, this technique may also involve the ingestion of a precursor solution, which is broken down by the body and the products exhaled into the gas sensing system.<sup>49</sup> Modern breath analysis has primarily relied on expensive, complicated analytical instruments (e.g., gas chromatograph/mass spectrometer, GC/MS) requiring trained technicians for operation and interpretation of gas measurements. Furthermore, such techniques often require frequent calibrations and additional equipment (e.g., condensate trap or other filters) to separate or remove gas species which interfere with the measurement (e.g., H<sub>2</sub>O).

GC/MS has been used to identify VOC biomarkers associated with lung cancer, while IR systems have been used to detect NO for monitoring the effectiveness of anti-inflammatory therapies.<sup>47-49</sup> Solid-state sensors (typically semiconducting, chemiresistors, or electrochemical sensors) used for breath analysis have also had some success, being developed for detecting, for example, CO, NO, and trace VOCs for various diagnostic applications.<sup>47-50</sup> However, most of these techniques are limited by their slow speed, high complexity, high cost, and/or long-term instability. Furthermore, most techniques (other than some of the solid-state devices) are not capable of directly sampling breath due to interference from, for example, relative humidity levels of ~100% common in human breath or they are susceptible to contamination and noise. Technological advances improving upon these limitations offer a chance to significantly benefit the breath-analysis market with the possibility for straightforward, inexpensive disease diagnostics and monitoring in hospital rooms, doctors' offices, and patient homes.

Therefore, there is a need for sensing systems capable of selectively detecting targeted biomarkers in a complex matrix (i.e., breath) and being used for low-cost, noninvasive disease diagnostics and monitoring. In some cases such sensing systems offer the chance to detect

diseases and disorders in their earliest stages, which may allow more effective treatments or be used as a means of preventative medicine.

#### **1.1.2.5 Other important applications**

In addition to the applications described above, there are many situations where knowledge of gas exposure history of humans and/or equipment to harmful gases may be useful. For example, chemical plant employees may be at risk for health problems (e.g., lung damage) after exposure to volatile organic compounds over time. A safety badge able to quantify the total amount of gas dosage over time could be used to determine whether a worker has been exposed to dangerous levels of toxins. In terms of equipment, knowledge of gas exposure history coupled to a fail-evident feature could save lives, time, and money. For example, a sensor capable of detecting gas phase sulfur (e.g., H<sub>2</sub>S or carbonyl sulfide, COS) might be used in an external reformer system for fuel cells, or in conjunction with a solid oxide fuel cell (SOFC) utilizing internal reforming of sulfur-rich fuels such as JP-8 diesel. Such gas sensors can also measure H<sub>2</sub>, CO, and/or CH<sub>4</sub> in the reformat environment in order to best utilize the fuel with the fuel cell.

There is also interest to use such multi-gas sensors to detect chemical/biological warfare agents. In particular, interested parties include the U.S. military and countries that have undergone attacks with such weapons in the past (e.g., Japan in 1995).<sup>51</sup> Many approaches have involved the use of standoff optical devices (e.g., infrared spectrometers), which as discussed above are expensive, bulky, and often have problems due to interference. The detection of harmful substances (e.g., sulfur mustard gas and nerve agents such as sarin) used in such weapons have been demonstrated with semiconducting sensors.<sup>52,53</sup> Unlike optical methods, such sensors do not allow direct standoff detection. However, there is potential to use solid-state gas sensors (e.g., advanced potentiometric gas sensors with superior selectivity) in fixed locations or attached to automated robotics (e.g., unmanned aerial vehicles, UAVs), soldiers to

scan an area of interest before potentially exposing themselves to dangerous chemicals or the possibility of early warning systems for large cities.

### **1.1.3 General Requirements of Gas Sensors**

Some correlation typically exists between components in a gas mixture, but as more gases are added the situation becomes more complex. For this reason selective detection of individual gases is critical. However, most gas sensors are either lacking in sensitivity and/or have insufficient selectivity for many applications. In general, the goal for the design of a gas sensor is to maximize sensitivity to the analyte and minimize cross-sensitivity (i.e., maximize selectivity) without sacrificing other parameters such as response time and long-term stability. There are several dozen sensor parameters that can be specified for a given device; however, only the most important are discussed below.

#### **1.1.3.1 Sensitivity**

Sensitivity refers to the amount of change in the sensor signal with a change in gas concentration. Any given sensing electrode must have sufficient sensitivity to the gas of interest so that a measurement can be made. The requirements for sensitivity will vary with the particular application. This can be approached from the perspective that the sensing materials should be designed for the maximum sensitivity regardless of the application (i.e., one material for several sensing systems). However, this could lead to problems where selectivity, discussed below, is of utmost importance for a particular application. As will be discussed in Chapters 3 through 5, the use of “active” enhancement modes could be used as an alternative for adjusting the sensitivity to a given application.

#### **1.1.3.2 Selectivity**

Selectivity refers to the ability of a device to measure one chemical species in the presence of others.<sup>20,54</sup> Most sensing materials are cross-sensitive to multiple species, which increases the

complexity of the sensing process when used in gas mixtures. In fact, most solid-state gas sensors are currently inadequate for commercial use as quantitative detectors because of poor selectivity.<sup>55,56</sup> As will be discussed in Chapters 3 through 5, the methods for “actively” enhancing a potentiometric gas sensor developed in this work can greatly improve the selectivity.

### **1.1.3.3 Response time**

A gas sensor is a transducer, where the response to the input stimuli (e.g., gas molecule) takes a finite amount of time to respond and to be converted into an electrical signal. This response time is often defined as the time interval ( $t_{90}$ ) needed for the sensor signal to reach 90% of the steady-state value.<sup>57</sup> There are often tradeoffs between response time, sensitivity, and selectivity. Therefore, the sensor design needs to consider whether the final application will be for dynamic control or long-term monitoring. With the use of “active” enhancements, there are reasons to believe that these factors may be tuned to the specific application without any need for design or material changes. This could significantly reduce R&D and manufacturing costs.

### **1.1.3.4 Repeatability, accuracy, and resolution**

As use of gas sensors becomes more widespread, the assurance of repeatability/reliability (i.e., precision) becomes more important. These will be discussed further in Chapter 8, which involves current commercialization efforts of the gas sensors developed in this work. The accuracy of gas sensor, or how closely the output measurement represents the actual value, is critical in applications where any large variance in the signal could result in undesirable consequences. On the other hand, a sensors resolution refers to the smallest change in the sensor input (e.g., gas concentration) to which the device will detect and respond with an output. Improvements in resolution will likely be very important for process-control and breath-analysis applications. The minimum detectable signal (MDS) of a gas sensor should be only a few molecules of the target species.<sup>66</sup> However, poor performance in terms of sensitivity, the data

acquisition electronics, and the signal-to-noise ratio (discussed below), currently limit the MDS to ppm in most cases and the upper range of ppb with advanced technology.

#### **1.1.3.5 Signal-to-noise ratio**

Noise is a sensor parameter that obscures the desired mapping of a real world input to a transduced sensor output.<sup>66</sup> It can come from many sources including intrinsically and extrinsically. Intrinsic noise for an electrical system includes thermally induced interference (i.e., Johnson or Nyquist noise from equilibrium thermal fluctuations in a conductor), white noise from nonequilibrium conditions (i.e., “shot” noise from random fluctuations in charge density), and “excess” noise (e.g., 1/f or “flicker” noise) from current processes.<sup>58</sup> In electrochemical systems and devices, the electrode-electrolyte interface is a source of noise; this includes thermal equilibrium noise from conductors, equilibrium excess noise from charge transfer kinetics, and relaxation currents from mass transfer processes.<sup>59</sup> For gas sensors there is also a source of noise from chemisorption, a process in which gas molecules interact (e.g., through local bonding) with the surface of gas sensitive materials.<sup>60</sup> In order for the sensor to produce a useful signal, the materials and sensor designs must be such that the signal-to-noise ratio is large than unity.

## **1.2 Research Objectives**

There were several objectives for this work, some of which followed as a result of work involving original objectives that did not go as planned. In all, the goal was to investigate methods for enhancing the performance of potentiometric gas sensors using sensor arrays, thermal and electric-field enhancements, surface science, and improvements in fabrication and testing procedures for R&D and commercialization purposes.

### **1.2.1 Sensor Arrays for Detecting Multiple Gas Species**

The first objective of this work was to create a multifunctional gas sensor array through the combination of multiple sensing electrode-pairs into a single, miniature sensor device, thus

allowing the detection of multiple gas species. Investigations included evaluation of crosstalk between sensing electrodes (i.e., the response of one affects another) when placed in close proximity to each other and the electrode arrangement with respect to each other and the rest of the device. This will be discussed in Chapters 4 and 5.

### **1.2.2 Thermal Enhancements**

The temperature dependence of sensitivity and selectivity of almost all solid-state gas sensors is well known. From this basis, the sensor array was improved through local heating of sensing electrode-pairs to different temperatures. Thermal enhancements also included the local heating of each electrode in an electrode-pair to a different temperature. These efforts will be discussed in Chapters 3 and 4, along with thermal modeling results and sensor design discussions.

### **1.2.3 Electric-Field Enhancements**

The concept for electric-field enhancements of a solid-state potentiometric gas sensor was a direct result of ‘failed’ sensor experiment that led to a hypothesis and validation of an idea. After the initial observations and formulation of hypotheses as to why there was an electric-field effect on gas sensing performance, the objectives for this work were expanded. The new objectives were to explore the use of electric fields to enhance the gas sensors; to gauge the effect of field strength, shape, and polarity; and to conceptually/experimentally explore the mechanisms behind the electric-field effect. This work can be found in Chapter 5.

### **1.2.4 Surface Science Analysis**

In past studies these potentiometric gas sensors have been investigated using temperature programmed techniques, diffuse reflectance infrared Fourier transform spectroscopy (DRIFTS), and X-ray photoelectron spectroscopy (XPS). The conclusions from these past experiments were used to help explain the sensing results from this work. Furthermore, in this work the electric-

field enhancement methods were investigated using temperature programmed techniques, XPS, ultraviolet photoelectron spectroscopy (UPS), and the Kelvin probe method. These results and the relationship of this work to past results are discussed in Chapters 4, 5 and 7.

### **1.2.5 Improved R&D and Commercialization Efforts**

Throughout the literature, gas sensor research often involves the use of hand-made samples, which makes comparison between results extremely difficult. The studies involving the gas sensor arrays and thermal/electric-field enhancements in this work were also almost all hand-made to a certain extent; but since most studies involved changes of the active nature, there was no need to compare multiple samples. However, in order to improve future R&D and commercialization efforts, the last objective of this work was to develop procedures for automated manufacturing and testing. As discussed in Chapters 6 and 8, this work included sensor design and processing studies involving automated screen-printing, rapid-prototyping, wire bonding, test setups, and analyses programs.

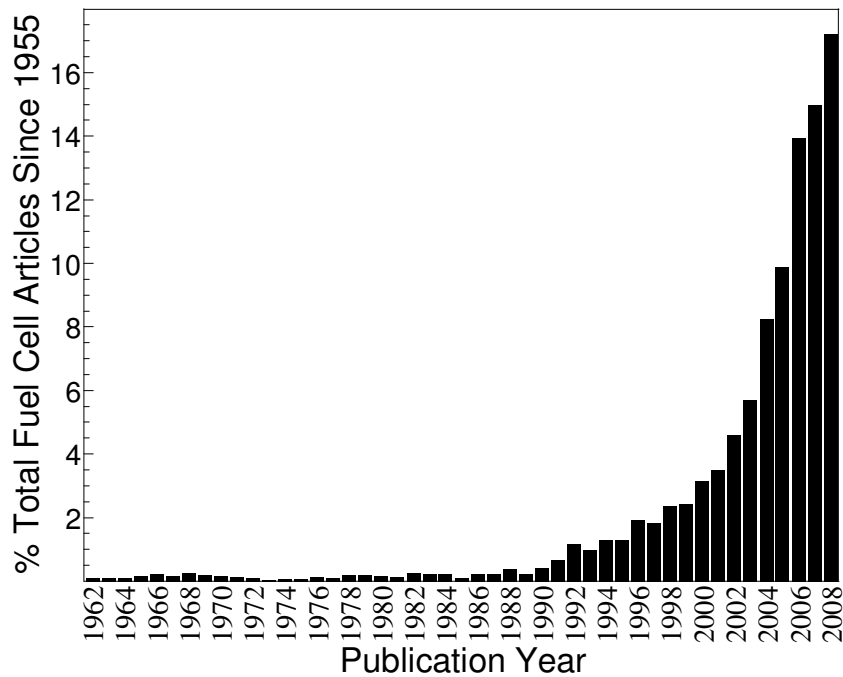


Figure 1-1. Trends in the number of publications involving fuel cells since 1955.

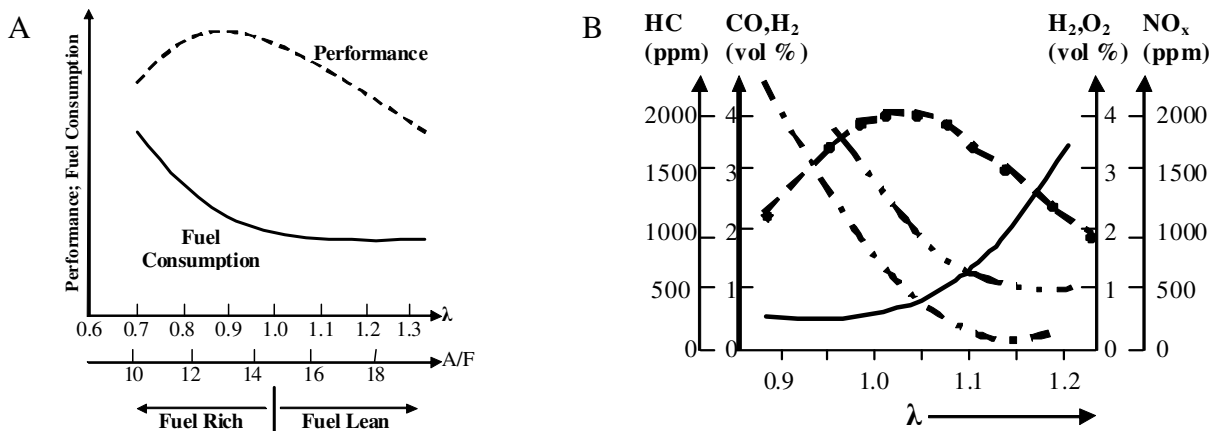


Figure 1-2. Relationship between fuel economy, air-to-fuel ratio, and pollutant emissions. Based on figures from Ertl and Knözinger.<sup>20</sup>

Table 1-1. Energy consumption data for the materials and chemical processing industries

	Chemicals	Mining <sup>†</sup>	Glass	Metal casting	Petroleum refining	Steel	Aluminum
Total Energy Consumption (10 <sup>15</sup> Btu)	6.1	1.125	0.206	0.236	7.1	2.0	1.0
As percentage of shipment value	5%	17%	5-7%	5%	1.7-4.5%	17%	8.2%
Percentage of total domestic use	6%	—	0.2%	0.2%	7.5%	2-3%	1%
Percentage of US manufacturing use	25%	—	1%	1%	29.1%	6.7%	3.3%

<sup>†</sup> Data from the mining industry is from 2000, while the others are all from 1998.

## CHAPTER 2 BACKGROUND AND LITERATURE REVIEW

### 2.1 Gas Sensors

Gas sensors are a technology that takes many forms and that have been around for a long time. In fact, the human nose is likely the most advanced gas sensor, capable of detecting over 10,000 ‘odors’; the human nose can also discriminate between odors at lower concentrations than detectable with a gas chromatograph or similar analytical system.<sup>61</sup> For this reason many gas sensor researchers prefer the term ‘electronic nose’ or ‘e-nose’, though this is typically reserved for sensor arrays employing elaborate pattern recognition algorithms to sense complex odors associated with smells such as coffee and other agricultural products.<sup>62</sup>

Much of the research on solid-state gas sensors, and in particular the potentiometric variety, has utilized combinatorial methods for materials development, where many materials are tested for sensing behavior and the ones with the best performance are selected. While this approach has merit, a more fundamental look at the overall contributions to the sensing mechanism allows a more systematic way to screen and design materials for particular applications.

Unlike analytical gas detection systems, most solid-state gas sensors are currently inadequate for commercial use because of poor selectivity. However, the solid-state sensors can be used in new applications where the use of analytical systems is not appropriate. However, to achieve sensors capable of meeting the criteria of the new applications a few areas of research and development must still be investigated. For instance, a firm understanding of the sensing mechanisms will support attempts to improve selectivity.

The following provides a literature review of gas sensor technology and issues typically dealt with in each category. More detail is covered for electrochemical gas sensors because they

are the oldest and largest group and include the specific type of sensor described in this Research Plan. This chapter also discusses fundamental theories for electrochemical gas sensors, setting a basis for the remainder of the work. Finally, some of the more effective experimental techniques used to investigate gas sensor mechanisms are discussed.

### **2.1.1 General Issues**

Several key gas sensor requirements were discussed in Chapter 1, leading engineers to have to simultaneously consider many aspects of the materials, chemical, electrical, mechanical, and other design issues. However, in general the goal for the design of any gas sensor is to make the device very sensitive and highly selective to the analyte with quick response. Any given sensing electrode must have sufficient sensitivity to the gas of interest so that a measurement can be made. Most sensing electrodes are cross-sensitive to multiple species, which increases the complexity of the sensing process when used in gas mixtures. Several techniques exist for improving selectivity, such as temperature modulation and the uses of physical or chemical filters. However, a good sensing material and understanding of the transduction mechanisms are still imperative. The most common techniques available for gas quantification are analytical detection systems. These include optical absorption/emissions detectors (e.g., Raman spectroscopy, FTIR, and chemiluminescence), gas chromatography, and mass spectrometry. Cost and size aside, these systems are limited in that real-time, online measurements are not easily achieved in many cases due to compensation methods for interference sources (e.g., soot or H<sub>2</sub>O) and limitations due to application-based restrictions (e.g., high pressure). Recent research efforts have therefore turned to improving alternative technology based on solid-state devices that can potentially overcome these limitations. A brief overview of solid-state gas sensor technology is provided below.

## **2.1.2 Solid-State Gas Sensor Technology**

### **2.1.2.1 Thermal sensors**

Thermal gas sensors include thermistors, pyroelectric devices, and catalytic gas sensors. An example of a catalytic sensor can be seen in Figure 2-1. These devices work off the first law of thermodynamics, converting the thermal energy released from a reaction to the electrical domain based on a change in temperature or heat flux through a sensing element. The sensitivity of these devices can be severely impaired if contaminated.<sup>63</sup>

### **2.1.2.2 Mass sensors**

This type of gas sensor converts mechanical energy to electrical energy via frequency shifts when an atom/molecule interacts with the device. They include piezoelectric-based microbridge devices and surface acoustic wave (SAW) sensors.<sup>63,64</sup> An example of a micromachined piezoelectric microbridge- and cantilever-based sensors can be seen in Figure 2-2. They have high sensitivity to many gases, but are also highly vulnerable to interference and limited to low temperatures.

### **2.1.2.3 Optical sensors**

Optical gas sensors convert energy from the chemical to the electromagnetic domain via absorption or fluorescence. The usual arrangement involves irradiating the sample with monochromatic radiation and observing the secondary radiation that is emitted.<sup>63</sup> An example of an optical sensing system with a solid-state detector based on gallium-nitride materials used in a combustion exhaust can be seen in Figure 2-3. These sensors offer a broad detection range and little time lag, but are particularly sensitive to noise.<sup>30</sup>

### **2.1.2.4 Electrochemical sensors**

Electrochemical sensors involve a direct transduction from the chemical to electrical domain, which involves electrode reactions and charge transport. This class of sensors can be

highly sensitive, selective, and operate at elevated temperatures. Electrochemical sensors can operate in conductometric, potentiometric, or amperometric modes. Conductometric (impedance-based) gas sensors generally consist of semiconducting oxides (e.g.,  $\text{SnO}_2$ ) as sensing layers on an insulator (e.g.,  $\text{Al}_2\text{O}_3$ ) as in Figure 2-4. Gas molecules interact with the semiconductor, acting in effect as donors or acceptors to influence the resistance, which can be detected and related to the gas concentration. While conductometric (or chemiresistive) sensors offer a simple design, they are very sensitive to oxygen concentrations, and therefore are limited to applications where the oxygen content does not vary greatly.<sup>65</sup> Potentiometric gas sensors incorporate electronic (or mixed electronic-ionic) conducting electrodes on a solid-electrolyte substrate, forming an electrochemical cell. One type of that has found widespread use in automobiles for several decades is known as the Lambda (oxygen) probe.<sup>20</sup> The most frequently used solid-electrolyte used in gas sensors is stabilized-zirconia (e.g.,  $\text{Y}_2\text{O}_3$  stabilized  $\text{ZrO}_2$ , or YSZ), which allows conduction of oxygen ions and provides a sensor that can respond quickly to changes in  $\text{PO}_2$ . As shown in Figure 2-5, the Lambda sensor typically consists of a closed-end YSZ tube with an internal platinum electrode kept at a constant high  $\text{PO}_2$  (air-reference) and an external platinum electrode that is exposed to an environment with lower and varying activity (e.g., an exhaust stream). The sensor response results from thermodynamic equilibrium and fast kinetic reactions at the interface.<sup>30</sup> Amperometric sensors are related to potentiometric sensors except that they operate away from equilibrium. As shown in Figure 2-5, a voltage is applied between the electrodes, providing the energy to drive reactions with the resulting current relating to gas concentration. For the specific case of automotive emission control, amperometric sensors can offer high selectivity in the detection of exhaust gas species but require expensive electronics attached to the sensor.<sup>66</sup>

### 2.1.3 Electrochemical Gas Sensor Theory

#### 2.1.3.1 Principles of electronic and ionic conduction

In ceramics there are two ways in which mobile electronic carriers can be generated: intrinsically (e.g., excitation across the band gap) and extrinsically (e.g., impurity doping or due to nonstoichiometry from reduction/oxidation).<sup>67</sup> Ionic conduction involves the diffusion of ions via lattice defects (i.e., vacancies and interstitials). Both modes of conduction depend on the concentration, magnitude of charge, and mobility of charged species.<sup>67,68</sup> Solid-electrolytes are materials often used to complete the circuit in electrochemical cells due to their high ionic conductivity and very low electronic conductivity. Electronic, ionic, or mixed conduction can be involved in the transduction process for solid-state gas sensors.

#### 2.1.3.2 Principles of solid-state electrochemistry

Electrochemical sensors involve the conversion of chemical energy to electrical energy. Therefore, an understanding of both types of energies is necessary. From thermodynamics, the free energy associated with a given system is defined with Equation 2-1, where  $G$  is the Gibbs free energy,  $H$  is the enthalpy,  $T$  is temperature, and  $S$  is entropy.

$$G = H - TS \quad (2-1)$$

For an isothermal process, this energy represents the work required for a reaction to proceed has the dependence in Equation 2-2, where  $\Delta G^0$  is the standard free energy change,  $R$  is the gas constant, and  $C$  is the concentration of products or reactants associated with the reaction.<sup>69</sup>

$$\Delta G = \Delta G^0 + RT \ln \frac{C_{\text{product}}}{C_{\text{reactant}}} \quad (2-2)$$

The chemical potential of a species  $i$  can be defined as the increase in the internal energy of a system composed of species  $j$  due to the addition of species  $i$  to the system.<sup>70</sup> Because the

Gibbs free energy is a function of internal potential energy, the chemical potential can be defined mathematically as in Equation 2-3, the partial molar change of free energy.

$$\mu_i = \left( \frac{\partial G}{\partial n} \right)_{T,P,n_{j \neq i}} \quad (2-3)$$

If  $i$  is a charged species (i.e., ion or electron), then the free energy will have an additional work.<sup>63,70</sup> This additional work is electrostatic in nature and results in several types of electrical potentials for electrochemical systems. An outer (Volta) potential ( $\psi$ ) exists between a charged metal surface and vacuum. An electrostatic potential drop, known as the surface potential ( $\chi$ ), also forms across the outer layer of surface atoms. Based on these two terms, an inner (Galvani) potential between the bulk and vacuum can be defined as the sum of the surface and outer potentials as in Equation 2-4.

$$\phi = \chi + \Psi \quad (2-4)$$

When considering two surfaces in contact with each other, a Galvani potential difference is formed due to the presence of charge at the interface between the two phases. The relationship between these electrical potentials is illustrated in Figure 2-6.<sup>63,68,70-73</sup>

An electrochemical potential can be defined based on combined electrical and chemical contributions involved in the increase in energy from addition of a charged species as in Equation 2-5.

$$\tilde{\mu}_i = (\mu_i + z_i F \chi) + z_i F \Psi \quad (2-5)$$

Equation 2-5 represents the link between the electrostatic and thermodynamic laws that govern the interconversion of electrical and chemical energy during electrochemical reactions.

At a solid-electrolyte/electrode/gas interface, a potential difference forms for a redox reaction as in Equation 2-6, in order to make the electron transfer thermodynamically or kinetically favorable.<sup>72</sup>



This interface is known as the triple-phase-boundary (TPB). From Equation 2-5 a relationship between this cell potential ( $E$ ) and the free energy change associated with the electrochemical reaction can be derived as Equation 2-7.<sup>69,71</sup>

$$\Delta G = -nFE \quad (2-7)$$

For reversible, thermodynamically controlled systems, therefore, the Nernst equation yields the resulting electromotive force (emf) in Equation 2-8, where  $E_0$  is the standard potential (i.e.,  $E$  when  $C_{\text{products}}$  equals  $C_{\text{reactants}}$ ),  $n$  is the number of electrons involved in the reaction, and  $F$  is Faraday's constant.

$$E = E^0 + \frac{RT}{nF} \ln \frac{C_{\text{products}}}{C_{\text{reactants}}} \quad (2-8)$$

As evident from Equation 2-8, the Nernst equation relates the emf developed at the TPB to the concentration of reactants and products.<sup>73</sup>

For non-equilibrium systems, the reaction can be either mass-transport or charge-transfer limited. For solid-state materials, the modes of mass transport are diffusion and electro-migration.<sup>67,72</sup> The driving force for diffusion is a concentration gradient, resulting in a separation of charge. This creates an electric field that drives migration. The generally accepted model for mass transport can involve multiple steps and begins with species transport in the gas phase.<sup>74</sup> As shown in Figure 2-7, there are several ways in which the electroactive species can then reach the TPB. The gas may adsorb at the (porous) electrode or on the solid-electrolyte, either by physisorption or chemisorption. The gas can adsorb and dissociate on the electrode, followed by surface or Knudsen (pore) diffusion of ionized species from the electrode to the TPB. The gas can also diffuse to the TPB through the bulk porous region of the electrode without forming an adsorbate (i.e., dissociation occurs at the TPB). Alternatively, the gas

adsorption and dissociation can occur on the surface of the solid-electrolyte, followed by transport via surface diffusion to the TPB. In each case, the ionic species undergo electrochemical reactions at or near the TPB and move into the solid-electrolyte. For YSZ,  $O^{2-}$  ions are then transported from the cathode to the anode via oxygen vacancies.<sup>68,74</sup>

In a charge-transfer limited case, the kinetics of electrochemical reactions determines the resulting current. The rates of the forward and backward reactions are related to charge transfer through the Butler-Volmer relation, Equation 2-9, where  $i_0$  is the exchange current density;  $\alpha$  is the charge-transfer coefficient; and  $\eta$  is the overpotential, or the difference between  $E$  and  $E_0$ .<sup>71</sup>

$$i = i_0 [C_O \exp(-\alpha(nF\eta)/RT) - C_R \exp((1-\alpha)(nF\eta)/RT)] \quad (2-9)$$

An example of the resulting current-potential curve is shown in Figure 2-8A. When  $E$  equals  $E_0$  there is no net current flowing and Equation 2-9 becomes Equation 2-10.

$$i = i_0 [\exp(-\alpha(nF\eta)/RT) - \exp((1-\alpha)(nF\eta)/RT)] \quad (2-10)$$

While there is no net current in this condition, a nonzero cathodic and anodic current exist, but with equal and opposite values equal in magnitude to the exchange current density.<sup>72</sup> For large negative and positive  $\eta$ , Equation 2-9 simplifies to Equations 2-11a and 2-11b, which is collectively known as the Tafel equation.

$$\ln(i) = \ln(i_0) - \alpha(nF\eta)/RT \quad (2-11a)$$

$$\ln(i) = \ln(i_0) + (1-\alpha)(nF\eta)/RT \quad (2-11b)$$

Equations 2-11a and 2-11b can be used to find values for  $i_0$  and  $\alpha$  from the extrapolation of the linear region of a Tafel plot as in Figure 2-8B. These relations are used when trying to determine the reaction kinetics.

### 2.1.3.3 Electrochemical promotion

In the field of catalysis there is a phenomenon known as promotion, in which a diffusion of adsorbed species from the metal onto the support (spillover), which can alter catalyst-support interaction and thereby enhance the catalytic reaction.<sup>75,76</sup> The function of the promoters can be classified as structural or electronic.<sup>75,77</sup> Structural promoters alter the population stabilize the dispersion of active species on the catalyst support, both of which may sharply enhance the catalytic properties of the solid. On the other hand, electronic promoters modify the chemisorptive bonding between reactants, intermediates and surface, thereby changing the catalytic process.

The so-called ‘classical’ promotion is to be distinguished from what has become known as electrochemical promotion, in which an applied bias directly to the anode and cathode of an electrochemical cell results in pumping of the mobile species (e.g., oxygen ions) from the cathode to the anode. This results in an electrochemically-controlled migration of the ions onto a catalyst electrode and causes an increased reaction rate beyond that predicted with Faraday’s Law, shown in Equation 2-12, where  $n$  is the moles of the substance involved in the reaction,  $I$  is the (constant) current passed through the cell for time  $t$ ,  $z$  is the valency of the ions, and  $F$  is Faraday’s constant ( $96,485 \text{ C mol}^{-1}$ ).<sup>78,79</sup>

$$n = \frac{I \cdot t}{F \cdot z} \quad (2-12)$$

Electrochemical promotion is also known as Non-Faradaic Electrochemically Modified Catalytic Activity (NEMCA). Much evidence in the literature suggests that NEMCA may affect such system characteristics as the work function, adsorbate bond strength, preferential adsorption sites, or intramolecular stretching frequencies.<sup>77,78,80-82</sup> These changes may alter the strength of

the chemisorptive bond of covalently bonded reactants and intermediates, thus changing activation energies and reaction rates.

#### 2.1.3.4 Semiconducting oxides

Semiconducting oxides are frequently used as sensing electrodes in both potentiometric and resistive electrochemical gas sensors.<sup>83</sup> Many of the sensing materials used in resistive gas sensors are transition metal oxides. Therefore, the surface reactions generally involve changes in the concentration of surface oxygen species such as  $O^{2-}$ .<sup>84</sup> These surface ions form as a result of charge transfer when adsorbed oxygen extracts electrons from the oxide in a reaction such as in Equation 2-13.



Other reactions with oxygen are possible and can result in additional charged or neutral molecular/atomic surface species, such as  $O^{-}$  and  $O_2^{-}$ . For n-type (p-type) materials, adsorbed oxygen acts as a surface donor (acceptor) state and results in a decrease (increase) in the major charge-carrier concentration. For the forward direction of electrochemical reactions like Equation 2-6, electrons are consumed at the surface, causing a positive space charge to develop as in Figure 2-9. An electric field forms between the positive charge and remaining electrons in the “depleted region,” which acts to oppose (and eventually stop) charge transfer.<sup>85</sup>

Any modification to the surface concentration of oxygen ions changes the surface state. This results in a change of carrier concentration and the resistance of the oxide.<sup>84</sup> Other than a direct change in  $PO_2$ , the oxygen ion concentration can change if a reducing gas (e.g., NO or CO) is introduced and reacts with adsorbed oxygen as in Equation 2-14.



For an n-type (p-type) material, reducing gases decrease (increase) the resistance because electrons are added to the material. The opposite is true for oxidizing gases (e.g., NO<sub>2</sub> or CO<sub>2</sub>).

The sensing process of conductimetric sensors can be separated into 'interaction' and 'transduction' steps. Interaction steps include surface, catalytic, grain-boundary, bulk, and TPB reactions and adsorption.<sup>74,86</sup> Transduction steps involve the way in which the sensor responds to the interaction steps and produces a signal.<sup>87</sup> Both steps depend on numerous factors, including whether the sensing layer is compact or porous. A compact layer does not allow gas molecules to penetrate beyond the surface, while the gas can interact with grain surfaces throughout a porous layer. Therefore, as shown in Figure 2-10A, conduction in a compact layer results only from the surface or bulk (depending on the layer thickness).<sup>86,88</sup> A porous layer, however, has an additional contribution from grain boundaries.

For a porous layer, Schottky barriers to conduction may also form in between semiconducting grains as seen in Figure 2-10B. Whether intergranular Schottky barriers form depends on how the grain diameter ( $d$ ) compares to the Debye length ( $\lambda_D$ ). The Debye length is a measure of the distance beyond which the disturbance at a junction no longer effects the electron distribution away from the junction.<sup>85</sup> Schottky barriers will form for large grains ( $d > \lambda_D$ ) and result in band bending, while there is a flatband condition for small grains as shown in Figure 2-10C. The size of the neck region between grains can also form a barrier for the same reason.<sup>88</sup>

Two additional sources of barriers to conduction are Ohmic contacts and rectifying (Schottky) junctions between semiconductor and metal electrodes. The relative work functions ( $\Phi$ ) of the materials determine which barrier forms at the junction.  $\Phi$  is the minimum energy to remove an electron from inside a metal to vacuum. For an n-type (p-type) semiconductor with

$\Phi_M > \Phi_S$ , a rectifying (Ohmic) barrier is formed; the opposite results when  $\Phi_M < \Phi_S$ .<sup>89</sup> These effects are important when considering the effects of current collectors on the sensor signal.

### 2.1.3.5 Mixed potential theory

Weppner et al. have designated three types of gas sensors based on solid-electrolytes.<sup>84,90</sup> Type I sensors include the  $\lambda$ -probe and involve the direct participation of a mobile ion in the solid-electrolyte coming to equilibrium with the species involved in charge transfer at the TPB. Type II sensors do not involve equilibria between a mobile ion in the electrolyte and the analyte, rather the species to be detected is incorporated into the solid-electrolyte. Type III sensors can have more than one reaction occurring at an electrode, and show non-Nernstian behavior.

Fleming first introduced the idea of mixed potential as an explanation for this non-Nernstian behavior.<sup>83,84</sup> The theory states that the sensor emf results from the simultaneous reactions of cathodic reduction and anodic oxidation on a single electrode. This can occur when multiple chemical species cause two or more (independent) charge transfer processes.<sup>90</sup> In this case, a mixed potential forms with a value that is somewhere between the Nernstian potentials of the individual processes. The system is not in equilibrium even though the net current is zero. For example, Figure 2-11A shows a mixed potential resulting from reactions A and B. When dissimilar electrodes are exposed to the same gas environment, the mixed potentials formed at the electrodes will most likely differ.<sup>84</sup> Figure 2-11B, shows how a potential difference from gold and platinum electrodes in one environment can result from their individual mixed potentials.

'Mixed Potential' sensors originally utilized only noble metal electrodes and had an air-reference. Researchers, however found that at high temperatures sensor stability decreased due to changes in electrode morphologies.<sup>83</sup> Therefore, metal oxide electrodes were investigated as

sensing electrodes because they have improved long-term thermal and chemical stability, reduced costs, and can show improved gas sensitivities.<sup>83</sup>

These properties led Wachsman to develop a new, more inclusive concept known as ‘Differential Electrode Equilibria’.<sup>65,91</sup> This has led other researchers such as Traversa et al. to perform studies that have suggested that mixed potential theory agrees with experimental data when sensors use metal electrodes (even in the same gas environment) and when they have semiconducting electrodes used with an air reference. However, when sensors have metal and semiconducting electrodes exposed to the same gas environment there are responses that the mixed potential theory cannot explain.<sup>83</sup> In fact, Wachsman et al. have shown that the methods for proposing mixed potential mechanisms can lead to false confirmations.<sup>92</sup> Both of these research groups have shown evidence that a more general theory is required to explain the mechanisms that create the overall emf response.

#### **2.1.3.6 Differential electrode equilibria theory**

The ‘Differential Electrode Equilibria’ theory states that the potential difference between a semiconducting metal oxide and a reference electrode in the same gas environment can be a result of combined heterogeneous catalytic, electrocatalytic (at the TPB), and semiconducting effects.<sup>65</sup> At higher temperatures (e.g., >600 °C) catalytic reactions dominate conductivity and the mixed potential theory can be a good descriptor. However, at lower temperatures there is a “semiconducting effect” in the sensing electrodes. This occurs as gases adsorb onto the surface causing changes to the Fermi level and thus the potential drop across the electrode. This being the case, the measured potential difference between the two electrodes depends on the rates of catalytic reactions at the electrodes, electrochemical reactions at the TPB, and band-bending in the oxide.

Recently, investigators have displayed evidence for this theory and shown that mixed potential does not always explain the sensor response.<sup>65,92-100</sup> Wachsman et al. and Traversa et al. have investigated p-type ( $\text{La}_2\text{CuO}_4$ ,  $\text{LaFeO}_3$ , and  $\text{La}_x\text{Sr}_{1-x}\text{FeO}_3$ ) and n-type ( $\text{Nb}_2\text{O}_5$ ,  $\text{WO}_3$ , and Ta-doped- $\text{TiO}_2$ ) metal oxides at elevated temperatures.

### 2.1.3.7 Electrolyte and gas sensing electrode materials

The primary components of a solid-state potentiometric gas sensor are the solid-electrolyte and the sensing electrode(s). Yttria-stabilized zirconia (YSZ) is the most widely used solid-electrolyte. At elevated temperatures, pure zirconia,  $\text{ZrO}_2$ , has a cubic-fluorite structure as shown in Figure 2-12. At lower temperatures, the material becomes tetragonal and then monoclinic.<sup>85</sup> In order to maintain the cubic-fluorite structure at lower temperatures, the zirconia is substitutionally doped with yttria,  $\text{Y}_2\text{O}_3$ , with the larger  $\text{Y}^{3+}$  cations stabilizing the crystal structure. This results in the formation of oxygen anion vacancies in order to maintain charge neutrality as shown in Equation 2-15 using the Kröger-Vink notation.



In addition to stabilizing the material, these oxygen vacancies are mobile at elevated temperatures, thus accounting for the ionic conductivity of the solid-electrolyte. For gas sensors, which typically require a fast response, a typical yttria dopant concentration is 8 mol% which gives the maximum ionic conductivity (e.g.,  $\sim 1.8 \text{ S cm}^2$  at  $800 \text{ }^\circ\text{C}$ ).<sup>68</sup> Because there is negligible electronic conduction in the YSZ, the sensing electrodes of a potentiometric gas sensor are kept from short circuiting, which allows an open circuit potential to be measured.

As mentioned above, one gas sensor material of interest for detecting  $\text{NO}_x$  gases is lanthanum copper oxide ( $\text{La}_2\text{CuO}_{4+\delta}$ ), a p-type metal-oxide. The “ $\delta$ ” in  $\text{La}_2\text{CuO}_{4+\delta}$  accommodates changes to the oxygen composition under certain conditions (e.g., low  $\text{PO}_2$  or very high

temperature) and signifies that this material can be nonstoichiometric. However, the operating  $\text{PO}_2$  and temperature of the gas sensor in this work are not within the ranges that results in nonstoichiometry.<sup>101,102</sup> At temperatures between 250 °C and 950 °C the material is tetragonal and can act as either a semiconductor (excess  $\text{O}^{2-}$ ) or as a metal ( $\text{O}^{2-}$  deficient). The crystal structure for the perovskite-type  $\text{La}_2\text{CuO}_4$  can be seen in Figure 2-13. The space group is  $I4/mmm$  and consists of alternating layers of perovskite-type ( $\text{LaCuO}_3$ ) and rocksalt-type ( $\text{LaO}$ ) units along the long axis.<sup>103,104</sup> XRD and mass spectrometry measurements have revealed that (at sufficiently high  $\text{PO}_2$ ) oxygen enters the  $\text{La}_2\text{CuO}_4$  lattice as  $\text{O}_i''$  and is compensated by holes ( $h'$ ).<sup>105</sup> Analogous to acceptor-doped semiconductors, conduction in the oxygen doped  $\text{La}_2\text{CuO}_{4+\delta}$  involves  $h'$  transport and the  $\text{O}_i''$  can be considered stationary due to low mobility. The  $\text{O}_i''$  form in the  $\text{La}_2\text{O}_2$  layers, while holes are created in the  $\text{CuO}_2$  planes by charge transfer with  $\text{O}^{2-}$  anions. Analysis of the conductivity tensor confirms this and shows conduction limited to the two-dimensional  $\text{CuO}_2$  planes perpendicular to the long axis.<sup>106</sup>

Electrical conductivity can also be influenced by grain size, which is controlled with the sintering process during fabrication. As the sintering temperature increases, larger grains grow by consuming smaller ones. This results in grains with less restrictive grain boundaries and, thus, increased conductivity. However, at certain sintering temperatures conductivity decreases as pathways are severed by cracks between grains.<sup>107</sup> Grain boundaries act as sinks to impurities and defects, resulting in space-charge regions between intergranular contacts.<sup>108</sup> The resultant band bending leads to potential (Schottky) barriers where charge carriers can become trapped. Therefore, a 'semiconducting effect' can influence the sensitivity because the energy barrier impedes hole transport between neighboring grains. This changes with the bulk/surface charge

ratio and is a function of temperature,  $\text{PO}_2$  (from the defect model  $\sigma_{\text{bulk}} \sim \text{PO}_2^{1/6}$ ), grain size, and intrinsic/extrinsic defect concentrations.

The potentiometric sensors studied in this work are primarily constructed from YSZ as a solid-electrolyte and  $\text{La}_2\text{CuO}_4$  as a sensing electrode. Pt was also used as a ‘psuedo-reference’ electrode and as heating elements/temperature sensors. However, the principles investigated in this work can be applied to other materials.

## 2.2 Related Work

### 2.2.1 Techniques for Studying Gas Sensor Mechanisms

Several types of experimental techniques may be used in any attempt to deconvolute the mechanisms responsible for determining the response of a gas sensor.<sup>109,110</sup> Any single technique is unlikely to yield enough information to make sound conclusions. The techniques include electrical and optical measurements with the most relevant types discussed below.

#### 2.2.1.1 Conductivity measurements

As discussed above, electronic and ionic conduction in a material can vary with changes in the concentration of mobile charged species. Resistance measurements as a function of varying  $\text{PO}_2$  are often used to determine the concentration of carriers in metal oxides. This is done with the construction of a Kröger-Vink diagram to determine defect equilibria.<sup>67</sup> For sensors that may be based on differential electrode equilibria, this method can provide insight into changes in conductivity due to band-bending. For instance, the theoretical 1/6 dependence of conductivity for  $\text{La}_2\text{CuO}_4$  has been confirmed on many occasions.<sup>93,101,102,111,112</sup> Furthermore, the responses of  $\text{La}_2\text{CuO}_4$  to several pollutant gases were compared in both the potentiometric and resistive configurations. Both the potentiometric and resistive sensors showed a negative response for oxidizing gases and a positive response for reducing gases.<sup>93</sup> The two types of sensors also both

showed improved response times and lower magnitudes at higher temperatures due to favorable kinetics.

### **2.2.1.2 Controlled-potential techniques**

The electrodes making up an electrochemical cell can be polarized to investigate the reactions occurring at the TPB.<sup>72</sup> Such controlled-potential techniques (i.e., voltammetry) can be used to drive redox reactions. For example,  $\text{La}_2\text{CuO}_4$  based samples were polarized in an experiment to demonstrate how assumptions made in the mixed potential theory can lead to different results regarding the sensing mechanism, thereby lending support for the differential electrode equilibria theory.<sup>92</sup> In a variant of these techniques, a voltage (or current) hysteresis loop is made and the resulting change in current (or voltage) can be measured and the peaks in the current-voltage plot related to the dissociation of chemical species at the TPB. This cyclic voltammetry technique was used to explore selective electrocatalytic reduction of NO with a series of  $\text{K}_2\text{NiF}_4$ -type perovskites, including  $\text{La}_2\text{CuO}_4$ .<sup>113,114</sup>

### **2.2.1.3 Electrochemical impedance spectroscopy**

One of the most popular experimental techniques for exploring gas sensor mechanisms is electrochemical impedance spectroscopy (EIS). Mass transport, rates of reactions, defects, microstructure, and compositional influences on conductivity can impede electron flow in an electrochemical cell.<sup>115</sup> A small signal sinusoidal voltage is applied to the electrode of interest, or working electrode (WE), and kept constant with respect to a reference electrode (RE) using feedback circuitry. The response current flows between the WE and the counter electrode (CE), and is used to calculate impedance. After performing EIS over a range of frequencies, data can be fit to an equivalent circuit. For example, the presence of high- and low-frequency features in the EIS spectrum provided an indication for nonelectrochemical contributions to the  $\text{NO}_x$  sensor response of a  $\text{La}_2\text{CuO}_4$ -Pt potentiometric sensor.<sup>116</sup> However, the analysis of EIS

data can be ambiguous to interpret and in some cases multiple equivalent circuits can fit the data.<sup>115,117</sup>

#### **2.2.1.4 Mass spectrometry**

Mass spectrometry can be used to investigate homogeneous and heterogeneous catalysis in a specific system. This technique is based on ionizing an analyte gas and characterizing the resulting ions for mass and charge. Experiments include catalytic conversion measurements or the investigation of reaction kinetics (i.e., temperature programmed reaction, TPR) and adsorption/desorption processes (i.e., temperature programmed desorption, TPD). For example, TPR and TPD experiments for  $\text{NO} + \text{O}_2$  and  $\text{NO}_2 + \text{O}_2$  over  $\text{La}_2\text{CuO}_4$  powder were performed using a quadrupole mass spectrometer.<sup>94</sup> The TPR results were believed to indicate that a catalytic mechanism for NO over LCO is unlikely because NO remains stable (i.e., no heterogeneous reactions).<sup>93-99</sup> From TPD experiments, the LCO has displayed strong adsorption of NO below 450 °C, while above this temperature the gas can adsorb and desorb quickly. This is believed to explain why the LCO based sensor shows very good sensitivity to NO starting around 450 °C. The TPR and TPD indicate that a deviation from the mixed potential theory for NO might be explained with the semiconducting effect. On the other hand, TPR experiments have also shown that  $\text{NO}_2$  is unstable over LCO above 450 °C and heterogeneously decomposes. This means that catalytic effects could be influencing the response.<sup>98</sup> However, the TPD for  $\text{NO}_2$  is more complicated than for NO and concrete conclusions are difficult to make.

#### **2.2.1.5 Kelvin probe work function measurements**

A Kelvin Probe (KP) is a non-contact, non-destructive surface science tool that allows in situ measurements of induced changes in the work function (WF) of a gas sensitive material due to modifications from adsorbed gases.<sup>118</sup> The basic idea of this method is to form a capacitor out of the studied electrode and a reference electrode.<sup>119</sup> A wire connecting one side of the reference

to a side of the sample completes the circuit and results in the formation of a contact potential difference (CPD) and electric field between them. The CPD is related to the differences in the WFs ( $\Delta\Phi$ ) of the two materials. The reference electrode (or, less commonly the sample) is mechanically set to vibrate vertically above the surface of the specimen. The equivalent capacitance is modulated as the gap between them changes. The relationship between compensating voltage ( $V_0$ ), the current ( $i$ ), and capacitance ( $C$ ) is shown in Equation 2-16, where  $Q$  is the charge on the capacitor plates and all voltages are assumed constant.<sup>109,118-124</sup>

$$i(t) = \frac{dQ}{dt} = \frac{d}{dt}(V_0 - \Delta\Phi)C = (V_0 - \Delta\Phi)\frac{dC}{dt} \quad (2-15)$$

$V_0$  is adjusted until equal to the CPD (i.e., where  $i(t)$  goes to zero). In a real experiment, care must be taken to ensure the WF of the KP reference electrode remains constant. Several techniques exist for overcoming this issue and make this a powerful technique.<sup>124,125</sup>

### 2.2.1.6 Electron spectroscopic techniques

Electron spectroscopy is a set of techniques in which the measurement of emitted electrons from a solid can yield information about the bulk and surface characteristics.<sup>75</sup> Electron spectroscopic methods allow non-destructive, quantitative determination of oxidization states, local chemical environment, electronic band structure, and elemental analysis of the surface and subsurface of an adsorbate-material system.<sup>126</sup> Photoelectron spectroscopy involves the photoemission of electrons following irradiation with electromagnetic energy (i.e., light).<sup>126-131</sup> In x-ray photoelectron spectroscopy (XPS) a high energy photon ionizes an atom, thereby ejecting a free electron from the strongly bound inner orbitals and the outer valence level orbitals. As the photoelectrons emitted from the sample reach the detector, a spectrum is collected with characteristic peaks.<sup>126</sup> The peak intensities depend on the photoionization cross-section, which corresponds to the number and type of atoms present. The number of peaks is

related to the number of occupied levels in the atoms with binding energies lower than that of the incident radiation. The position of the peaks is dependent on the binding energy of the particular orbit of the electron and therefore gives elemental information. The XPS spectrum may also consist of many complex features, including *doublet peaks* used in elemental identification; *multiplet splitting* which provides information on chemical bonding; and '*shake-up*' *satellite peaks* used in chemical-state identification. These appear as a result of coupling between electrons and atoms in the solid and are related to relaxation processes as the photoelectron passes through the surface into vacuum.<sup>126,128-130</sup>

Ultraviolet photoelectron spectroscopy (UPS) is related to XPS and, in fact, the photoionization process is identical.<sup>126</sup> However, the lower energy ultraviolet radiation results mostly in information (i.e., electrons) from the surface of the solid. While XPS is generally used to characterize the bulk and subsurface regions of a solid, UPS primarily yields information about the electronic structure at the surface and can be used to study valence and electron bands or as a means to identify adsorbed surface species and investigate surface binding energies.<sup>75,126,131</sup>

Auger electron spectroscopy (AES) measures Auger electrons that are emitted during XPS as a result of electron decay, providing additional spectra to deconvolute the compositional information.<sup>126</sup> Auger electrons can also be emitted when a beam of electrons is incident on a surface, but there is no need to do this if the experiment already involves irradiation with x-rays.

### **2.2.2 Electric-Field Effects in Surface Processes and Solid-State Devices**

Certain gas sensors known as CHEMFETs, or chemical field-effect transistors, are related to the standard electronic semiconductor devices such as MOSFETs.<sup>63</sup> An electric field applied to a semiconductor results in modification of the carrier concentration, and these devices use this effect (through the use of a gate voltage) to control an electron channel through the device.<sup>63,89</sup>

In the CHEMFET, a gas sensitive material acts as the gate and provides a means to detect species when the electron conduction channel is opened from a change in the gate field. The research groups of Doll et al and others have developed a modified version of the CHEMFET, called work function sensors or gate-refreshable CHEMFETs, in which the device takes advantage of the Wolkenstein's concept of 'electroadsorptive' effect in order to enhance reversibility.<sup>132-135</sup> Another method of refreshing the sensor involves the use of UV illumination. Furthermore, Tuller et al have investigated the use of photo-induced improvements in chemiresistive gas sensor sensitivity and selectivity, and photo-activated catalysis in solid oxide fuel cells.<sup>136,137</sup> Also, NEMCA involves the electric-field from the double layer created by spillover ions, and the process has been used in electrochemical reactors for industrial processes and discussed for use in other solid-state ionic technology such as batteries and fuel cells.<sup>138</sup> These phenomena can be described with Wolkenstein's electronic theory of chemisorption which will be discussed in detail in Chapter 5.

### **2.2.3 Other Important Electrolytes and Sensing Electrodes**

Tables 2-1 and 2-2 list some of the important electrolyte and sensing electrode materials used in gas sensors. As can be seen, most of the materials can be used to sense multiple gases. This is why improvements in the understanding of sensing mechanisms and the development of new materials is so important to the success of such devices. However, the general volume of materials knowledge from most types of solid-state gas sensors can be used to improve and enhance the performance and capabilities of the potentiometric gas sensors based on differential electrode equilibria.

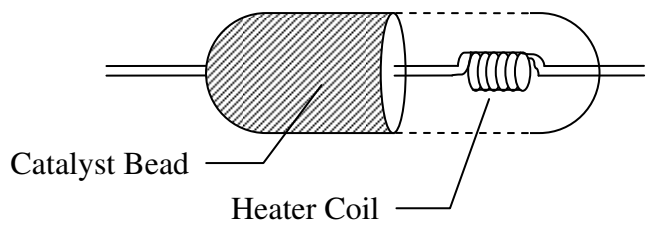


Figure 2-1. Solid-state ‘thermal’ (catalyst) gas sensor. Based on a figure from Azad et al.<sup>87</sup>

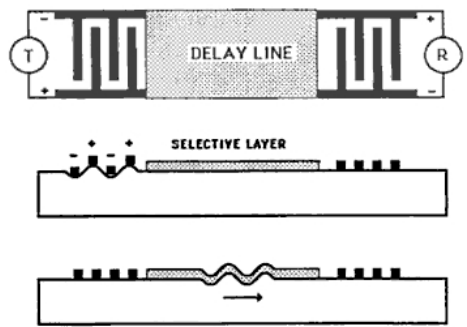


Figure 2-2. Solid-state ‘mass’ gas sensor. From Jinata.<sup>63</sup>

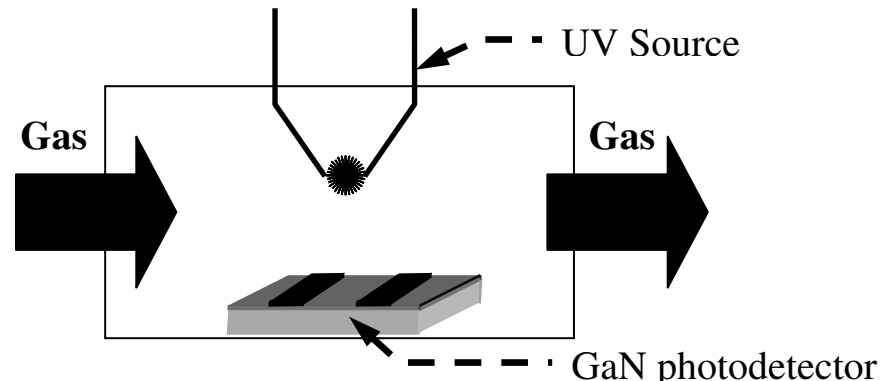


Figure 2-3. Conceptual representation of a solid-state ‘optical’ gas sensor.

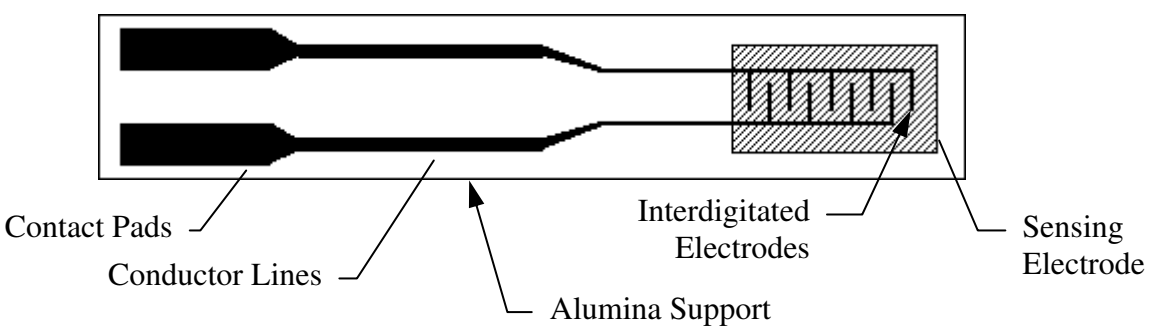


Figure 2-4. Solid-state ‘electrochemical’ (chemiresistive) gas sensor. Based on a figure in Barsan and Weimar.<sup>88</sup>

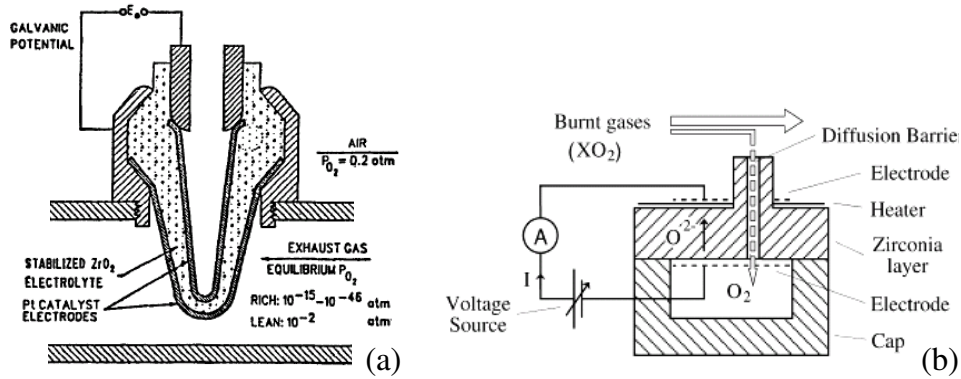


Figure 2-5. Schematics of Lambda (oxygen) probe and an amperometric gas sensor. From Azad et al.<sup>87</sup>

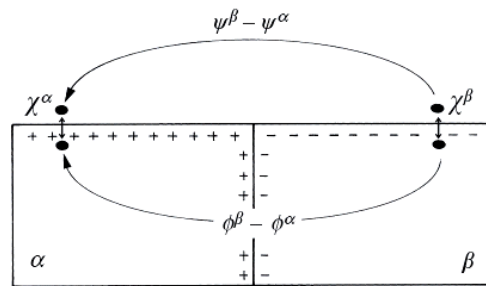


Figure 2-6. Relationship between Volta, surface, and Galvani potentials in a metal. From Girault.<sup>70</sup>

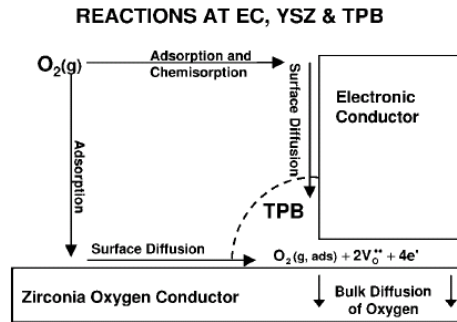


Figure 2-7. Illustration of various reaction paths that can occur at the electrical conductor, electrolyte, and triple-phase-boundary in an electrochemical device. From Nowotny et al.<sup>74</sup>

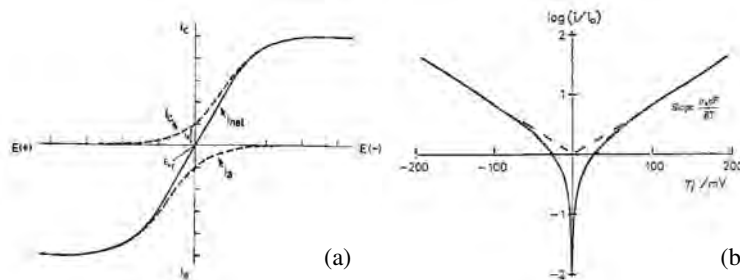


Figure 2-8. Current-potential curve from Butler-Volmer equation and Tafel plot. From Wang.<sup>72</sup>

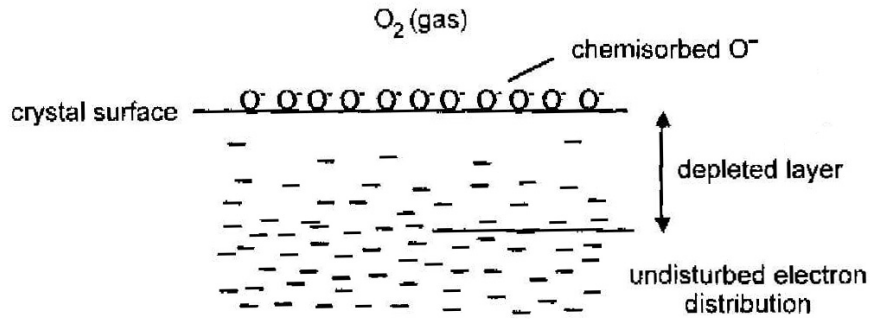


Figure 2-9. Formation of depleted surface layer during chemisorption of  $O_2$  gas. From Moulson and Herbert.<sup>85</sup>

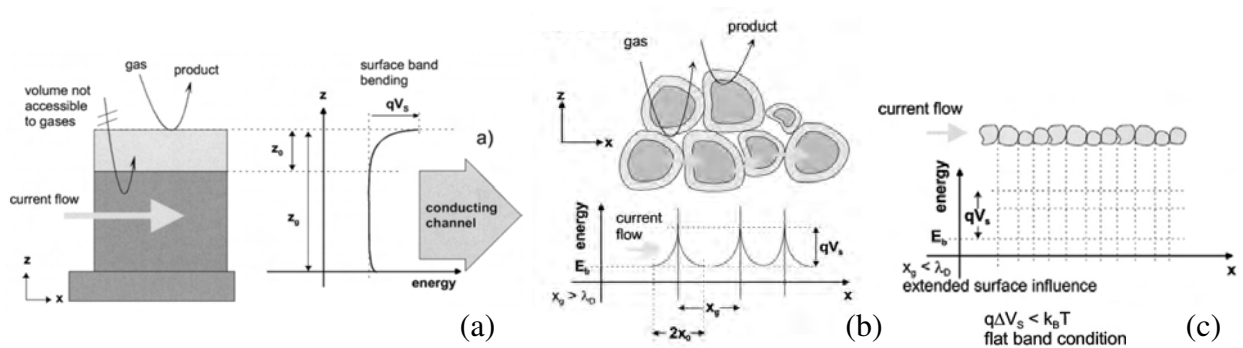


Figure 2-10. Schematic showing barriers to conduction. From Barsan and Weimar.<sup>88</sup>

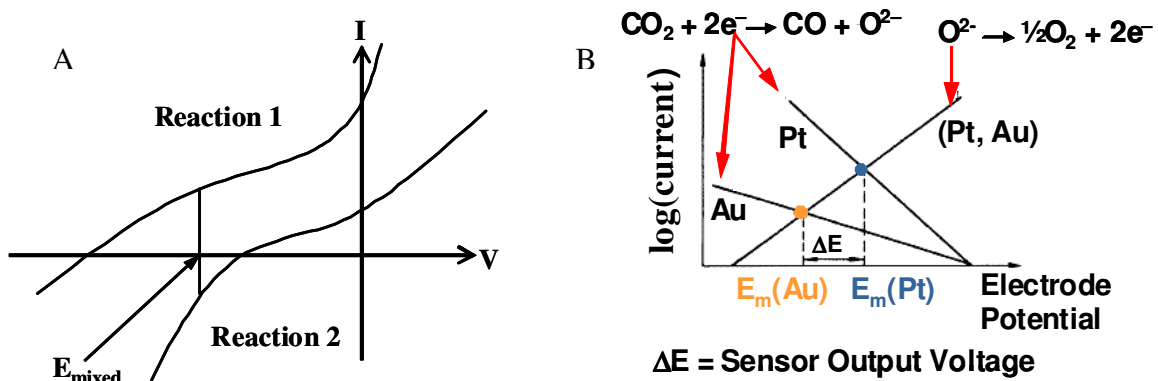


Figure 2-11. Basic concept of mixed potential theory.

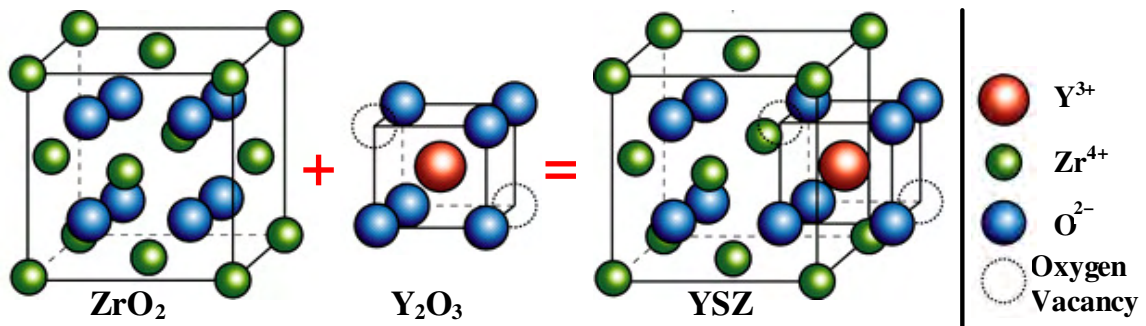


Figure 2-12. Cubic-fluorite structure of yttria-stabilized zirconia (YSZ) solid electrolyte.

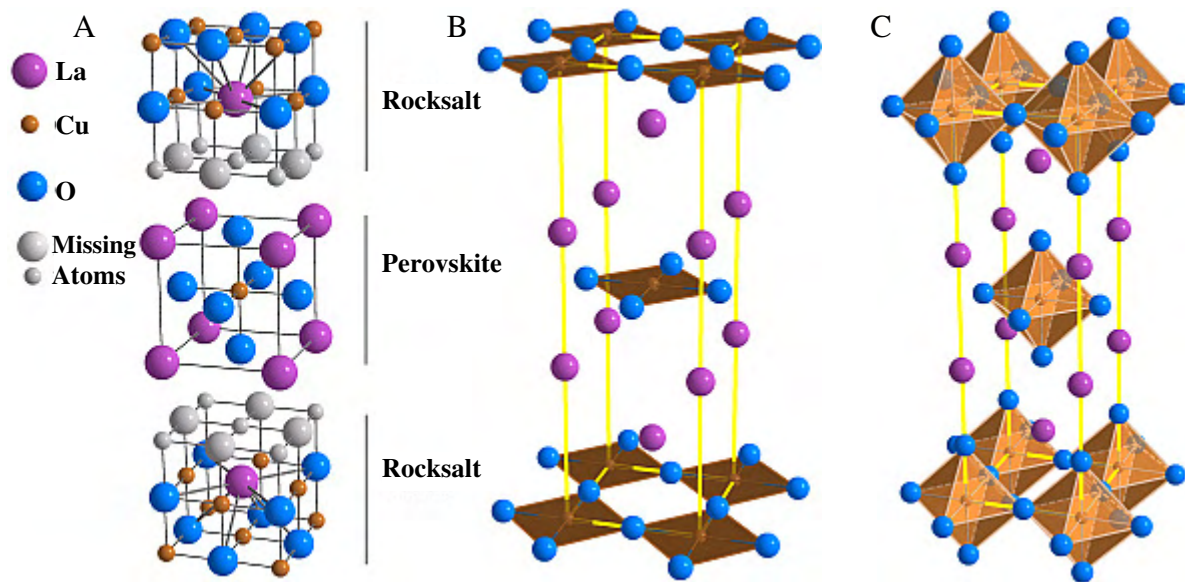


Figure 2-13.  $\text{La}_2\text{CuO}_4$  crystal structure illustrating perovskite-type nature.

Table 2-1. Key electrolytes for gas sensors

Material	Gas
YSZ	CO, CO <sub>2</sub> , NO <sub>x</sub> , O <sub>2</sub> , various hydrocarbons
β-Al <sub>2</sub> O <sub>3</sub>	CO <sub>2</sub> , AsO <sub>x</sub>
Nafion (NaSiCON)	SO <sub>x</sub>

Table 2-2. Key sensing electrodes for gas sensors

Material	Gas
SnO <sub>2</sub>	CH <sub>4</sub> , CO, NO <sub>x</sub> , H <sub>2</sub> , H <sub>2</sub> S, H <sub>2</sub> O
LaFeO <sub>3</sub>	C <sub>2</sub> H <sub>5</sub> OH, NO <sub>x</sub>
WO <sub>3</sub>	H <sub>2</sub> S, O <sub>3</sub> , NO <sub>x</sub> , NH <sub>3</sub> , H <sub>2</sub> , C <sub>2</sub> H <sub>6</sub> O, CO
ZnO	CO, CH <sub>4</sub> , C <sub>3</sub> H <sub>8</sub> , C <sub>2</sub> H <sub>6</sub>

## CHAPTER 3 DIFFERENTIAL ELECTRODE TEMPERATURE EFFECT

### 3.1 Introduction

Solid-state potentiometric gas sensors based on semiconducting metal-oxides show much promise as NO<sub>x</sub> detectors for applications ranging from emissions control in combustion exhausts to disease diagnostics breath-analysis.<sup>30,50</sup> They are sensitive to ppm and sub-ppm levels of NO<sub>x</sub>, CO, and HCs and have fast response times.<sup>1,65,91,139</sup> However, the selectivity of these sensors is currently inadequate for commercial application.<sup>55,56</sup> In fact, this is the major limitation of most solid-state gas sensors.<sup>140</sup> One approach for improving selectivity is the use of an array with multiple sensing electrodes, each with a different selectivity. During operation the signals from the array are entered into linear algorithms established during an initial calibration process. The array can then be used to find the concentrations of each measurant (e.g., NO). This approach was used for quantitative determination of CO, NO, NO<sub>2</sub>, and O<sub>3</sub> in ambient air environmental monitoring with resistance-type sensing elements.<sup>141,142</sup> Therefore, this work is aimed at improving selectivity of solid-state potentiometric gas sensors through local thermal modifications of the sensing electrodes using two investigatory gas sensor arrays. These were tested as an initial proof of concept and to understand changes in sensitivity, selectivity, and other observed phenomena.

### 3.2 Background

Potentiometric gas sensors based on measuring the potential difference between a semiconducting metal oxide and a noble metal pseudo-reference electrode in the same gas environment offer highly selective devices that are easily manufactured and robust in harsh environments.<sup>143,144</sup> These devices were originally thought to be governed solely by mixed potential, where an electromotive force is produced at the gas/electrode/solid-electrolyte

interface as a result of competing anodic and cathodic reactions occurring at a single electrode.<sup>83</sup> Recent evidence, however, suggests that the more inclusive differential electrode equilibria theory describes sensor responses that cannot be explained with the mixed potential theory alone.<sup>65,91-93,96-98,100,116,139,145,146</sup> This theory predicts that the potential difference of an electrode-pair can result from the individual equilibria of the electrodes, including differences in heterogeneous catalytic reactions, semiconductor band-bending, and/or electrocatalytic (mixed potential) reactions.

A well-suited material for NO<sub>x</sub> detection in combustion exhausts is La<sub>2</sub>CuO<sub>4</sub> (LCO), a p-type semiconducting metal-oxide. As with most gas sensing electrode materials, the sensitivity of LCO to NO and NO<sub>2</sub> varies with temperature.<sup>147</sup> At higher temperatures, a loss in NO sensitivity results in improved NO<sub>2</sub> selectivity with potentiometric gas sensors using a La<sub>2</sub>CuO<sub>4</sub>-Pt electrode-pair. This means that thermal modification of individual electrodes in an array may result in improved selectivity. To achieve maximum selectivity for each gas, an array can have, for instance, two La<sub>2</sub>CuO<sub>4</sub> electrodes kept at different temperatures using a heater. The selectivity of individual sensing elements can then be adjusted using this 'differential temperature effect' to achieve sufficient signal disparity for accurately calculating pollutant concentrations.

Heating elements and resistance-temperature-devices (RTD) typically utilize platinum when designed for high-temperatures. Platinum is an industry standard for high-temperature gas sensors because of excellent durability and chemical and thermal stability, even in harsh environments. Though the choice of material is fairly straightforward, the actual heater and temperature sensor designs need to be considered. In general, surface temperature measurements are very difficult and some of the best methods available include use of optical infrared sensors

and RTDs. This is especially true in high-temperature environments due to the influence of the surrounding gas. However, platinum RTDs can be calibrated using a simple polynomial equation (see Appendix A for details).<sup>148</sup> Furthermore, heating elements can be used not only to heat another object but also concurrently as a temperature sensor.<sup>149,150</sup> If the resistance of the heater can be accurately determined, then the temperature of the Platinum element can be calculated.

### **3.3 Experimental**

This work involved the study of two investigatory sensor arrays to study the differential temperature effect. Figure 3-1 shows the first design, which consisted of two LCO sensing electrodes (LCO1 and LCO2) and a platinum pseudo-reference on the top with C-shaped Pt elements on the opposite side aligned with the electrodes. Many samples were made with four Platinum elements on the back, but for the initial experiments only three were used; one heater/temperature sensor aligned with the LCO1 sensing electrode and two temperature sensors.

In order to gauge the effectiveness of the investigatory sensor array design (e.g., sensing electrode spacing with respect to the heater and each other), thermal analysis was used as a tool to determine the temperature profile of the device when heated locally. Finite Element Modeling was performed using the device geometry (e.g., heater and substrate dimensions) and the characteristic properties of the system and device materials.<sup>151</sup> The properties were determined through experiment and from available material datasheets. One of the resulting thermal models for the can be seen in Figure 3-2 for an ambient furnace temperature of 450 °C and a heater temperature of approximately 515 °C. The thermal gradient between the top and bottom of the substrate was found to be negligible because the substrate is very thin (~0.1 mm). This means that Platinum temperature sensors provide good estimates for the real temperature of the sensing electrodes, even though they are on opposite sides of the substrate.

The second investigatory sensor array consists of two LCO and two Platinum sensing electrodes as shown in Figure 3-3. This yields a total of six distinct signals from four sensing electrodes: these are sensing electrodes of similar temperature and different material; different temperature and different material; and different temperature and similar material. As with the first investigatory array, all of the C-shaped Platinum elements aligned with the sensing electrodes (on the opposite side of the substrate) are used as temperature sensors. However, in the second array the inner LCO and Pt electrodes are heated (LCO(2) and Pt(3)), while the outer LCO and Pt electrodes (LCO(1) and Pt(4)) remain near the furnace temperature.

Platinum elements were tested using serpentine and C-shaped patterns on planar YSZ substrates and calibrated with custom software as described elsewhere.<sup>151</sup> The software also calculated the temperatures for each electrode during the tests. Calculated temperatures agree with results from the thermal modeling. Once repeatability and stability were confirmed, different coplanar sensing electrodes were tested with a heater on the opposite side.

### **3.3.1 Sample Preparation**

Platinum paste (Heraeus) was screen-printed as C-shaped Platinum elements on planar YSZ substrates (Marketech) and sintered at sufficiently high temperature to achieve good adhesion and a dense conduction layer. LCO powder was synthesized using a wet-chemical route (auto ignition lean) and characterized in past experiments.<sup>147</sup> The LCO powder was mixed with Polyethylene Glycol (PEG 8000, Fischer Scientific) to form screen printing ink. Then, the Pt and LCO sensing electrodes were coated onto the opposite side of the YSZ, aligned with the middle of a corresponding Platinum element using a manual screen printer. Finally, the arrays were sintered at a lower temperature of 800 °C for 8 hours. X-ray diffraction (XRD) was used to confirm phase purity.

### 3.3.2 Test Setup

The experimental setup consisted of a quartz furnace tube with sample holder and wire guides, two computers, and a bank of mass flow controllers with control box. For these initial experiments a Keithley 2400 Sourcemeter, Keithley 2000 Digital Multimeter (DMM) with 10-channel scancard, and a Keithley 2000-20 DMM with 20-channel scancard were used to control the heater, monitor the electrode temperatures, and acquire the OCP measurements from the sensing electrodes. Two DMMs were used to avoid any possible complications associated with differences in the measurement ranges for the Platinum elements and the sensing electrodes. The sensor array was connected to the instruments with a custom wire-harness.

### 3.3.3 Testing Procedures

Prior to testing the gas sensor array, custom software (NI LabVIEW™, Version 7.1) was used to calibrate the Platinum elements on the surface of the YSZ substrate. The software measured the resistances of the Platinum elements as the furnace ramped to 750 °C from room temperature at 2-5 °C/min. Data was acquired using a Eurotherm 2408 furnace controller and a Keithley 2000-20. The resistance data was then fit to a polynomial equation describing the temperature dependence of the platinum resistance using either the 'Curve Fit Tool' in MATLAB™ (Version 7.0) or within the LabView program. The software was then used to verify the calibration by calculating the temperature of the Pt elements while varying the furnace between 450 °C and 650 °C. This allowed a direct comparison of the predicted temperatures with the value measured using a thermocouple in the furnace.

The first-generation investigatory array testing was completed prior to the start of the second-generation array tests. The investigatory arrays were initially tested with the furnace at 450 °C, 500 °C, and 550 °C to gauge performance with all electrodes at the same temperature

(i.e., no heater bias was applied). Custom software (NI LabVIEW™, Version 7.1) controlled the furnace ambient temperature, the mass flow controllers, and the heater power source, while simultaneously measuring the investigatory array signals. The software also calculated the temperatures for each electrode using voltage and current measurements from the DMMs. All equipment was periodically calibrated to ensure the accuracy of the measurements.

All tests using the investigatory sensor arrays were conducted in 3% O<sub>2</sub> with N<sub>2</sub> balance at a total flow rate of 100 ccm (cc/minute). The software applied voltage incrementally across the Platinum heaters until various setpoints were reached. The furnace ambient was maintained at 450 °C during all tests with the first-generation array and at 500 °C with the second-generation array. The temperature of each Platinum element was monitored simultaneously during the heater ramp and sensor experiments. At each setpoint, the system was allowed to equilibrate for approximately one hour. The software then successively stepped gas concentrations (0, 50, 100, 200, 400, and 650 ppm) of NO and NO<sub>2</sub>, one gas at a time, while measuring the corresponding open-circuit potential with a Keithley 2000.

### **3.3.4 3D Reconstruction of Sensing Electrodes with FIB/SEM**

A focused-ion beam/scanning electron microscope system (FIB-SEM, FEI, Inc.) was used to mill through the as-deposited Pt and LCO sensing electrodes, with a micrograph image taken for each slice. The slices were then reconstructed in three dimensions (Amira-ResolveRT version 4.0, VSG) in order to quantify microstructure (e.g., particle shape) and phase fractions (e.g., pore and compositional fractions) of the materials. These techniques are only recently being used in gas sensors, but have been investigated in similar ceramic technology (e.g., solid oxide fuel cells).<sup>152</sup>

### 3.4 Results and Discussion

The curve fits for the Pt elements were very good ( $R^2=1$ ) and allowed accurate determination of surface temperatures. Table 3-1 shows the calculated electrode temperatures and power consumption for three heater voltage setpoints during tests with the first-generation investigatory array. The FEM results agreed closely with the measured values ( $T_{LCO1}$ ,  $T_{Pt}$ , and  $T_{LCO2}$ ), which represent average temperatures for the Platinum elements. The second-generation array was also in agreement with thermal modeling. Additional details are in Appendix A.

#### 3.4.1 Proof of Concept

The results for the first-generation investigatory array provided evidence that the use of a differential temperature between two sensing electrodes can be used to modify device performance. Figure 3-4 shows the steady-state sensitivity plots for LCO1 and LCO2 versus the Pt pseudo-reference for NO and NO<sub>2</sub> gas steps at several heater bias setpoints. The responses were positive for NO at all concentrations but saturated at higher values. For NO<sub>2</sub> the responses were negative at low concentrations and became positive at higher concentrations. As the heater temperature increases, LCO1-Pt sensitivity to NO steps decreases (Figure 3-4A), while the measured value for NO<sub>2</sub> steps still shows sensitivity (Figure 3-4B). LCO2-Pt has a similar sensitivity to NO<sub>2</sub> (Figure 3-4D) as LCO1-Pt, though interestingly shows improved sensitivity to NO as heater temperature increases (Figure 3-4C).

The decreasing sensitivity of LCO1-Pt to NO as the heater temperature increases is an improvement over the unheated sensor because the response of LCO versus Platinum is generally positive for increasing concentrations of NO and negative for NO<sub>2</sub>. Therefore, the overall sensitivity is decreased if both gases are present because the responses tend to cancel each other. With the use of the differential temperature effect, a sensor array should not have

this problem and the NO and NO<sub>2</sub> concentrations should be able to be determined with the measurements from both electrode pairs.

### 3.4.2 Changes in Sensitivity

The second-generation investigatory sensor array was used to further explore the differential temperature effect. To get an idea of the sensitivity trends with changes in absolute electrode temperatures, logarithmic fits of the steady-state sensor response versus gas concentration plots (e.g., see Figure 3-5) were made for each sensing electrode-pair at all heater setpoints. Each curve represents a different heater setpoint, which in turn represents the sensitivity for a distinct temperature difference (dT) between the electrodes. The slopes of these plots represent the sensitivity (mV change in signal per decade change in gas concentration). Figures 3-6 through 3-11 show the six unique signals for NO and NO<sub>2</sub> gas steps, grouped as electrode-pairs made of electrodes of similar materials and dissimilar temperatures; electrodes of dissimilar materials and similar temperature; and electrodes of dissimilar materials and dissimilar temperatures.

As seen in Figures 3-6 and 3-7, the NO sensitivity of the LCO(4)-LCO(2) electrode-pair significantly rises as the temperature of the LCO(2) electrode increases beyond the temperature of LCO(4). In fact there is almost an increase of ten times the initial sensitivity when no temperature difference exists between the electrodes. In contrast, as the heater setpoints increase, the NO<sub>2</sub> sensitivity decreases to almost zero. There is a slight increase in sensitivity at later setpoints, but at least over a small range of the setpoints this electrode-pair is insensitive to NO<sub>2</sub>. Therefore this electrode-pair was effectively NO selective.

The sensitivity trends with increasing heater setpoint for the Pt(3)-Pt(1) electrode-pair can also be seen in Figures 3-6 and 3-7. The NO sensitivity initially becomes more negative than the case without local heating, and then becomes more positive as the temperature difference

increases. The NO<sub>2</sub> sensitivity initially goes more negative and decreases rather significantly, and then moves in the positive direction as the temperature difference increases further. After the initial change in sensitivity, the decreasing NO sensitivity is much slower than the change for NO<sub>2</sub> sensitivity.

The sensitivity trends for LCO(2)-Pt(3) can be seen in Figures 3-8 and 3-9. The NO sensitivity decreases to almost zero, which effectively makes this electrode-pair selective to NO<sub>2</sub>. However, the NO<sub>2</sub> sensitivity becomes more positive and changes from a negative response to a positive response as the temperature difference between the electrodes increases. Therefore, this electrode-pair is selective to NO<sub>2</sub>. Note that there was a slight difference in the temperature that resulted in small changes in sensitivity.

As can be seen in Figure 3-8 and 3-9 for the LCO(4)-Pt(1) electrode-pair, the NO sensitivity remains nearly fixed at the level where the signal is without localized heating. However, the NO<sub>2</sub> sensitivity becomes more positive and changes from a negative response to a positive response as the temperature difference between the electrodes increases.

Figures 3-10 and 3-11 shows the NO and NO<sub>2</sub> sensitivity trends for the LCO(2)-Pt(1) electrode-pair. The NO sensitivity becomes increasingly negative as the temperature difference between the electrodes is increased. Also, the sensitivity to NO<sub>2</sub> becomes more positive and increases nearly five times compared to the sensitivity without a temperature difference between the two electrodes. There was a very large change in NO sensitivity between the first and second heater setpoints, while the NO<sub>2</sub> sensitivity remained near its initial value. However, after the first few heater setpoints, there were larger changes in NO<sub>2</sub> sensitivity compared to NO sensitivity as the heater temperature increased further.

Finally, the trends in sensitivity of NO and NO<sub>2</sub> for the LCO(4)-Pt(3) electrode-pair are displayed in Figures 3-10 and 3-11. The sensitivity to NO nearly doubles with respect to the condition without a difference in temperature between the electrodes. Also, the sensitivity to NO<sub>2</sub> becomes more positive and changes from a negative response to a positive response as the temperature difference between the electrodes increases.

### 3.4.3 Baseline Shifts

There were variations in the temperature difference between sensing electrodes in a given sensing electrode-pair as the heater setpoints increased. In some cases this change was large, while in others the temperature of both electrodes remained about the same. As this occurred, there was an increase or decrease in the baseline voltage measured in only 3% O<sub>2</sub> with N<sub>2</sub> balance (i.e., 0 ppm NO or NO<sub>2</sub>). For large differences in electrode temperature, the baseline shift tended to be greater than for small differences in electrode temperature. The trends of the baseline shift for the Pt(1)-LCO(4), LCO(2)-LCO(4), LCO(2)-Pt(1), and Pt(3)-Pt(1) electrode-pairs is shown in Figure 3-12.

The resulting baseline voltage was negative if the sensing electrode at higher temperature was attached to the positive terminal of the voltmeter and the lower temperature sensing electrode to the negative terminal. This trend was also seen with the first-generation array.

A potentiometric gas sensor with electrodes at the same temperature typically returns to a value near zero after the gas (e.g., NO or NO<sub>2</sub>) concentration returns to 0 ppm, and only O<sub>2</sub> (N<sub>2</sub> balance) is flowing. This can be explained with the Nernst equation where, for an unheated sensor, the oxygen concentrations and the temperatures for the electrodes are equal and therefore the potential difference (E) is zero.<sup>150</sup> When the Nernst equation is expanded as in Equation 3-1, the temperature of each electrode becomes important.

$$E_{ab} = E_a - E_b = \frac{RT}{4F} \ln \left( \frac{P_{O_2,b}}{P_{O_2,a}} \right) = \frac{RT_b}{4F} \ln(P_{O_2,b}) - \frac{RT_a}{4F} \ln(P_{O_2,a}) \quad (3-1)$$

In deriving the Nernst equation, one assumes that the Electrode/YSZ interface is at equilibrium with the gas phase.<sup>153,154</sup> Therefore, the potential difference between two electrodes depends on the temperature and partial pressure of oxygen at each electrode. In the unheated case when no reactive gas is present, the oxygen in the gas phase is in equilibrium with the oxygen in the YSZ. Therefore, Equation 3-1 applies and the measured potential difference can be described as Nernstian. When a gas mixture with reacting gases is present, the possibility arises for a departure from equilibrium with the gas phase because of competing reactions occurring at the electrodes.<sup>84,153,154</sup> This non-equilibrium situation does not follow Equation 3-1, and the measured signals are called non-Nernstian. In this case one has to consider the activities of the gas species present rather than their partial pressures, as shown in Equation 3-2.

$$E_{ab} = E_a - E_b = \frac{RT}{4F} \ln \left( \frac{a_{O_2,a}}{a_{O_2,b}} \right) = \frac{RT_b}{4F} \ln(a_{O_2,b}) - \frac{RT_a}{4F} \ln(a_{O_2,a}) \quad (3-2)$$

Theoretically, the observed baseline shifts in the current work could have occurred due to the differences in electrode temperature as explained with Equation 3-1. However, using the electrode temperatures measured with the Pt elements, theoretical calculations are far from the observed values for baseline shifts in only O<sub>2</sub>. Therefore, this indicates that the shifts in the baseline measurements do not follow the Nernst equation (though still not technically classified as “non-Nernstian”). If local thermal modifications result in changes in the activity, then Equation 2 might give values of the EMF which are close to the measured baselines. However, at this time no satisfactory explanation exists to explain the observed baseline shifts.

The nature of a potentiometric measurement is such that each electrode in an electrode-pair contributes to the measured (potential difference) signal. This being the case, changes to the sensitivity of an electrode-pair are possible through modification of the individual temperatures of each electrode. As mentioned above, with the introduction of reactive gas mixtures the Nernst equation may not apply due to non-equilibrium conditions. Others have claimed that the non-Nernstian signal arises due to the formation of a mixed potential due to competing reactions at the electrodes.<sup>84</sup> However, we have been working to explain the more general theory of differential electrode equilibria” for the origins of these signals. This theory takes into consideration differences in electrode equilibria arising from such sources as mixed potential, catalytic activity, and the semiconducting response of electrodes. Therefore, the trends in sensitivity with local thermal modification of electrodes theoretically could be a result of changes to any of these electrode equilibria contributions.

#### **3.4.4 3D Reconstructions and Analysis**

Figure 3-13 shows 3D reconstructions for a porous Pt electrode on YSZ and a porous LCO electrode. The scale in these images is different; the Pt electrode had large pores (e.g., YSZ electrolyte can be seen through electrode) and particle sizes on the order of 0.75 to 1 micron, while the LCO electrode had plate-like particles (i.e., a tortuous gas pathway) with pores and particle sizes on the order of 0.15 to 0.25 microns. From these reconstructions, the phase fraction and tortuosity were calculated. Phase fractions as a function of depth from the electrode (i.e., Pt or LCO) surface are shown in Figures 3-13A and 3-13B. The Pt and porous phases remain fairly even (50% / 50%) throughout most of the electrode, until the porosity begins to increase near the Pt/YSZ interface. The LCO electrode, on the other hand, consisted of nano-sized grains, and therefore had a much greater phase-fraction consisting of porosity.

The tortuosity of the electrodes can be seen in Figures 3-14C and 3-14D for Pt and LCO, respectively. Here we can see that the nano-sized LCO resulted in a more highly tortuous gas pathway than the Pt electrode. The tortuosity of the LCO electrode can be visualized in Figure 3-15, where the nodal network is shown. The tortuosity dictates the relative kinetics of mass transport between the electrodes, and thus will result in different contributions to the individual EMFs formed at the Pt and LCO. Furthermore, this can be related to the relative effect of differential electrode temperatures.

### **3.5 Conclusions**

Two investigatory gas sensor arrays with integrated Platinum heaters and temperature sensors have been fabricated and tested to investigate the differential electrode temperature effect. Modulating the temperature of individual sensing electrodes was shown to change selectivity and should allow detection of NO and NO<sub>2</sub> in NO<sub>x</sub> gas mixtures. Furthermore, additional sensing electrode materials can be added to the array to detect more gas species (e.g., CO). While several explanations were offered to explain the baseline shifts with differences in electrode temperatures, there is still not definitive proof as to their origin. However, the baseline shifts do not take away from the enhancements in selectivity now possible with this technique; the responses were still reversible. Though future experiments will aim to resolve the baseline shift question, possibly using a modified form of Solid Electrolyte Potentiometry (SEP) to investigate the contribution of thermal gradients as a source of the non-equilibrium conditions.

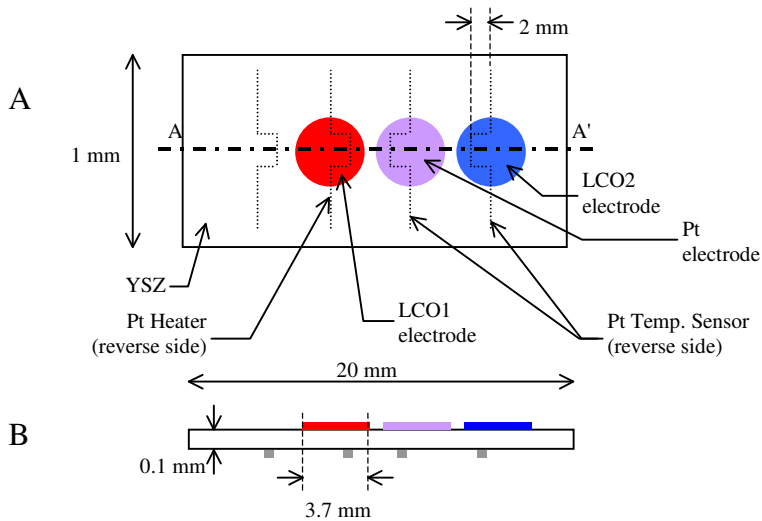


Figure 3-1. Schematic of first-generation investigatory gas sensor array. The top view is and the cross-section through A-A' are shown in A) and B), respectively.

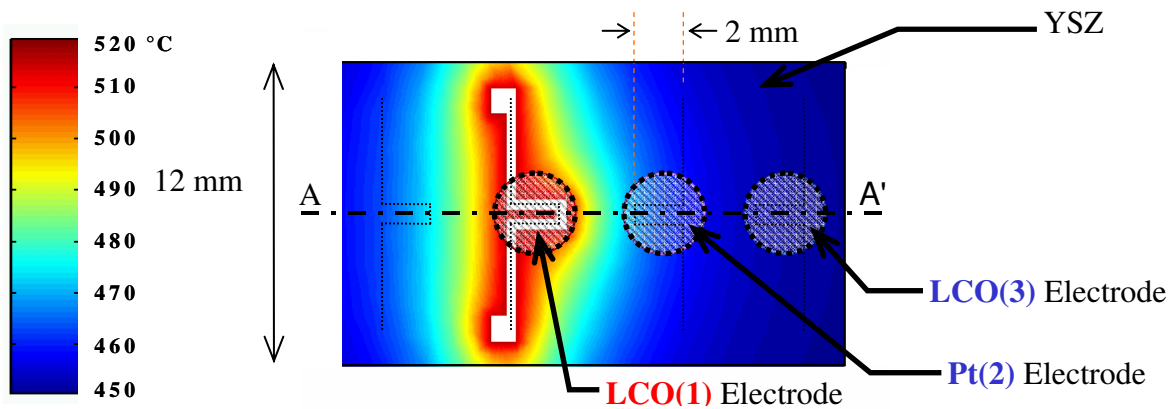


Figure 3-2. Thermal model for first-generation investigatory gas sensor array.

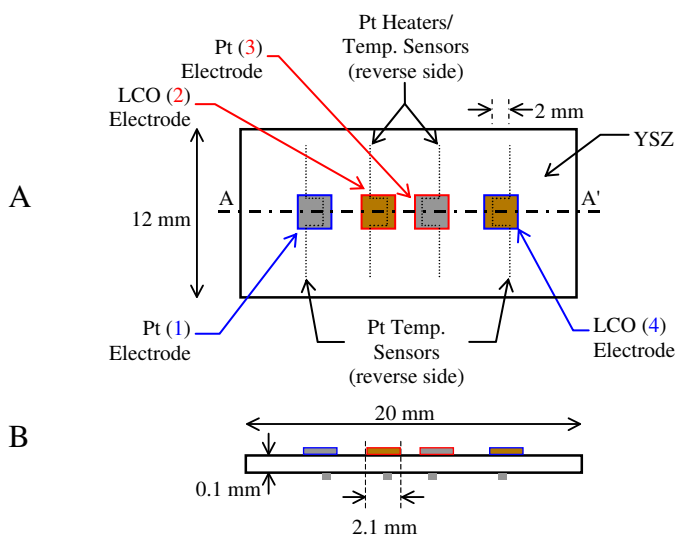


Figure 3-3. Schematic of second-generation investigatory array. The top view is and the cross-section through A-A' are shown in A) and B), respectively.

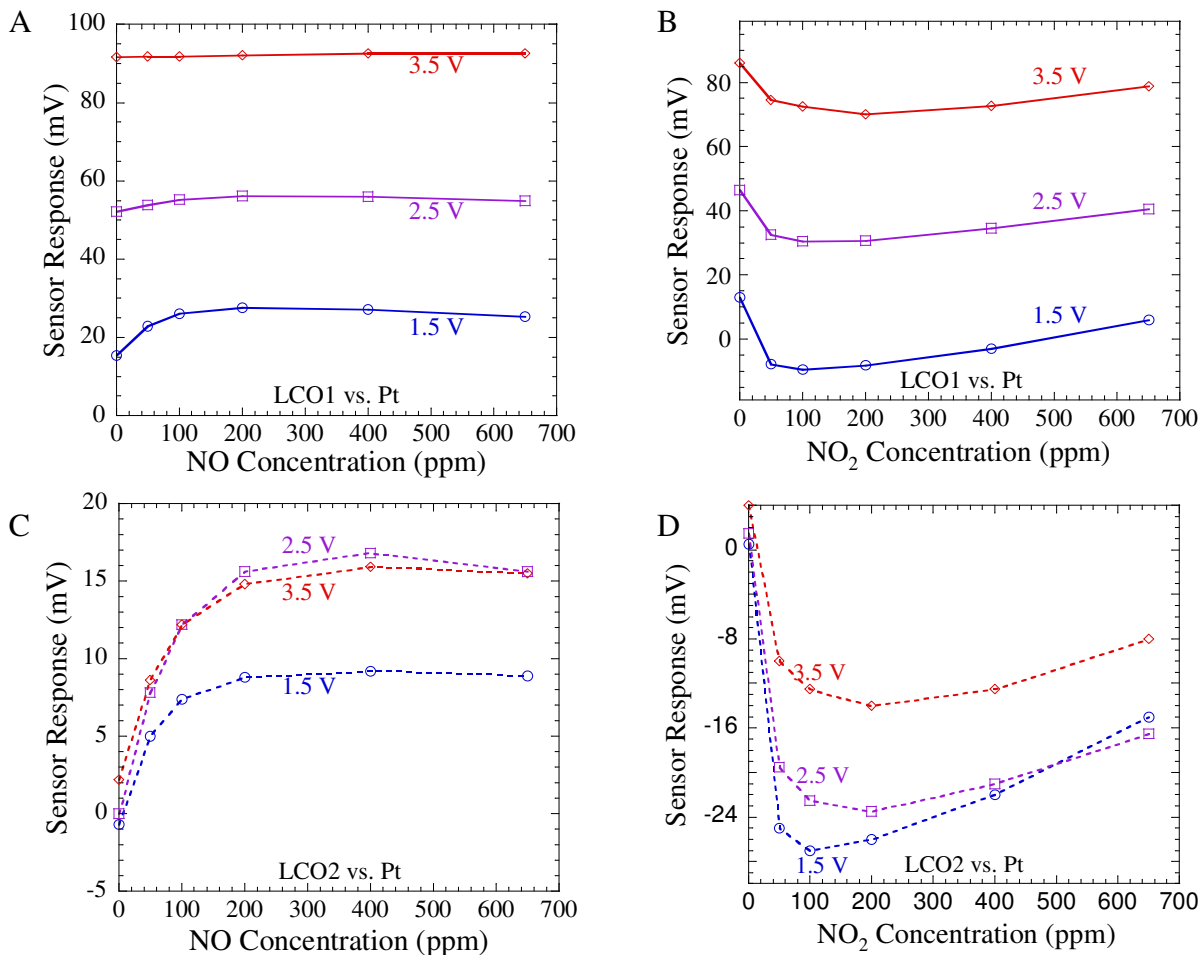


Figure 3-4.  $\text{La}_2\text{CuO}_4\text{-Pt}$  sensor response to  $\text{NO}_x$  as a function of heater voltage setpoint. LCO1-Pt is shown in A) and B) for NO and  $\text{NO}_2$ , respectively. The response of LCO2-Pt is shown in C) for NO and D) for  $\text{NO}_2$ .

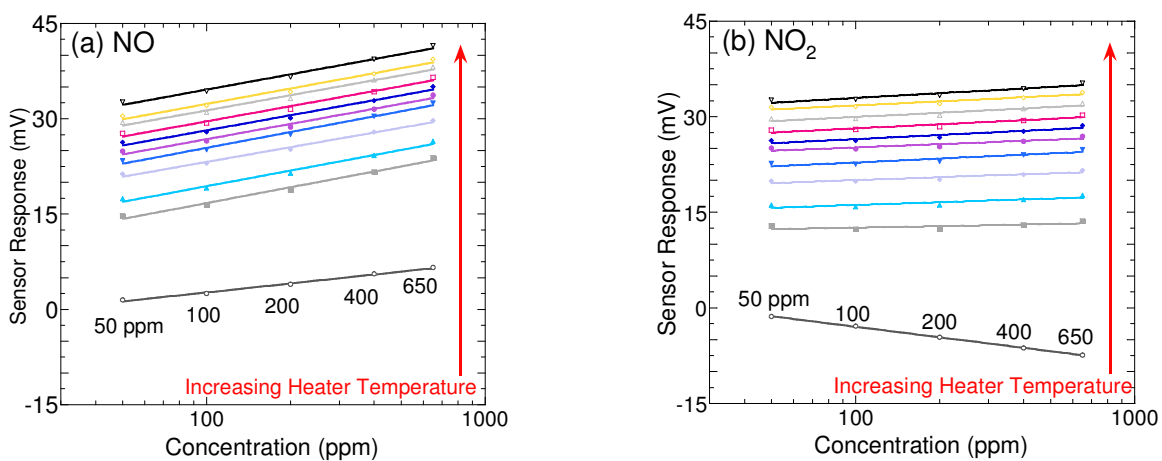


Figure 3-5. Plots of steady-state sensor response versus gas concentration for Pt(3)-LCO(4). The results for NO and  $\text{NO}_2$  gas steps can be seen in A) and B) respectively. The slopes from (log scale) plots such as these were used to obtain trends in sensitivity as heater temperature increased.

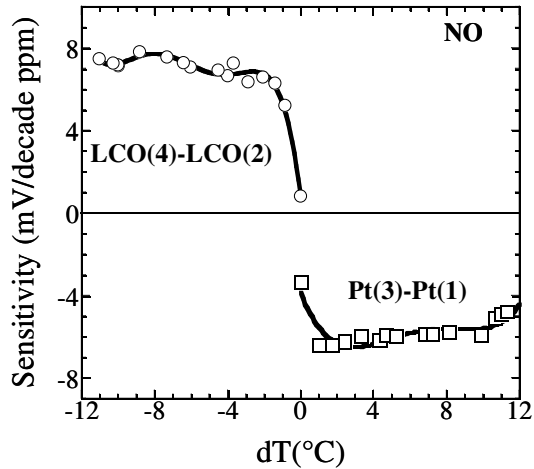


Figure 3-6. NO sensor response from the LCO(4)-LCO(2) and Pt(3)-Pt(1) signals as a function of the difference in temperature between the electrodes of each electrode-pair.

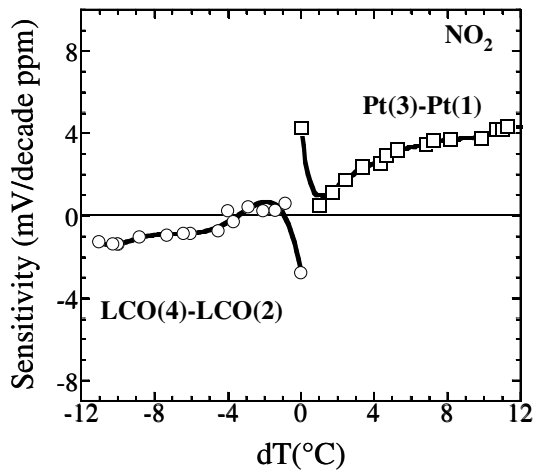


Figure 3-7. NO<sub>2</sub> sensor response from the LCO(4)-LCO(2) and Pt(3)-Pt(1) signals as a function of the difference in temperature between the electrodes of each electrode-pair.

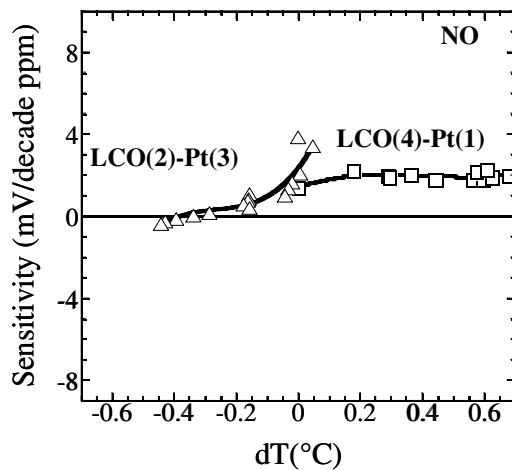


Figure 3-8. NO sensor response from the LCO(2)-Pt(3) and LCO(4)-Pt(1) signals as a function of the difference in temperature between the electrodes of each electrode-pair.

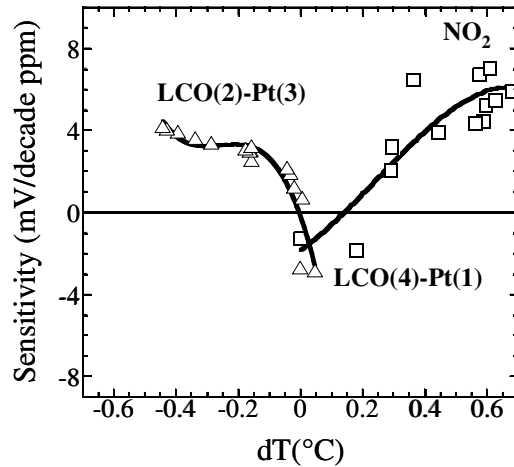


Figure 3-9. NO<sub>2</sub> sensor response from the LCO(2)-Pt(3) and LCO(4)-Pt(1) signals as a function of the difference in temperature between the electrodes of each electrode-pair.

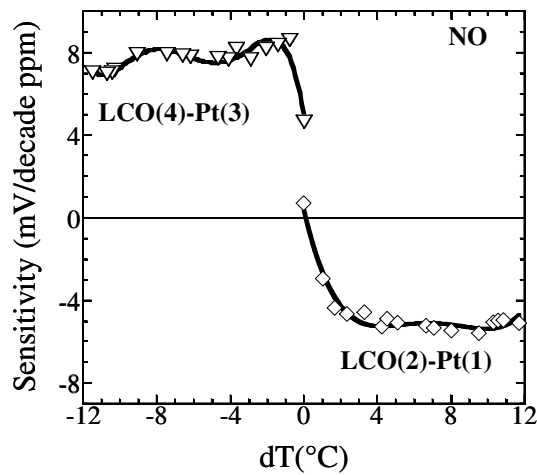


Figure 3-10. NO sensor response from the LCO(4)-Pt(3) and LCO(2)-Pt(1) signals as a function of the difference in temperature between the electrodes of each electrode-pair.

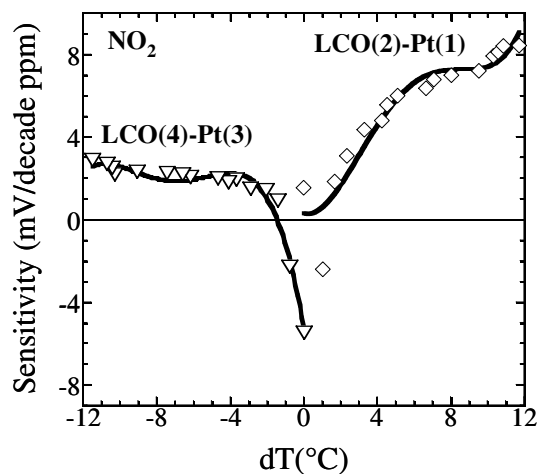


Figure 3-11. NO<sub>2</sub> sensor response from the LCO(4)-Pt(3) and LCO(2)-Pt(1) signals as a function of the difference in temperature between the electrodes of each electrode-pair.

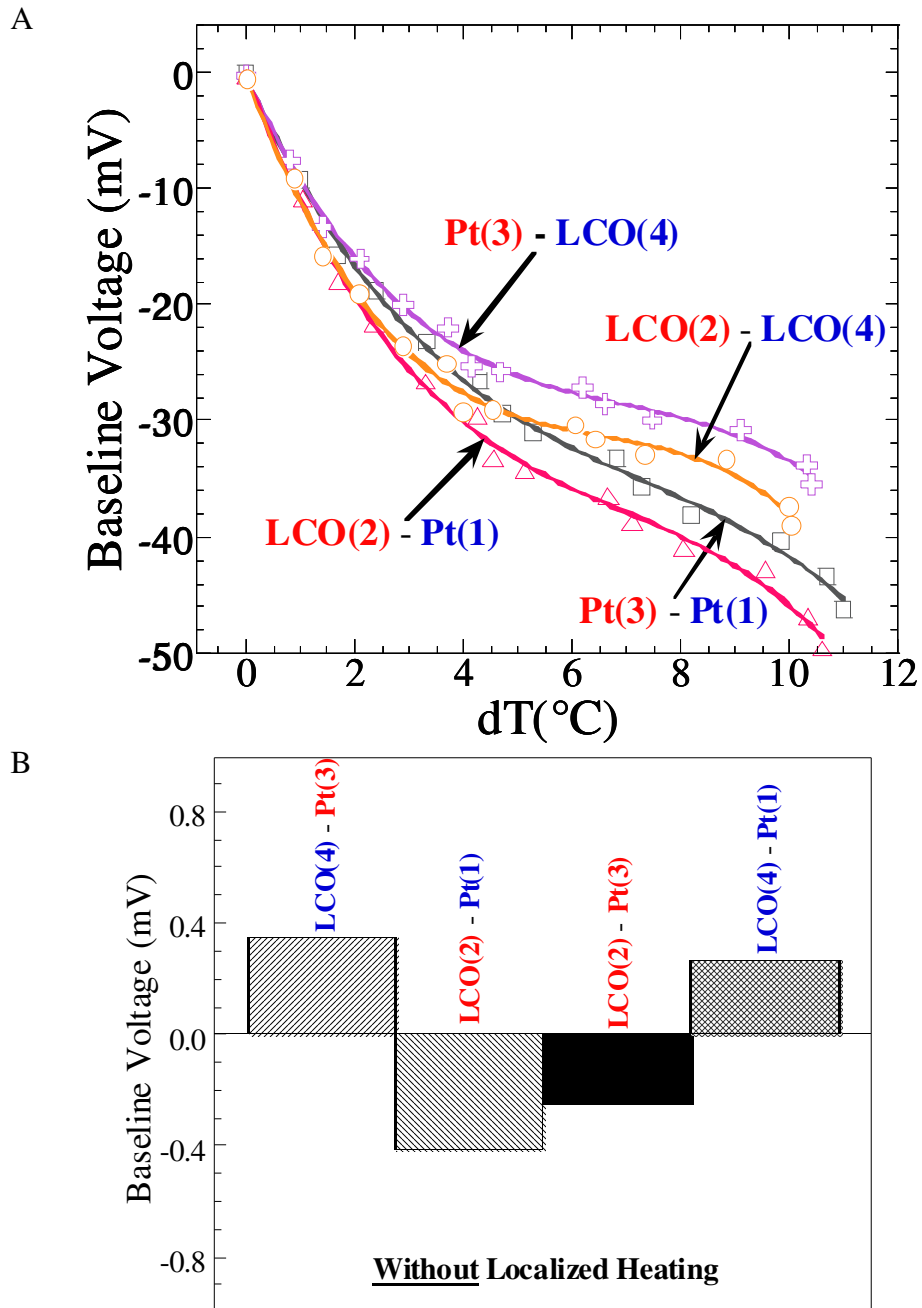


Figure 3-12. Baseline shifts versus difference in temperature between the electrodes of each electrode-pair.

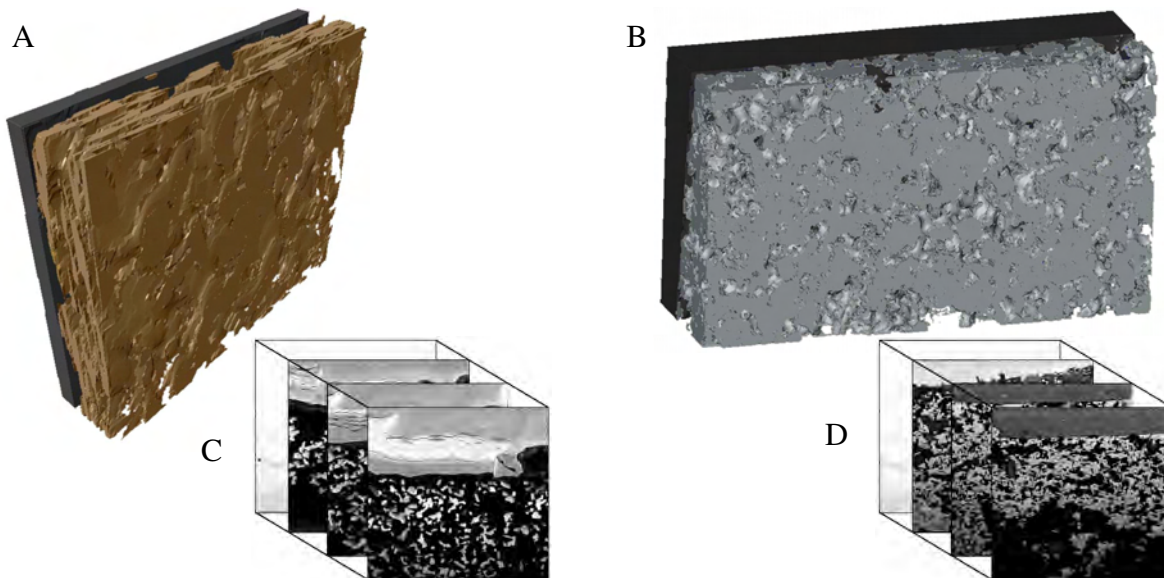


Figure 3-13. 3D reconstructions of two electrode materials made using images from FIB-SEM slices. A) shows the reconstruction for LCO/YSZ, while B) shows that of Pt/YSZ. C) and D) show the reconstruction concept for LCO/YSZ and Pt/YSZ, respectively.

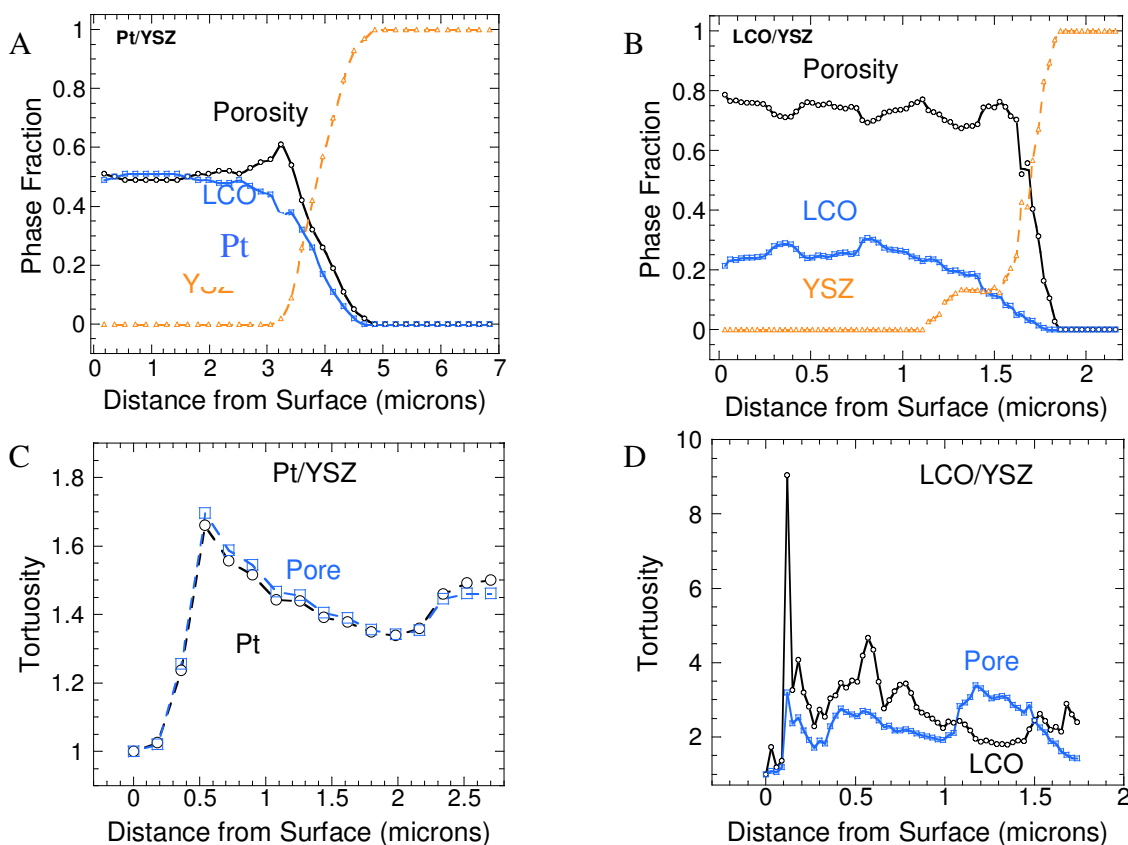


Figure 3-14. Phase fraction and tortuosity as determined from 3D reconstruction of Pt/YSZ and LCO/YSZ. A) and C) show the results for the Pt/YSZ sample, while those of the LCO/YSZ sample can be seen in B) and D).

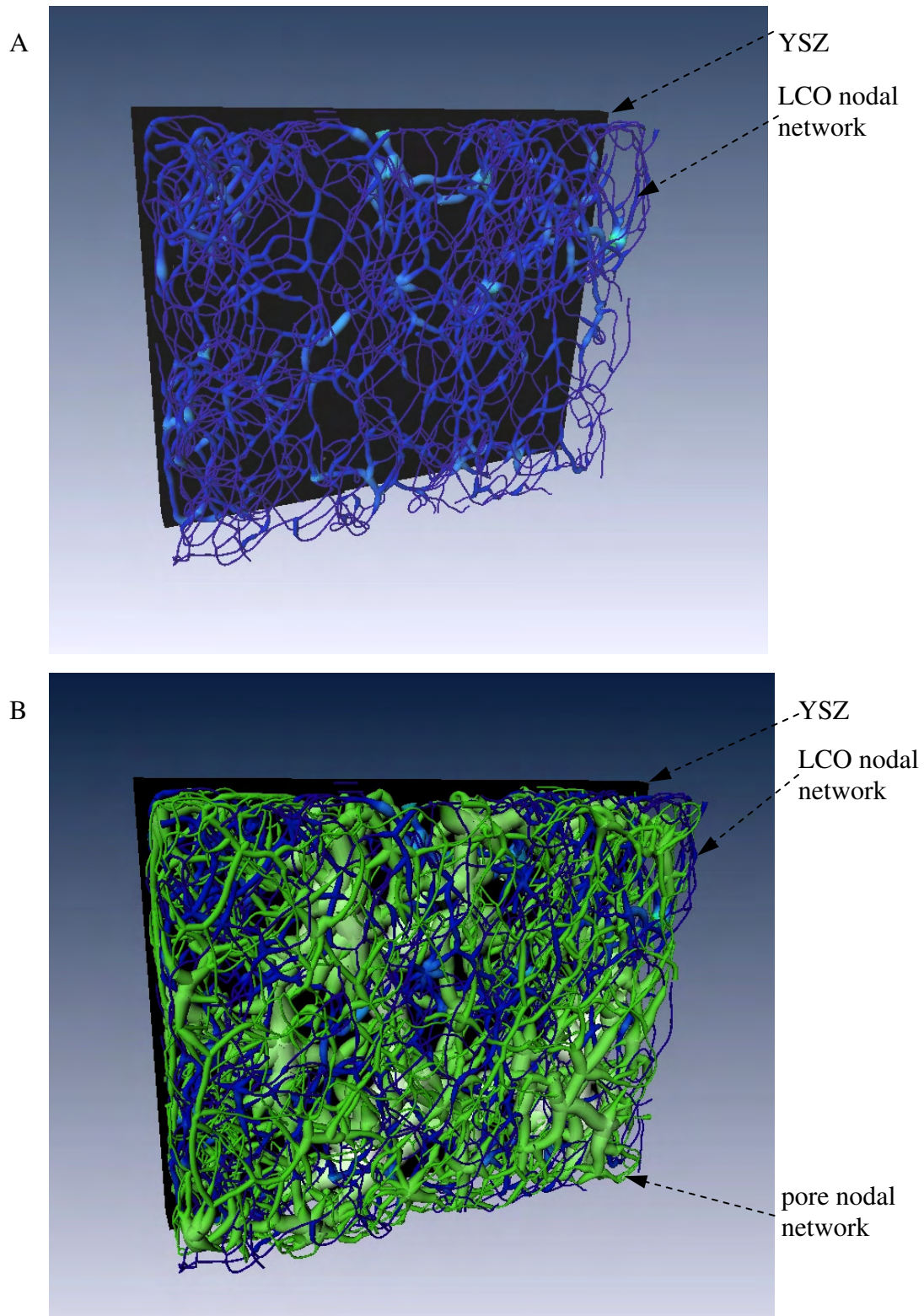


Figure 3-15. 3D skeleton reconstruction of LCO and pore structure on YSZ. In A) the LCO nodal network is in blue, while B) has the additional nodal network of the pores shown in green. The YSZ is shown in black.

Table 3-1. Surface temperature measurements and heater power at three voltage setpoints

Setpoint	Applied voltage (V)	Heater power (mW)	T <sub>LCO1</sub> (°C)	T <sub>Pt</sub> (°C)	T <sub>LCO2</sub> (°C)
1	1.5	70	460	452	450
2	2.5	185	484	454	451
3	3.5	360	515	457	452

## CHAPTER 4 THERMALLY ENHANCED GAS SENSOR ARRAY

### 4.1 Introduction

Gas sensors are needed to monitor and control emissions in combustion exhausts and industrial processes due to concern for health, environmental, and economic issues. The gas mixtures of interest involve such species as  $N_2$ ,  $O_2$ ,  $CO_2$ ,  $CO$ ,  $NO$ , and  $NO_2$ . In gas mixtures, some correlation typically exists between components, but as more gases are added the determination of individual gas concentrations from sensor signals becomes increasingly difficult. Selective detection of individual gases is critical if complex gas mixtures are to be easily analyzed. However, currently available detection methods for these gases are non-selective, expensive, or ill-suited for harsh environments. Therefore, there is a need for low cost, robust devices for applications such as with on-board diagnostic systems in automobiles. Of particular interest is the potentiometric gas sensor, whose signal consists of the potential difference between two sensing electrodes on the surface of a solid electrolyte.

Many solid-state gas sensor arrays are heated (using various means), while some merely operate at ambient temperatures.<sup>141,143,151,155-157</sup> In the former, the entire device tends to be heated to a single temperature. In other instances, the sensing electrodes and associated components (e.g., electrolyte and/or heaters) exist as separate devices, each operating at the optimal temperature, housed in a single enclosure.<sup>141</sup> In Chapter 3, it was shown that a single device with multiple sensing electrodes locally heated to different temperatures can significantly improve selectivity and sensitivity.<sup>157</sup> These potentiometric gas sensor arrays show promise for selective detection over a large range of gas concentrations and temperatures. Furthermore, the indirect and direct detection of individual  $NO$  and  $NO_2$  concentrations were demonstrated using various sensor array designs.

In this study the effects of ambient temperature, gas flow rates, and the local electrode temperature on the sensor signal were examined. The gas sensor array was also tested using different gas mixtures of O<sub>2</sub>, NO<sub>x</sub>, and CO<sub>x</sub>. Depending on the combination of these parameters, the sensor showed variations in sensitivity and selectivity. In addition, temperature programmed reaction (TPR), temperature programmed desorption (TPD), x-ray photoelectron spectroscopy (XPS), and diffuse reflectance infrared Fourier transform spectroscopy (DRIFTS) data from past work was used to explain the more significant results.

## 4.2 Background

Solid-state potentiometric gas sensors have been demonstrated as highly selective devices that are easily manufactured and can withstand harsh environments.<sup>143</sup> These sensors are based on measurements of the potential difference between two different electrodes, often a semiconducting metal-oxide and noble metal (pseudo-reference) electrode in the same gas environment. Three general categories of potentiometric gas sensors exist as described by Wiemhofer and Gopel, Moseley, and others.<sup>84,158-160</sup> The first type of sensor is based on the thermodynamic equilibration of the gas with either a mobile or immobile component of the electrolyte. These sensors probe the electro-chemical potential of the electrons (i.e., the Fermi level) in the solid ionic conductor at the gas/electrode/solid-electrolyte interface (i.e., triple phase boundary, or TPB). The second class of sensor utilizes an auxiliary phase that couples the chemical potential of an analyte to an unrelated mobile ion in the solid electrolyte. The last class of sensors involves the simultaneous presence of multiple, competing anodic and cathodic electrochemical reactions occurring at each TPB (i.e., mixed potential), when the electrodes are exposed to the same environment. Recent evidence, however, suggests that the differential electrode equilibria theory more appropriately describes the response of this type of sensor. This theory is based on the idea that the measured potential difference results from dissimilar

equilibria (such as from variations in heterogeneous catalytic reactions, adsorptive-based band-bending, and/or electrocatalytic reactions) generated at each electrode.<sup>65</sup>

In order to fully evaluate the semiconducting effect on the potential generated at each electrode, one needs to consider the relationship between the Fermi level and adsorption equilibria. The Fermi level is essentially the electrochemical potential of the electrons in the electrodes. Were the electrodes of the electrochemical cells connected, their Fermi levels would eventually become equal as equilibration occurred. However, since the potentiometric sensor operates at open-circuit conditions, the cell voltage is equivalent to a difference in the Fermi levels between the electrodes.<sup>159</sup> With the use of a semiconducting material, the Fermi level of the electrode can change as gas adsorbs on the surface.<sup>161</sup> Our recent work utilizing XPS, DRIFTS, and temperature programmed techniques has provided evidence for the formation of charged surface complexes upon exposure to various pollutant gases.<sup>96-98,145,146</sup> The results have suggested, at least in the case of NO, that the sensor response is primarily an adsorptive effect.<sup>146</sup> For NO<sub>2</sub> there exists the possibility that the adsorptive effect also alters the supply of electrons to the electrocatalytic reactions occurring at the TPB. As a result of evidence from chemiresistive and potentiometric gas sensor research, these effects should dominate with many other semiconducting electrodes.<sup>139,162</sup>

### **4.3 Experimental**

For the prototype gas sensor arrays discussed in this work, manual screenprinting was utilized to construct the various elements of each device. Due to the numerous materials and patterns used, fabrication involved several steps of deposition, drying, and sintering. After a device was made and loaded into the test setup, an initial calibration was conducted for the heating elements and temperature sensors. Gas sensor experiments without localized heating were also performed at this time. The sensor array was then evaluated for changes in

performance as the result of local thermal modification. This included experiments to see the effect of flow rate, ambient and local electrode temperature, gas mixture composition.

#### **4.3.1 Sample Preparation**

$\text{La}_2\text{CuO}_4$  (LCO) powder was synthesized using a wet-chemical route and made into an ink as described previously.<sup>157</sup> Pt ink (Heraeus) was screenprinted as C-shaped elements on planar yttria-stabilized zirconia (YSZ) substrates (Marketech) and sintered at sufficiently high temperature to achieve good adhesion and dense microstructure. Then, Pt and LCO sensing electrodes were deposited onto the opposite side of the YSZ. As shown in Figure 4-1, the device consisted of two Pt and two LCO sensing electrodes, coplanar on the surface of a YSZ substrate. On the opposite side of the YSZ, aligned with the sensing electrodes were C-shaped Pt elements. The inner two Pt elements were used as heaters and temperature sensors, while the outer two acted only as temperature sensors. The array provided six unique signals based on three sets of different electrode-pairs. These are electrodes of different materials with similar temperatures, different materials with different temperatures, and similar materials with different temperatures.

#### **4.3.2 Automated Experimental Setup**

The test setup was a controlled gas environment consisting of a quartz tube with sample holder that placed the device within the hot zone of a furnace. A custom wire-harness coupled the device to various pieces of electronic equipment as described in past work.<sup>157</sup> Mass flow controllers were attached to a manifold in order to control the gas composition and total flow rate during experiments. A computer using a custom program (NI LabVIEW™, Version 7.1) controlled the heating elements, calculated local surface temperatures, monitored and adjusted the ambient furnace temperature, recorded the array signals, and changed gas concentrations during experiments.

### 4.3.3 Experimental Procedure

Prior to testing the gas sensor array, custom software was used to calibrate the C-shaped Pt elements. As demonstrated in past results, the calculated temperatures agreed with results from thermal modeling<sup>151,157</sup>. Subsequently, the software applied power to the Pt heaters aligned with LCO(2) and Pt(3). The temperature of each Pt element was monitored simultaneously during the heater ramp and sensor experiments as described previously. During the heater ramps, 3 % O<sub>2</sub> and 97 % N<sub>2</sub> flowed through the quartz tube. After an appropriate delay, the software stepped through two up/down loops for gas concentrations (0, 50, 100, 200, 400, and 650 ppm) of NO and NO<sub>2</sub> successively in 3 % O<sub>2</sub> with N<sub>2</sub> balance, while measuring the corresponding open-circuit potential of each sensing electrode-pair. When gas mixture experiments were being tested, a static gas of NO<sub>2</sub> (NO) was introduced at the beginning of the NO (NO<sub>2</sub>) gas stepping sequence and the system was allowed to equilibrate before proceeding. After NO (0 and 200 ppm static NO<sub>2</sub>) gas steps were run, the program tested the sensor array for NO<sub>2</sub> (0 and 200 ppm static NO) gas steps. After all the respective gas stepping runs were completed at a particular ambient temperature the program adjusted the furnace setpoint. Furnace temperatures varied from 650 °C to 500 °C. This procedure was repeated for various Pt heater setpoints. Also, total flow rates of 100 to 300 ccm were tested.

## 4.4 Results and Discussion

The prototype gas sensor array was tested for various gas mixtures, flow rates, and ambient/surface temperature combinations. As mentioned earlier, a total of six sensor signals were monitored during all experiments. Each signal and experimental condition verified that the thermal modification of individual potentiometric sensing electrodes can result in enhanced sensor performance. However, only the most significant results will be discussed in detail.

#### 4.4.1 NO<sub>x</sub> Gas Mixtures

The NO<sub>x</sub> gas mixture results shown here are for NO (0 and 200 ppm NO<sub>2</sub>) gas steps and NO<sub>2</sub> (0 and 200 ppm NO) gas steps. The total flow rate was 300 ccm and the ambient temperature was 600 °C for the data shown. Under these conditions the prototype gas sensor array provided very clear proof that individual changes in local electrode temperatures improved the sensitivity and selectivity of the device.

##### 4.4.1.1 NO<sub>2</sub> selectivity

The LCO(2)-Pt(1) sensor response (linear scale) to NO<sub>2</sub> gas steps for various heater setpoints is shown in Figure 4-2. Also marked in the figure are the changes in the measured signals between the 0 ppm NO<sub>2</sub> baseline (i.e., only 3% O<sub>2</sub>, N<sub>2</sub> balance) and the 200 ppm NO<sub>2</sub> gas step. Without the use of the heaters, a change from 0 ppm to 200 ppm NO<sub>2</sub> modified the response by approximately 3.5 mV. When a small amount of power was delivered to the heaters (~21 mW), the measured voltage difference changed to 5 mV upon introduction 200 ppm NO<sub>2</sub>. At even higher power settings, the voltage difference change was 6.5 mV. As heater power increased, so did the temperature of the LCO(2) electrode. Due to the location of the other electrodes relative to the heaters, the Pt(1) electrode temperature varied slightly but remained close to that of the ambient. These changes in local electrode temperature were what caused the variations in sensor output.

Figure 4-3 represents the LCO(2)-Pt(1) sensor response (log scale) to NO<sub>2</sub> for gas mixtures with static concentrations of 0 ppm NO (solid lines) and 200 ppm NO (dashed lines). The square, circle, and diamond symbols represent the conditions where 0, ~21, and ~81 mW of total power were delivered to the Pt heating elements. As can be seen for NO<sub>2</sub>, the slope of each set of lines (i.e., the sensitivity, or mV change in signal per decade change in gas concentration) increased in magnitude as additional heater power was supplied. Furthermore, the sensitivity

was mostly unaltered when NO was added to the NO<sub>2</sub> gas steps. This is significant because the results indicate that the LCO(2)-Pt(1) electrode-pair was NO<sub>2</sub> selective.

Figure 4-4 shows the sensor response for NO gas exposure (log scale) with 0 ppm NO<sub>2</sub> (solid lines) and 200 ppm NO<sub>2</sub> (dashed lines). The positive sensitivity to NO decreased toward zero as the heater power increased. Also marked in this figure for each heater setpoint are the approximate shifts in NO sensitivity when 200 ppm NO<sub>2</sub> was added to the gas mixture. The shifts were all negative as expected when considering the larger (negative) response to NO<sub>2</sub> as seen in Figures 4-2 and 4-3. For low power levels, the shift was more prominent at larger NO concentrations. This was likely due to the fact that the response to NO and NO<sub>2</sub> were in opposite directions and had different slopes (i.e., sensitivities). Without the use of the heaters, the shift in the sensor response was 0.18 to 1.3 mV along the entire NO concentration range. For ~21 mW of heater power, the shift was between 3.2 and 3.7 mV. Therefore, as the heater power increased the shift became more uniform over the entire range of NO concentrations probed. At approximately 81 mW the heater power was sufficient to reduce the NO sensitivity to such a degree that the response curve was essentially horizontal. When 200 ppm NO<sub>2</sub> was introduced for this setpoint, the curve remained horizontal but shifted to more negative values by 6.8 mV.

When the results for NO (0 ppm and 200 ppm NO<sub>2</sub>) in Figure 4-4 are compared to the changes in voltage between the 0 ppm NO<sub>2</sub> baseline and 200 ppm NO<sub>2</sub> gas step (Figure 4-2), the improved NO<sub>2</sub> selectivity due to changes in local electrode temperature becomes apparent. Without the use of the heating elements, the measured shift of the LCO(2)-Pt(1) electrode-pair when 200 ppm NO<sub>2</sub> was added to the NO gas mixture was (3.32 to 2.2 mV) lower than the expected value. This was a significant amount when considering the overall magnitude of the response. In a gas sensor, this type of discrepancy can be debilitating when trying to determine

individual concentrations of species in a gas mixture because the actual voltage measured would be different from the anticipated value. However, the much improved NO<sub>2</sub> selectivity achieved for a heater setpoint of ~81 mW had a difference of only 0.3 mV from what was expected.

In summary, the LCO(2)-Pt(1) electrode-pair demonstrated that the array was capable of NO<sub>2</sub> selectivity through the use of local thermal modifications to (primarily) one of the electrodes. The NO and NO<sub>2</sub> sensitivity (mV/decade ppm) as a function of total heater power is shown in Figure 4-5 for the various NO<sub>x</sub> mixtures. As is clear from the plot, the NO sensitivity went to zero (when heater power was ~81 mW) even in the presence of 200 ppm NO<sub>2</sub>. Furthermore, the NO<sub>2</sub> sensitivity almost doubled at the same heater setpoint that the NO<sub>2</sub> selectivity was achieved. The overall improvements to the device are clear when considering these changes in sensitivity and the more consistent voltage shifts observed with exposure of gas mixtures to NO and NO<sub>2</sub>. Understanding why these improvements happened will be integral to the design of the next generation sensor arrays.

#### **4.4.1.2 Total NO<sub>x</sub> sensitivity**

Another relevant array signal to consider is that of the LCO(2)-LCO(4) electrode-pair. Referring to Figure 4-1, the temperature of LCO(2) became elevated with respect to the LCO(4) electrode (as well as the ambient) when power was delivered to the heaters because of the location of the electrodes about the array. Furthermore, without the use of the heaters one would expect zero NO<sub>x</sub> sensitivity for this signal since the sensing electrodes are made of the same material and due to the symmetric arrangement of the Pt and LCO sensing electrodes. However, as can be seen in Figure 4-6, while there was minimal NO sensitivity there was a more evident NO<sub>2</sub> response even without the use of the heaters. This can be explained, at least in part, as a result of the fabrication process, in which slight variations in the manual screenprinting parameters might have caused differences in the geometry of the electrodes and/or in the

microstructure of the various sensing structures (e.g., electrode and electrode/electrolyte interface) on the device. The properties of these sensor features have been shown to affect the responses of potentiometric and chemiresistive sensors.<sup>147,163-165</sup> However, this does not change the underlying significance of the results from this electrode-pair signal.

Figure 4-7 shows how the LCO(2)-LCO(4) electrode-pair was able to detect total NO<sub>x</sub> concentrations when NO and NO<sub>2</sub> co-existed in a gas mixture. This data represents the case for ~81 mW of total heater power, where the square symbols represent NO gas steps and the circle symbols are for NO<sub>2</sub> gas steps. Filled symbols (dashed lines) represent the instances when NO<sub>x</sub> gas mixtures were tested. The response to NO<sub>2</sub> and NO gas steps always showed a negative slope (i.e., sensitivity) at this ambient temperature, even when NO<sub>x</sub> gas mixtures were present. Furthermore, the shift in the LCO(2)-LCO(4) signal was always a larger (more negative) value regardless of whether NO was added to NO<sub>2</sub> gas steps, or NO<sub>2</sub> during NO gas steps. As with the LCO(2)-Pt(1) signal, this was likely a result of the fact that the LCO(2)-LCO(4) signal had negative sensitivity for both NO and NO<sub>2</sub> gas steps. Figures 4-6 and 4-7 both show that only minor changes in sensitivity occurred as a result of the shifts in sensor response when 200 ppm NO (NO<sub>2</sub>) was added during NO<sub>2</sub> (NO) gas steps. The total-NO<sub>x</sub> sensing capabilities of the LCO(2)-LCO(4) electrode-pair was further demonstrated with the fact that the signal had a distinct value for each combination of NO and NO<sub>2</sub> concentrations. Furthermore, the results for the NO and NO<sub>2</sub> gas steps were in agreement. In order to fully understand the reasons why this electrode-pair was able to provide total-NO<sub>x</sub> sensing, there is a need to compare the results from the signal to the conclusions that have been drawn in previous work.

#### **4.4.1.3 Possible explanations for sensing electrode-pair response**

Because the LCO(2)-LCO(4) signal resulted from two electrodes of the same, well-studied, (p-type) semiconducting material, there is the opportunity to relate the sensor response directly to

the results from XPS, DRIFTS, and temperature-programmed reaction (TPR) and desorption (TPD) experiments that have been conducted in the past.<sup>98,145,146</sup> During NO adsorption, the formation of a nitrite,  $\text{NO}_2^-$ , surface species has been proposed to remove one electron from LCO for every NO molecule adsorbed, which would raise the potential (i.e., Fermi level) of the electrode. Isotopically labeled oxygen TPR and TPD results suggested that this occurs as the NO molecule consumes a subsurface oxygen ion from the LCO, without the involvement of any adsorbed oxygen. Thus, the locally removed electron maintains charge neutrality after the adsorbate takes the lattice oxygen, which is an acceptor dopant in the LCO.<sup>145,146,166</sup> Upon desorption, the oxygen is returned to the LCO lattice, which explains the reversibility of the sensor response. Nitrate,  $\text{NO}_3^-$ , formation from the adsorbed  $\text{NO}_2^-$  would result in the extraction of a total of 3 electrons (2 more after conversion from nitrite) from LCO for every original NO molecule adsorbed. On the other hand, nitrite formation from an  $\text{NO}_2$  molecule would cause a single hole to be removed from the LCO (thereby lowering the potential) to maintain charge neutrality. In this case, a lattice oxygen is not removed from the LCO. However, nitrate formation from the  $\text{NO}_2$ -spurred nitrite species would take a lattice oxygen and remove an electron from LCO (thereby raising the potential). On LCO, nitrite and nitrate groups exist in varying amounts at different temperatures for both NO and  $\text{NO}_2$  adsorption due to inherent differences in the complex stabilities.<sup>145,166-168</sup> Furthermore, the proposed mechanisms for  $\text{NO}_2$  and NO adsorption involve the interconversion between nitrite and nitrate species during some overlapping temperature range. Consequently, the ratio of nitrate: nitrite species in both the NO and  $\text{NO}_2$  adsorption cases will change depending on the temperature. As the temperature increases past some critical point, the ratio will be greater than unity as the nitrite group begins to convert into the more stable nitrate species in greater numbers.<sup>145,146</sup>

In the DRIFTS and XPS work, the gases were adsorbed at 225 °C and quenched in order to maximize surface coverage for the full range of adsorbate species evolving during the TPD experiments. Those studies were aimed at identifying the surface complex species, while the labeled oxygen experiments were conducted to assign the species to the various TPD peaks and understand the role of LCO lattice oxygen in the sensing mechanism.<sup>98,145,146</sup> While the desorption peaks in the TPD experiments were below the temperature range investigated in this paper, under continuous flow conditions there will be NO<sub>x</sub> adsorbed on the surface of LCO even at these higher temperatures. Above the peak temperatures the rate of desorption merely exceeds the rate of adsorption, and NO<sub>x</sub> adsorbates still exist on the surface. Also note that the past TPD results were for powder samples.<sup>97,98,145,146,169</sup> Therefore, the temperatures of the desorption peaks, and hence the range of temperatures at which each surface species exist, will shift upward with a solid electrode due to decreased surface area.<sup>170,171</sup> In addition, the La<sub>2</sub>CuO<sub>4</sub> from the previous experimental studies contained minor copper oxide phase impurities, which could account for some of the operating temperatures differences seen in the current investigation.<sup>98</sup> Subsequent work has utilized inductively coupled plasma (ICP) spectroscopy to verify precursor concentrations prior to powder synthesis, which has minimized impurities. In fact, LCO sensors have been manually fabricated on separate occasions with resulting optimum sensing performance from 400 – 600 °C in some instances and 500 – 700 °C in others.<sup>98,147,157,164,165</sup> Furthermore, we have shown that geometrical and microstructural differences can affect the range of operating temperatures, sensitivity, and response time of these sensors.<sup>147,165</sup> Finally, more recent results demonstrated that sample configuration (i.e., proximity of catalyst layers or method of electronic lead attachment) can alter performance.<sup>164</sup> In light of the preceding

comments, we believe that the proposed mechanisms are likely to have remained the same for the LCO(2)-LCO(4) signal as described in the analysis below.

When power was applied to the heaters, the LCO(2)-LCO(4) signal showed a negative response to increasing concentrations of both NO and NO<sub>2</sub>. Normally if an electrode-pair of a potentiometric gas sensor is sensitive to both NO and NO<sub>2</sub>, the responses are in opposite directions.<sup>98,147</sup> This happens to cause a drop in the measured signal for simultaneous NO<sub>x</sub> exposure. Therefore, the LCO(2)-LCO(4) signal may have an advantage for total-NO<sub>x</sub> sensing. For the reasons mentioned above, there is only one other known case where a potentiometric gas sensor has been used to detect total NO<sub>x</sub> without a drop in response magnitude.<sup>172</sup> However, in these devices the sensor really only detected NO<sub>2</sub> because a PtY filter (upstream of the sensor) selectively converted NO into NO<sub>2</sub> before being exposed to the sensing elements. There are a few more examples of total-NO<sub>x</sub> sensors, but most do not actually qualify as such.

As the total heater power increased for the array, the temperature at the LCO(2) electrode increased relative to LCO(4) and the ambient. In the case of NO gas steps, the negative response for the LCO(2)-LCO(4) signal may have been due to decreased total (nitrite and nitrate) surface coverage at the LCO(2) electrode compared with the lower temperature LCO(4). This would lower the total amount of charge injected into LCO(2), and hence decrease the extent of band-bending. Though no direct experimental proof exists, we believe that the LCO(2) Fermi level would decrease (relative to the previous value) even if there was an increase in the nitrate:nitrite ratio, which as discussed before would occur because the nitrate is the more thermally stable group. Therefore as the heater power increased, the potential of LCO(2) would have decreased and the resulting electrode-pair measurement would become more negative, as observed.

In the case of NO<sub>2</sub> gas steps, the ratio of nitrate:nitrite species would have also risen as the LCO(2) temperature increased. However, the temperatures at which these complexes existed would be higher than that of the corresponding species resulting from NO adsorption.<sup>98,145,146</sup> Furthermore, past TPD experiments showed approximately a 2:1 ratio for NO<sub>2</sub> to NO surface coverage on LCO.<sup>98</sup> Therefore without the use of the heaters, the higher overall surface coverage during NO<sub>2</sub> exposure was likely the cause for the nearly double NO<sub>2</sub> sensitivity when compared to that of NO (Figure 4-6). Interestingly, when the heater power was increased, the difference between the NO and NO<sub>2</sub> sensitivities also increased. In fact with a total heater power of ~81 mW, the NO<sub>2</sub> sensitivity was approximately triple the NO sensitivity. As with the case of NO exposure, there is the possibility that differences in the nitrate:nitrite ratio as the temperature of LCO(2) increased were the cause for the changes in NO<sub>2</sub> response. However, without additional experiments there is no way to determine whether the modified NO<sub>2</sub> sensitivity was due to this or changes in surface coverage. But these observations do demonstrate the importance of adsorptive properties in determining the voltage response of a potentiometric sensor involving at least one semiconducting electrode.

#### **4.4.1.4 Determining NO and NO<sub>2</sub> concentrations**

In general, gas sensors require a calibration in order to correlate the output of the transducer to the known value of input (i.e., gas concentration). In this work, the sensor array prototype was demonstrated to have the capability of NO<sub>2</sub> selectivity with the LCO(2)-Pt(1) signal and to sense total-NO<sub>x</sub> using the LCO(2)-LCO(4) electrode-pair. Therefore, simple linear math can be used to determine the individual NO and NO<sub>2</sub> concentrations from the calibration curves of these two signals (e.g., Figures 4-4 and 4-6). For example, suppose the sensor array outputs a value of approximately 26.5 mV for the LCO(2)-LCO(4) electrode-pair and 27.5 mV for the LCO(2)-Pt(1) signal. Then, using the calibration curve for LCO(2)-LCO(4) the predicted

concentration of pollutant gases is 400 ppm of total-NO<sub>x</sub>. While this is useful in and of itself, determination of the individual concentrations of NO and NO<sub>2</sub> requires use of the LCO(2)-Pt(1) calibration curve. This works out to a value of 200 ppm NO, which after subtraction leaves 200 ppm of NO<sub>2</sub>. This scenario can be extended to additional gas mixtures, and may involve any other species when utilizing numerous electrode-pairs. Note, however, that the picture presented above is oversimplified because the calibration curves have only been made for NO (0 and 200 ppm NO<sub>2</sub>) and NO<sub>2</sub> (0 and 200 ppm NO).

We believe the capability to sense total-NO<sub>x</sub> with the LCO(2)-LCO(4) signal is due in part to the fact that both NO and NO<sub>2</sub> adsorption result in the creation of nitrite and nitrate surface complexes. At higher temperatures, the nitrate species will exist in relatively higher numbers. Furthermore, the resulting species from both NO and NO<sub>2</sub> adsorption caused the measured electrode-pair potential to go more negative. From this and the previously mentioned concepts, we believe that mixtures of NO<sub>x</sub> in different ratios (100:300 or 300:100 ppm NO to NO<sub>2</sub>) at a particular temperature differential between electrodes could result in unique responses that are parallel and shifted with respect to the curves shown in Figure 4-7. Therefore even though the level of response to NO and NO<sub>2</sub> are unequal, there may be the possibility to utilize this signal for total-NO<sub>x</sub> measurements. This hypothesis will be experimentally verified in future work. However, even if this ends up not being the case, the LCO(2)-LCO(4) electrode-pair can still be used to determine total-NO<sub>x</sub> by utilizing the NO<sub>2</sub>-selective signal when both electrodes are at the same temperature and the response when they are at different temperatures (Figure 4-6).

#### **4.4.2 Other Gas Sensor Array Results**

The effects of local electrode temperature and NO<sub>x</sub> gas mixtures have already been discussed. The following will briefly review the effect of total gas flow rates, ambient temperature, and exposure to other gases on these findings. The results presented are primarily

for the LCO(2)-LCO(4) electrode-pair. However, other signals will be referred to when appropriate.

#### **4.4.2.1 Effect of ambient temperature**

The effect of local electrode and NO<sub>x</sub> gas mixtures for the LCO(2)-LCO(4) electrode-pair varied depending on the ambient temperature of the furnace. For instance, at 500 °C, 550 °C, and 600 °C this signal had almost zero NO sensitivity without localized heating. As the total heater power increased, the NO sensitivity became increasingly negative, with a larger change in sensitivity for lower ambient temperatures. As discussed earlier, this probably had to do with increased surface coverage at lower temperatures. Furthermore, at lower temperatures LCO is further away from the extrinsic-intrinsic transition, allowing adsorption to have a larger effect on band-bending. At 500 °C, there was a relatively large positive NO<sub>2</sub> sensitivity without localized heating, which transitioned into a small negative response as total heater power increased. When the ambient temperature was 550 °C and 600 °C, there were small negative responses without the use of the heaters. Under these conditions, the signal also became increasingly negative as total heater power increased. A possible reason for the positive NO<sub>2</sub> response at 500 °C was that the LCO(4) electrode had a smaller ratio of nitrate:nitrite species than LCO(2). This resulted in a smaller potential at LCO(4) compared to LCO(2), because the nitrite complex formed from NO<sub>2</sub> injected more electrons into LCO than those removed during nitrate formation. The transition from positive to negative NO<sub>2</sub> response probably occurred as the surface coverage at the LCO(2) electrode decreased with increasing heater power. Overall, this electrode-pair had the characteristics of a good total-NO<sub>x</sub> signal at ambient temperatures of 550 °C and 600 °C using a total heater power of less than 85 mW in both cases. Moreover, the LCO(2)-Pt(1) electrode-pair retained the capability of NO<sub>2</sub> selectivity at 550 °C, though with slightly less NO<sub>2</sub> sensitivity.

These results indicate that the prototype gas sensor array was able to selectively determine individual concentrations of NO and NO<sub>2</sub> over a fairly large ambient temperature range.

#### **4.4.2.2 Response time**

The response times of the LCO(2)-LCO(4) sensor were relatively fast and can be seen in Table 4-1 for 500 °C and 600 °C at two different heater setpoints. Note that the actual power delivered at these ambient temperatures was slightly different because the automation program set the same voltages at each furnace setpoint, but the inherent resistance of the heating elements changed with temperature. Along with any changes in the thermal transport properties, this resulted in slight variations in the temperature differences between the electrodes at each furnace setpoint. As expected, the response time was (slightly) faster at higher ambient temperatures. However, in some cases the response time was slightly slower when using localized heating. This may have been due to minor thermal-gradients that thermal models predicted in the LCO(4) electrode due to the arrangement of the sensing electrodes with respect to the heaters.<sup>157</sup> Local equilibria may have taken more time when a thermal gradient was present in the electrode. Interestingly, this effect was more apparent during exposure to NO.

#### **4.4.2.3 Effect of total flow rate**

Past results were conducted at 500 °C and under a total flow rate of 100 ccm.<sup>151,157</sup> Under these conditions, the LCO(2)-LCO(4) electrode-pair was able to achieve NO selectivity at various heater setpoints, while the Pt(3)-LCO(4) signal resulted in NO<sub>2</sub> selectivity. Furthermore, the Pt(3)-LCO(2) signal was able to attain both NO and NO<sub>2</sub> selectivity depending on the temperature difference between the electrodes. In terms of LCO(2)-LCO(4), higher flow rates produced total-NO<sub>x</sub> sensing capabilities. Another observation to note was that the response time of this electrode-pair was much slower (~200 s) when the total flow rate was only 100 ccm. This is more than 12 times as slow when compared to the case when total flow rate was 300 ccm

(Table 4-1). This result corresponds with the observation of others, and has been suggested to occur due to mass-transfer limitations that change the local rates of equilibration.<sup>173-175</sup>

#### 4.4.2.4 Responses to other gases

For LCO(2)-LCO(4), there was some minor cross-sensitivity of NO or NO<sub>2</sub> with CO, though more work needs to be done with these gas mixtures. However, the initial results indicated that the likely result will be an electrode-pair capable of total-NO<sub>x</sub>+CO detection. Past TPD experiments showed that the presence of CO allowed NO to desorb beyond the normal temperature threshold.<sup>98</sup> In terms of LCO(2)-LCO(4) there was a greater effect of CO on NO than NO<sub>2</sub>, which was probably due to surface reactions of CO with lattice oxygen. As mentioned earlier, the formation of nitrite and nitrate surface species from NO requires lattice oxygen. Conversely, only the formation of the nitrate complex from NO<sub>2</sub> requires lattice oxygen. At zero and low heater power levels, there was a relatively large CO<sub>2</sub> effect on NO sensitivity (500 °C to 600 °C). This was expected as past TPD results have shown that CO<sub>2</sub> prevents NO chemisorption at high temperatures.<sup>98,169</sup> However, with 81 mW of total heater power the NO<sub>x</sub> response of LCO(2)-LCO(4) was mostly unchanged when up to 10% CO<sub>2</sub> was introduced during NO<sub>2</sub> gas steps and up to 20% CO<sub>2</sub> during NO gas steps (550 °C and 600 °C). Furthermore, CO<sub>2</sub> caused only minor shifts in the LCO(2)-Pt(1) NO response, while maintaining zero sensitivity to NO and not really affecting NO<sub>2</sub> sensitivity. The CO<sub>2</sub>-induced shifts during NO gas steps improved considerably as heater power increased. This electrode-pair was not sensitive to CO, even when NO was introduced to the gas mixture. NO<sub>2</sub>, on the other hand, caused shifts without much change in slope.

## 4.5 Conclusions

This work has shown how modification of local electrode temperatures in a potentiometric gas sensor array can lead to a device with the capability of selectively determining individual NO

and NO<sub>2</sub> concentrations. Additionally, the sensitivity to both NO and NO<sub>2</sub> was simultaneously enhanced. The gas sensor array prototype proved to be a device capable of selective NO<sub>x</sub> detection even in the presence of large concentrations of CO<sub>2</sub>. There was a small effect of CO on the NO<sub>x</sub> response of the LCO(2)-Pt(1) and LCO(2)-LCO(4) signals. This can likely be solved with the introduction of a CO selective signal into the array. Then linear math calculations can be used to determine individual concentrations of CO, CO<sub>2</sub>, NO, and NO<sub>2</sub>. The sensor signals were related to past results using temperature programmed techniques, XPS, and DRIFTS experiments. Furthermore, this work emphasized the importance of adsorption equilibria in the sensing mechanism for potentiometric gas sensors with electrodes in a single gas environment and involving at least one semiconducting electrode. Future work will involve addition of new materials and optimization of electrode geometry and microstructure, which should result in larger responses while maintaining selectivity. Furthermore, to elucidate the band-bending and resultant Fermi level shift process, new experiments will be conducted with a Kelvin probe capable of UHV and atmospheric measurements, which is inline with an electron spectroscopic (XPS, UPS, and AES) system.

As mentioned before, a total of six sensor signals were monitored using only two materials arranged as four electrodes in the array. As a result, this work has opened up the possibility for conducting simultaneous, combinatorial materials research in the area of potentiometric gas sensors. Thus far, we have achieved differences in electrode temperature exceeding 50 °C. In order to achieve larger thermal gradients on the device, future arrays will utilize rigid structural supports to improve thermal shock resistance allow an increased number of sensing electrodes. We will also investigate possible cross-talk and proximity effects using designs that separate the individual electrode-pairs onto separate regions of YSZ coatings on the surface of the structural

support. Furthermore, there exists the possibility of incorporating other methods of actively changing the differential electrode equilibria such as with the use of an external electric field.<sup>176</sup> All of this future work will be more easily conducted thanks to on going research of fabricating solid-state ionic devices with a rapid-prototype machine.<sup>177</sup>

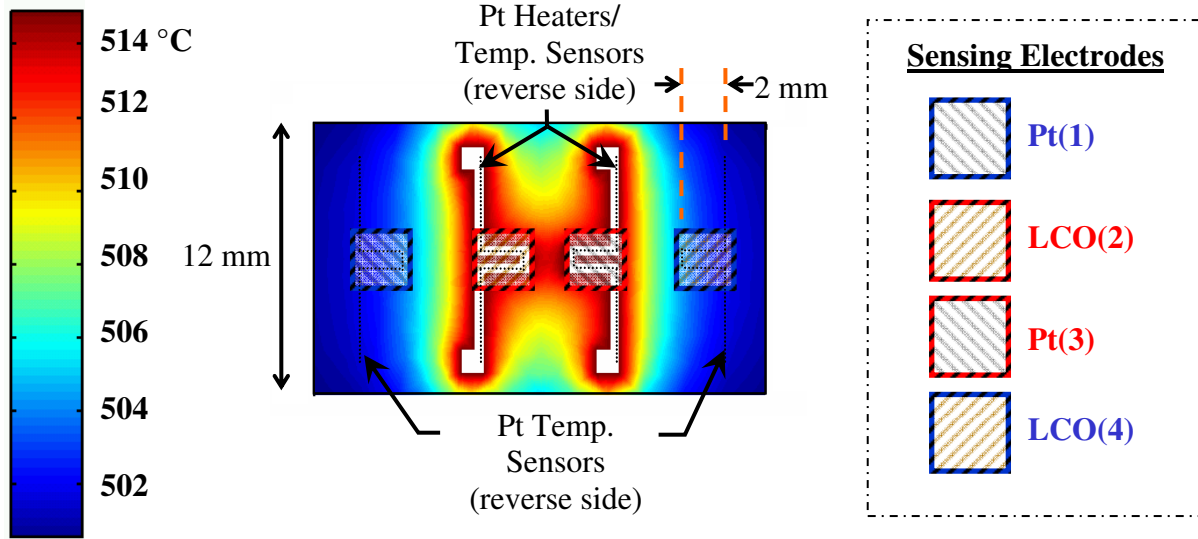


Figure 4-1. Schematic of second-generation gas sensor array. The device consisted of four sensing electrodes using two materials, Pt and LCO, which were staggered on a YSZ substrate. Each sensing electrode was aligned with a C-shaped Pt element, which had been deposited on the opposite side of the YSZ substrate. In the experimental work presented, only the two inner Pt elements were used as heaters, while all four were used as temperature sensors.

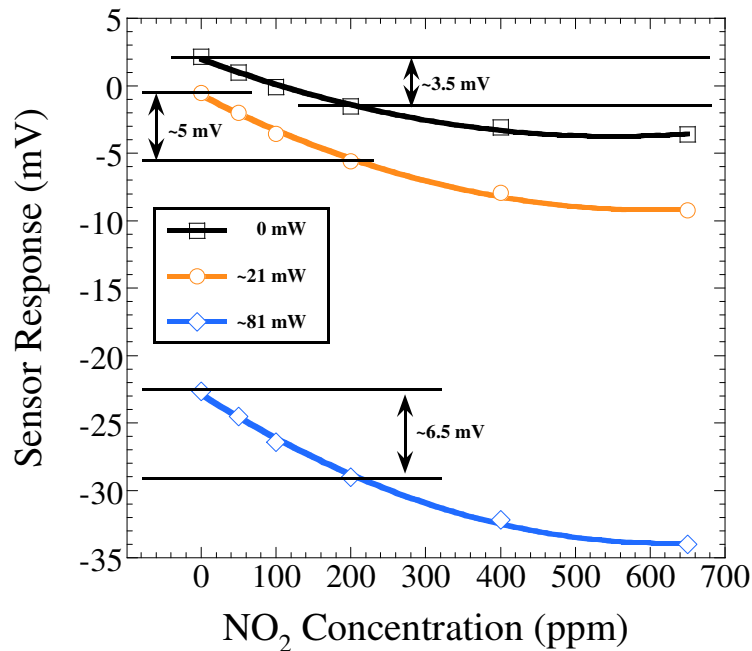


Figure 4-2. NO<sub>2</sub> sensor response at three different total heater power settings with an ambient temperature of 600 °C. Also shown are each of the voltage changes when 200 ppm NO<sub>2</sub> was introduced compared to the cases with only 3% O<sub>2</sub>, N<sub>2</sub> balance.

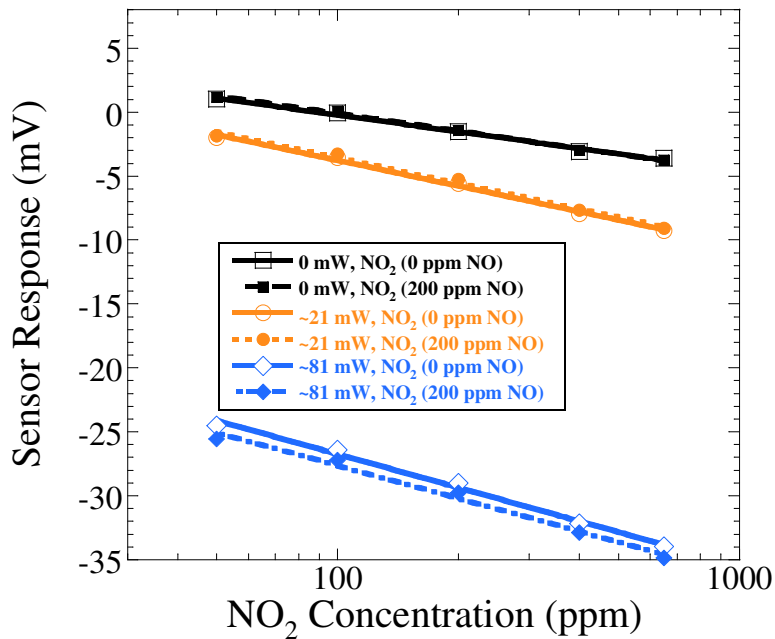


Figure 4-3. Response to  $\text{NO}_2$  gas steps with and without 200 ppm NO for the LCO(2)-Pt(1) electrode-pair and an ambient temperature of 600 °C. Square, circle, and diamond symbols represent cases with 0, ~21, and ~81 mW of total heater power (solid lines, open symbols – both NO and  $\text{NO}_2$ ; dashed lines, closed symbols – only  $\text{NO}_2$ ).

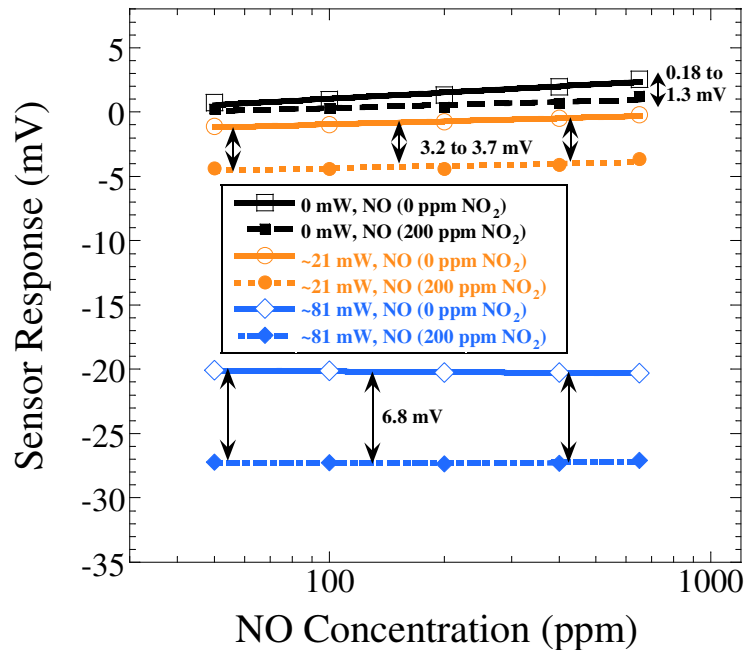


Figure 4-4. Response to NO gas steps with and without 200 ppm  $\text{NO}_2$  for the LCO(2)-Pt(1) electrode-pair for an ambient temperature of 600 °C. Square, circle, and diamond symbols represent cases with 0, ~21, and ~81 mW of total heater power delivered to the heating elements (solid lines, open symbols – both NO and  $\text{NO}_2$ ; dashed lines, closed symbols – only  $\text{NO}_2$ ).

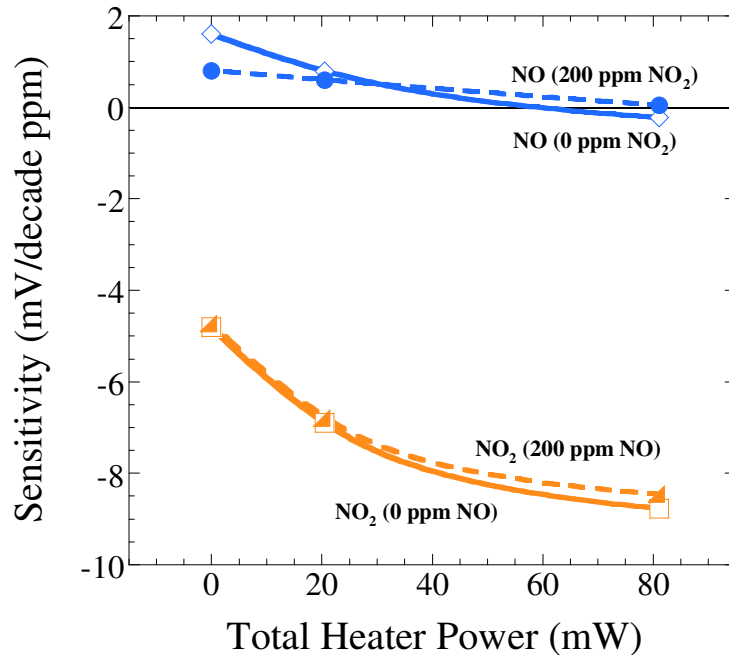


Figure 4-5. Sensitivity versus total heater power for LCO(2)-Pt(1) electrode-pair with an ambient temperature of 600 °C. NO sensitivity, both with and without 200 ppm NO<sub>2</sub> present, went to zero at higher heater levels.

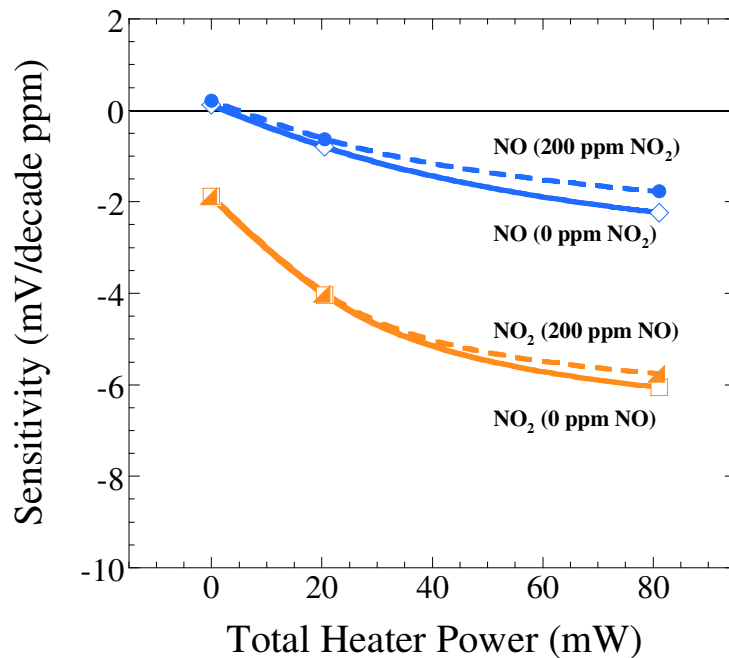


Figure 4-6. Sensitivity versus total heater power for LCO(2)-LCO(4) sensing electrode-pair with an ambient temperature of 600 °C. As can be seen, the signal showed some NO<sub>2</sub> selectivity without the use of the heaters. As heater power increased, the electrode-pair became capable of total-NO<sub>x</sub> detection.

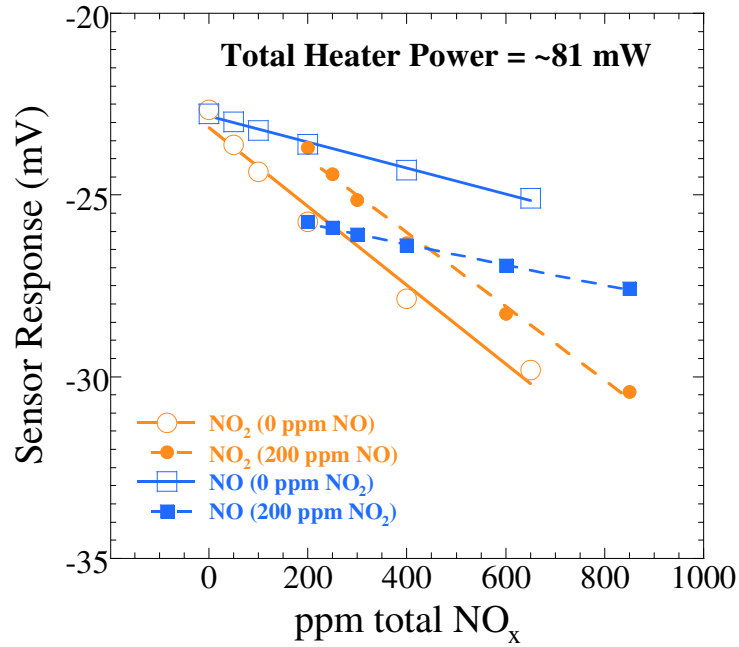


Figure 4-7. Total NO<sub>x</sub> sensitivity for LCO(2)-LCO(4) sensing electrode-pair when total heater power was ~81 mW with an ambient temperature of 600 °C.

Table 4-1. Typical NO<sub>x</sub> response times at 500 °C and 600 °C (at different heater setpoints, 300 ccm total flow rate)

Response Time Conditions	500 °C (0 mW)	500 °C (~87 mW)	600 °C (0 mW)	600 °C (~81 mW)
NO gas steps	7 s	18 s	N/A	15 s
NO <sub>2</sub> gas steps	12 s	15 s	12 s	12 s

CHAPTER 5  
ELECTRIC-FIELD ENHANCEMENTS IN POTENTIOMETRIC GAS SENSORS AND  
OTHER SOLID-STATE IONIC DEVICES

**5.1 Introduction**

Many solid-state ionic devices involve interactions between adsorbed gas species and electrode and/or electrolyte materials. These adsorbates and the surface atoms of the solid(s) have individual local electric fields resulting from their respective charge distributions.<sup>178,179</sup> The way in which these fields interact with each other can influence reaction mechanisms, and ultimately the performance, in solid-state ionic devices. This means that a device may be enhanced if the properties of these fields can be favorably modified. Therefore, the primary focus of this work was to explore the use of an externally-generated electric field to enhance the performance of solid-state ionic devices. Particular attention was given to the effect of an electric field on potentiometric gas sensors.

Recent developments have expanded the number of possible applications for these non-Nernstian potentiometric gas sensors and improved the chance that they will be successfully commercialized.<sup>151,157</sup> Such devices are particularly attractive for applications requiring quantitative detection of multiple species in complex gas mixtures (e.g., O<sub>2</sub>, NO<sub>x</sub>, CO<sub>x</sub>, H<sub>2</sub>O, and hydrocarbons). The gas sensors must be highly sensitive and selective to the species of interest without substantial interference from other gases. In many cases the sensors must also be capable of surviving in thermally and chemically harsh environments.

The sensing mechanisms of these devices are summarized in the differential electrode equilibria theory, which includes contributions from electrochemical reactions (mixed potential), heterogeneous catalysis, and band-bending when at least one semiconducting electrode is used.<sup>65,91</sup> In order to fully evaluate the semiconducting effect on the potential generated at each electrode, one needs to consider the relationship between the Fermi level and adsorption

equilibria. The Fermi level is essentially the electrochemical potential of the electrons in the electrodes. Were the electrodes of the electrochemical cells connected, their Fermi levels would eventually become equal as equilibration occurred. However, since the potentiometric sensor operates at open-circuit conditions, the cell voltage is equivalent to a difference in the Fermi levels between the electrodes.<sup>159</sup> With the use of a semiconducting material, the Fermi level of the electrode can change as gas adsorbs on the surface.<sup>161</sup> Therefore, if the local field-interaction of adsorbates and the surface is able to be modified, this likely affects the sensing mechanism and device output. This opens the possibility for actively enhanced gas sensors.

The active enhancement of these gas sensors was accomplished through the use of indirectly-generated electric fields that do not result in charge reaching the electrolyte or electrodes making up the cell (i.e., essentially zero current flow). This is a significant distinction from electric-fields generated with a direct bias to an electrochemical cell, which can drive electrochemical reactions but has an upper limit in terms of maximum field strength due to risk from Joule heating or material decomposition. We have successfully demonstrated that through the use of these externally-generated electric fields, the sensitivity of the potentiometric gas sensors can be increased significantly and they can be made more selective.

Several configurations were used to investigate the electric-field effect. Initially experiments involved a planar gas sensor with all sensing electrodes in the same gas environment. This sensor was used to investigate the influence of field shape, magnitude, and polarity. The next sample was air-reference based, where changes in the potential of the sensing electrode to varying analyte concentration were measured in conjunction with gas analysis of the effluent coming off this electrode. A third configuration took the form of a capacitor-type chip made from the sensing electrode material (i.e., without solid electrolyte). This sample was used

in temperature programmed desorption (TPD) experiments to investigate the effect of the electric field on chemisorption. In all of the configurations, an electric field was generated at the surface of the samples with an applied voltage to electrodes which allow charge to accumulate near the surface but prevent charge transfer to the device. When possible the direction of the field was changed to see the influence of positive and negative fields.

## 5.2 Background

The effect of electric fields on surface reactions in UHV conditions can be found in the literature as early as the 1960s.<sup>161,178,179</sup> Most researchers believe that an electric field can influence a reaction due to electrostatic mechanisms, chemical mechanisms, or contributions from both. Electrostatic mechanisms include changes in adsorbate charge density, which can affect bond length or alter molecular bending modes and frequency. On the other hand, chemical mechanisms relate to changes in orbitals and donation/backdonation between adsorbate and adsorbent. Also included in this category are changes in Pauli repulsion, which may affect the stability of surface complex formation.

In electrochemistry there is another effect, known as electrochemical promotion, which involves the use of an applied bias to alter catalysis. Electrochemical promotion, which is also known as Non-Faradaic Electrochemically Modified Catalytic Activity (NEMCA), involves the direct voltage or current bias of the cell using a power supply.<sup>180</sup> For an oxygen-ion conducting solid electrolyte, this results in an electrochemically controlled migration of oxygen ions onto the catalyst electrode and causes an increased reaction rate beyond that predicted with Faraday's Law.<sup>78,79</sup> Much evidence in the literature suggests that the bias may affect such system characteristics as the work function, adsorbate bond strength, preferential adsorption sites, or intramolecular stretching frequencies.<sup>77,78,80-82,181</sup> These changes may alter the strength of the chemisorptive bond of covalently bonded reactants and intermediates, thus changing activation

energies and reaction rates. Other work has shown that electrochemical promotion can be used to electrochemically enhance NO<sub>x</sub> reduction on LaBO<sub>3</sub> perovskites (where B is a transition metal or rare earth metal).<sup>113</sup>

### **5.2.1 Electronic Theory of Catalysis and Chemisorption on Semiconductors**

The theories for the relationship between catalysis and chemisorption involving semiconductors has been discussed and formulated by such researchers as Wolkenstein, Hauffe, Madou, and Morrison.<sup>159,161,182,183</sup> Typical catalyst materials are metals, with noble metals (e.g., Pt or Pd) often having the highest activity for many reactions. However, it has long been known that semiconductors also represent a large class of important catalysts. In fact, many metal and noble-metal catalysts actually have a thin semiconducting oxide layer at their surface that is often responsible for catalytic activity.<sup>161,184</sup> In most cases there is a relationship between the catalytic activity, work function, and electrical conductivity of a semiconductor for a particular reaction. Semiconducting properties will have an effect as long as a certain stage of the reaction has at least one elementary step involving free electrons or holes at the surface. Furthermore, metal/semiconductor interactions can drastically change such reactions being catalyzed on the metal. The properties of semiconductor catalysts can also change reaction rates, which determine in part the path that a reaction takes. These processes may result from changes to the semiconducting oxide Fermi level because in terms of chemisorption, the Fermi level position, amongst other things, determines the adsorptivity of acceptor and donor molecules, surface charge, and relative fraction of surface complexes formed.

### **5.2.2 Related Work**

In chemical field effect transistors, or CHEMFETs, a gas sensitive material acts as the gate of a standard (metal-oxide-semiconductor) MOSFET device and provides a means to detect species when the electron conduction channel is opened from a change in the gate field. The

research groups of Doll et al. and others have developed a modified version of the CHEMFET, called work function sensors or gate-refreshable CHEMFETs, in which the device takes advantage of Wolkenstein's concept of the 'electroadsorptive' effect (discussed below) in order to enhance reversibility.<sup>132-135</sup> Another method of refreshing the sensor involves the use of UV illumination to change the sensing electrode Fermi level. Furthermore, Tuller et al. have investigated the use of photo-induced improvements in chemiresistive gas sensor sensitivity and selectivity, and photo-activated catalysis in solid oxide fuel cells.<sup>136,137</sup>

### **5.3 Experimental**

Initial experiments involved a planar device with sensing electrodes in a single gas environment. This device had electric-field electrodes, which were electrically (and ionically) isolated from the rest of the device. The second sample was an air-reference sensor used to concurrently measure changes in sensor response and gas composition over the sensing electrode. The third sample consisted of a capacitor-type device built around the sensing electrode material for use with TPD experiments. In all samples, the working electrode was  $\text{La}_2\text{CuO}_4$  (LCO), which was prepared using powder synthesized with the auto-ignition (lean) wet-synthesis technique, followed with calcination at 650 °C for 8 hours. The use of a mass spectrometer to monitor gas effluent required a high surface-area sensing electrode. Therefore the air-reference and TPD samples were made from a solid, porous bar of LCO.

#### **5.3.1 Sample Preparation**

##### **5.3.1.1 Planar sensor**

For the planar sensor in Figure 5-1A through 5-1C, two adjacent square rings (with rounded corners) of  $\text{Al}_2\text{O}_3$  paste were deposited on both the top and bottom of a thin (100  $\mu\text{m}$ ), commercial YSZ substrate (Marketch). The  $\text{Al}_2\text{O}_3$  paste was prepared using powder (Alcoa) and a commercial vehicle (ESL). In order to achieve dense layers, the sample was sintered at

1450 °C for 3 hours. Following this step, gold (Engelhard) conduction layers were carefully deposited on top of the now dense Al<sub>2</sub>O<sub>3</sub> layers. Gold wires were also attached to the gold paste. Note, that the width of the gold layer was smaller than that of the Al<sub>2</sub>O<sub>3</sub> to prevent contact with the YSZ. After drying, another layer of Al<sub>2</sub>O<sub>3</sub> was applied as a cover. Using LCO and Pt (Heraeus) pastes, square electrodes of both materials were then deposited in the center opening of each square Al<sub>2</sub>O<sub>3</sub> ring, in contact with the YSZ. The LCO paste was prepared using powder mixed with Polyethylene Glycol 8000 (PEG 8000, Fischer Scientific). Pt wires were attached to the Pt and LCO electrodes using the same respective pastes as used in the last steps. The sample was sintered at 800 °C for 10 hours.

### **5.3.1.2 Air-reference sample**

Unlike the planar gas sensor, the air-reference sample in Figure 5-1D and 5-1E had only one ring of Al<sub>2</sub>O<sub>3</sub>/Au/Al<sub>2</sub>O<sub>3</sub> (prepared in the same way as above), on the side of the YSZ substrate that contained the Pt air-reference (with attached Pt wire). In order to achieve the high surface-area sensing electrode needed for the mass spectrometer, 2 grams of LCO powder was combined with graphite to produce a 97:3 LCO/carbon ratio, mixed with 5 mL of 10% polyvinyl butyral (PVB, Alfa Aesar) in ethanol and then uniaxially pressed at 2000 psi for 2 minutes. The bar was then sintered for 10 hours at 800 °C. A segment of the LCO was cut from the bar using a diamond saw and ground to size using fine-grit SiC on a polishing wheel. The high surface area, porous LCO was attached to the YSZ using PEG 8000/LCO paste. On the opposite side of the YSZ was a Pt air-reference centered in an Al<sub>2</sub>O<sub>3</sub>/Au/Al<sub>2</sub>O<sub>3</sub> ring prepared similarly to the electrodes of the planar sensor described above. A Pt wire was then attached to the LCO using the same paste. Both the top face of the porous LCO and the Pt wire were capped with a thin Al<sub>2</sub>O<sub>3</sub> section. The Al<sub>2</sub>O<sub>3</sub> was prepared in the same way as the high surface-area LCO, except that the sintering temperature was 1450 °C for a half-hour. A gold contact and wire were

attached to the top of the alumina section, and dried. The entire device was dried and then sintered at 800 °C for 10 hours. This configuration was assembled differently from the planar sensor due to constraints of the air-reference test setup.

### **5.3.1.3 TPD “capacitor-chip” sample**

As seen in Figure 5-2, the capacitor-type chip consisted of a 1.25 mm by 1.25 mm by 4 mm porous LCO rectangle sandwiched between two thin segments of Al<sub>2</sub>O<sub>3</sub>. The Al<sub>2</sub>O<sub>3</sub> segments were attached to the LCO with Al<sub>2</sub>O<sub>3</sub> paste. Gold contacts and wires were attached to the Al<sub>2</sub>O<sub>3</sub> and dried. The entire chip was then sintered at 800 °C for 10 hours.

### **5.3.2 Experimental Setups**

The planar sensor was tested in a standard quartz tube reactor with square sample holder, placing the sensor in the furnace hot zone. Sensor leads connected to gold wires running down the reactor inside alumina wire-guides. Wires terminated at BNC connectors reinforced with steel tubing and epoxy outside the furnace. The air-reference sensor was tested in a reactor consisting of a hollow alumina tube with a flat notch on the outside of the curved portion as shown in Figure 5-3. A hole was drilled into the center of the notch so that the air-reference sample rested on a flat face in the middle of the tube. In this way, the high surface-area LCO electrode was exposed to various reactive gases from inside the alumina tube, while the air-reference remained at constant oxygen partial pressure. A smaller, solid Al<sub>2</sub>O<sub>3</sub> rod was inserted into the hollow tube in order to reduce dead volume. Ceramic cement (Ceramabond) was used to seal the sensor to the reactor tube. This alumina reactor was placed inside a larger tube that lined a small, cylindrical furnace. The effluent was sampled using a quadrupole mass spectrometer (Extrel). To perform device analysis via TPD, a reactor tube (Figure 5-2) was constructed using 4 mm inner-diameter quartz tubing welded to a short section of a 2 mm inner-diameter tube. This configuration allowed for the insertion of a full device into the tube center for rapid heating,

while maintaining minimal dead volume downstream of the sample into the mass spectrometer. The sample was loaded into the wider end and was connected to gold wires supported in small alumina tubes which remained in the upstream volume.

For experiments in the planar sensor and air-reference reactors, the gas environment was controlled using a manifold of mass flow controllers (MFCs, MKS Instruments). For TPD experiments a separate MFC setup for mass spectrometry measurements was used. In all tests, at least one Keithley 2000 digital multimeter with scanning card was used to monitor the sensor signals and applied field bias. Either a Keithley 2400 SourceMeter or a Hewlett-Packard 6681A was used to apply constant potential to the field electrodes and ensure zero current conditions. A custom LabVIEW program controlled/monitored the furnace temperature, gas concentration, field bias and the sensor signal.

### **5.3.3 Testing Procedures**

For the planar sensor, total flow rates were fixed at 300 ccm (3% O<sub>2</sub> with N<sub>2</sub> balance), while NO<sub>x</sub> was stepped at concentrations of 0, 50, 100, 200, 400, and 650 ppm. NO was stepped up and down twice, with each step held for 300 seconds. The same sequence was then repeated for NO<sub>2</sub>. This gas stepping scheme was conducted at 550, 500, and 450 °C. After the entire thermal cycling of gas steps was complete and the furnace returned to 550 °C, the electric-field bias was changed between 0 to ±8 V. For the bias scheme tested, “+” refers to a positive (negative) bias applied to the top (bottom) field rings, while “-” refers to the opposite case. Following a change in bias, a testing delay of one hour was used to ensure complete re-equilibration of the device. This sample was also used to test various bias schemes of the field electrodes, providing various electric-field “shapes.” These field-electrode configurations are summarized in Table 5-1 and illustrated in Figure 5-4. These electric-field vector-contour maps show relative field strengths and spatial orientation for the sensor prototype using the various

charging schemes. While not shown, it should be noted that the field contours also extend through substrate and other parts of device (i.e., the field penetrates the device).

In order to match the planar sensor setup as closely as possible, testing of the air-reference device involved the same gas conditions except with a total flow rate of 50 ccm. The same electric-field biases were applied between the Au/Al<sub>2</sub>O<sub>3</sub> layer atop the LCO and the Al<sub>2</sub>O<sub>3</sub>/Au/Al<sub>2</sub>O<sub>3</sub> ring surrounding the Pt air-reference. The effluent gases coming off the high surface-area LCO were analyzed with mass spectrometry. Since those gases contained N<sub>2</sub> as a balance gas, the minor identifier m/z ratios of 14 and 28 were unavailable to determine conversion of NO<sub>2</sub> to NO or the reverse. As a result, only the major m/z ratio for the gas being tested can be used to make definitive conclusions.

The LCO capacitor-type sample was exposed to 1% NO<sub>x</sub>/1% O<sub>2</sub> gas mixtures (He balance) at 300 °C with a total flow rate of 30 ccm, and subsequently cooled at 5 °C/minute to 25 °C under gas atmosphere. The sample was then outgassed under pure He for 8 hours to remove residual NO<sub>x</sub> species from the reactor chamber. Following outgassing, the sample was heated at 10 °C/minute to 600 °C. During heating, the effluent from the reactor was analyzed via mass spectrometry to determine the desorption points of the NO<sub>x</sub> from the LCO surface. This experiment was performed at 0, 2, 5, and 8 V across the device (polarity being irrelevant due to the device configuration).

### **5.3.4 Electric-Field Simulations**

In order to better understand this electric field effect and to assist in future designs, the field-electrodes were modeled using analytical and numerical expressions (Mathcad, Version 12.0), while Finite Element Modeling was used to picture the field distribution (i.e., shape) for each field-bias scheme (MatLAB, Version 7.0). The simple relation for a parallel plate capacitor, which is known by most engineers and scientists, cannot be used to predict the field

strength. Therefore, the electric field was modeled using charged ring and charged annulus disk configurations, as shown in Figure 5-5. Also shown in Figure 5-5 is the configuration and shape of one of the actual field-electrodes (i.e., a square ring with rounded corners); the dimensions of the inner radius and outer radius were 1.5 mm and 3.5 mm, respectively. Any differences between the modeled and real configurations would likely occur near the corners of the field-electrode. Though this is believed to be insignificant future modeling will resolve this issue.

The capacitance of the electric-field electrodes was measured at 450 °C using a precision LCR meter (Agilent 4284A). This value was used to determine the charge stored in the field electrodes for the different bias setpoints using the relation in Equation 5-1.

$$Q = C \cdot V \quad (5-1)$$

In this relation Q, C, and V represent the stored charge, measured capacitance, and applied voltage, respectively.<sup>185</sup>

The electric field along the axis of a charged disk with a hole in the center is computed with Equation 5-2.

$$E_z = -\left(\frac{2}{3\pi\epsilon_0}\right)\left(\frac{Q}{R^2}\right)\left(\frac{z}{\sqrt{z^2 + R^2}} - \frac{z}{\sqrt{z^2 + 0.25R^2}}\right) \quad (5-2)$$

Equation 5-2 is derived from the relation between voltage, charge, and the electric field of a ring charge called Poisson's equation, as shown in Equation 5-3.

$$\nabla^2 V = \frac{\rho_v}{\epsilon} = \nabla \cdot E \quad (5-3)$$

In Poisson's equation, V, ρ, ε, and E are voltage vector, (volume) charge, permittivity, and electric field vector.

When considering the off-axis regions of a field-electrode, the situation is much more complex. In this case, analytical expressions for the variation of the electric field in the radial

and axial directions can be derived using (complete) elliptic integrals of the first and second kind. A closed form solution is not possible, such that numerical methods must be used to solve these expressions which are shown in Equations 5-4 and 5-5.<sup>186,187</sup>

$$E_r = \frac{Q}{4\pi\epsilon_0} \frac{2}{\pi\xi^{3/2}(1-k)} \frac{1}{k} \left[ 2R \cdot K(\sqrt{k}) \cdot (1-k) - E(\sqrt{k}) \cdot (2R - k \cdot (r + R)) \right] \quad (5-4)$$

$$E_z = \frac{Q}{4\pi\epsilon_0} \cdot \frac{2}{\pi\xi^{3/2}(1-k)} \cdot z \cdot E(\sqrt{k}) \quad (5-5)$$

In Equations 5-4 and 5-5, Q is the charge, R is the ring radius, r is the distance along the radial direction, and z is the distance along the axis. K and E are the complete elliptic integrals of the first kind and second kind, respectively.<sup>188</sup>  $\xi$  and k are defined in Equations 5-6 and 5-7.

$$\xi = r^2 + R^2 + z^2 + 2rR \quad (5-6)$$

$$k = \frac{4rR}{\xi} \quad (5-7)$$

Equations 5-4 and 5-5 were solved numerically using Mathcad with a convergence criterion (TOL) of 0.02 for various radial and axial distances. Equation 5-2 was solved analytically for a range of axial distances. The electric field magnitudes were tested for field-electrode biases of 1, 5, and 8 V. In evaluating the analytical and numerical solutions, the electric fields generated at the top and bottom field-electrodes were superimposed to obtain the total field distribution. There may also be the need to consider the effect of each field-electrode on each other, which will be done in future work.

## 5.4 Results and Discussion

### 5.4.1 Electric-Field Simulations

The measured capacitance of the field-electrodes between 450 and 550 °C was ~ 20 nF. Figure 5-6 shows the resultant solutions for the electric field (5 V) along the z-axis of the field

electrode for the top and bottom capacitors using the analytical formula found in Equation 5-2. These fields were modeled with an outer ring radius ( $R$ ) of 1.75 mm. Also shown are the superimposed field for the case in which the top capacitor has  $+Q$  and the bottom capacitor has  $-Q$  (i.e.,  $+/-$ ) as in Figure 5-6A, and the opposite case (i.e.,  $-Q$  top and  $+Q$  bottom, or  $-/+$ ) as in Figure 5-6B. Field strengths are given in terms of  $V/\text{\AA}$  in order to compare the relative field strengths in this work to the UHV surface science and modeling results found throughout the literature.<sup>189-192</sup> At the exact center of the ring (i.e., in-plane and  $z = 0$  mm) the field components are zero  $V/\text{\AA}$ , but increase as axial distance becomes larger before peaking around 1 mm. However, the (superimposed) total field has a Gaussian distribution with a maximum ( $\sim 0.01$   $V/\text{\AA}$  for 5 V) at  $z = 0$  mm that tapers off around 1 mm.

Figures 5-7 and 5-8 show the numerical solutions to Equations 5-4 and 5-5 for the (off-axis) axial and radial electric-field strengths. In order to obtain similar axial values as in the analytical case, the numerical solutions were modeled using a ring radius ( $R$ ) located between the inner and outer radii of the annulus (i.e.,  $R = 1.25$  mm). The electric field is linearly proportional to the applied bias, which results in peak field strengths of approximately  $\pm 0.002$ ,  $0.01$ , and  $0.02$   $V/\text{\AA}$  for 1, 5, and 8 V field-biases as shown in Figure 5-7A ( $+Q/-Q$ ) and 5-7B ( $-Q/+Q$ ).

The radial field distributions in the vicinity of the sensing electrodes for the  $+Q/-Q$  and  $-Q/+Q$  cases are shown in Figures 5-8A and 5-8B, respectively. The field strength does not become appreciable in the region of the sensing electrode until the distance above field electrode capacitor (i.e., the center of the YSZ) exceeds  $\sim 10 - 100$  microns. Therefore, the field does likely penetrate the sensing electrodes and beyond in the surrounding space.

### 5.4.2 Field-Enhanced Sensor

The results for the electric-field enhanced gas sensor are shown in Figures 5-9 through 5-13. The testing configuration and conditions will be described and then discussed in terms of the effect of field shape, field strength, and field polarity. Finally, the implications of these results on future sensor design will be discussed.

Figure 5-9 shows the NO<sub>x</sub> sensor results for field-bias scheme 1 with positive polarity for several temperatures, showing the effect on sensitivity. In this scheme, the results are compared for the sensor having no externally-generated electric field (solid) with field created using +1 V bias (dashed) from top Al<sub>2</sub>O<sub>3</sub>/Au/Al<sub>2</sub>O<sub>3</sub> rings to bottom rings. The ambient temperatures were varied between 600 and 450 °C.

Figure 5-10 shows NO<sub>x</sub> sensor results for field-bias scheme 1 with negative polarity, showing the effect of field-bias magnitude on sensitivity at 500 °C. In this scheme, the results are compared for the sensor with an electric field created using a 0, -1, -5, and -8 V bias from top Al<sub>2</sub>O<sub>3</sub>/Au/Al<sub>2</sub>O<sub>3</sub> rings to bottom rings.

Figure 5-11 shows the NO<sub>x</sub> sensor results for field-bias scheme 2 with positive/negative polarities and multiple field-bias magnitudes, showing enhanced selectivity, at 500 °C. In this scheme, the results are compared for the sensor with an electric field created using a 5, 1.5, 0, -0.2, and -0.5 V bias between the top and bottom field-electrodes around the LCO sensing element, and the opposite polarities biased between those around the Pt electrode.

The NO<sub>x</sub> sensor results for field-bias scheme 3 with negative polarities and multiple field-bias magnitudes is shown in Figure 5-12 with trends in sensitivity at 500 °C. In this scheme, the field electrodes around the LCO sensing element were biased, while those around the Pt sensing electrode were left floating (i.e., unbiased).

Figure 5-13 shows the NO<sub>x</sub> sensor results for field-bias scheme 4 with positive/negative polarities and multiple field-bias magnitudes, showing trends in sensitivity at 450 °C. In this scheme, a positive (or negative) bias was applied to the electric field electrodes surrounding the Pt sensing electrode, with a negative (or positive) bias applied to the corresponding electric field electrode on the opposite side of the substrate; the field electrodes around the LCO sensing electrode were left floating (i.e., unbiased). The trends for effect of the electric-field shape, magnitude, and polarity are summarized in Table 5-2.

#### **5.4.2.1 Influence of electric-field shapes**

During active shaping, the electric field distribution may be effectively made into to any desired (contour) profile with respect to specific locations on the device (e.g., local reaction zones) or to the entire device/support. The electric fields may also penetrate any point within the device. Furthermore, the field strengths at various points in the device/support may differ. The field shapes are illustrated in Figure 5-4 for the four field schemes. When the field is symmetric with respect to top and bottom of the sensor (e.g., as in bias scheme 1), there were negative shifts in the absolute sensitivity when a positive field-bias was used, and positive shifts for negative field-biases for both NO and NO<sub>2</sub> gas exposure (Figures 5-9 and 5-10). The extent of the changes depended on field magnitude, field polarity, and the nature of the gas.

In bias scheme 2, the field around the LCO and Pt electrodes were oriented opposite from one another as illustrated in Figure 5-4B. In this case, a positive (negative) shift in absolute sensitivity occurred during NO gas exposure for a positive (negative) field bias as seen in Figure 5-11. On the other hand, during NO<sub>2</sub> gas exposure a positive field bias resulted in a negative shift in absolute sensitivity. While a -0.5 V field bias resulted in a positive shift in the sensitivity, there was a discrepancy at -0.25 V field bias for NO<sub>2</sub>. This may have been a result of the relatively small field not being unable to completely reverse the polarization that occurred as

a result of testing positive field biases first. Trends with regard to the effect of field-shape were less apparent in bias schemes 3 and 4.

#### **5.4.2.2 Influence of electric-field magnitude**

The effect of the field magnitude depended on the particular bias scheme, and thus the electric field shape, being used. In some instances the sensitivity did not change at all, while in other cases the sensitivity increased dramatically. Other times the selectivity was enhanced. For example, in bias scheme 1 increasing the magnitude of the field-bias when the polarity was positive decreased the sensitivity (Figure 5-9). Whereas, in bias scheme 3, the sensor became NO<sub>2</sub> selective when the field bias of -0.5 V was used (Figure 5-12). Interestingly, the signal was very similar for field biases of -0.5 V and +5 V during NO<sub>2</sub> (but not NO) gas exposure. Similarly, the +5 V and +1.5 V field biases resulted in almost identical signals during NO (but not NO<sub>2</sub>) gas exposure. This may be a result of changes in the field distribution over the entire sensor as field-bias magnitude changes.

#### **5.4.2.3 Influence of electric-field polarity**

The effect of the field polarity depended on the particular bias scheme, and thus the electric field shape, used. In some instances the sensitivity did not change at all, while in other cases the sensitivity increased dramatically. Selectivity also changed with electric-field polarity in certain cases.

In bias scheme 1, a negative field polarity resulted in extremely large changes in sensor response (Figure 5-10). For example, at 500 °C NO sensitivity increased approximately 20 times that of the unbiased case, while that of NO<sub>2</sub> increased around 10 times. On the other hand, positive field-polarities had almost no effect during exposure to NO from 450–650 °C, while there were relatively large effects (e.g., an increase of ~1.75 in sensitivity at 450 and 500 °C) during NO<sub>2</sub> exposure. This highlights the importance of field polarity and may have something

to do with the changes in the charge distribution of the adsorbate-surface bond, as is discussed elsewhere.<sup>176</sup>

### 5.4.3 Air-Reference Results

The results for the air-reference sensor are shown in Figures 5-14 and 5-15. The sensor signals were very low at 550 °C and 500 °C, which resulted in little or no change in sensitivity with applied field (not shown), except for the -8 V setpoint with NO at 500 °C. However, as seen in Figure 5-14, at all temperatures, alteration of the field bias produced changes in the gas composition coming off the LCO sensing electrode as detected with mass spectrometry. These plots were made using the measured NO<sub>x</sub> compositions from the 650 ppm NO or NO<sub>2</sub> feed composition of the respective gas steps. These plots are in terms of electric-field bias voltage because of the difficulty in ensuring that modeled field-strengths accurately represent reality when applied to handmade samples. As evident from both plots in Figure 5-14, there were significant changes in NO<sub>x</sub> levels for both NO and NO<sub>2</sub> gas steps. Surprisingly, when compared to NO TPR measurements on LCO powder we see that the high surface-area LCO electrode in this device resulted in some conversion of NO to NO<sub>2</sub>.<sup>98</sup> This might be explained as a result of the gas species having a longer resident time to react as they are trapped in the pores of the solid LCO electrode. Furthermore, in the case of the NO<sub>2</sub> gas steps, a shoulder/peak evolves in the measured NO<sub>2</sub> curves (around -5 V field bias) as temperature increases.

A focused-ion beam/scanning electron microscope system (FIB-SEM, FEI) was used to mill through the as-deposited Pt and LCO sensing electrodes, with a micrograph image taken for each slice. The slices were then reconstructed in three dimensions (Amira-ResolveRT version 4.0, VSG) in order to quantify microstructure (e.g., particle shape) and phase fractions (e.g., pore and compositional fractions) of the LCO nanomaterial. These techniques are only recently being used in gas sensors, but have been investigated in similar ceramic technology (e.g., solid oxide

fuel cells). This was done in an order to determine if there was any correlation between these characteristics and the difference in the TPDs and gas evolution seen during these experiments. The reconstruction concept is shown in Figure 5-16A where several SEM slices (60 nm between each) are stacked, with the space (i.e., particles and pores) between slices is interpolated. Figure 5-16B shows the reconstructed surface (19.9  $\mu\text{m}$  by 21.3  $\mu\text{m}$  by 11.28  $\mu\text{m}$ ) of the bulk porous LCO sample, with Figure 5-16C emphasizing the pores in black. For comparison, Figures 5-17 shows the microstructure of LCO powder such as that used in the original temperature programmed experiments. The loose powder consists of mesopores ( $\sim 30\text{-}50$  nm) and macropores ( $\sim 50$  nm – 2  $\mu\text{m}$ ). This representative powder agglomerate has an overall diameter of  $\sim 15$  – 25  $\mu\text{m}$ .

Relative fractional area was derived from the reconstruction as approximately 51% for the LCO and 49% for the pores throughout the bulk of the sample. The volume normalized surface area of the bulk porous LCO electrode was  $2.089 \mu\text{m}^{-1}$ . Relating this value to the measured mass and volume of the larger sample (188.9 mm by 3.34 mm by 0.94 mm) from which the slices were made a simple estimate of the specific surface area of the bulk porous electrode is  $5.77 \text{ m}^2/\text{g}$ . When compared to the specific surface area of the powder ( $\sim 7.5$  – 10  $\text{m}^2/\text{g}$ ), it is clear that the values are close. The derived average particle and pore size was 1.52  $\mu\text{m}$  and 1.35  $\mu\text{m}$ , respectively, using the BET derivation from the surface area (i.e., assuming spherical particles). However, as the LCO particles consist of elongated platelets (with unit particles typically ranging from 200 nm to 750 nm) this value is more representative of the (connected) consolidated structures.

Mass spectrometer measured effluent for powder and screen printed LCO electrodes have not detected any appreciable NO conversion to  $\text{NO}_2$ . One reason may be that the bulk porous

LCO electrode had a much larger surface area than the screen-printed sample. In comparison to the powder, the increased pore size is the main difference and may have contributed to the detectable NO conversion to NO<sub>2</sub>.

At 450 °C, there were significant changes for both NO and NO<sub>2</sub> sensitivity as the electric field was created on the device. The sensitivity (mV/decade ppm NO<sub>x</sub>) to gas steps and concentrations measured during the 650 ppm NO or NO<sub>2</sub> feed composition can be seen in Figure 5-15. In the case of NO gas steps, from region I to II a decreasing (+) field bias resulted in concurrent increases of NO and NO<sub>2</sub> concentrations without much change in sensitivity. In region II, a transition from (+) to (-) field bias occurred with the result of a sharp decrease in measured NO and a more gradual decrease in NO<sub>2</sub>. This difference in the change of species concentrations appears to have caused the sensitivity to decrease in going from region II to III. With a further decrease in the now (-) field bias there resulted a continuing decrease in NO<sub>2</sub> levels with essentially no change in NO. This was accompanied with a dramatic increase in the NO sensitivity of the device. Finally in transition from region III to IV, there was a relatively large decrease in sensitivity as the NO and NO<sub>2</sub> concentrations dropped in response to a more (-) field bias.

Now considering the four regions of inflection in Figure 5-15 for NO<sub>2</sub> gas steps at 450 °C, there appear to have been more complicated changes to the sensing mechanism. In going from region I to II, there was a sharp increase in the NO<sub>2</sub> concentration accompanied with a slower decrease in NO. This resulted in a sharp shift in the NO<sub>2</sub> sensitivity to smaller, more positive values. In the middle of region II, there was a crossover of the NO and NO<sub>2</sub> concentrations with a concomitant dip in NO<sub>2</sub> sensitivity. After a small increase at the more (-) end of region II, there was a sharp decrease in NO<sub>2</sub> sensitivity as region III begins. Also during this transition

was a second crossover of the NO and NO<sub>2</sub> concentrations as the amount of NO<sub>2</sub> decreased sharply and NO more slowly increased. As region III nears region IV, the measured NO concentration began to inflect and decreased while the NO<sub>2</sub> continued to decrease. As a result, the NO<sub>2</sub> sensitivity increased slightly in region IV.

#### **5.4.4 “Capacitor-Chip” Results**

The effect of the electric field on the desorption profile of LCO was measured in a small dead-volume reactor tube. The desorption series performed on this LCO capacitor-type sample was 1% NO/1% O<sub>2</sub> for various electric-field bias conditions. The desorption profile under 0 V field bias shows an NO spectra similar to the powder samples in previous results, but at lower temperatures as shown in Figure 5-18.<sup>98</sup> The sample exhibits easy desorption of NO from the surface, with 3 peaks in the region below 400 °C. In other work, these peaks have been attributed to covalent/ionic NO, NO nitrites, and NO nitrates.<sup>98,145,146</sup> The NO spectrum slowly tapers downward above these temperatures, as the pores began to exhaust NO<sub>x</sub> species from the pellet interior. As the electric-field voltage setpoint increased, the desorption peaks for NO shifted to higher temperatures, while maintaining similar initial peak shapes, albeit different intensities. The peak temperatures in the solid sample were slightly higher than in the powder sample. In addition to the upward temperature shift of the peaks, the lingering desorption of NO at high temperatures was expressed as more defined peaks. These peaks sharply reduce to zero concentration as the system approaches 600 °C. This shift was accompanied by the appearance of substantial NO<sub>2</sub> desorption peaks at the same temperatures as NO desorption, also shown in Figure 5-18.

The area underneath the peaks increased for NO and decreased for NO<sub>2</sub> when the field bias was changed to 2 V from 0 V. The next bias application of 5 V resulted in a minor increase in peak temperatures with concurrent minor decrease in the intensity of the low temperature NO

peak at ~300 °C, a doubling of the peak sizes for NO<sub>2</sub> desorption and a decrease in the high-temperature NO peak roughly equivalent to the increase in NO<sub>2</sub> emission. The 8 V field bias did not change NO peak placement, but the high temperature NO peak returned to a larger area, and the NO<sub>2</sub> desorption peaks returned to the 2 V level, albeit with slightly higher peak temperatures. Total amount of NO<sub>x</sub> adsorbed during NO TPD experiments, as calculated from the area under the TPD curves, can be seen in Table 5-3.

Identical experiments using 1% NO<sub>2</sub>/1% O<sub>2</sub> were subsequently performed on the sample, with desorption spectra shown in Figure 5-19. Again, the spectra obtained from 0 V approximated the results from powder samples, though the amount of NO desorbed at the higher temperature peak was larger compared to the NO<sub>2</sub> desorption peak for the solid sample experiment.<sup>98</sup> Increase in field voltage from 0 V to 2 V caused a 300 ppm drop in NO<sub>2</sub> peak desorption at 325 °C, but the peak at 425 °C was roughly equivalent to the 0 V desorption. NO concentration at the low temperature peak was slightly reduced from the 0 V sample, but again remained roughly constant over the higher temperature region. Stepping the voltage to 5 V resulted in an increase of NO and NO<sub>2</sub> at the low temperature peak, and a decrease for both gases at the high temperature peak against the 2 V case. The 5 V case produced the least amount of NO desorption of all the NO<sub>2</sub> adsorption experiments. At 8 V, the NO<sub>2</sub> signal dropped below the concentration at 2 V for the lower peak, and the 5 V level for the high peak. Overall, this bias generated the lowest level of NO<sub>2</sub> emission. NO emission at the low temperature peak was slightly above the 2 V case, and slightly above the 5 V case at the high temperature peak. Table 5-4 show the total amount of NO<sub>x</sub> adsorbed during NO<sub>2</sub> TPD experiments. Figure 5-20 summarizes the results from Tables 5-3 and 5-4.

From the planar gas sensor results, a clear difference was seen in the effect of field directionality on sensitivity and for different (reducing or oxidizing) gases. As mentioned earlier, the effects of the field scheme discussed in this paper were one of many studied. With other field “shape” schemes, the results differed. This included those in which a field existed around only one of the sensing electrodes (Pt or LCO). In the air-reference experiments, several regions of inflection in the sensitivity and mass spectrometer measurements were observed. Regions III and IV occurred at approximately the same electric-field biases in both the cases for NO and NO<sub>2</sub> gas steps. However, region II was much larger than region I for the NO<sub>2</sub> gas steps, while the opposite was true for the NO gas steps. These results indicate that the changes in sensitivity are related to the changes in gas composition.

#### **5.4.5 Discussion**

Based on previous results from XPS, DRIFTS, and temperature programmed techniques using normal and labeled oxygen we can make a few comments as to what might cause the electric-field effect with the gas sensor. From this past work, the primary mechanism for NO and NO<sub>2</sub> sensitivity has been concluded to occur as a result of surface complex formation, which either injects electrons or holes into the p-type LCO thereby changing the Fermi level and thus potential of the semiconductor.<sup>145,146</sup> Furthermore, the change in chemisorptive properties due to the presence of an electric field was first described as the “electroadsorptive” effect by Wolkenstein in 1955.<sup>161</sup>

Under the effect of an external electric field an adsorbate may undergo long-range influences such as changes in the bond angle or bond length. The bond angle and bond length depend, in part, on the geometry of the site and the charge distribution of the surface and adsorbate. In dipolar adsorbates (e.g., NO), the levels of the oxygen atom are raised with respect to the nitrogen near surface because of the net positive dipole. An external electric field can

electrostatically influence this adsorbate dipole and the extent of interaction depends on the field direction (total energy increases if dipole moment is opposite field direction). The field can result in extending the bond length or bending of molecular axis away from surface normal to move oxygen atom into regions with smaller field energy. A less mentioned effect is the possibility that the external electric field may also cause polarization of the adsorbate, surface or bulk solid.

Some of the possible reasons for this effect with LCO are the electrostatic interaction of surface complexes and orientation of the  $\text{NO}_x$  molecules for adsorption. Complexes remaining on the electrode surface at moderate to high temperatures in the non-modified case all possessed negative charge, and while the adsorbate layer was not entirely independent of the surface, a preferential orientation of electrons towards the surface of a complex would, by simple repulsion, tend to force the charged complex further from the surface, and make it more likely to desorb intact. There is also the possibility of polarization of the LCO, which is paramagnetic at these temperatures, due to the electric fields.<sup>193-195</sup> As a result, during the desorption step, the orientation of electron orbitals interacting with the charged surface complexes may allow the release of an oxygen from certain zones of the surface to nitrite complexes during decomposition. The modification of bonding in these zones due to the orientation changes might allow for the separation of an  $\text{NO}_2$  molecule during the nitrate/nitrite transition, which in the non-modified case decomposes without oxygen release.<sup>98,145,146</sup> These processes may be a result of changes to the Fermi level of the semiconducting oxide. This is due to the fact that in terms of chemisorption, the position of the Fermi level, amongst other things, determines the adsorptivity of acceptor and donor molecules, the surface charge, and the relative fraction of surface complexes formed.<sup>161</sup> Also, the possibility of gas-phase orientation of  $\text{NO}_x$  may play a role, as

the adsorption bonding direction can play a role in the statistical complex formation due to the different formation mechanisms. As polar molecules, both NO and NO<sub>2</sub> would show some degree of rotational shift in the electric field generated from the field-electrodes. There are likely many other possible explanations for the observed electric-field effects involving the LCO, as discussed in the background. However, at this time there is not enough experimental evidence to say which are actually occurring.

There was an electric-field effect on the sensing response even when only the Pt electrode of the LCO/YSZ/Pt planar sample was involved. The literature has both experimental and modeling results for the effect of large electric fields ( $\sim 0.1 - 1 \text{ V/\AA}$  or larger) on NO adsorption on Pt.<sup>190,196</sup> The evidence suggests that the fields influence the electronic structure of the adsorbates and can affect the bond angle and hence bond strength. As the modeled field strengths in this work approach these field strengths, there is a chance that the same effect is occurring.

Furthermore, from NEMCA research there exists the possibility that a migration and (reverse) spillover of oxygen ions from the YSZ onto the electrode can alter the reactions. Under NEMCA conditions, when a bias is directly applied to metal electrodes on YSZ, the resulting current and electric-field causes an electrochemical supply of oxygen ions to migrate across the cell and onto the catalyst electrode. The spreading of the oxygen ions onto the catalyst surface is accompanied with the formation of an effective electrochemical (dipole) double-layer, and associated (strong) electric field, that increases the electrode work function.<sup>68,77,78,81,82,180,181,196,197</sup> The dipole layer is believed to enhance reactions due to a beneficial weakening of the binding energies of (gas-phase induced) chemisorbed oxygen. This causes catalytic reactions to proceed at higher rates because weakened bonds allow these oxygen surface species to more easily

oxidize other adsorbed species. Therefore, in terms of the observed field effect involving only the Pt electrode, the lack of any appreciable current applied to the device suggests that the field-induced migration and (reverse) spillover of oxygen ions might still occur but would be limited to the original  $O^{2-}$  concentration in the YSZ. Since these oxygen ions are less reactive than adsorbed oxygen and primarily act as the source of a large local-field, the spillover-ions are not likely to be consumed. The dipole layer would therefore be present until the bias applied to the field-electrodes is removed. Clearly, further investigation is needed to verify which, if any, of these explanations correctly describes the electric-field effects for the entire LCO/YSZ/Pt device.

## 5.5 Conclusions

This work has shown that an externally-generated electric field at the surface of an electrochemical cell (without the passage of ionic or electronic current) can dramatically influence the sensitivity of a gas sensor. Furthermore, using three types of samples (planar gas sensor, air-reference sample, and capacitor-type chip) we have shown that there are changes in catalytic conversion, shifts in adsorption energies, and modifications to the sensor signals. The effect of field shape, field magnitude, and field polarity have been explored using several different electric-field bias schemes. In the case of the air-reference sample, there seems to have been correlation between the gas concentration measurements and the sensitivity of the device as the field bias was changed.

The electric field distribution and strength has been modeled using both analytical and numerical models. The results indicate that the field strength about the field-electrodes is large enough to affect the adsorbate bonding and the Fermi level of the semiconducting LCO. For the tested configurations (i.e., +/– and –/+), superposition of the top and bottom rings of the field-electrode resulted in a decrease in the overall field strength. While not tested with an actual sensor, the models predict an increase in field strength for the same field biases using a different

configuration (i.e., +/+ or -/-) as shown in Figure 5-21. Many more field configurations are likely possible by increasing the geometry, spacing, and number of field-electrodes.

Future work will try to broaden the understanding of this electric-field effect with a surface science investigation using a Kelvin probe system capable of UHV and atmospheric measurements, which is inline with an electron spectroscopic system. Any changes in chemical and electronic (valence) structure should be detectable. Eventually, using simultaneous conductivity measurements, the Kelvin probe measurements will allow determination of changes in the WF (and therefore, the Fermi level of the surface) of the LCO as the electric field bias is applied. Furthermore, the use of a 3D direct-write system will permit a more-controlled geometry in the fabrication of the field electrodes.<sup>177</sup> This will allow us to make samples from the bottom up with field-electrodes that more closely match those modeled. Eventually the electric-field effect will be tested in other solid-state ionic devices, such as solid oxide fuel cells and gas separation membranes, to see if similar enhancements are possible.

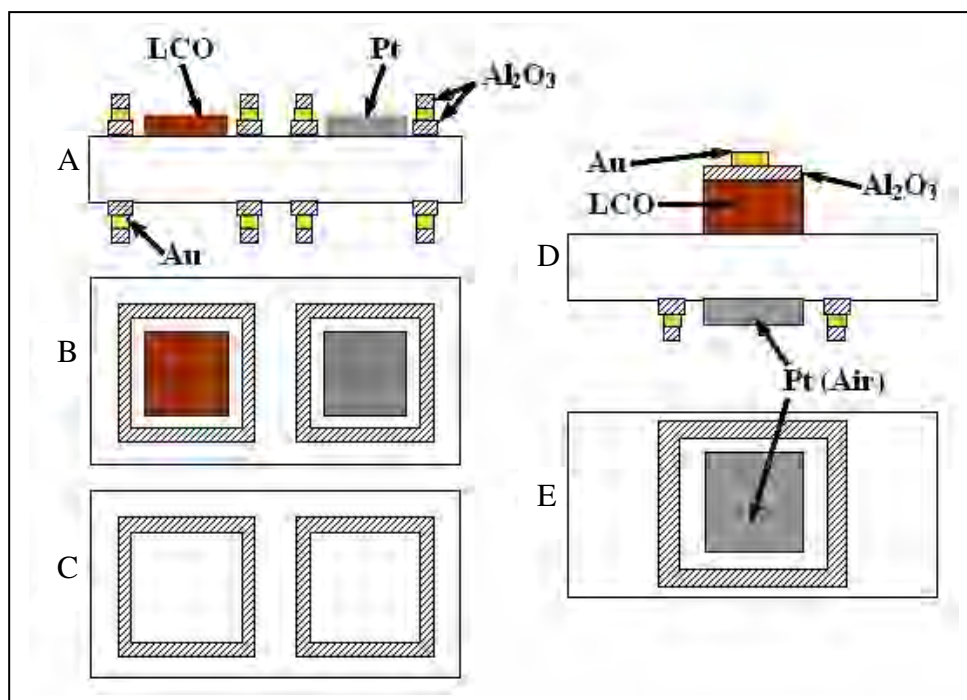


Figure 5-1. Planar sensor and air-reference configurations. A cross-section of planar sensor (A) shows dense  $\text{Al}_2\text{O}_3$  layers in contact with thin YSZ substrate. As seen in the top (B) and bottom (C) views, the LCO and Pt electrodes, which exist only the top surface, are in the middle of the  $\text{Al}_2\text{O}_3/\text{Au}/\text{Al}_2\text{O}_3$  electric-field rings. In (D) a cross-section of the air-reference sample shows a thick, high surface-area LCO electrode attached to the YSZ. Attached to the LCO is an  $\text{Al}_2\text{O}_3$  section with Au conductor on top.

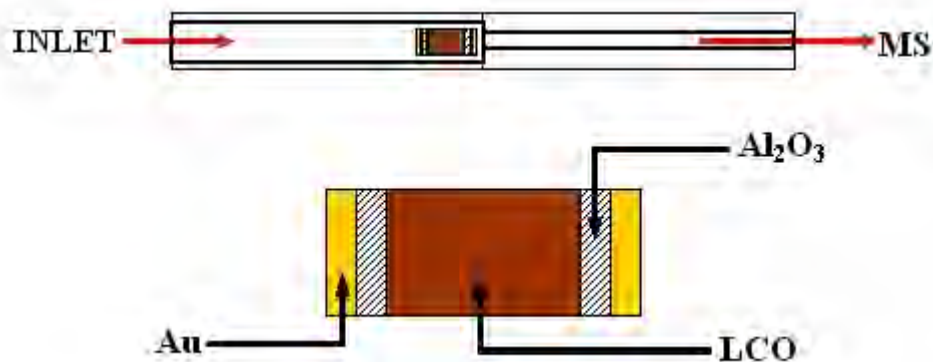


Figure 5-2. LCO capacitor-type chip used in TPD experiments. A high surface-area LCO rectangle was sandwiched between two  $\text{Al}_2\text{O}_3/\text{Au}$  field electrodes. Tests were conducted inside a low-dead volume quartz reactor, with effluent going to a mass spectrometer.

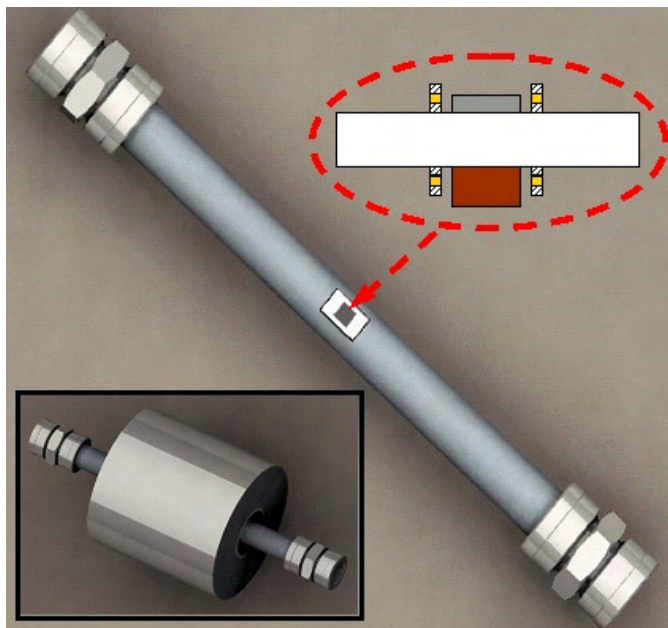


Figure 5-3. Test setup for air-reference with gas effluent measurements.

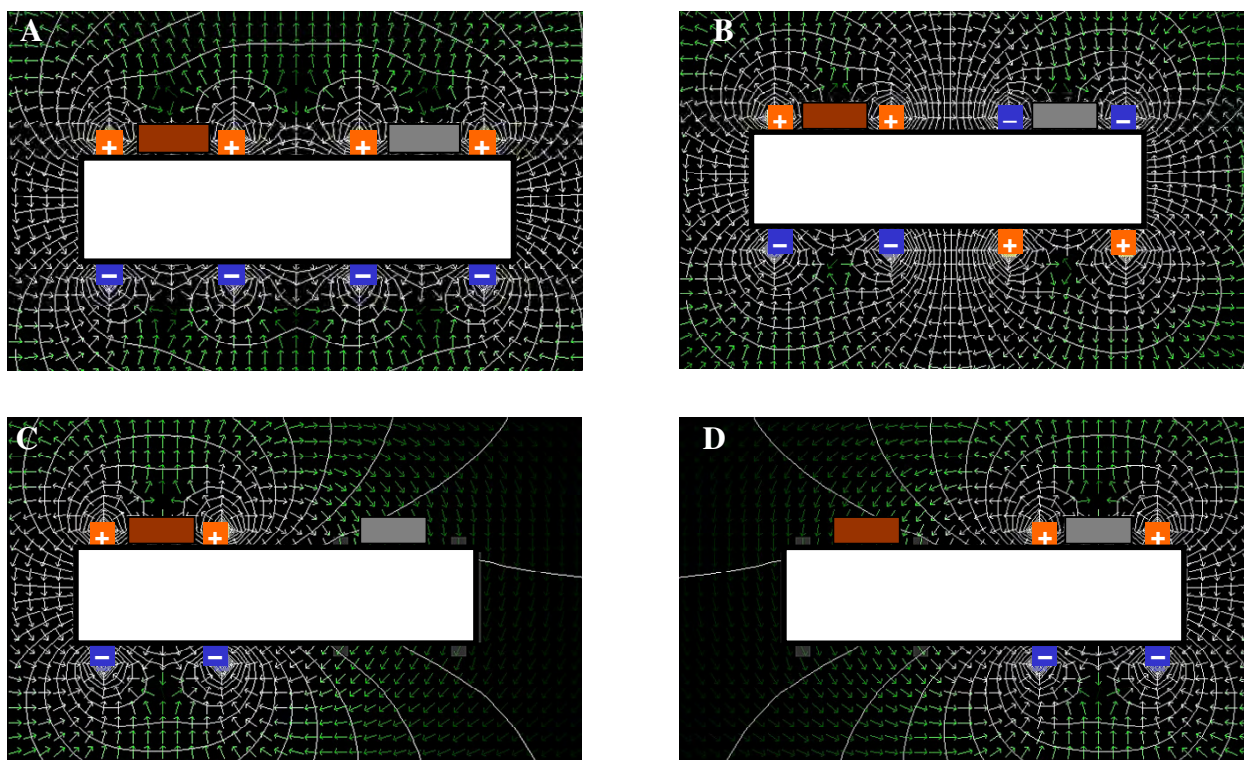


Figure 5-4. 2D contour and vector plots of electric-field shapes for bias schemes tested with the field-enhanced sensor. Bias schemes 1, 2, 3, and 4 are shown in A), B), C) and D).

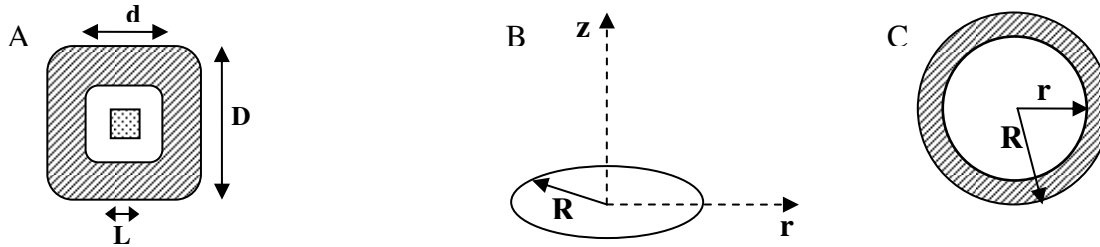


Figure 5-5. Geometry for numerical and analytical calculations of electric-field strength. A) represents the actual geometry of a field electrode, where  $d$  ( $2r$ ),  $D$  ( $2R$ ), and  $L$  had dimensions of 1.5, 3.5, and 1 mm. B) shows the arrangement for the numerical calculation of the off-axis electric field of a ring of charge, while C) represents the geometry used in the analytical electric-field solution for an annulus disk of charge.

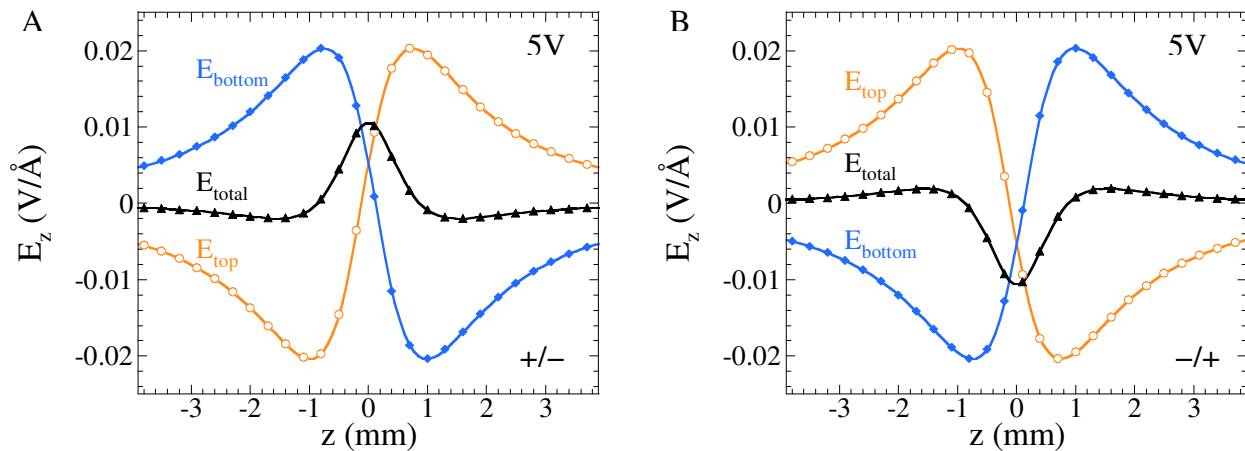


Figure 5-6. Analytical results for the electric field in the  $z$ -direction along the central axis of a charged annulus and effect of superposition. A) shows case for  $+Q$  on the top capacitor and  $-Q$  on the bottom, while B) is for  $-Q$  on top and  $+Q$  on the bottom.

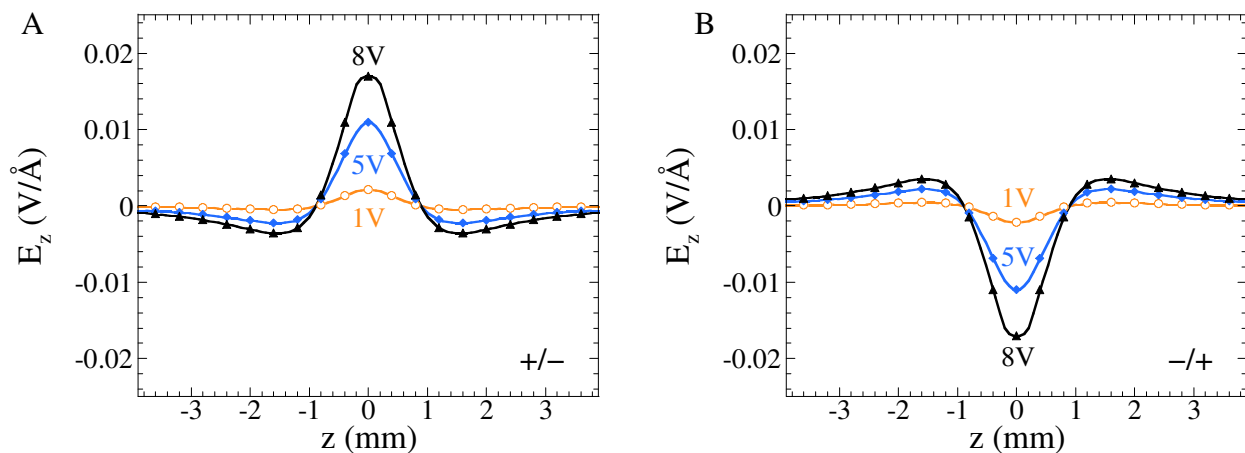


Figure 5-7. Results of numerical analysis for the off-axis electric field of a ring of charge as a function of distance ( $z$ ) from the plane of the ring along the central axis for field-biases of 1, 5, and 8 V. A) shows results for  $+Q/-Q$ , while B) is for  $-Q/+Q$ .

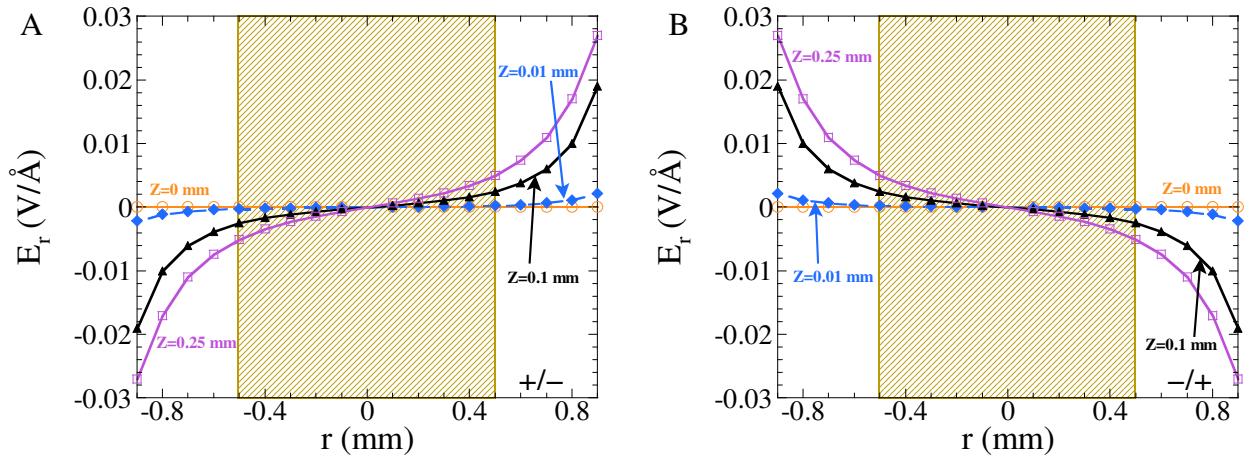


Figure 5-8. Results of numerical analysis for the off-axis electric field of a ring of charge as a function of distance ( $r$ ) from the center of the ring along the radial direction. A) shows case for  $+Q/-Q$  resulting from a 5 V applied bias (at  $z$  values of 0, 0.01, 0.1, and 0.25 mm), while B) is  $-Q/+Q$ . The relative location of either sensing electrode ( $L = 1$  mm) is shown as the shaded region.

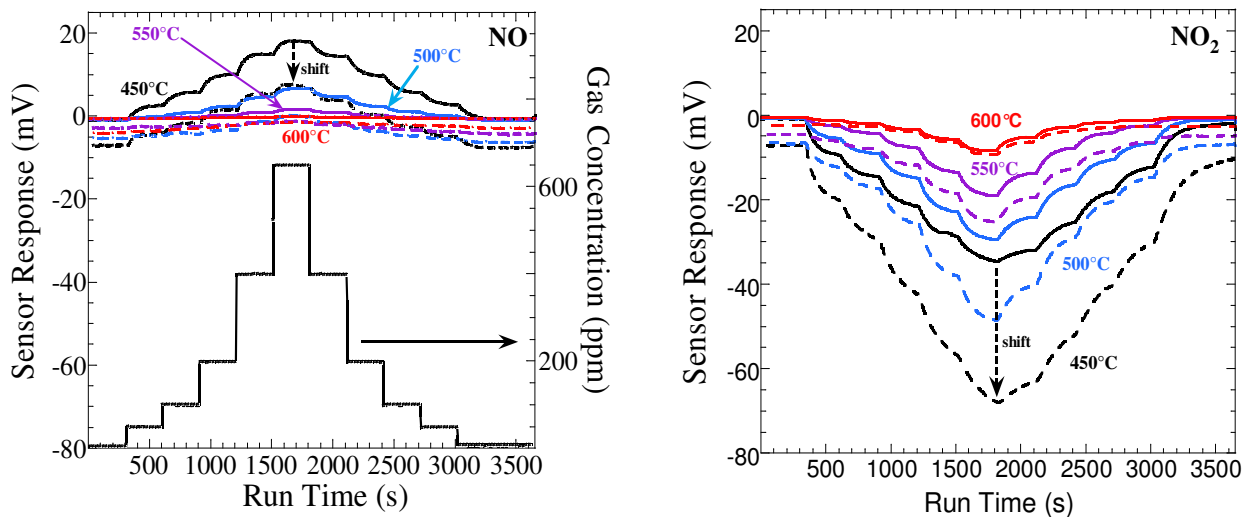


Figure 5-9.  $\text{NO}_x$  sensor results for field-bias scheme 1 with positive polarity for several temperatures, showing the effect on sensitivity. In this scheme, the results are compared for the sensor having no externally-generated electric field (solid) with field created using +1 V bias (dashed) from top  $\text{Al}_2\text{O}_3/\text{Au}/\text{Al}_2\text{O}_3$  rings to bottom rings. The ambient temperatures were varied between 600 and 450 °C.

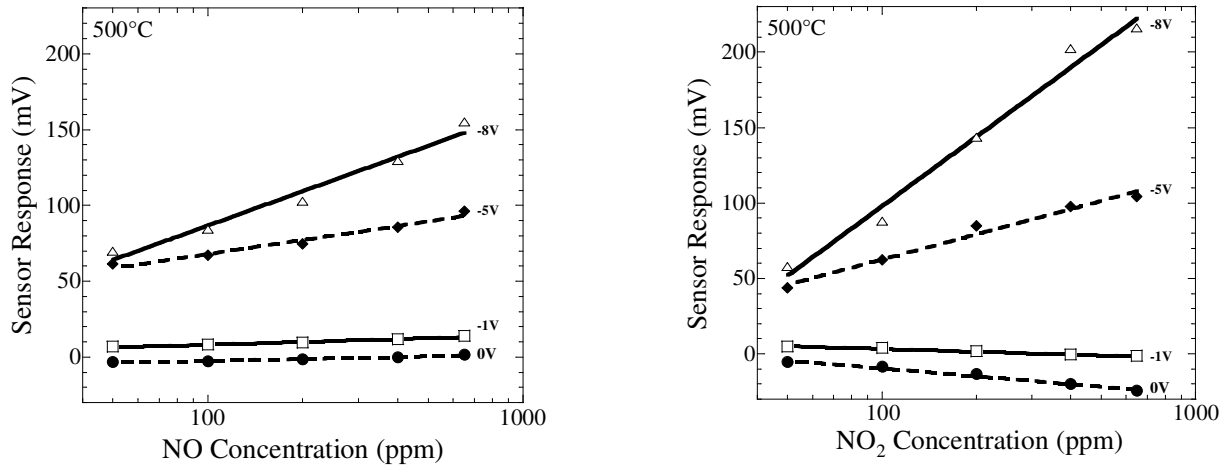


Figure 5-10.  $\text{NO}_x$  sensor results for field-bias scheme 1 with negative polarity, showing the effect of field-bias magnitude on sensitivity at 500 °C. In this scheme, the results are compared for the sensor with an electric field created using a 0, -1, -5, and -8 V bias from top  $\text{Al}_2\text{O}_3/\text{Au}/\text{Al}_2\text{O}_3$  rings to bottom rings.

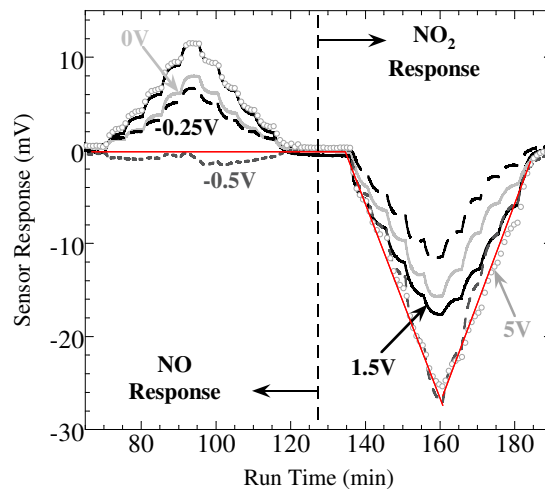


Figure 5-11.  $\text{NO}_x$  sensor results for field-bias scheme 2 with positive/negative polarities and multiple field-bias magnitudes, showing enhanced selectivity, at 500 °C. In this scheme, the results are compared for the sensor with an electric field created using a 5, 1.5, 0, -0.2, and -0.5 V bias between the top and bottom field-electrodes around the LCO sensing element, and the opposite polarities biased between those around the Pt electrode.

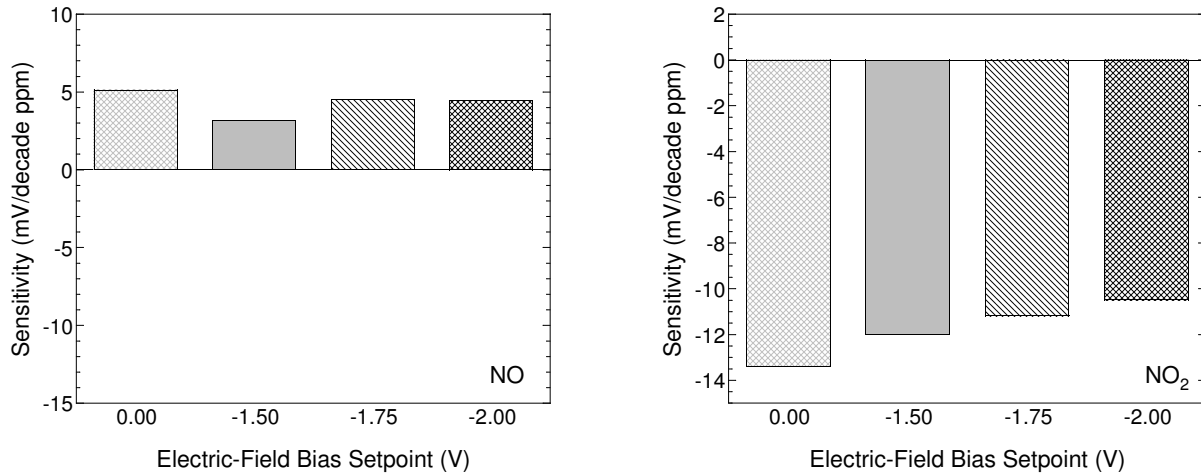


Figure 5-12.  $\text{NO}_x$  sensor results for field-bias scheme 3 with negative polarities and multiple field-bias magnitudes, showing trends in sensitivity at 500 °C. In this scheme, the field electrodes around the LCO sensing element were biased, while those around the Pt sensing electrode were left floating (i.e., unbiased).

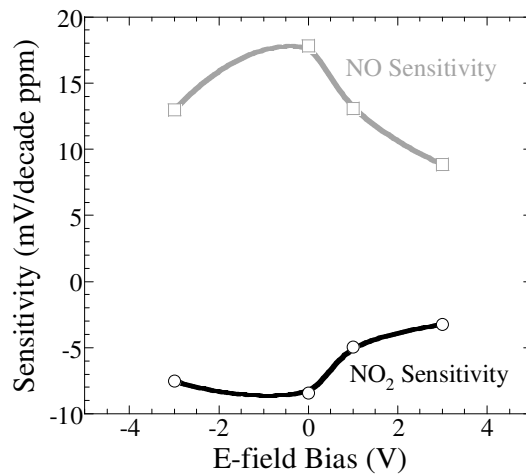


Figure 5-13.  $\text{NO}_x$  sensor results for field-bias scheme 4 with positive/negative polarities and multiple field-bias magnitudes, showing trends in sensitivity at 450 °C. In this scheme, a positive (or negative) bias was applied to the electric field electrodes surrounding the Pt sensing electrode, with a negative (or positive) bias applied to the corresponding electric field electrode on the opposite side of the substrate; the field electrodes around the LCO sensing electrode were left floating (i.e., unbiased).

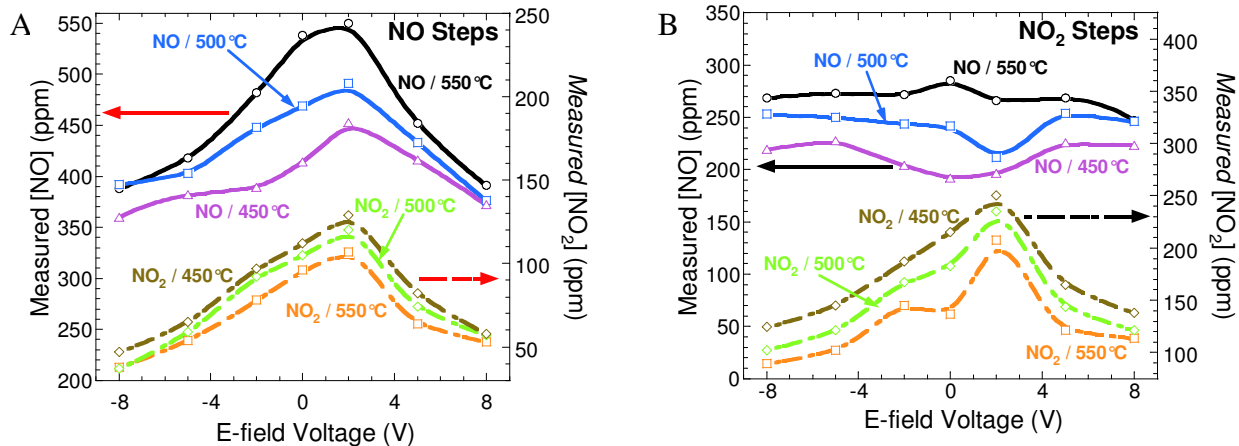


Figure 5-14. Mass spectrometer measured NO<sub>x</sub> concentrations versus applied electric-field voltage during 650 ppm NO feed and 650 ppm NO<sub>2</sub> feed using air-reference sample. NO feed conditions are shown in A), while NO<sub>2</sub> feed conditions are shown in B) Mass spectrometry results were measured simultaneously with sensor response.

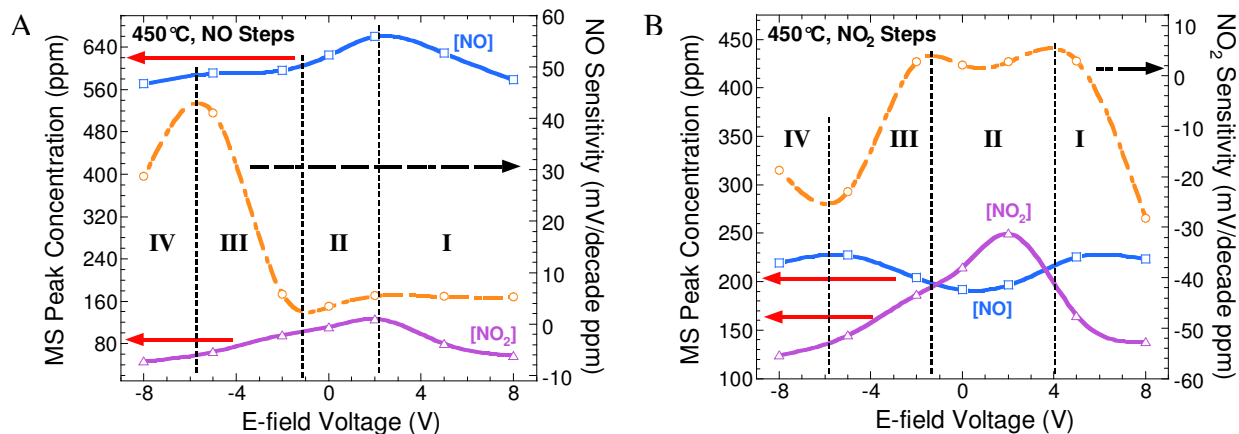


Figure 5-15. Mass spectrometer measured NO<sub>x</sub> concentrations and air-reference sample sensitivity versus applied electric-field voltage during 650 ppm NO feed and 650 ppm NO<sub>2</sub> feed. The changes in air-reference sample sensitivity were to gas steps of 0, 50, 100, 200, 400, and 650 ppm NO in A), or NO<sub>2</sub> in B) as the field-strength varied. Four regions of inflection are seen for both experiments.

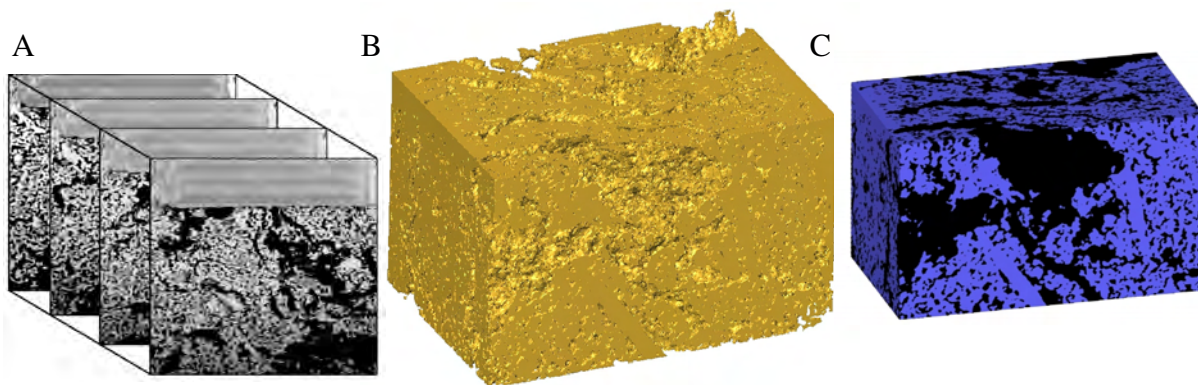


Figure 5-16 FIB-SEM reconstruction of bulk porous LCO used in air-reference sample. A) illustrates the reconstruction concept, while B) and C) show the resulting surface- and pore-emphasized 3D models.

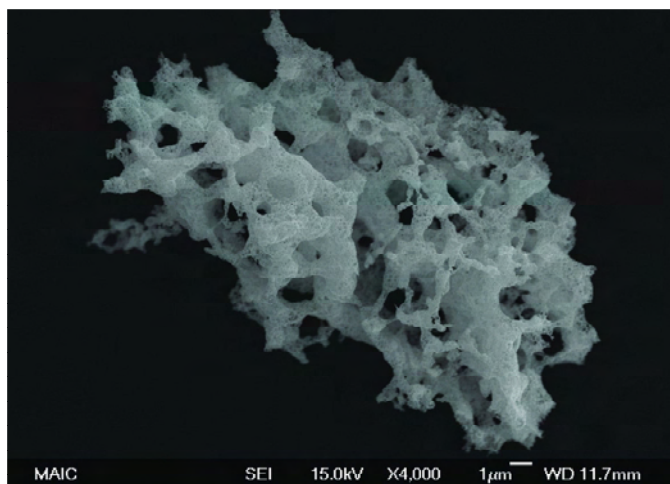


Figure 5-17. SEM image of LCO powder (scale-bar is 1  $\mu\text{m}$ ). Modified from Wachsmann.<sup>139</sup>

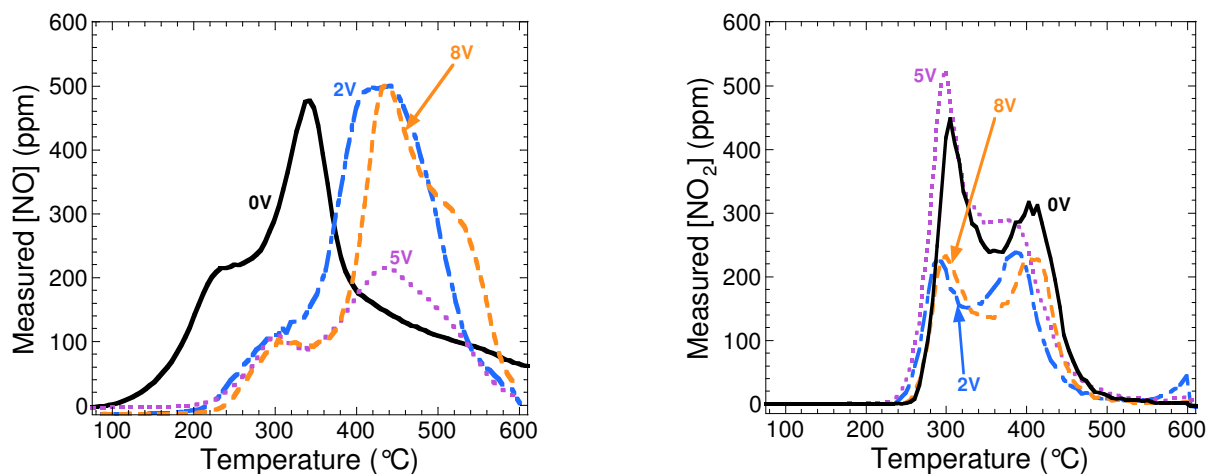


Figure 5-18. Measured NO and NO<sub>2</sub> desorption profiles for 1% NO/1% O<sub>2</sub> TPD at various electric-field biases across the capacitor-type chip.

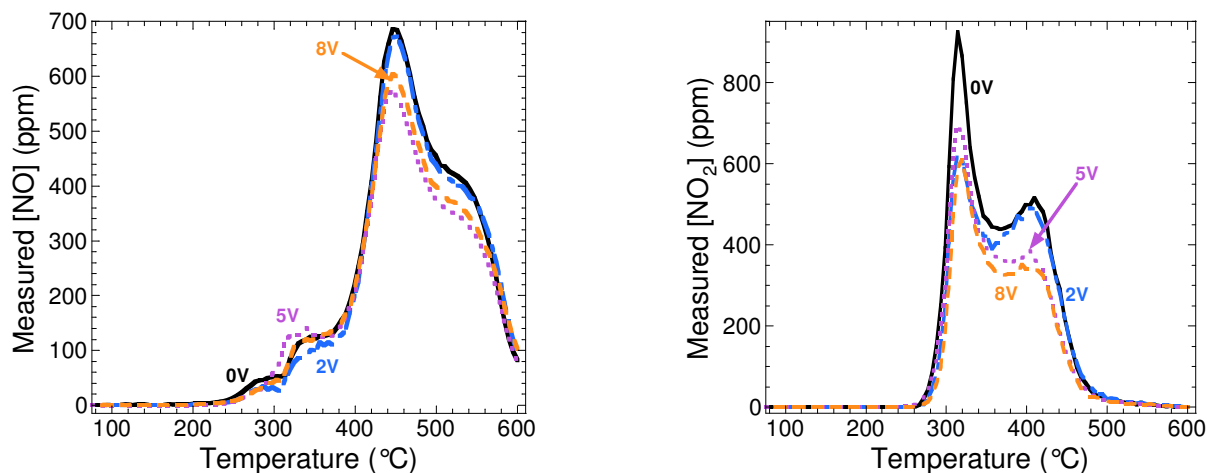


Figure 5-19. Measured NO and NO<sub>2</sub> desorption profiles for 1% NO<sub>2</sub>/1% O<sub>2</sub> TPD at various electric-field biases across the capacitor-type chip.

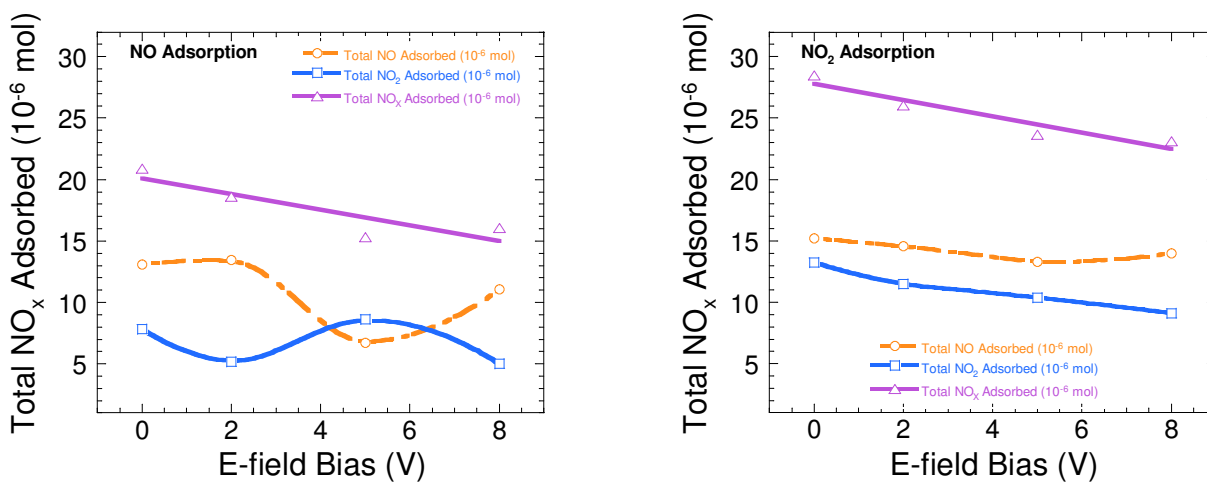


Figure 5-20. Adsorbate concentration versus E-field bias for NO and NO<sub>2</sub> adsorption.

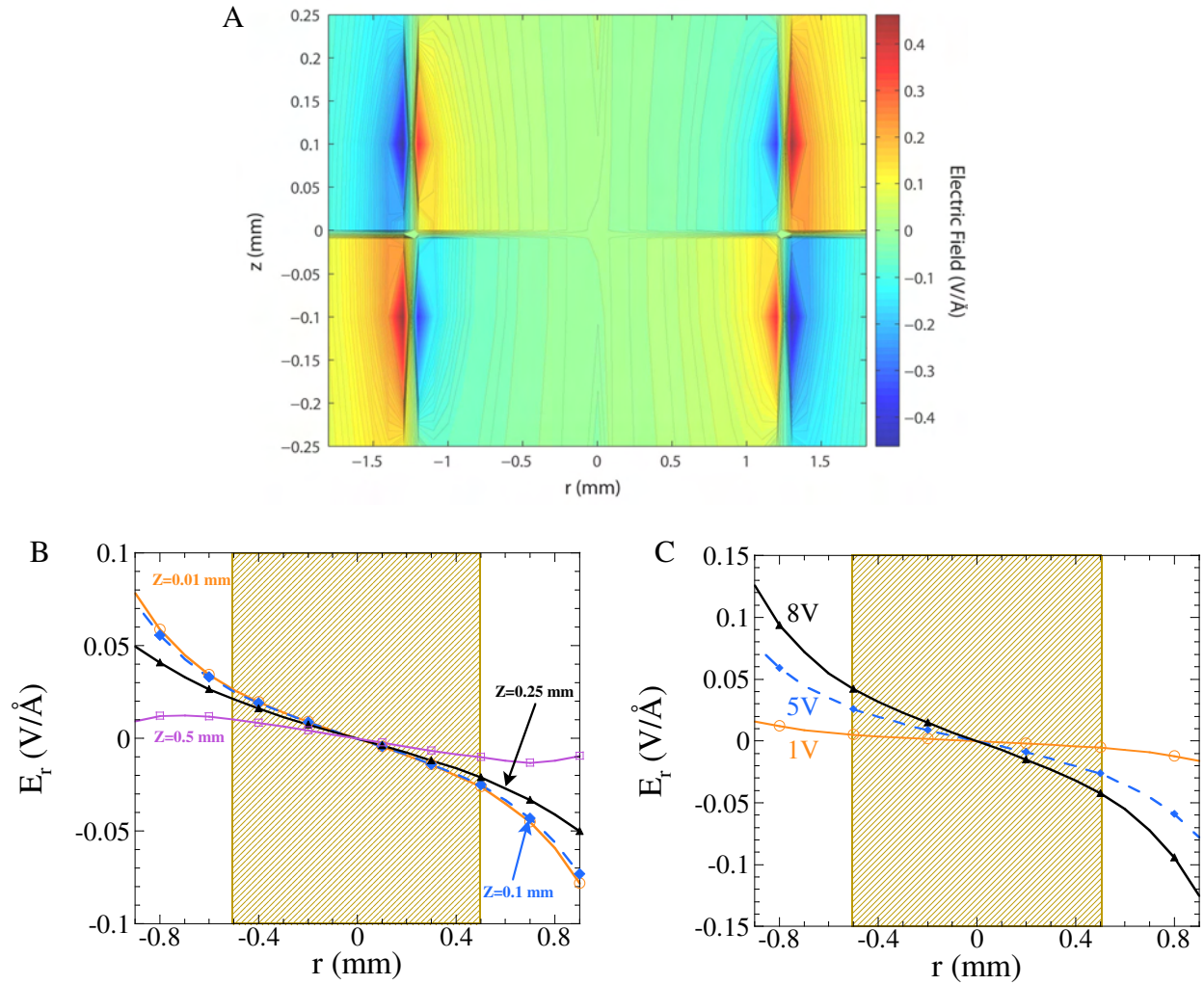


Figure 5-21. Modeled field-strength for field-electrodes with +Q on top and bottom. A) shows variations in electric-field strength (5 V) along a cross section of a field-electrode. The radial field component for this configuration can be seen in B) for several values of  $z$  and C) for several field-biases ( $z = 0$  mm).

Table 5-1. Field-bias schemes to investigate the effect of field shape, magnitude, and polarity

Bias Scheme #	Top Field-Electrode (LCO)	Top Field-Electrode (Pt)	Bottom Field-Electrode (LCO)	Bottom Field-Electrode (Pt)
1	+ (-) charge	+ (-) charge	- (+) charge	- (+) charge
2	+ (-) charge	- (+) charge	- (+) charge	+ (-) charge
3	+ (-) charge	floating	- (+) charge	floating
4	floating	+ (-) charge	floating	- (+) charge

Table 5-2. Summary of trends for field-bias schemes 1-4

Bias Scheme #	Field Bias	NO Gas Exposure	NO <sub>2</sub> Gas Exposure
1	+	Negative Shift (down)	Negative Shift (down)
	-	Positive Shift (up)	Positive Shift (up)
2	+	Positive Shift (up)	Negative Shift (down)
	-	Negative Shift (down)	Varies with field magnitude
3	+	N/A	N/A
	-	No Apparent Effect	Negative Shift (down)
4	+	Negative Shift (down)	Positive Shift (up)
	-	Negative Shift (down)	No Apparent Effect

## CHAPTER 6 DIRECT-WRITE RAPID PROTOTYPING

### 6.1 Introduction

In a perfect world, scientists and engineers would be able to visualize an idea, and then rapidly and easily convert the concept into reality. Often, this is not the case as a device or sample may require deposition of novel materials into complex patterns with small feature size. The material deposition may be for the investigation of device designs (e.g., fuel cells, gas sensors, or batteries) or the fundamental science of such devices. To complicate matters, many techniques (e.g., screenprinting or photolithography) are not compatible with certain materials or require individual masks/screens for each design or pattern. Also, the iterative design of devices can be time consuming and expensive with these processes. In addition, the most economical methods are not capable of fine-line features (i.e., mesoscale). Thus, there is great need for techniques to rapidly prototype samples and devices using virtually any material.

The realization of rapid-prototype designs using various materials for solid-state ionic devices and research can now be achieved with the use of a direct-write dispensing machine (e.g., 3Dn 450 HP/nScript, Inc). This rapid-prototype system can deposit ceramic, metallic, and polymeric materials in any pattern using predefined CAD files. The machine is capable of depositing materials ranging from low viscosity inks to high viscosity pastes/slurries (e.g., 1 to over 1,000,000 cP). Furthermore, the deposition is additive and material waste is minimized when compared to other techniques. As shown in Figure 6-1, multiple print heads allow simultaneous printing of different materials and the system can also be configured to produce compositional gradients between functional layers for good adhesion at interfaces. Using novel pump technology with picoliter volume control, the direct-write machine can deposit materials with feature sizes below 10 microns while larger area patterns can be rastered at speeds up to 500

mm/s. In addition, the system has the capabilities of x, y, and z motion with a resolution on the order of 0.1 microns and material can be deposited on flat surfaces or conformally over rough/3D surfaces. This is possible through surface mapping with a laser sensor. Using advanced software, the system can make true three dimensional (3D) or two dimensional (2D) features using layer-by-layer deposition. Therefore, the machine can be used to precisely vary the geometry of layers as device properties are investigated and improved.

In order to utilize the full capabilities of this direct-write technique, there is a need to develop materials with properties that are optimized for the desired deposition quality. The material parameters that can affect the deposition include particle size and shape, particle-size distribution, viscosity of paste/ink, and particle loading. As a tool for the development of solid-state ionic devices, fuel cell and gas sensor materials (electrodes and electrolytes) were developed for use with the rapid-prototype machine. Deposition of common metallization materials (e.g., Pt, Au, and Ag) was also accomplished.

This paper covers the various types of available rapid-prototype techniques and advantages of the nScript system for scientific and device research in the area of solid-state ionics. Results from automated combinatorial testing of the machine process parameters (e.g., stage speed and pump backing pressure) are covered next. Then the material properties making up the inks or pastes used during the combinatorial tests will be related to the machine process parameters and ultimately the deposition quality. The starting materials and final depositions were characterized using various techniques. After the initial material development phase, the system will be able to quickly and easily fabricate entire devices even when there are changes in design and material properties. Furthermore, the use of such rapid-prototype machines ensures that all experimental samples are accurately produced with repeatable depositions. Coupled with the capability to

specify a wide range of controlled material properties, this tool has the potential to be a pivotal instrument for advancing research and rapid design analysis.

## 6.2 Background

As mentioned previously, the goal of this work was to develop procedures and materials in order to eventually use this direct-write technique for rapid prototyping of solid-state ionic devices. The main devices of interest, fuel cells and gas sensors, have two primary components, namely electrolytes and electrodes. Solid oxide fuel cells (SOFCs) are needed as fuel-flexible power sources that will help during the transition from a society that uses combustion engines to a hydrogen economy. One current problem with SOFCs are the requirement of high operating temperature and resultant need for expensive materials. However, with the use of a direct-write technique new materials can be investigated and entire devices fabricated in an attempt to overcome this and other limitations. For the fuel cells a dense, leak free electrolyte is critical to the performance of the device.<sup>198</sup> Furthermore, the electrolyte should be thin to reduce Ohmic losses. In terms of an entire cell (anode/electrolyte/cathode), the device may be tubular or planar. While each approach has advantages, our research focuses on the design of planar cells. In particular one of the goals of this work is to use the direct-write machine to make micro fuel cell stacks. Though there are several issues (e.g., cracking during drying) that need to be considered, this fabrication can even be done from the bottom-up, thereby reducing leakage between cells and theoretically improving performance.

The second application being investigated involves the direct-write fabrication of potentiometric gas sensor arrays for gas analysis in combustion exhausts, industrial processes, and medical applications. Recently, new potentiometric gas sensor arrays have been designed in such a way that they have significantly improved selectivity and sensitivity.<sup>199-204</sup> Several layers may be used in the device construction including structural supports, solid-electrolytes, sensing

electrodes, and metallization (e.g., for heating elements, temperature sensors, etc.). The direct-write deposition technique will allow us to rapidly run through an iterative process of simulation and experimental verification of sensor design.

Conventional fabrication methods in solid-state ionics include tape casting, tape calendaring/pressing, extrusion, chemical and physical vapor deposition, spin-coating, dip-coating, spray pyrolysis, and many other related techniques.<sup>198,205,206</sup> As mentioned in the introduction, one of the main drawbacks in using these types of techniques is the amount of time, money, and effort needed to make devices and experimental samples. The use of direct-write methods to make gas sensors has been accomplished by others in the past, but mainly using ink-jetting techniques.<sup>207</sup> As far as we know, there are only a few SOFC devices that have been developed using direct-write technology.<sup>208</sup> Though they did not achieve high power densities, the capabilities of the method used in this work should allow us to achieve more impressive results.

There are various types of direct-write methods, with the generic term referring to the programmable transfer of a patterned material. This can involve subtractive or additive pattern transfer. The former relates to the removal of material (which may have been deposited in previous steps), while the latter refers to simply adding the patterned material on the surface of a substrate. Most subtractive methods of deposition, such as those used in microelectronics fabrication, are not direct-write technologies. Though advances in laser micromachining, e-beam lithography, focused ion beam (FIB) milling, and laser transfer of materials have allowed this area to reach into new applications of rapid prototyping.<sup>209,210</sup> For solid-state ionic devices, however, the additive approach is more applicable because of the wide range of materials (some of which are expensive) involved in their fabrication.

Several types of additive direct-write techniques exist, including aerosol spraying and ink-jetting.<sup>209,210</sup> As shown in Table 6-1, each method has its own benefits and range of capabilities, even when compared to more standard solid-state ionic device fabrication techniques such as screenprinting. Another type of direct-write method is syringe dispensing, which involves material deposition as a result of positive-pressure displacement of fluid controlled with a plunger. On the other hand, the nScript system utilizes a novel air pressure-backed pump with a sealed-valve that prevents, rather than causes, fluid flow. In other words, the material flows around an open valve into the ceramic tip because of the backing pressure and is quickly drawn back via the vacuum created when the sealed-valve retreats into the pump. This nScript micro-dispensing technology allows for superior start/stop dispensing and fine-line control. Compared to other direct-write techniques, this method offers the most flexibility, speed, and capability to create three-dimensional structures or to deposit films conformally over a surface. Key machine parameters are backing pressure, relative gantry and pump-valve speed, and path taken during deposition. Important material parameters are particle size and particle-size distribution, slurry viscosity, evaporation rate of slurry solvent, and the wetting properties of slurry and substrate.

### **6.3 Experimental**

In order to use the direct-write machine for fabrication of fuel cells and gas sensors, there was the need to develop materials with ideal properties from the standpoint of the deposition technique and the final quality of the structure being printed. Namely, the electrodes should show sufficient connectivity amongst the particles and open porosity for the gas to interact with the electrode and at the triple phase boundary (i.e., gas, electrode, and electrolyte interface); the electrolytes should be dense and uniform, with the ability to control thickness. Furthermore, the materials must possess sufficient rheological properties so as to ensure proper flow through the pump nozzle without resulting in any clogs.

### 6.3.1 Ceramic Powders

Powder samples of Gadolinia-doped Ceria (GDC, Rhodia) for the fuel cells and Yttria-stabilized Zirconia (8 mol% YSZ, Tosoh) for the gas sensors were obtained for the electrolyte materials. The electrode materials tested included  $\text{WO}_3$  (Alfa Aesar),  $\text{TiO}_2$  (Alfa Aesar), and  $\text{La}_2\text{CuO}_4$  (LCO) for the gas sensors, and  $(\text{La,Sr})(\text{Co,Fe})\text{O}_3$  (LSCF, Praxair) and  $\text{LaMnO}_3$  (LSM, Praxair) for the fuel cells. Most of the powders were purchased directly from the manufacturer and used as is or underwent further processing using ball-milling and/or filtering with a sieve. The LCO powder was prepared using the autoignition synthesis technique as explained elsewhere.<sup>147</sup> Particle size and particle-size distribution were measured via laser diffraction using a Coulter LS230. Ultrasonication of the powder in water ensured dispersion during the particle size measurements.

### 6.3.2 Electrodes

Initial attempts of making slurries for the nScript utilized a commercial binder vehicle (ESL) as a way of standardizing results. Metallization for the devices utilized commercial pastes of Pt (Heraeus), Au (Engelhard), and Ag (Dupont).

Electrode pastes were prepared by combining the vehicle, powder, and a dispersant in a container and initiating various de-airing and mixing cycles using a centrifugal mixer (Thinky, ARE-250). Pastes were then loaded into 3 mL syringes (EFD) for use with the nScript. This was repeated for various solids-loading (25 to 60 wt%, relative to vehicle). Prior to use with the direct-write system, a final mixing step was conducted in order to rid the pastes of any air trapped during transfer to the syringes.

### 6.3.3 Electrolytes

To achieve a more dense, sintered GDC layer, a slurry with relatively high solids-loading (~35 vol%) was prepared. This was achieved by mixing a water-based solution of sub-micron

GDC powder until nearly saturated, followed by the drop-wise addition of a polyelectrolyte (Darvan-C) to disperse the particles. The process was repeated until polyelectrolyte additions no longer had an effect on the flow properties of the slurry. De-ionized water was also added drop-wise until the slurry again exhibited a water-like viscosity. A small amount (1 wt%) of binder solution (36 wt% polyvinyl alcohol dissolved in water) and 2/3 wt% plasticizer (ethylene glycol) were added to the well-dispersed GDC slurry, and ball milled for 12 hours. To increase the viscosity of the slurry, a 2 M water-based dissolved cerium nitrate solution was added with a dropper and shaken until the slurry appeared creamy. For de-airing, the slurry was transferred to a 30 mL plastic syringe, capped off, and the plunger pulled back to create an internal vacuum. The syringe was knocked against a hard surface to pull air pockets out from the bulk of the slurry. This process was repeated until no evidence of air pockets could be observed. The paste was directly transferred to the 3 mL feed syringes used by the rapid prototyping equipment.

YSZ was made into slurries using two different methods. The first consisted of the same commercial binder and preparation method used with the electrode pastes. The second slurry involved ball milling of a mixture of YSZ powder, fish oil, dibutyl phthalate (DBP), polyvinyl butyral (PVB), toluene, ethanol, and polyethylene glycol (PEG 8000). This was essentially a slurry used in tape casting.

#### **6.3.4 Direct-Write Machine Preparation**

After loading a syringe into a pre-cleaned and calibrated nScript pump there were a few tasks that needed to be performed before deposition. The first step was to prime the pump by opening the valve slightly and increasing the backing pressure until the material began to flow. Good material-flow was characterized as continuous flow without air-bubbles and that did not creep up the sides of the tip. Then a pre-made CAD file with all of the machine/tool path information imbedded inside was opened in the computer. The final action needed before

deposition was to bring the tip within 25 to 200  $\mu\text{m}$  of the surface of a substrate. For the fuel cells, a tape cast NiO-GDC anode support acted as the substrate, while a thin (~100-200  $\mu\text{m}$ ) YSZ substrate was used for the gas sensors. Most of the substrates used during these experiments were fabricated in our facilities using a tape caster (Labcast, Pro-Cast). In certain instances, manufactured 8 mol% YSZ substrates (Marketech) were also used with the gas sensor materials. In the case of depositing, for instance, a GDC slurry on NiO-GDC or YSZ slurry on YSZ, the substrates were typically only presintered at low temperature in order to match shrinkage rates upon final densification. For the electrodes, the pastes were deposited on fully sintered substrates.

### **6.3.5 Initial Combinatorial Experiments**

There were two sets of experiments used as an initial probe of the machine capabilities. These included tests with various line patterns and then rastered shapes. In this way we judged the difficulty in using typical solid-state ionic materials with this direct-write technique. The material chosen for these experiments was the LCO gas sensor material, which was deposited on YSZ. As shown in Figure 6-2, the line tests consisted of making two sets of lines for each of three gantry speeds (2.5, 7.5, and 18 mm/s), with all other machine parameters fixed. This was repeated for three different backing pressures (2, 10, and 25 psi).

The second general experiment that was conducted involved the rastering of a circular LCO electrode onto YSZ by starting with a spiral pattern and ending with a circle. Deposition quality was tested for variations in gantry speed (7.5, 15, 25, 50, 100, 250 mm/s), backing pressure (1, 2, 10, 50 psi), and distance of the pump tip from the surface of the substrate. Following the lessons learned in these experiments several complex patterns were deposited using the electrode materials.

For the electrolytes, materials were deposited in square, rectangular and grid patterns using fuel cell and gas sensor materials. Three-dimensional structures were also attempted by printing layer-by-layer using a high-solids-loading paste (as in the case of YSZ prepared with the ESL vehicle). Due to the sticky nature of the vehicle and slow drying rate, it was necessary to compensate for the interaction of each subsequent layer with the material being deposited. This was accomplished by extending the dimensions out for each additional layer. Another way we tested the capabilities of 3D printing was with the high-solids loading GDC slurry, which was tailored to keep its shape and dry relatively quickly. Deposition with the YSZ tape casting slurry was also tested.

Following deposition, the samples were dried in an oven at 60 °C to 80 °C and then transferred to either a burnout/presintering furnace (Carbolite, BWF) or high temperature furnace (Carbolite, HTF) for final sintering. SEM images were taken using a field-emission SEM (JEOL, JSM-6335F) and a thermionic SEM (JEOL, JSM-6400) in either secondary electron or backscatter imaging modes. Cross-sections were prepared by mounting sintered samples in epoxy and polishing down using a grinder/polisher with fine SiC and then diamond paste with polishing cloth.

#### **6.4 Results and Discussion**

As a result of this work, solid-state ionic device materials can be processed for good deposition quality and small feature sizes when used with the nScripT direct-write technique. The ability to use this method has come from analysis of particle size and particle-size distribution, resulting electrolyte and electrode deposition characteristics, and the initial line and rastered-shape experiments.

### 6.4.1 Powder Particle Size Analysis

In order to deposit materials with as small a feature size as possible, it was necessary to ensure particle sizes were less than the inner diameter of the tips (as small as 12.5  $\mu\text{m}$ ) used with the nScript. Figure 6-3 shows the laser diffraction measurements for LCO and GDC powders, which had representative primary distributions of submicron particles. For example most of the particles in the LCO powder were around 750 nm in diameter (d90), though the mean was about half as large. This was a rather broad range of particle sizes, when compared to the ball-milled GDC which had a narrow, primary peak of 150 nm particles.

### 6.4.2 Electrolyte Deposition

Initial attempts to use the ESL vehicle with a high-solids loading of GDC powder were mostly unsuccessful. This was likely due to the isoelectric point of GDC and powder particle size, which resulted in agglomeration and tip clogging.<sup>211</sup> However, the situation improved when moving to the slurry prepared using GDC powder mixed with a polyelectrolyte for dispersion control.<sup>212</sup> Figure 6-4A shows a cross-section of a NiO-GDC anode layer that was spin-coated with a GDC solution. As is clear from the image and inset of the top surface, the spin-coated GDC had some porosity. As shown in Figure 6-4B, the nScript-deposited high solids-loading GDC resulted in a much denser layer when compared to the spin-coated GDC. Note that the thickness of this dense layer was about 4 times as large as the spin-coated layer. However, as shown later this can be reduced through modification of machine parameters.

A paste of YSZ using the ESL vehicle has also been successfully deposited. The YSZ paste was deposited onto a presintered YSZ tape to form U-shaped channels that might be used in YSZ-based micro fuel cells or to separate regions on a gas sensor array to minimize interference amongst the sensing electrodes.<sup>199</sup> Up to four layers have been deposited without a drying step, resulting in structures with a thickness of approximately 250  $\mu\text{m}$ .

The YSZ tape-casting slurry was deposited directly onto a sheet of mylar and built up layer-by-layer into a structure with a gas channel and internal compartment as shown in Figure 6-5. After drying, the structure did not break when removed from the carrier film. This ability to print electrolytes and other materials in three dimensions will be extremely useful in the construction of future solid-state ionic devices.

### **6.4.3 Electrode Deposition**

The nScript direct-write technique has been successfully used to deposit both fuel cell and gas sensor electrode materials. However, the results shown here are for the  $\text{WO}_3$  and LCO gas sensor materials. Figure 6-6 shows the typical electrode microstructure obtained from the nScript-deposited pastes. The results are typical for each electrode material because their preparation was standardized as discussed earlier. The general micro-structure for  $\text{WO}_3$  was uniform and can be seen in Figure 6-6A. This electrode shows a well connected, porous network of sintered particles as illustrated in 6-6B. Furthermore, the quality of the pastes was such that we were easily able to deposit the  $\text{WO}_3$  in patterns with very fine feature sizes. For example, Figure 6-6C shows a section of a  $\text{WO}_3$  spiral deposited on YSZ. The linewidth of the spiral was less than 18  $\mu\text{m}$ .

### **6.4.4 Lines and Rastered Patterns**

#### **6.4.4.1 Line tests**

Some of the results for the line tests can be seen in Figure 6-7. These are plots of the average deposition linewidth and thickness (as measured with SEM) versus the backing-pressure of the nScript pump. Gantry speeds of 2.5, 7.5, and 18 mm/s are represented with the circle, square, and triangle symbols, respectively. The lines were on the order of 4 to 5 mm in length. The measured linewidths varied from  $\sim 275 \mu\text{m}$  to  $\sim 85 \mu\text{m}$  for the given variable machine parameters, all else constant. However, much smaller variations were seen in the thickness

values (~2.75  $\mu\text{m}$  to 5.6  $\mu\text{m}$ ). As evident from the plots, there was a parabolic relationship between the thickness/linewidth and backing pressure. On average, higher backing pressures yielded thicker, wider lines. As the gantry speed increased at a given pressure setting, the linewidth changed by approximately 40-50%, while the thickness had a variation of 50-60%. Additionally, the effect of the pressure was more prevalent at higher gantry speeds.

#### **6.4.4.2 Rastered patterns**

After the line tests, the same LCO paste was deposited into circular patterns on YSZ. For these experiments the backing pressure, gantry speed, and distance of the tip from the substrate were varied. Figure 6-8 demonstrates the effect of backing pressure on the thickness of the rastered patterns. Thickness was measured from cross-sections, near the centers of the LCO circles. A 50% increase in backing pressure resulted in a 60% change in thickness. With a tip-to-surface height of ~100 microns, the best results were with gantry speeds of 25, 50, and 100 mm/s while higher speeds led to rippled edges. For other heights and settings the ideal speeds were different, but overall the combinatorial approach allowed for rapid assessment and improvement in the deposition quality.

#### **6.4.4.3 Relationship between machine and material properties**

From these test materials the deposition quality can be related to the material properties and machine parameters. The various nScript feed materials were either fluid inks (~ 50 – 500 cP), tacky pastes (~ 500 – 100k cP), or thick slurries (> 100k cP) as compared to viscosity standards (Brookfield Engineering Laboratories). In addition to material properties, the gantry speed, backing pressure, and tip-to-surface height determined the linewidth, thickness, and quality (e.g., rippled edges) of the depositions. For less viscous feed materials, little to no pressure was needed to achieve flow conditions inside the nScript pump and tip. However, thick depositions with such inks required several layers because increased pressure or valve opening

caused spreading across the substrate. This is likely only desirable if the goal is to have a continuous thin, rastered electrode. Otherwise, use of quick drying solvents (e.g., ethanol) will allow the deposited material to dry before being able to spread. Multilayer deposition with pastes was also difficult because the material crept up the ceramic tip if depositions were made too far from a surface. However, machine parameter and tool path tuning was capable of partially overcoming the tackiness problem, as mentioned earlier for YSZ. Thick slurries were primarily for high solids-loading depositions, such as for the dense GDC layer. Such slurries may also be useful for freeform, 3D prototyping because of their shape-retention and consolidation properties. In terms of solid-state ionics devices, the ceramic- or metal-dispersed inks, pastes, and slurries may require particular properties (e.g., solid-loadings) that prevent tailoring of the feed fluid viscosity. For these cases, the nScript machine parameters allow some flexibility in terms of tailoring thickness and feature size.

Taking what was learned from the line and rastered circle experiments, deposition of more complicated patterns was merely a process of designing CAD files and assigning the appropriate machine parameters to the vector paths. Figure 6-9A demonstrates the scaling capability of this direct-write technique. These various size circular electrodes were made with a single tip size either by rastering or opening/closing the pump valve very quickly. The machine was even able to deposit the sensing electrode material into the shape of ‘The Electrochemical Society’ and ‘‘American Ceramic Society’’ (ACERS) logo using LCO paste and GDC slurry, as seen in Figures 6-9B and 6-9C. These demonstrations were accomplished at speeds comparable to an ink-jet printer and required only about 5 to 10 seconds to deposit. Furthermore, in terms of ease in material development, the nScript direct-write technique was far superior.

#### **6.4.5 Design and Performance Results**

Figure 6-10 shows preliminary results of direct-write sealing and deposition of gas channels for SOFCs. Conceptually, the idea is to build all the components of a micro-SOFC from the bottom up and then to place it in a manifold such as that shown in Figure 6-11. Initial performance results from nScript-deposited cathodes can be seen in Figure 6-12. The power output was relatively good and can be improved significantly using a bilayer electrolyte and anode functional layers.<sup>213</sup>

The nScript direct-write method was also used to make prototype heater designs for a gas sensor array. Some preliminary results can be found in Figure 6-13. There are 5 microheaters on an alumina substrate. The width of the active area of the heaters is approximately 1 mm. The features of the active area cannot be seen with the naked eye.

### **6.5 Conclusions**

This work has successfully demonstrated the flexibility of the nScript-deposition technique for the fabrication of solid-state ionic devices. Structures with features below 18  $\mu\text{m}$  and a variety of thicknesses have been easily achieved. Furthermore, this work has shown that even complex patterns can be deposited rapidly using practically any material. Now that a materials understanding has been developed for this direct-write technique, the next step will be to build actual devices. Progress is already underway for the iterative simulation and design process for the gas sensor array. The multilayer gas channels mentioned earlier will be used in the construction of a micro fuel cell from the bottom up. With the conformal-printing capabilities of this technique, there is also the possibility of depositing materials onto tubular fuel cells or proton-exchange membranes. Furthermore, the nScript tool will be used to fabricate samples for investigations of a promising new method for actively enhancing the performance of solid-state ionic devices with the use of external electric fields.<sup>203</sup> In the future, additional

capabilities will be integrated into the machine such as ink-jet heads or spray nozzles for thin depositions and an on-the-fly laser micromachining/sintering system to achieve finer features and improved multilayer fabrication. In collaboration with nScript, the Florida Institute for Sustainable Energy is also working toward making materials that can be deposited at the submicron feature size level. In conclusion, this tool will be extremely useful as the next generation solid-state ionic devices are researched and developed.



Figure 6-1. Close up view of the nScript 3Dn 450 HP dual pump assemblies with fine ceramic tips in action. Florida Institute for Sustainable Energy (FISE) and nScript logos were printed from a CAD file using silver paste (Dupont) on Kapton polyimide film.

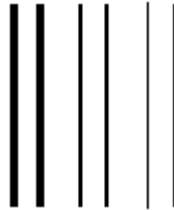


Figure 6-2. Pattern emulated during line tests with LCO. Two sets of lines for three different gantry speeds were deposited successively. This was repeated for three backing pressures, up to 25% of the maximum machine setting.

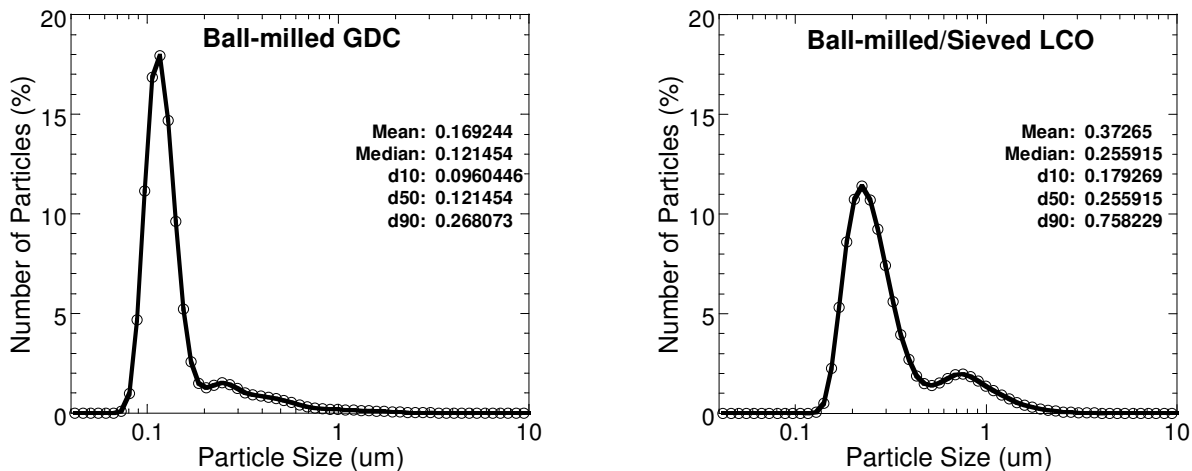


Figure 6-3. Typical particle-size distributions of powders used in this work. Shown are particle-size distributions for ball-milled GDC and ball-milled/sieved LCO powders. In all powders used, the average particle size was submicron and the largest particles had diameters less than the smallest inner-diameter tip used with the nScript.

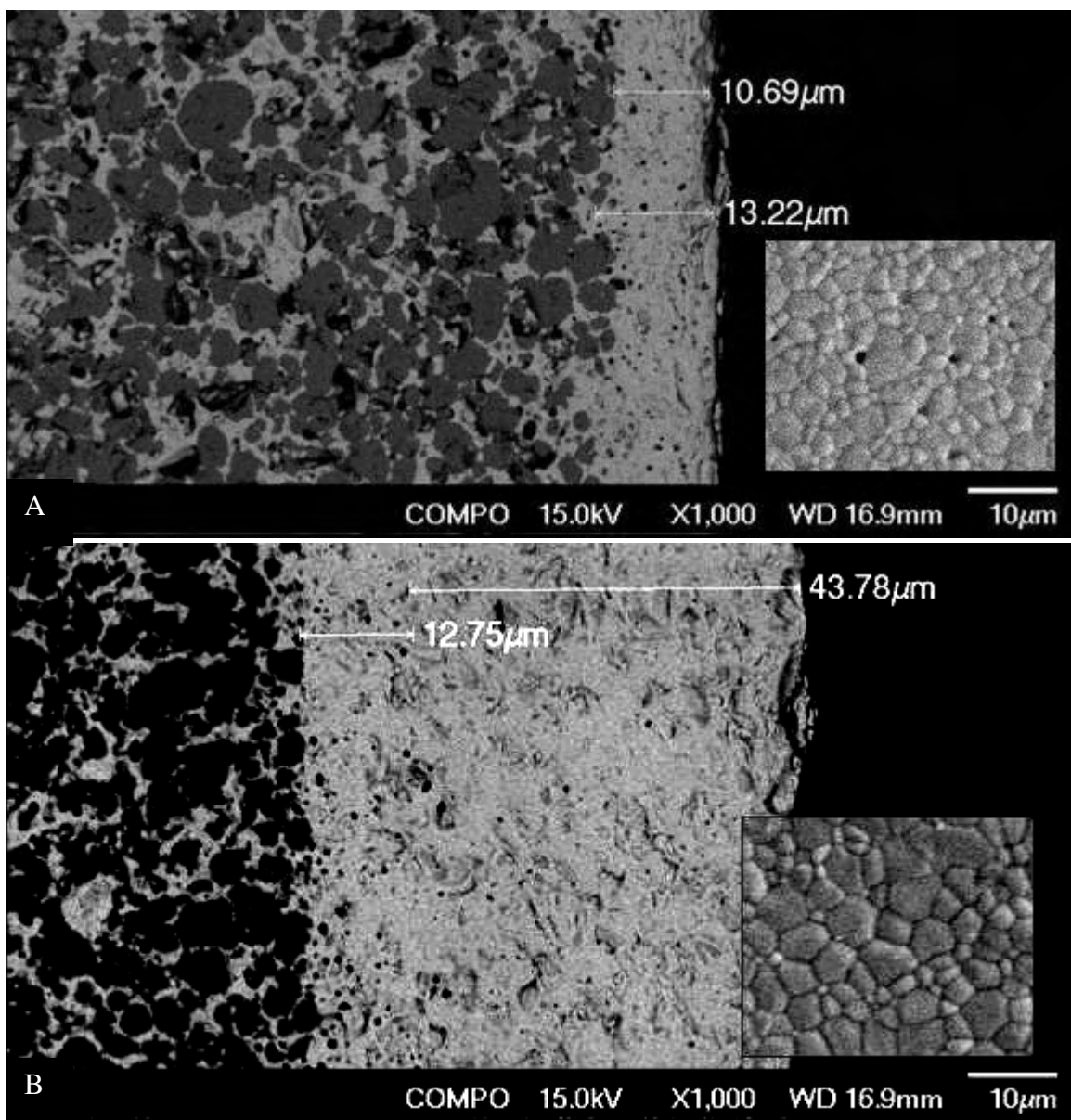


Figure 6-4. Comparison of spin-coated and nScrypt-deposited GDC electrolyte. A cross-section of a NiO-GDC anode with relatively porous, spin-coated GDC layer on top is shown in A). The inset shows the top surface of the spin-coated GDC. B) shows the same structure as in A), except on top of the spin-coated GDC is an nScrypt-deposited dense GDC layer. The inset shows that this layer is indeed dense.

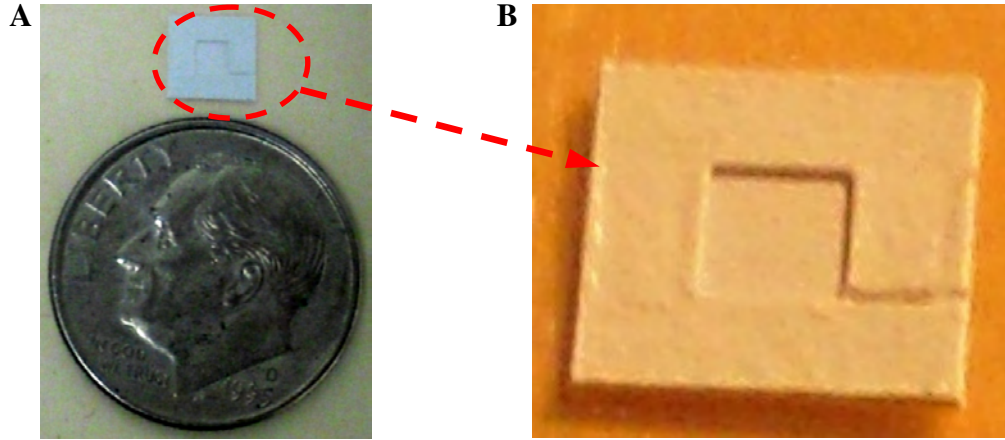


Figure 6-5. Example of “3D” YSZ structure made with the rapid prototype system. In A), the scale of the structure is compared to the features on a U.S. dime, while a close-up is shown in B). The small sample was made with YSZ from the bottom up with a gas channel (lower right portion of right image) leading to an open chamber.

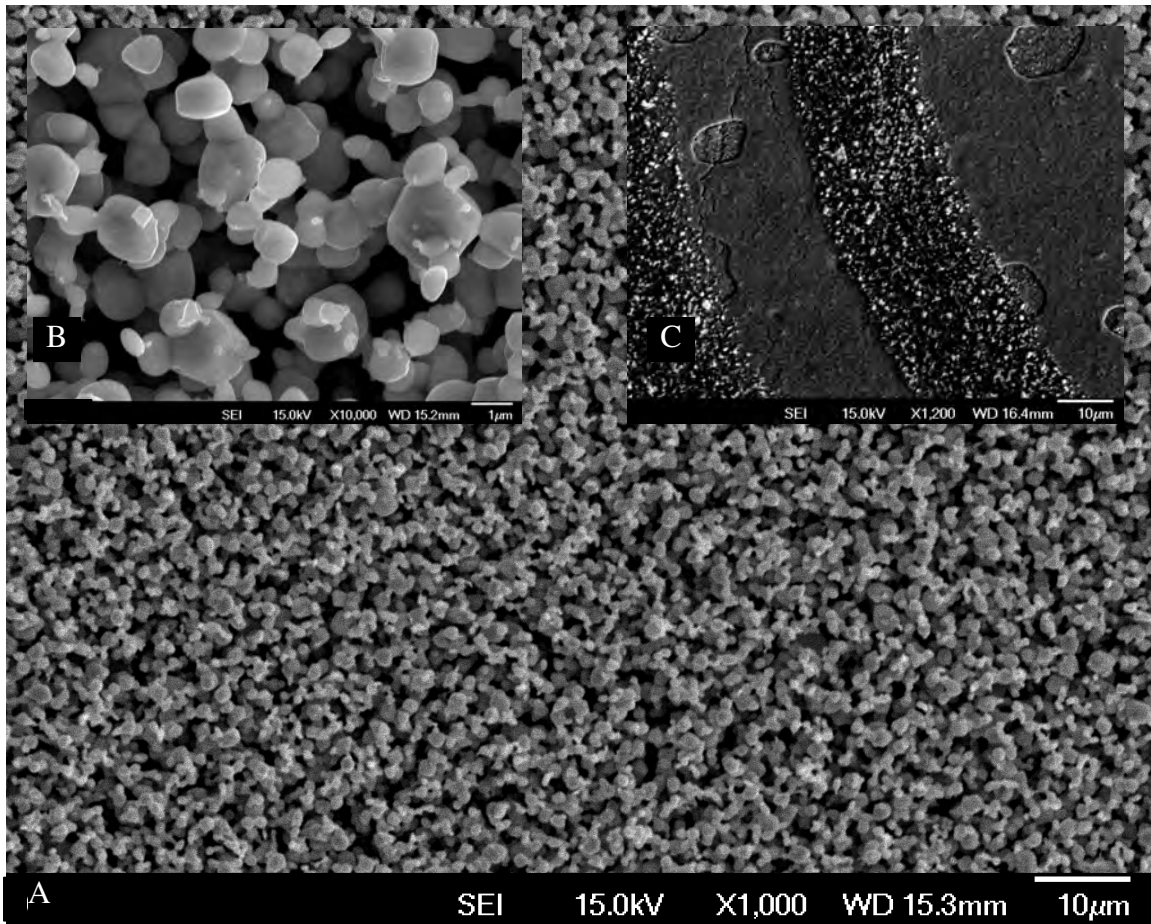


Figure 6-6. Typical electrode microstructure for nScript deposited pastes. The general microstructure for the  $\text{WO}_3$  can be seen in A), while the individual sintered particles are shown in B). A spiral with linewidths below  $\sim 18 \mu\text{m}$  was made from  $\text{WO}_3$  deposited on YSZ as shown in C). The scale bars are  $10 \mu\text{m}$  for A) and C), and  $1 \mu\text{m}$  for B).

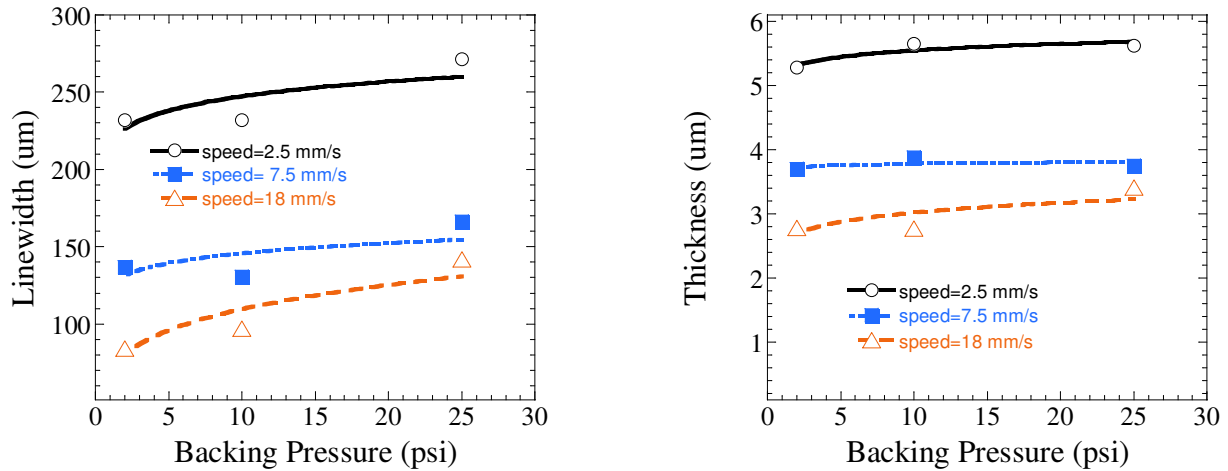


Figure 6-7. Effect of backing pressure and gantry speed on the linewidth and thickness during line tests with LCO deposited on YSZ. Larger backing pressures gave thicker, wider lines. However, the effect was lessened at slower gantry speeds.

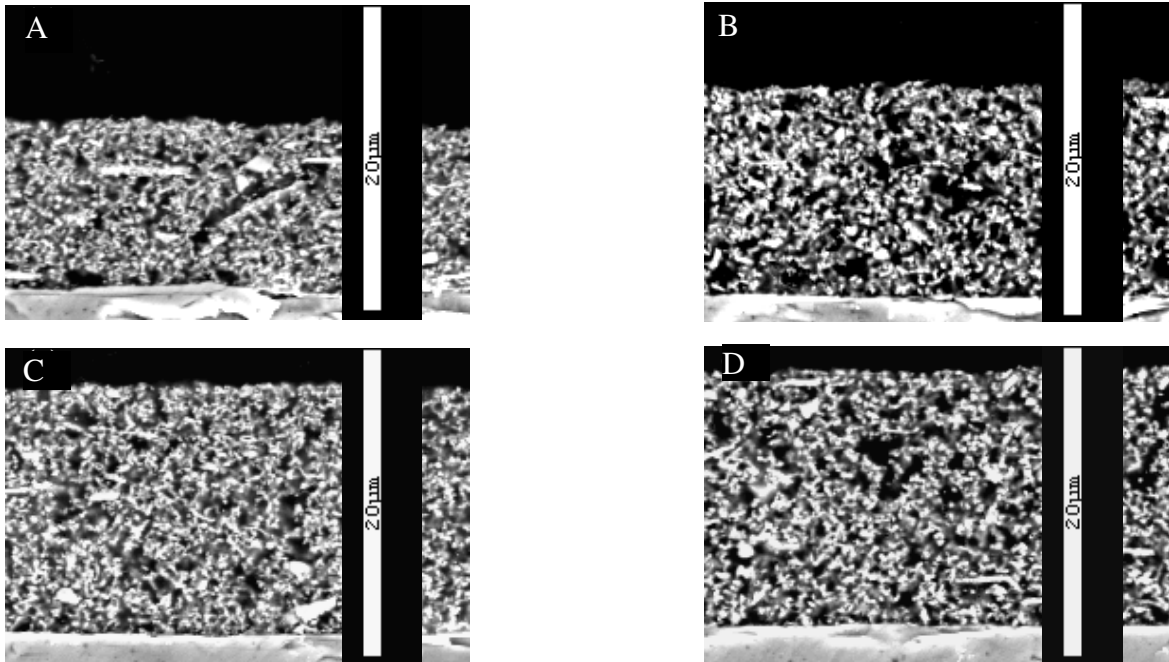


Figure 6-8. Cross-sections of circular LCO samples made during rastered pattern experiments. The backing pressures used were 1, 2, 10, and 50 psi in A)-D). The thicknesses of these circular patterns were approximately 11.1, 14.3, 16.5 and 17.5  $\mu\text{m}$ .

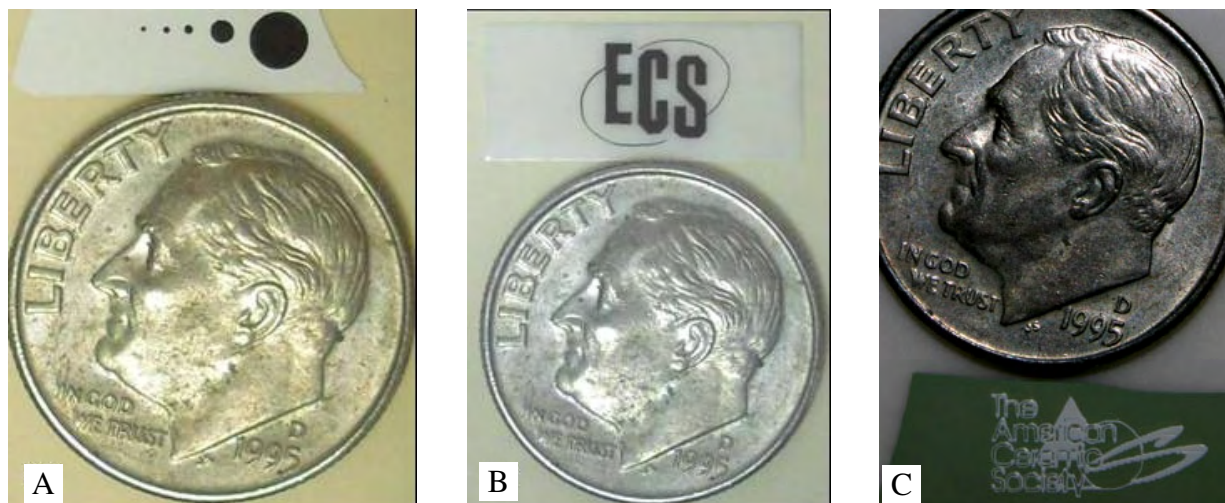


Figure 6-9. Examples of scaling and complex pattern capabilities of nScript-deposition technique. A) and B) are  $\text{La}_2\text{CuO}_4$  on YSZ; C) is GDC on NiO-GDC. The size of the circular electrodes increased from left to right in A) as the gantry moved in increasingly larger spiral patterns (ending in a circle). Furthermore, the pump parameters were the same for each circle. In a matter of seconds, the machine effectively made a gas sensor in the form of the ECS logo in B) and two-thirds of a fuel cell in the form of the ACERS logo in C).

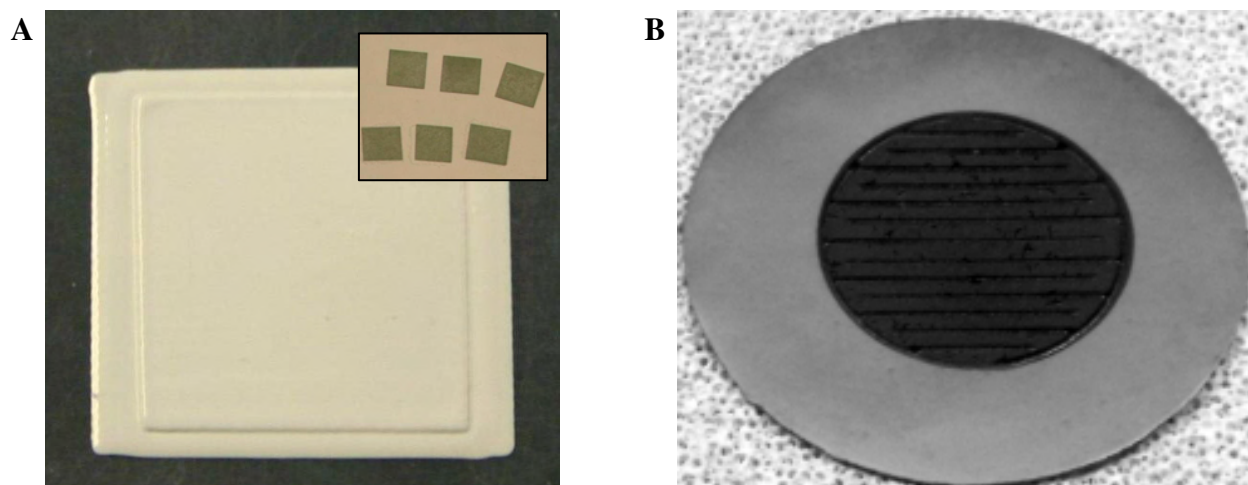


Figure 6-10 Direct-write fuel cell sealing and deposition of gas channels. A) shows the as-dried first attempt of using the nScript system to deposit a GDC electrolyte on a NiO anode (see inset), while simultaneously sealing the sides of the (porous) anode. B) shows an example of an LSCF cathode deposited on a GDC electrolyte film (supported by a Ni-GDC anode) with gas channels made out of the same material. The wall of the channels is  $\sim 0.25$  mm, with  $\sim 1.25$  mm in between each wall.

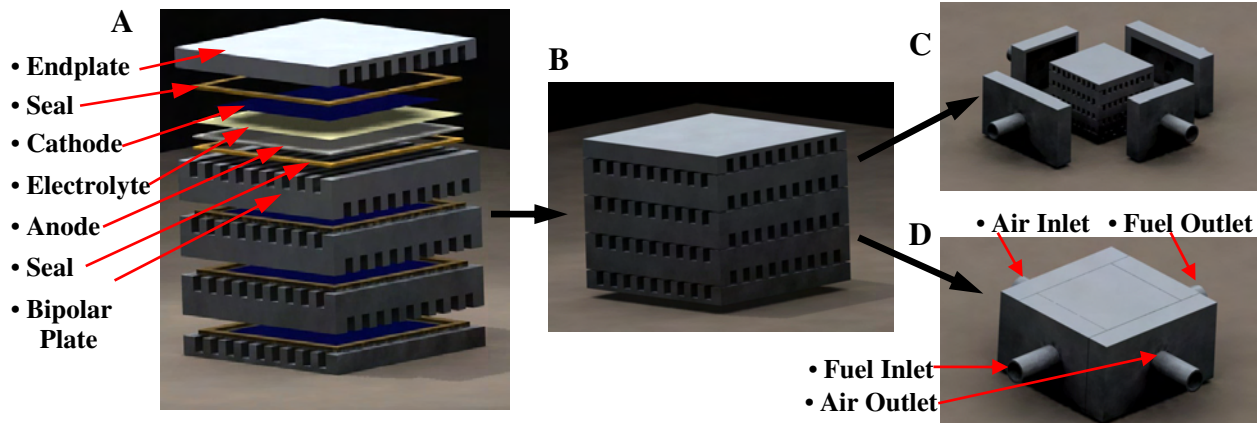


Figure 6-11. One possible micro IT-SOFC stack configuration. An exploded view of the stack can be seen in A), where the endplates, seals, cathode, electrolyte, anode, and bipolar plates can be seen. The complete stack can be seen in B) with fuel and air ports shown. C) shows an exploded view of one possible external manifold arrangement for the inlet and outlet of the fuel and air lines, while D) illustrates how the complete stack and manifold might look.

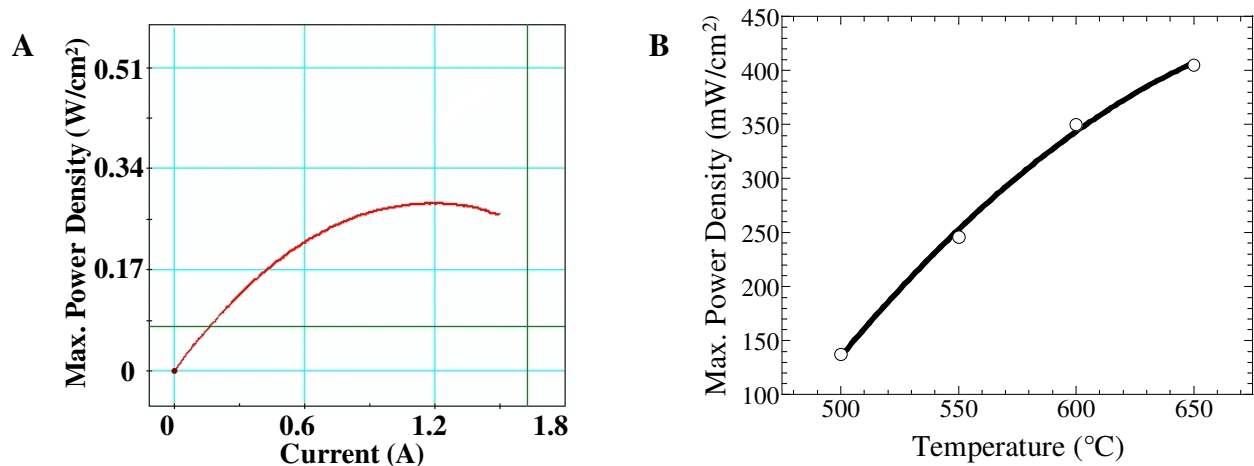


Figure 6-12. Performance results for IT-SOFC consisting of rapid-prototyped LSCF cathode on top of a spin-coated GDC electrolyte film supported by a Ni-GDC anode. In A), the maximum power density and impedance are shown for 600 °C. In B), the trend in maximum power density with temperature can be seen.

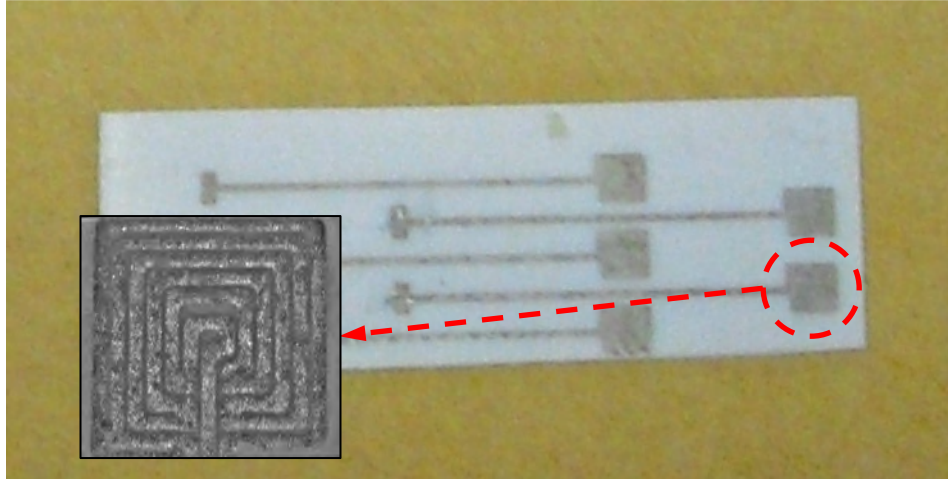


Figure 6-13. nScript deposited microheaters for future gas sensor arrays.

Table 6-1. Comparison of different “additive” direct-write fabrication methods to a more standard technique

Method	Viscosity	Minimum feature size	Advantages	Disadvantages
Novel pressure-backed valve pump technology (nScript)	1 to 10 cP	< 10 $\mu\text{m}$	Speed; flexibility; conformal and 3D printing	New; tip clogging
Ink Jet	1 to 10 cP	~70 $\mu\text{m}$	Well-known	Overspray; low solids-loading only
Aerosol	1 to 5000 cP	~10-25 $\mu\text{m}$	Conformal and 3D printing	Overspray; low solids-loading only; material limitations
Screenprinting	5000 to $0.5 \times 10^6$ cP	> 75-100 $\mu\text{m}$	Fast; well-known; larger areas	Pin holes, material waste

CHAPTER 7  
EXTENDED SURFACE SCIENCE STUDY OF SOLID-STATE GAS SENSORS BASED ON  
THE DIFFERENTIAL ELECTRODE EQUILIBRIA THEORY

**7.1 Introduction**

Surface science techniques have been used to explore the sensing mechanisms of a variety of solid-state gas sensors (e.g., chemiresistive, potentiometric, and amperometric).<sup>110</sup> These include x-ray photoelectron spectroscopy (XPS), ultraviolet electron spectroscopy (UPS), Fourier transform infrared (FTIR) spectroscopy, and the Kelvin method.

Of particular interest is the study of surface properties for potentiometric gas sensors based on the Differential Electrode Equilibria theory. In such devices, the voltage measured between two sensing electrodes in the same gas environment can depend on differences in contributions from electrochemical reactions (mixed potential), heterogeneous catalysis (changes in local gas concentrations), kinetics, and band-bending (when at least one semiconducting electrode is used).<sup>65,91</sup> In other words, differences in the various equilibria between the two electrodes are what determine the measured sensor output. The characteristic equilibria of an electrode depend on the material and gases in question. For instance, with the use of a semiconducting material the Fermi level of the electrode can change as gas adsorbs on the surface.

Various surface science techniques have been used to study the Differential Electrode Equilibria theory, including temperature programmed techniques (with and without labeled oxygen), infrared spectroscopy, and XPS. The past research has primarily focused on the p-type semiconducting oxide,  $\text{La}_2\text{CuO}_4$  (LCO). This work aims to extend these studies in order to further understand the sensing mechanisms. In particular, the past XPS measurements were made using LCO powder with an older XPS system which limited resolution to 0.1 eV steps and had considerable noise due to the use of a poly-chromatic Mg  $K\alpha$  source.<sup>146</sup> This resulted in poorly resolved features with only the O 1s peaks used as a point of analysis. In fact, the Cu

peaks were not seen at all with the powder samples. An electrode of screen printed LCO on yttria stabilized zirconia (YSZ) was also surveyed with 0.5 eV steps. In this case a weak Cu peak was observed, but was lost after three weeks of thermal cycling.

When investigating an oxide sample containing lanthanum, an Mg K $\alpha$  source should be avoided because the O 1s line coincides with the La MNN auger peaks.<sup>214</sup> Therefore, in this work an Al K $\alpha$  monochromatic source is used to investigate the O 1s, C 1s, N 1s, La 3d, and Cu 2p lines. Because the proposed sensing mechanisms from past work relied in part on interpretation of unresolved XPS data, a clearer picture of the key features of the spectra will help lend credit to these ideas. Furthermore, this work will also investigate changes to the valence structure of La<sub>2</sub>CuO<sub>4</sub> as a result of relevant pretreatments through the use of valence XPS and UPS. This yields specific information about the band bending that occurs when gases adsorb on the surface. The photoelectron spectra were also measured at several emission angles (i.e., angle resolved photoelectron spectroscopy) in order to probe various depths in the crystal surface.

This work also constitutes an ongoing investigation of electric-field enhanced solid-state ionic devices.<sup>176</sup> In past work, localized electric fields were demonstrated as a means to enhance both the sensitivity and selectivity of potentiometric gas sensors. Furthermore, gas evolving over the electric-field enhanced sensing electrode was shown to correlate with the changes in sensor response. Temperature programmed desorption experiments also revealed changes in the total NO<sub>x</sub> adsorbed when the electric field was applied. Therefore, the goals of this work were to obtain more information about the LCO sensing mechanism through improved and expanded surface science techniques and to further explore the electric field effect.

## 7.2 Background

### 7.2.1 Surface Science Techniques

#### 7.2.1.1 Electron spectroscopy

Electron spectroscopy is a set of techniques in which the measurement of emitted electrons from a solid can yield information about the bulk and surface characteristics.<sup>75</sup> Electron spectroscopic methods allow non-destructive, quantitative determination of oxidization states, local chemical environment, electronic band structure, and elemental analysis of the surface and subsurface of an adsorbate-material system.<sup>126</sup>

In XPS a high energy photon ionizes an atom, thereby ejecting a free electron from the strongly bound inner orbitals and the outer valence level orbitals. As the photoelectrons emitted from the sample reach the detector, a spectrum is collected with characteristic peaks.<sup>126</sup> UPS is related to XPS and, in fact, the photoionization process is identical.<sup>126</sup> However, the lower energy ultraviolet radiation results mostly in information (i.e., electrons) from the outer surface of the solid. While XPS is generally used to characterize the bulk and subsurface regions of a solid, UPS primarily yields information about the electronic structure at the surface and can be used to study valence bands or as a means to identify adsorbed surface species and investigate surface binding energies.<sup>75,126,131</sup>

#### 7.2.1.2 Kelvin probe

A Kelvin probe (KP) is a non-contact, non-destructive surface science tool that allows in situ measurements of induced changes in the work function (WF) of a gas sensitive material due to modifications from adsorbed gases.<sup>118</sup> The basic idea of this method is to form a vibrating capacitor out of the studied electrode and a reference electrode.<sup>119</sup> A wire connecting one side of the reference to a side of the sample completes the circuit and results in the formation of a contact potential difference (CPD) and electric field between them (Figure 7-1). The CPD is

related to the differences in the WFs ( $\Delta\Phi$ ) of the two materials. The reference electrode (or, less commonly the sample) is mechanically set to vibrate vertically above the surface of the specimen. The equivalent capacitance is modulated as the gap between them changes.

The relationship between compensating voltage ( $V_0$ ), the current ( $i$ ), and capacitance ( $C$ ) is shown in Equation 7-1, where  $Q$  is the charge on the capacitor plates and all voltages are assumed constant.<sup>109,119-124,215</sup>

$$i(t) = \frac{dQ}{dt} = \frac{d}{dt}(V_0 - \Delta\Phi)C = (V_0 - \Delta\Phi)\frac{dC}{dt} \quad (7-1)$$

$V_0$  is adjusted until equal to the CPD (i.e., where  $i(t)$  goes to zero). In a real experiment, care must be taken to ensure the WF of the KP reference electrode remains constant. Several techniques exist for overcoming this issue and make this a powerful technique.<sup>124,125</sup>

### 7.2.2 Related Work

The Differential Electrode Equilibria theory has been studied for both p-type and n-type semiconducting oxides.<sup>139</sup> However, the model material has been p-type LCO, which has been studied extensively and shown to have  $\text{NO}_x$  sensing mechanisms that occur in part as a result of surface complex formation. This can either result in electron or hole injection into the LCO, thereby changing the Fermi level and thus potential of the semiconductor.  $\text{NO}$  and  $\text{NO}_2$  adsorption both result in the formation of nitrite,  $\text{NO}_2^-$ , and nitrate,  $\text{NO}_3^-$ , surface species. However, the way in which these surface species form on the LCO surface and interact with surface and subsurface oxygen determines the sensor response. Furthermore, there are varying degrees of interconversion between nitrite and nitrate species during some overlapping temperature range. Therefore, one way to alter the sensing response is to interact with this charge transfer, surface-complex forming process. This is one way in which the applied (local) electric field is believed to influence the sensing mechanism, thus resulting in enhanced gas

sensor performance. While much has been learned about the Differential Electrode Equilibria theory, there is still a need for additional research. This is especially true if future efforts in modeling the sensing mechanism are to be successful.

The electric-field enhanced potentiometric gas sensor utilizes a novel technique for providing relatively large localized fields about the sensing electrodes without charge transfer to the device. Normally, a direct applied bias to an electrochemical cell will drive reactions and/or pump ions from one side of the cell to other. This is the method used in another type of well-studied enhancement of electrochemical cells called electrochemical promotion (or Non-Faradaic Electrochemical Modification of Catalytic Activity, NEMCA).<sup>77</sup> Led by the research of Vayenas et. al it has been shown through electroanalytical and surface science techniques (e.g., XPS) that the enhanced catalytic activity that occurs with direct bias is a result of reverse spillover of pumped oxygen ions onto the working electrode.<sup>78</sup> The spreading of the electroactive surface species over the catalyst surface is accompanied with the formation of an effective electrochemical (dipole) double-layer, and associated (strong) electric field, that increases the electrode work function.<sup>68,77,78,81,82,180,181,196,197</sup> The dipole layer is believed to enhance reactions due to a beneficial weakening of the binding energies of (gas-phase induced) chemisorbed oxygen.

A considerable amount of research has been performed using Kelvin probes to study chemiresistive gas sensors.<sup>110,118</sup> This is not the case for the potentiometric variety, but the same information would be useful here. Some researchers have had success in the simultaneous monitoring of changes in resistance and work function to determine the contribution of band bending, surface dipoles, and electron affinity on the work function.<sup>120,121</sup>

## 7.3 Experimental

### 7.3.1 Sample Preparation

$\text{La}_2\text{CuO}_4$  powder was synthesized using an amorphous citrate autoignition (fuel lean) technique. Prior to synthesis, inductively coupled plasma (ICP) spectroscopy was used to verify the concentrations of starting salts (i.e., lanthanum nitrate and copper nitrate). The synthesized powder was calcined at 600 °C for 10 hours to rid the sample of any remaining salts. Phase purity was verified with XRD.

Alumina and (8 mol %) YSZ substrates were prepared from starting powders (Alcoa; Tosoh), a water-based tape-casting system (Polymer Innovations), and a tape caster (HED International). Thin, rectangular alumina pieces were cut from the tape and laminated using a heated uniaxial press (Carver). Circular YSZ disks were made in a similar fashion using a single round punch. Both materials were sintered at 1500 °C for 4 hours, resulting in final dimensions of approximately 15 mm X 16 mm X 250  $\mu\text{m}$  for the alumina, while the YSZ was  $\sim$  125  $\mu\text{m}$  thick with a diameter of  $\sim$  6 mm. LCO paste (i.e., powder mixed with an ESL vehicle) was applied to the top surface of the YSZ, dried, and sintered at 800 °C for 8 hours. Using ceramic cement (Ceramabond) the sintered alumina was attached to a small, stainless steel platen (for sample transfer in the UHV test setup), with the LCO-deposited YSZ disc subsequently attached to the center of the alumina in same manner. Furthermore, a gold contact pad for sample grounding (to the KP and electron spectrometer) was applied to one side of the alumina surface and connected to the edge of the LCO sample. Two thin tantalum strips were spot-welded to the platen to tack down sides of the  $\text{Al}_2\text{O}_3$  layer. After drying for 1 hour, the whole sample/platen assembly was placed into a tube furnace at 550 °C for 2.5 hours to burn out the organics in the ceramic cement and sinter the gold contact.

In order to explore the electric-field effect two small, thin semi-circular (ID ~ 6.5 mm; OD ~ 8 mm; thickness ~ 250  $\mu\text{m}$ ) electric-field electrode rings were placed around the YSZ disk. A circular ring was punched out of laminated  $\text{Al}_2\text{O}_3$  tapes using two round punches of different size. This was cut in half to give the semi-circular field electrodes which were attached to the  $\text{Al}_2\text{O}_3$  layer (on top of the platen) with ceramic cement. A thin layer of gold (Englehard) was applied to the tops of the semi-circular field electrodes and gold leads were attached. The field-electrodes were electrically isolated from the YSZ and the LCO as shown in Figure 7-2.

### **7.3.2 UHV Test Setup**

X-ray (Omicron; monochromatic Al  $K\alpha$  (1486.6 eV)) and ultraviolet (Omicron; He I (21.2 eV)) sources were utilized during photoemission spectroscopy experiments. The x-ray source and hemispherical analyzer were aligned and calibrated to very high accuracy using a precision silver reference standard (Ag 3d) which was cleaned with an integrated argon ion gun (FIG-5CE). The UV source was calibrated to the He I emission line. Charge compensation was provided with an integrated electron beam (Omicron). The base pressure of the UHV chamber was on the order of  $10^{-10}$  torr for XPS and  $10^{-9}$  torr for UPS measurements.

#### **7.3.2.1 Photoemission spectrometer**

X-ray (Omicron; monochromatic Al  $K\alpha$  (1486.6 eV)) and ultraviolet (Omicron; He I (21.2 eV)) sources were utilized during photoemission spectroscopy experiments. Sample and reference materials were cleaned as necessary with an integrated FIG-5CE argon ion gun. Reduction of sample charging was possible using an electron beam (Omicron).

#### **7.3.2.2 Kelvin probe**

The Kelvin probe (KP6500, McAllister Tech. Services) allowed a detailed investigation of the surface properties of the LCO sensing material. Unlike most other Kelvin probe systems, the KP6500 does not utilize a lock-in amplifier which attempt to measure the null point (i.e., the

backing voltage that causes  $i(t)$  to go to zero) directly. Rather, the system measures the non-null points because they have a much better signal-to-noise ratio (i.e., more accurate measurement).<sup>216</sup> Operation about the null point also has the advantage of ensuring that even weakly bound adsorbates will not be desorbed due to the measurement itself. Furthermore, the Kelvin method has the advantage over other work function measurement techniques (e.g., thermionic) of providing a mean work function instead of a weighted average that is biased towards low work function patches. The KP 6500 software also provides improved repeatability between measurements through the use of gradient tracking, which ensures a constant separation between the sample and the tip, thus reducing spurious noise from stray capacitance.<sup>217,218</sup>

The CPD measurements in this work were collected in an atmospheric test stand, which housed the Kelvin probe horizontally and allowed the sample to be moved towards the tip via a linear translator. Before and after measurements, the probe tip was calibrated and compared to literature work function values using flame-annealed gold and platinum (thick and thin) films and HPOG (highly ordered pyrolytic graphite).

### **7.3.3 Testing Procedures**

#### **7.3.3.1 Pretreatment**

Prior to surface science measurements, the samples were pretreated ex-situ in a quartz reactor, which was placed inside a temperature controlled furnace. The quartz tube was attached to a manifold with gas composition and flow rate regulated by mass flow controllers. All gases used were ultra high purity. The pretreatments used in this investigation are summarized in Table 7-1. Once a sample was loaded into the furnace, a background gas of 21% O<sub>2</sub> and 79% N<sub>2</sub> was flowed through the reactor at 300 cc/min as the temperature ramped to 500 °C at 15°C/min. Upon reaching this setpoint and remaining there for ~2 hours, the reactor was cooled to 300 °C and 650 ppm of the reactive gas of interest was added to the gas stream for 1 hour. Then, the

temperature was lowered to room temperature with the reactive gas continuing to flow. Finally, the samples were removed and immediately transferred to the UHV test setup for photoelectron measurement or to the atmospheric Kelvin probe setup. Following the studies under UHV conditions or with the Kelvin probe, the sample was heated under oxygen and kept at 500 °C for 2 hours in the quartz reactor to restore the LCO surface and oxygen sublattice.

For the sample used in the study of the electric-field effect, the only difference in pretreatment was the additional use of a localized electric-field bias during exposure to the gas of interest; a power supply (Keithley 2400 SourceMeter) was connected to the gold leads attached to the field electrodes and the voltage was set to 8 Volts. Such ex-situ pretreatments are still valuable when compared to in-situ conditioning (which will be done in future studies) because adsorbate species tend to stay bound to the surface of oxides for long periods of time and NEMCA research has shown that electroactive promoted species, such as those that may exist in the case of electric-field pretreated samples, can exist on the surface of solids for well over 24 hours.<sup>78</sup>

### **7.3.3.2 Surface science measurements**

For the angle resolved XPS (ARXPS), the sample under study was first probed at a takeoff angle of 55° (i.e., the photoemitted electron trajectory with respect to the surface normal) as illustrated in Figure 7-2. This was followed with measurements at 75° (i.e., more surface sensitive) and 15° (i.e., less surface sensitive). Prior to photoelectron measurements, the sample position was optimized to maximize the signal intensity as measured with the analyzer. These angles are sufficient for gaining an accurate view of the change in electronic structure and atomic composition as a function of depth from the surface, as has been shown in the literature.<sup>219,220</sup>

For each set of pretreatments an XPS survey scan was measured from 1386 to 50 eV with a 1 eV step size. Subsequently, high resolution core-level XPS measurements were collected at

910-950 (925-965), 810-850 (825-865), 508-525 (523-540), and 265-281 (280-296) with 0.05 eV steps. The peaks of interest were for carbon (C 1s), nitrogen (N 1s), oxygen (O 1s), lanthanum (La 3d), and copper (Cu 2p). The He I ultraviolet spectra were measured from -5 to 30 eV with a step size of 0.05 eV. The survey, core level XPS, and (XPS/UPS) valence spectra were measured with 1, 10, and 20 scan sweeps, respectively, in order to improve the signal-to-noise ratio and to obtain more highly resolved peaks. Additionally, the pass energy of the hemispherical analyzer was set to 50, 20, and 10 eV for the survey, core level, and XPS/UPS valence measurements, respectively.

LCO samples were investigated for pretreatments of O<sub>2</sub>, NO<sub>2</sub>, NO, and NO with a localized electric field (i.e., 'NO+Efield' or 8 V applied to the field electrodes). Furthermore, at various points in this investigation the spectra were recorded before, during, and after raising the temperature of the sample (using a radiative heater integrated into the photoelectron system's sample holder) in order to gauge the relative thermal stability of surface species.

The photoemission spectra were analyzed using the XPSpeaks and CasaXPS (Casa Software Ltd., V2.3.15) software packages.<sup>221</sup> Peak position, area, and full width half maximum (FWHM) for each spectra were determined after Shirley background correction and Lorentzian/Gaussian curve fitting. Peak area and intensity ratios were also calculated.

Kelvin probe measurements were conducted using samples prepared in the same manner as for the photoelectron measurements. The calibrated Kelvin probe tip (amplitude=120; gradient=0.5; vibrational frequency=606.8 Hz) was set to vibrate over the sample. CPD measurements were only recorded after a stable value was achieved (e.g., typically after 5 to 10 minutes). The CPD was verified using both 4 mm and 2 mm stainless steel probe tips.

The Kelvin probe was used to measure the CPD of an n-type WO<sub>3</sub> (Alfa Aesar) electrode in addition to the primary sample of interest (i.e., p-type La<sub>2</sub>CuO<sub>4</sub>) in order to relate the differences in surface potential to previous potentiometric gas sensor investigations using these materials.<sup>96,97</sup> This electrode was prepared in the same manner as the LCO samples.

## 7.4 Results and Discussion

The results from the photoelectron spectroscopy measurements are presented below. There are slight discrepancies between the ARXPS (75, 55, and 15°) and the high resolution core-level XPS measurements (55°), which are attributed to minor differences between samples.

### 7.4.1 Photoelectron Spectra

#### 7.4.1.1 Angle resolved photoelectron spectra

X-ray photoemission spectra were recorded at three angles (15°, 55°, and 75°) for the O<sub>2</sub>, NO, and NO<sub>2</sub> pretreatments. The C 1s peaks were similar in each case, with a main graphitic carbon peak around 284.6 eV (not shown). In the cases with NO<sub>x</sub> adsorbed on the LCO surface, there was a slight broadening of the high binding energy side of the C 1s curve. This may have been due to the presence of C–N bonds (285.2–288.4 eV), which tend to overlap with the C 1s line (284.2–285.1).<sup>222</sup> There were also smaller peaks around 289 and 293 which are ascribed to carbonate species, pi-pi shakeup satellites, and/or hydrocarbons. The use of so called ‘advantageous carbon’ to adjust the spectra was not necessary because of the high quality calibration of the photoelectron system to the silver reference. Furthermore, the C 1s peak did not shift more than ±0.2 eV at any time and the error associated with the advantageous carbon calibration technique has the same order of magnitude and other potentially limiting issues.<sup>222</sup>

Variations in the O 1s signal for each pretreatment with changes in the takeoff angle can be seen Figure 7-3. As the takeoff angle increases the surface sensitivity increases, as clearly visualized by the decreasing (overall) intensity. When considering the O<sub>2</sub> pretreatment, the O 1s

spectrum appears to consist of two main peaks with a separation around 2.75 eV. However, the O 1s signal consists of no less than 3 superimposed peaks, as verified with curve fitting. The lowest binding energy peak attributed to the metal oxide lattice oxygen. This agrees well with other (Al K $\alpha$ ) XPS results on LCO and other related perovskite materials.<sup>214,219,224-230</sup>

At a takeoff angle of 75°, the increased surface sensitivity caused the higher binding energy peaks (I and II) to increase in intensity with respect to peak I. This emphasizes the fact that peaks I and II are likely bound surface species such as adsorbed oxygen, hydroxides, and carbonates (530.8–531.5 eV). Furthermore, the peak(s) associated with these surface species are significantly attenuated after thermal cycling in UHV as seen in the O 1s spectra for a different sample before, during, and after in-situ heating to 250 °C at a takeoff angle of 55° (Figure 7-4).

For the NO pretreatment, the spectrum measured at a takeoff angle of 15° contains a nitrate peak (IV) with a much lower intensity than at 55° and 75° when compared to that at lower binding energy O 1s components. In the case of the NO<sub>2</sub> pretreatment, the nitrate peak intensity was also attenuated at a takeoff of 15°. However, the highest peak intensity for the entire O 1s spectrum was around 530 eV (peak II). This was likely a result of the relaxed sublattice after the oxygen are pulled at for nitrate and nitrite complex formation.<sup>146</sup> However, this may be associated with a separate oxygen state, such as that related to spillover with NEMCA.<sup>78</sup>

#### **7.4.1.2 High resolution core-level XPS**

In order to take a closer look at the surface properties of the La<sub>2</sub>CuO<sub>4</sub>, new photoelectron measurements were made using a different sample which also had a set of field-electrodes. The C 1s, N 1s, O 1s, La 3d, and Cu 2p spectra are presented in Figures 7-5 through 7-9 for several pretreatments, including one case with the application of a localized electric field.

The C 1s footprint is shown in Figure 7-5 for the O<sub>2</sub>, NO<sub>2</sub>, NO, and NO with the localized electric field (i.e., ‘NO+Efield’). The binding energies of the primary peak attributed to graphitic

carbon (~284.5 eV) remains fairly constant for each pretreatment. The presence of NO<sub>x</sub> in the pretreatment reduced the intensity of the peak around a binding energy of 289 eV, which is associated with carbonates. This may be related to surface reactions between the two species during pretreatment conditions, which has been shown in other work to occur on LCO.<sup>98</sup> The peak at even higher binding energy (~292 eV) was present in all pretreatments except for the NO+Efield case.

Spectra of the N 1s orbital can be seen in Figure 7-6 for pretreatments 1, 2, and 4. The peak located around 404 eV can be attributed to nitrite surface complexes, while the nitrate species are found at higher binding energies (~407 eV).<sup>222,231,232</sup> While the results are only shown for O<sub>2</sub>, NO<sub>2</sub>, and NO+Efield, the N 1s peak for NO was observed from the survey scan (not shown) and had a nitrite peak with comparable position and intensity as the NO<sub>2</sub> pretreatment but with a smaller nitrate peak. As evident from the lack of any peaks in the O<sub>2</sub> pretreatment, there were not any nitrite or nitrate species formed during this case. A summary of the findings from the N 1s spectra can be found in Table 7-2.

Figure 7-7 shows changes in the O 1s related peaks between the different pretreatments. As was the case with the ARXPS results (Figure 7-3), there are 3 discernible peaks for the O<sub>2</sub> pretreatment and 4 peaks for NO<sub>x</sub> exposure. As was the case with the past (Mg K $\alpha$  source) results, and similarly found in other work, there was peak splitting of the O 1s spectra when NO<sub>x</sub> was adsorbed on the surface.<sup>146</sup> Peak I is from the metal oxide lattice; peaks II and III are contaminate surface species or adsorbed oxygen; and peak IV is related to the oxygen of nitrate or nitrite complexes. The peak locations of the O 1s spectra for each pretreatment can be found in Table 7-3.

Peak I shifted only slightly for the NO gas exposure (to lower binding energies), while a large shift ( $> 2$  eV) occurred for the NO+Efield case. The NO<sub>2</sub> pretreatment resulted in no change in the peak I position, and maintained the same overall shape as the O<sub>2</sub> case for the first three peaks with a minor decrease in intensity. With respect to the NO<sub>2</sub> pretreatment, NO caused all of the peaks to shift slightly to lower binding energies. Furthermore, the NO+Efield pretreatment was shifted to even higher binding energies than the NO<sub>2</sub> case (for most of the peaks) and had a significantly more pronounced nitrite/nitrate complex peak. The position of peak IV for NO<sub>2</sub> was about 0.7 eV higher than for NO. For the NO+Efield pretreatment, this position of the nitrite/nitrate complex peak was 1 eV higher than the NO case.

Unlike the previous XPS studies involving LCO for potentiometric gas sensing, the Cu 2p peaks were detected and changes with pretreatment can be seen in Figure 7-8. The Cu 2p family of peaks is made up of the Cu 2p<sub>3/2</sub> (933.6 eV) and Cu 2p<sub>1/2</sub> (953.5 eV) lines, each with a smaller satellite peak at higher binding energies. The spectrum is similar to that of CuO and has the characteristic Cu<sup>2+</sup> related satellites of the Cu 2p<sub>3/2</sub> line.<sup>130,224,230</sup> The peaks shift to higher binding energies for the NO pretreatment case, and even higher binding energies for NO<sub>2</sub>. For NO+Efield pretreatment the Cu 2p<sub>3/2</sub> peak (I) has moved to higher energies and has become asymmetric. This was also the case for the NO<sub>2</sub> pretreatment but to lesser extent. The NO peak (I) shifted to lower binding energies with respect to the O<sub>2</sub> pretreatment and also had a slight asymmetry but in the opposite direction of that for the NO<sub>2</sub> and NO+Efield pretreatments. The peak positions for the Cu 2p orbital can be found in Table 7-4.

Furthermore, when the takeoff angle was varied, the degree of these shifts differed (not shown). Compared to the position for NO at 15°, the Cu 2p peak shifted to higher binding energies by 17.7% and 50% for 55° and 75°, respectively. For NO<sub>2</sub> the shifts were 7.1% and

40.9%. This indicates that while the NO adsorbate bond had a less drastic shift (i.e., a weaker bond) there was a greater influence at the surface. This may have something to do with surface band bending, as explained with the valence structure results.

Spectra of the La 3d orbitals are shown in Figure 7-9. Both La 3d<sub>5/2</sub> and La 3d<sub>3/2</sub> have split peaks that are similar to those of La<sub>2</sub>O<sub>3</sub> with the main peaks around 834.5 eV and 850 eV, respectively.<sup>233</sup> The satellite separation for both primary peaks is approximately +4 eV, which agrees with other results from the literature.<sup>214</sup> The O<sub>2</sub> and NO<sub>2</sub> pretreatments had almost identical La 3d peaks, albeit with a slightly shifted peak (to higher binding energies) and lower intensity for the NO<sub>2</sub> case. The NO+Efield pretreatment resulted in peaks that were slightly shifted to higher binding energies, but retained the same relative intensity. The La 3d peaks of the NO pretreatment, however, were noticeably shifted to lower binding energies and had larger relative intensities. Furthermore, the peak separation between La 3d<sub>5/2</sub> and its satellite decreased by 0.5 eV for the NO<sub>2</sub> case, which has been suggested to be a result of smaller coupling of the 4f levels to the valence level.<sup>214</sup> On the other hand, the splitting increased by 0.1 and 0.2 eV for the NO and NO+Efield pretreatments, respectively. This would suggest increased coupling for these cases. The degree of coupling may be related to changes in oxygen defects and/or the length of the La-O bond. The peak positions for the La 3d orbital can be found in Table 7-5.

In addition, at a takeoff angle of 75° the La 3d peaks for the NO and NO<sub>2</sub> pretreatment were identical, and shifted to higher binding energies with respect to the O<sub>2</sub> pretreatment (not shown). As the takeoff angle decreased (i.e., less surface sensitive) the peaks for the NO pretreatment shifted in between those of the NO<sub>2</sub> and O<sub>2</sub> pretreatments (i.e., to lower binding energies). Once again, this suggests that the influence of NO is more strongly related to the surface than for NO<sub>2</sub>.

### 7.4.1.3 Valence spectra

The theoretical density of states (DOS) for  $\text{La}_2\text{CuO}_4$  was calculated by Mattheiss and is presented in Figure 7-10A as a comparison to the XPS-measured valence structure of the  $\text{O}_2$ ,  $\text{NO}_2$ ,  $\text{NO}$ , and  $\text{NO}$  with local electric field (i.e., 'NO+Efield') pretreatments shown in Figure 7-10B.<sup>234</sup> The structure results primarily from the O 2p orbitals of the Cu-O bond and the Cu 3d orbitals at slightly lower binding energies.<sup>130,224,234</sup>

The Fermi level was determined graphically as the distance halfway between the onset of the valence curve and the first significant change in the slope, indicating an increase in the DOS. Compared to the Fermi level in the  $\text{O}_2$  pretreatment case, there was a shift (up with respect to the conduction band) of -0.30 eV for  $\text{NO}$  exposure and (down) +0.20 eV for  $\text{NO}_2$ . On the other hand, the Fermi level shifted (down) +0.10 eV when the  $\text{NO}$  exposure was performed with the localized electric field. In addition to the Fermi level shifts, another key take away from Figure 7-10 is that the valence edge (i.e., the DOS) changed with the pretreatment. For the  $\text{O}_2$ ,  $\text{NO}_2$ , and  $\text{NO}$  pretreatments the valence edge appeared between 1.7 and 2 eV, which is comparable to results from the literature.<sup>130,224</sup> However, the valence edge was at ~2.4 eV for the NO+Efield pretreatment.

In order to see the changes in the valence structure more clearly, Figure 7-11 shows the difference spectra of the  $\text{NO}_2$ ,  $\text{NO}$ , and NO+Efield pretreatments versus the  $\text{O}_2$  standard case. There was a decrease in the DOS of the LCO system, except near the valence band edge, when  $\text{NO}_2$  was adsorbed on the surface. On the other hand, both the  $\text{NO}$  and the NO+Efield resulted in increased DOS. Also emphasized in the difference spectrum of the NO+Efield pretreatment is the shift in the valence edge over the other pretreatments.

The UPS results (at a takeoff angle of  $55^\circ$ ) for the  $\text{O}_2$  pretreatment are compared to the XPS valence measurements in Figure 7-12. The overall shape of the He I spectra is similar to

the XPS results except that at higher binding energies there is almost a plateau in the signal. Furthermore, the peak of the He I spectra appears shifted to higher energies. This is believed to have been a result of contamination on the LCO surface, because the C 2p orbital results in photoemission with a binding energy slightly higher than the O 2p orbital.<sup>224</sup> Furthermore, the high binding energy plateau increased with takeoff angle (not shown). As UPS is an extremely surface sensitive technique, the cleanliness of the sample is important; however, pretreatments were performed in the quartz reactor due to limitations with the current UHV test setup. Therefore, future studies will likely utilize in-situ sample cleaning with an ion gun, followed with pretreatments in a separate chamber inline with the photoelectron measurement chamber without the need to expose the surface to atmospheric contaminants. Regardless, when the low binding energy region of the spectrum is magnified (Figure 7-12), the shape of the UPS measurements matches the XPS valence spectra.

The localized electric field provided by the field-electrodes appears to have resulted in a combination of the NO and NO<sub>2</sub> cases. In particular, the valence structure of NO+Efield pretreatment has the O 2p character of the NO pretreatment and the Cu 3d character of the NO<sub>2</sub> pretreatment. This interpretation is in agreement with the core level XPS results.

#### **7.4.2 Contact Potential Difference**

The Kelvin probe measurements were recorded as the CPD (in Volts) between the sample and the reference electrode. Kelvin probe measurements are usually used as a means to obtain relative information with respect to the change in work function. However, if proper care is taken during calibration and sample measurements, the calculated (absolute) work function can be representative of the actual value.

The changes in CPD (i.e., work function) with exposure to 650 ppm NO or NO<sub>2</sub> are presented in Figure 7-13 for both the La<sub>2</sub>CuO<sub>4</sub> and WO<sub>3</sub> electrodes. Both NO and NO caused

positive changes in the work function of the LCO and negative changes for the  $\text{WO}_3$ . The fact that the CPD changes were in opposite directions for the n-type and p-type material is an indicator that the measurements reflect the true state of the surface, at least qualitatively.

Past work has shown that the NO response of LCO is primarily associated with band bending related to adsorption. On the other hand, the  $\text{NO}_2$  response of LCO was deemed to have possible contributions from band bending, electrochemical reactions, and heterogeneous catalysis (i.e., changes in the local  $\text{P}_{\text{O}_2}$ ). The LCO had a (slightly) smaller change in work function for NO than for  $\text{NO}_2$ , which is may be partly due to the fact that LCO adsorbs twice as much  $\text{NO}_2$  than NO.<sup>98</sup>

The  $\text{NO}_2$  sensor response of  $\text{WO}_3$  has been concluded to have greater contributions due to heterogeneous reactions rather than from band bending. For NO, the results were less obvious than for LCO but may have contributions from both heterogeneous catalysis and band bending. Therefore, the fact that the change in work function was greater for the NO exposure compared to the  $\text{NO}_2$  is not surprising. Furthermore, these results confirm that there are changes in the surface potential of these materials as a result of  $\text{NO}_x$  adsorption.

These CPD results are preliminary and more work is needed. When utilizing the calibration curve of the reference electrode, the absolute work function was calculated as 5.27 eV for the LCO, and 4.98 eV for the  $\text{WO}_3$ . These values are close to those in the literature, including one case where Kelvin probe measurements were made for LCO.<sup>214,235</sup> Despite this outcome, future investigations will involve a special Kelvin probe chamber attached to the UHV test setup. This chamber consists of a small UHV-compatible spherical cube (Kimball Physics Inc.) with multiple conflat flange ports for sample transport and various electrical connections and gas/vacuum fittings. The gap between the tip of the KP reference electrode and the surface

of the sample under study can be precisely adjusted using two linear translators attached to the upper and lower port of the chamber, respectively. Conditions for the future Kelvin probe experiments will be adjustable from vacuum conditions to atmospheric pressure.

## **7.5 Conclusions**

This work has revealed significant information about changes to the  $\text{La}_2\text{CuO}_4$  band structure during interaction with adsorbed  $\text{NO}_x$  species. This was accomplished through the use of angle resolved XPS and UPS and through work function change measurements using the Kelvin method. However, more analysis is needed to determine if the conclusions made in past work need to be altered.

This work has also given some additional insight into sensor performance enhancements using localized electric fields. As work in this area continues, this information will be useful in terms of designing new materials, new designs, and new applications for this effect. Furthermore, with the addition of a heated stage for in-situ Kelvin probe measurements, the transient data can be used to explore such fundamental science as the kinetics of electron transfer between adsorbates and surfaces.

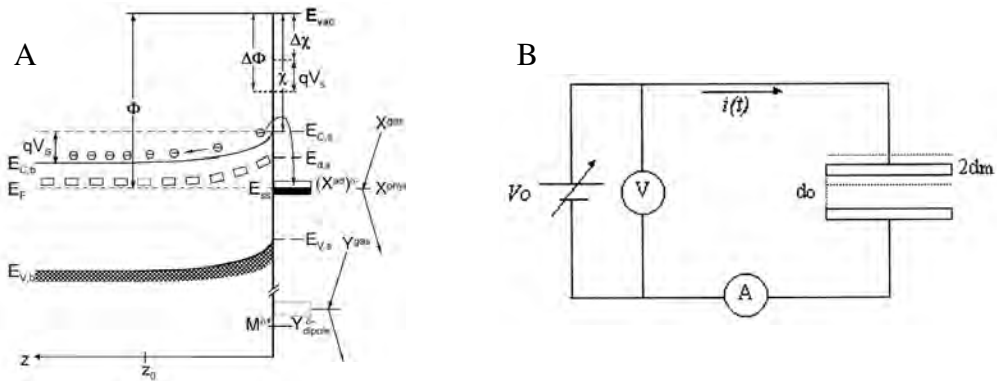


Figure 7-1. Band model of a semiconductor showing the influence of surface adsorbates on the work function and basic circuit concept of a Kelvin probe. The former can be seen in A), while the latter is shown in B). From Sahm et al.<sup>120</sup>

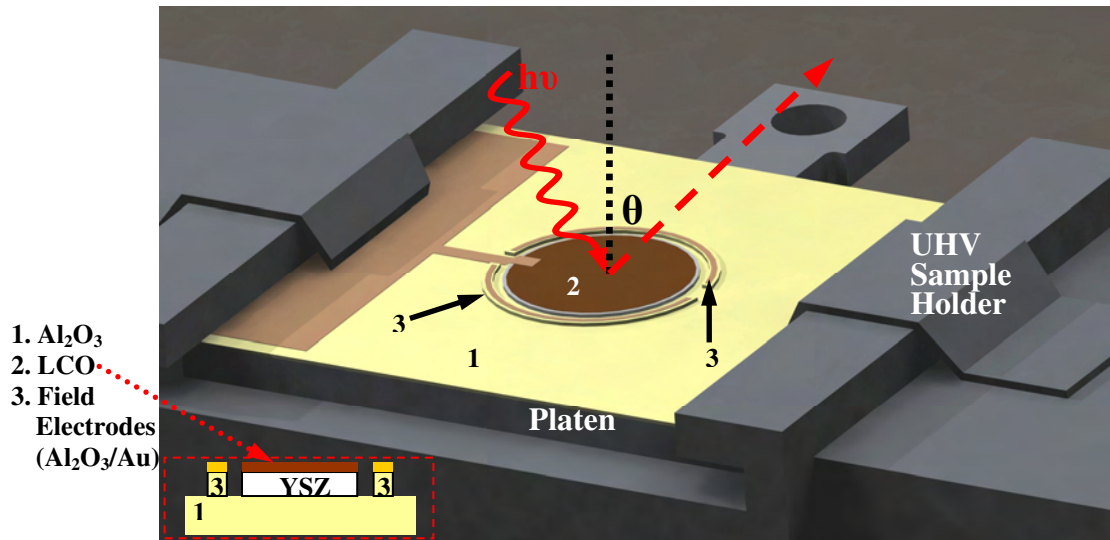


Figure 7-2. Depiction of the sample/platen in the UHV holder and the arrangement for angle resolved photoelectron measurements. The sample under study was a  $\text{La}_2\text{CuO}_4$  electrode coated on top of a YSZ disk, which was attached to an alumina covered stainless steel platen. The two half-ring field electrodes were used to apply a localized electric field during one of the pretreatments. As the sample holder was rotated the angle ( $\theta$ ) between the photoemitted electrons and the surface normal varied.

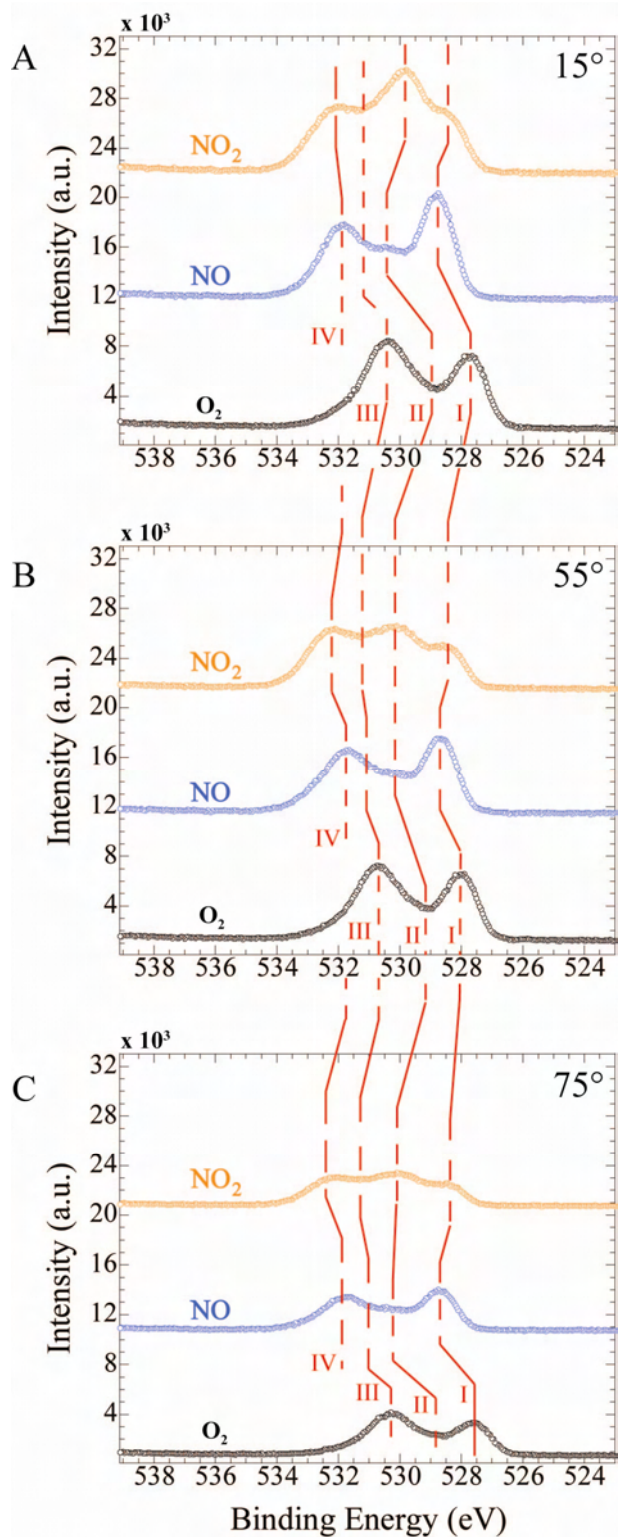


Figure 7-3. O 1s photoelectron spectra at 15, 55, and 75° for O<sub>2</sub>, NO, and NO<sub>2</sub> pretreatments. The surface sensitivity of the spectra is lowest in A), then increases progressively in B) and C).

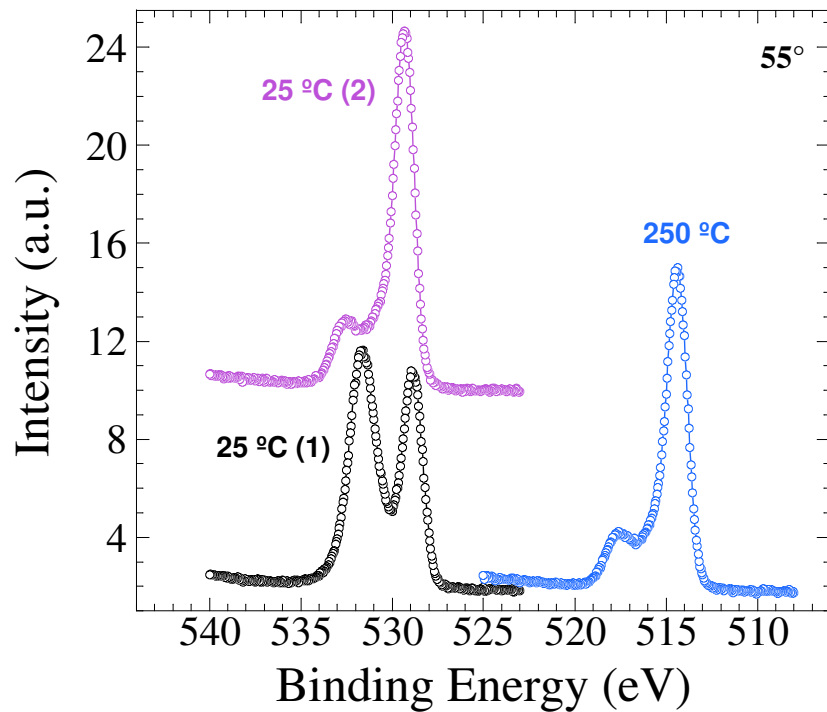


Figure 7-4. Comparison of the O 1s spectrum before, during, and after in-situ heating to 250 °C.

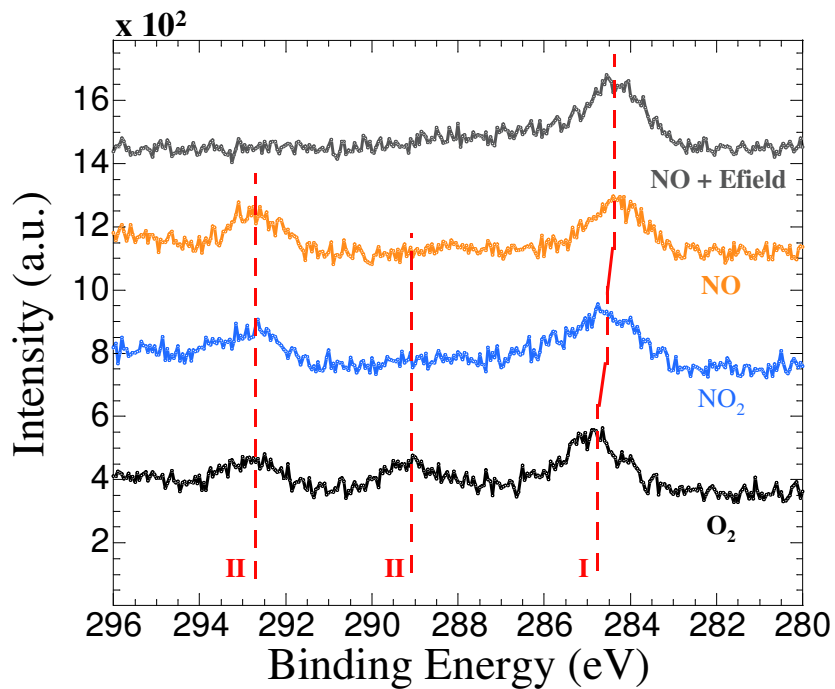


Figure 7-5. Comparison of the C 1s x-ray photoelectron spectra for O<sub>2</sub>, NO<sub>2</sub>, NO, and NO+Efield pretreatments with a takeoff angle of 55°. Three species are discernable from peaks I, II, and III.

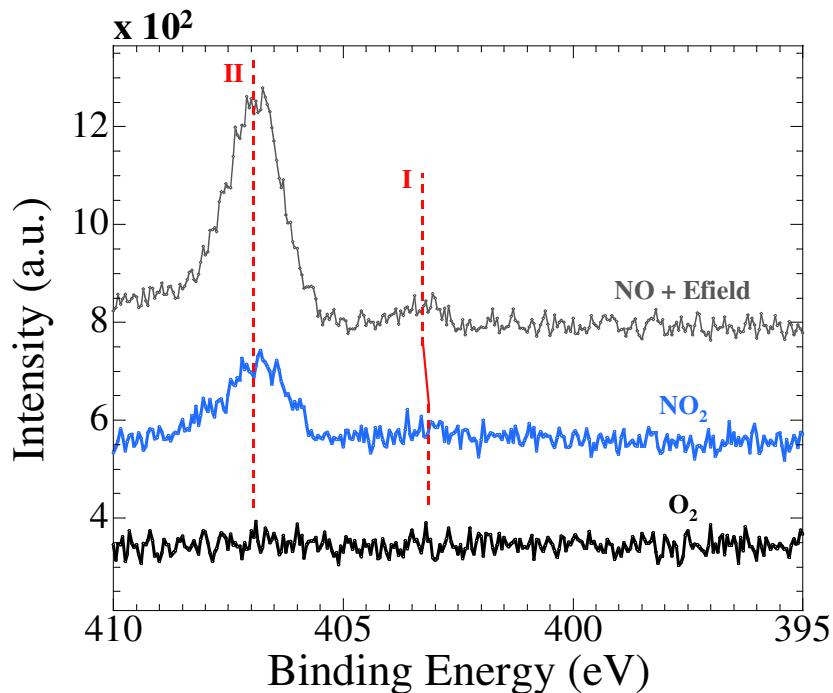


Figure 7-6. Comparison of the N 1s x-ray photoelectron spectra for O<sub>2</sub>, NO<sub>2</sub>, and NO+Efield pretreatments with a takeoff angle of 55°. Peaks designated as I are associated with nitrite complexes (~ 404 eV), while nitrates (II) occur around 407 eV.

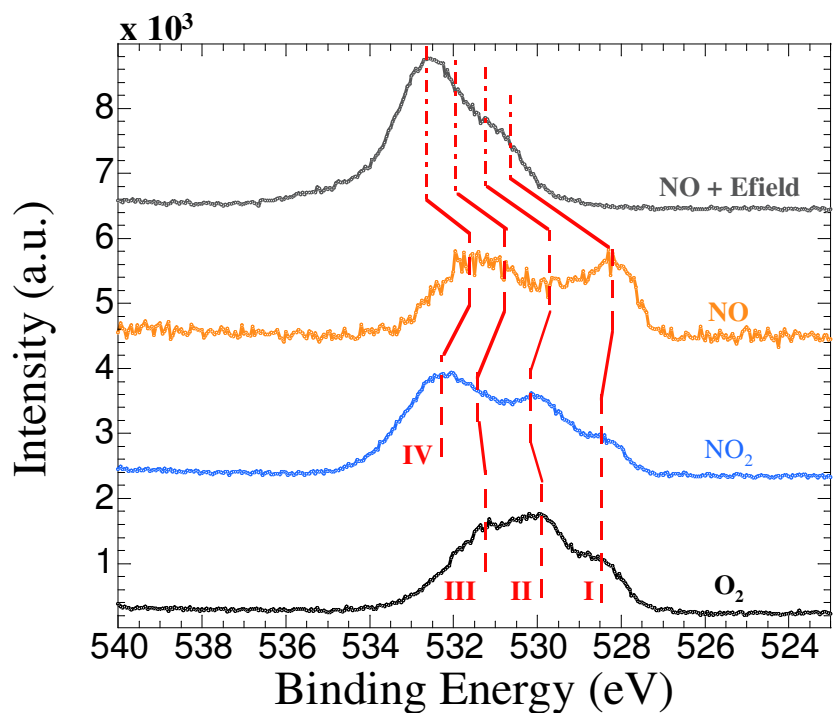


Figure 7-7. Comparison of the O 1s x-ray photoelectron spectra for O<sub>2</sub>, NO<sub>2</sub>, NO, and NO+Efield pretreatments with a takeoff angle of 55°. Four species are discernable as peaks I, II, III and IV.

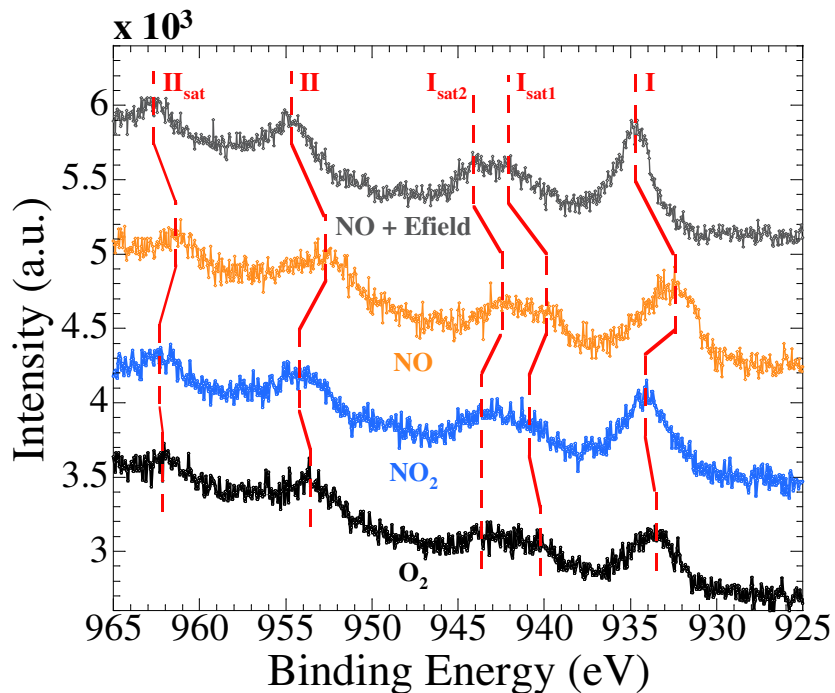


Figure 7-8. Comparison of the Cu 2p x-ray photoelectron spectra for O<sub>2</sub>, NO<sub>2</sub>, NO, and NO+Efield pretreatments with a takeoff angle of 55°. Changes in the Cu 2p<sub>3/2</sub> (I) and 2p<sub>1/2</sub> (II) peaks (with associated satellites) are clearly seen.

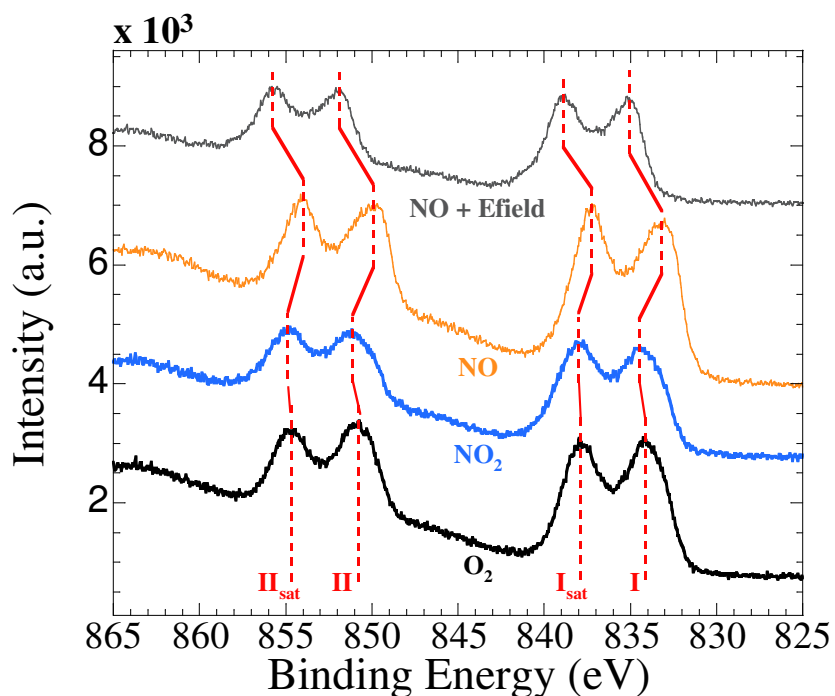


Figure 7-9. Comparison of the La 3d x-ray photoelectron spectra for O<sub>2</sub>, NO<sub>2</sub>, NO, and NO+Efield pretreatments with a takeoff angle of 55°. Changes in the La 3d<sub>5/2</sub> (I) and 3d<sub>3/2</sub> (II) peaks (with associated satellites) are delineated.

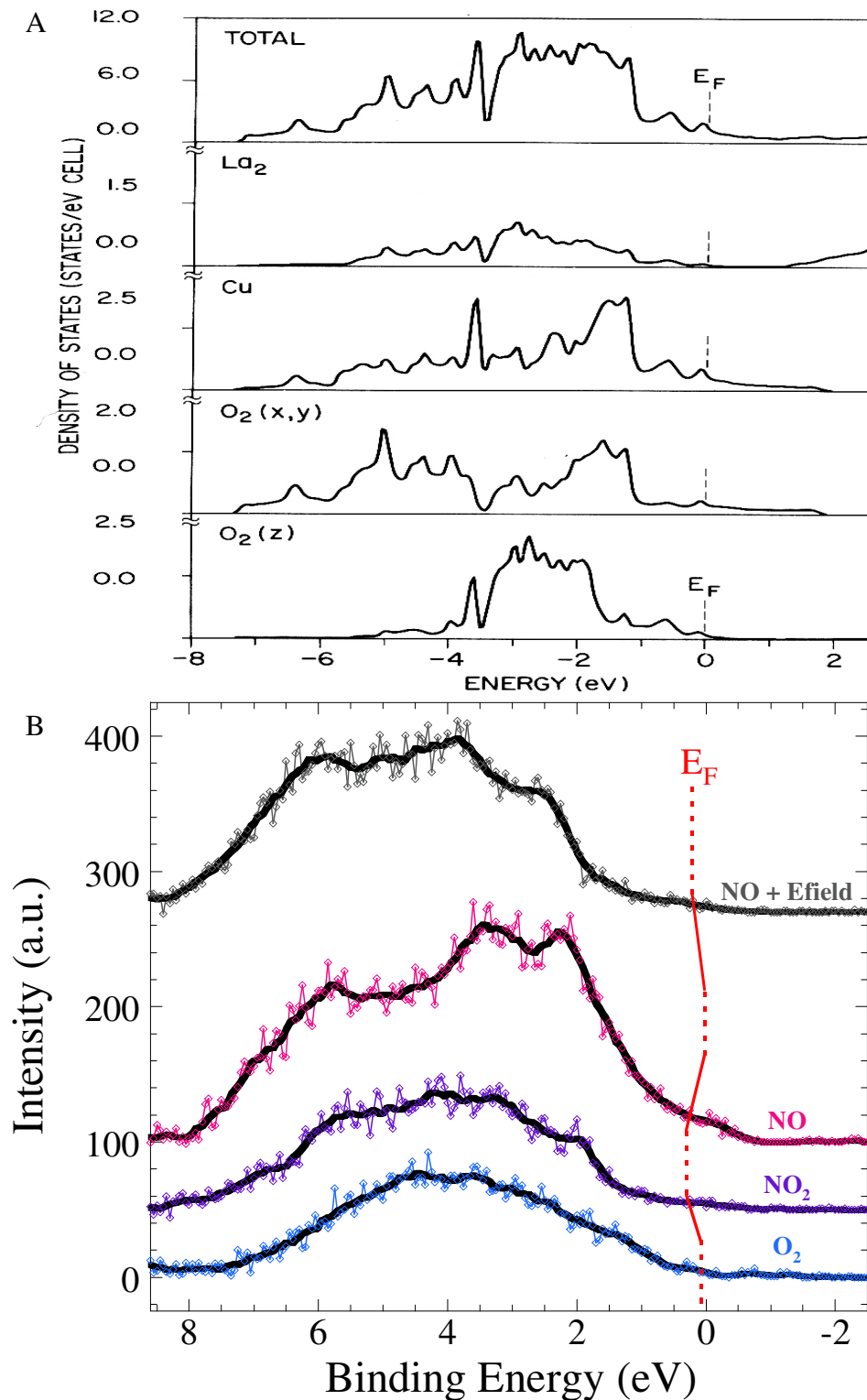


Figure 7-10. Theoretical density of states for  $\text{La}_2\text{CuO}_4$  compared with experimental XPS valence spectra for  $\text{O}_2$ ,  $\text{NO}_2$ , NO, and  $\text{NO} + \text{Efield}$  pretreatments. A) shows the theoretical DOS as calculated by Mattheiss, while B) shows the valence band structure as measured with XPS.<sup>234</sup> The major contributions to the valence structure are the O 2p orbital of the Cu-O bond and the Cu 3d orbitals.

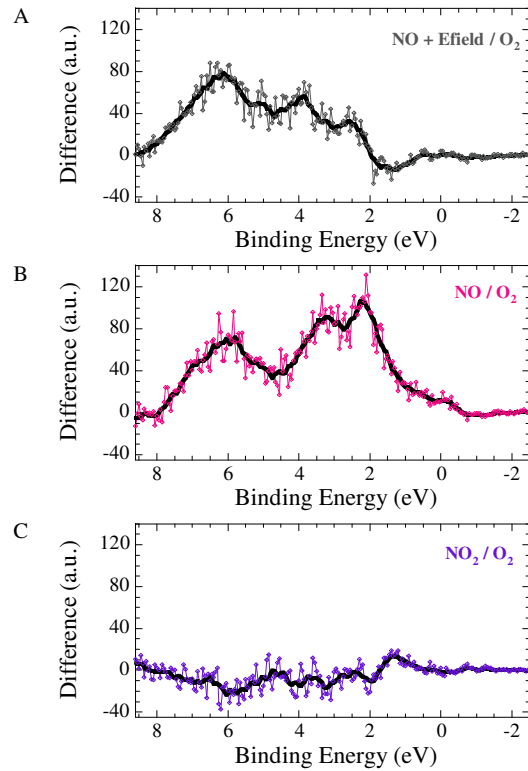


Figure 7-11. Difference spectra of valence structure. The results for for NO+Efield, NO, and NO<sub>2</sub> versus O<sub>2</sub> can be found in A), B), and C), respectively.

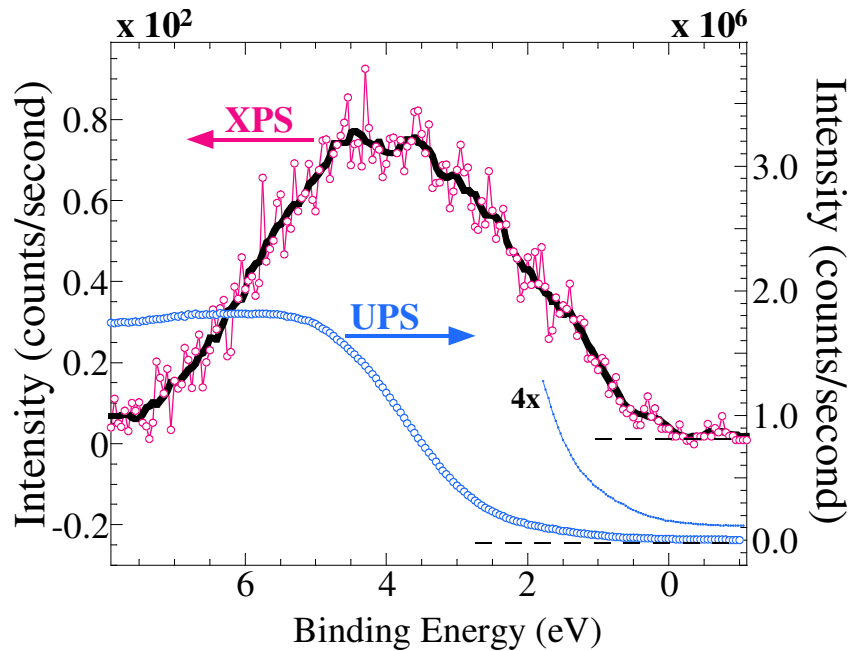


Figure 7-12. Comparison of the XPS and UPS valence spectra for the O<sub>2</sub> pretreatment. The curves are similar near the Fermi level; however, at higher energies the difference is likely a result of surface contamination which has a greater impact in UPS.

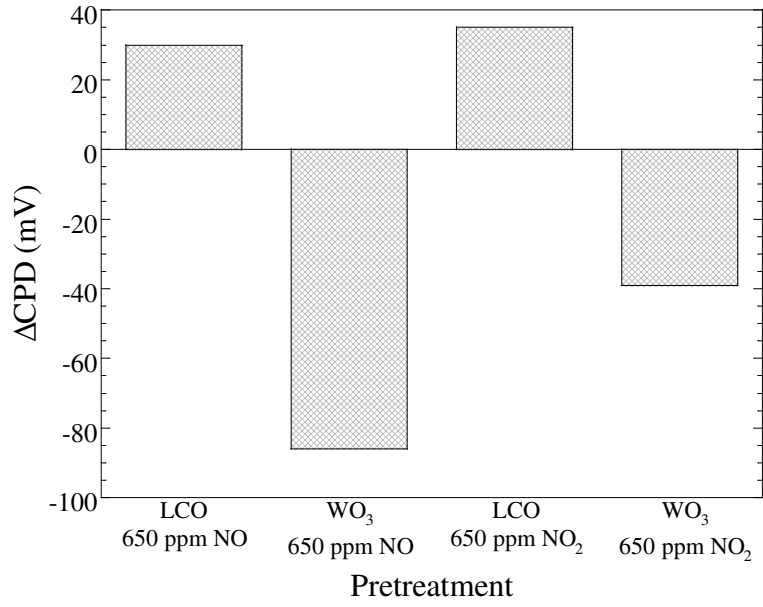


Figure 7-13. Comparison of the change in contact potential difference (i.e., work function) of  $\text{La}_2\text{CuO}_4$  and  $\text{WO}_3$  to NO and  $\text{NO}_2$  pretreatments.

Table 7-1. Ex-situ pretreatments for surface science study

Pretreatment	Adsorption gas conditions	Field-electrode bias (V)
1	21% O <sub>2</sub> (N <sub>2</sub> balance)	0
2	650 ppm NO <sub>2</sub> (21% O <sub>2</sub> , N <sub>2</sub> balance)	0
3	650 ppm NO (21% O <sub>2</sub> , N <sub>2</sub> balance)	0
4	650 ppm NO (21% O <sub>2</sub> , N <sub>2</sub> balance)	8

Table 7-2. XPS peak positions for N 1s family

Pretreatment	Peak I (eV)	Peak II (eV)
1	n/a	n/a
2	403.4	406.6
4	403.6	406.6

Table 7-3. XPS peak positions for O 1s family

Pretreatment	Peak I (eV)	Peak II (eV)	Peak III	Peak IV (eV)
1	528.5	529.9	531.3	n/a
2	528.5	530.4	531.5	532.3
3	528.2	529.7	530.7	531.6
4	530.6	531.4	532.0	532.6

Table 7-4. XPS peak positions for Cu 2p family

Pretreatment	Peak I (eV)	Peak I <sub>sat</sub> (eV)	Peak I <sub>sat2</sub> (eV)	Peak II (eV)	Peak II <sub>sat</sub> (eV)
1	933.7	940.2	944.8	953.2	962.5
2	934.0	940.8	944.8	954.0	962.5
3	932.2	940.2	942.5	952.8	961.5
4	934.9	942.0	944.1	954.8	963.0

Table 7-5. XPS peak positions for La 3d family

Pretreatment	Peak I (eV)	Peak I <sub>sat</sub> (eV)	Peak II (eV)	Peak II <sub>sat</sub> (eV)
1	834.2	837.9	850.8	854.7
2	834.8	838.0	855.0	851.2
3	833.5	837.3	854.0	850.0
4	835.0	838.9	851.9	855.6

## CHAPTER 8 TOWARDS THE COMMERCIALIZATION OF MINIATURE SOLID-STATE POTENTIOMETRIC GAS SENSORS

### 8.1 Introduction

Gas sensors are devices that can be used to improve a manufacturing process, ensure the safety and health of humans and the environment, or to guarantee national security.

Development of gas sensors has been an ongoing process for over 100 years, yet only a few technologies have been commercially successful on a large scale.

Currently available methods for detecting multiple gases in complex mixtures are expensive, bulky, non-selective, or ill-suited for many applications.<sup>1</sup> However, a new type of electrochemical, potentiometric (voltage output) sensor offers a low-cost, robust alternative with significantly improved selectivity, stability, and more. This opens the possibility for gas sensors to be used in many significant applications (e.g., improved energy efficiency, reduced pollutant emissions, process control, and noninvasive disease diagnostics/monitoring) for industries including energy production; transportation, heavy and materials handling equipment; materials and chemical processing; and medicine.

A new type of (electrochemical) potentiometric gas sensor shows much promise for being used in many of these areas. While much progress has been made, concurrent efforts are needed in terms of scale-up for commercialization and fundamental research to improve the devices. In general, gas sensor research often involves the use of samples made by hand or with some manual process, which introduces variability that makes comparison between results extremely difficult. This includes past studies involving potentiometric gas sensor arrays and thermal/electric-field enhancements; but since these studies involved the comparison of active changes to a particular device, there was no need to compare multiple samples. However, in order to improve future R&D and commercialization efforts, the objective of this work was to

develop procedures for automated manufacturing and testing. This included sensor design and processing studies involving standardized powder/slurry/ink preparation, automated screen-printing, rapid-prototyping, wire bonding, multi-sensor test setups, and analyses programs.

## **8.2 Background**

Many researchers talk about limits to miniaturization of gas sensors. This has to do with manufacturing issues, noise issues, and proximity issues (i.e., cross-talk). There are also issues with manufacturability of novel sensing materials, which may not be compatible with such miniaturization techniques as microelectronic lithographic processing. Furthermore, many solid-state gas sensors have not been readily commercialized for the selective detection and quantification of gases due to limits in the materials or device physics.

## **8.3 Experimental**

The focus of this work was to expand upon the fabrication techniques being used in lab-based sensor research and development in order to scale-up for future commercialization. This involved selection of the best automated industrial manufacturing equipment, setup/modification of the equipment, and development of the processes needed to make sensors using batch fabrication with the equipment. This effort also involved the development of batch testing setups, procedures, and software.

Planar solid-state potentiometric gas sensors were fabricated using conventional thick film ceramic technology in a manner similar to that portrayed in Figure 8-1. For example, alumina substrates were made with tape casting using a commercial water-based binder system. This is a very low cost and scalable process. The slips were cast on a tape caster and laminated to various thicknesses using a lamination press under controlled temperature and pressure. Large square sheets with scored sections cut into the laminated tapes allowed separation of individual devices after fabrication, and permitted multiple devices to be processed simultaneously in order to

reduce variability between sensors. YSZ electrolyte films were deposited onto the surface of the alumina supports using spin coating, with a final high temperature co-firing step bonding the two. The YSZ film was coated with electrode compositions by screen printing using an industrial machine with automatic alignment, squeegee pressure-feedback, and other features that ensure repeatable and accurate depositions. Substrates were coated with both single and multiple compositions (i.e., multi-functional sensors). Furthermore, heating and temperature sensor structures were also incorporated into the sensors as shown in Figure 8-2.

### **8.3.1 Fabrication of Rigid Substrate and Electrolyte Layer**

Depending on the application, this gas sensor technology may be deployed under normal ambient conditions (e.g., environmental monitoring) or in (thermally and/or chemically) harsh environments that require robust materials and designs to prevent device failure. In order to have a robust sensor capable of sustaining large thermal gradients and other stress-inducing phenomena (e.g., mechanical vibrations), the sensor design must include a strong substrate support (e.g., Al<sub>2</sub>O<sub>3</sub> or 3 mol% YSZ). The designs must also consider the heat transfer through the device, utilizing such features as membrane heaters or particular regions separated by low-thermal conductivity materials. As a start, this work utilized alumina supports coated with YSZ electrolyte films. The processing and fabrication procedures are outlined below.

#### **8.3.1.1 Water-based tape casting**

Tape casting is a processing technique for making thin ceramic layers (e.g., 0.1 to 0.5 mm), which can be used to make substrates or other parts through shaping and laminating processes.<sup>236</sup> In tape casting, a ceramic slurry (i.e., a mixture of binder(s), dispersants, ceramic powder, etc.) is poured into a reservoir above a moving carrier material (e.g., Mylar film). A “doctor blade” sits at the front of the reservoir slightly above the surface of the carrier. The gap and movement of the carrier work to cast the slurry from the reservoir into long, thin sheets (e.g., 9 x 9 inches and

100 microns thick) of greentape. The carrier moves into a heated region of the tape caster, where the solvents are evaporated, thus producing a flexible and machinable material that can be rolled up and stored until needed. Any organics from the slurry are burned out at intermediate temperatures ( $> 400\text{ }^{\circ}\text{C}$ ), while high-temperature ( $> 1000\text{ }^{\circ}\text{C}$ ) sintering consolidates the ceramic into a solid piece.

While traditional tape casting generally involves organic solvents (e.g., ethyl alcohol or toluene), a more environmentally friendly and cheaper option involves the use of an advanced, commercial water-based acrylic binder system. This system has several advantages when compared to organic solvent-based or other water-based (e.g. latex or polyvinyl alcohol) tape casting slurries including: superior processing control (resistant to changes in humidity; viscosity controlled by water concentration without changing final tape composition; can be milled without slurry destabilization; simple de-airing process; more uniform greentape (little to no binder or ceramic segregation); higher ceramic loadings and tape densities possible; easily laminated; non-flammable; low toxicity; and easily recycled.<sup>236,237</sup>

The alumina tape-casting slurry was prepared in a two-stage process using a water-based system (Polymer Innovations, Inc). In the first stage, alumina powder (grade A16SG, Alcoa) was mixed with a water-based binder solution (WB4101; contains binder for base starting strength and plasticizer for flexibility), defoaming agent (DF002; to further deter air bubble formation), and deionized water. The slurry was ball-milled (zirconia milling media) for more than 24 hours to ensure an even distribution of ceramic particles throughout the suspension and to breakup soft agglomerates.

Prior to casting, the milling media was removed and the slurry was mixed and defoamed using a mixer (Thinky, ARE-250); the former step involved the use of planetary centrifugal

forces, while the latter utilized only centrifugal forces. This process further homogenized the slurry composition and prevented air bubbles from introducing defects in the final ceramic.

The slurry was then poured into the tape caster reservoir, where the material was deposited into a thin film (~100-150  $\mu\text{m}$ ) as it was pulled onto the moving carrier at the gap set with the doctor blade. After a few hours the dried tape was removed from the tape caster. The greentape was subsequently shaped, laminated, trimmed, and scored before undergoing several heat treatments and the deposition of an electrolyte film.

### **8.3.1.2 Tape shaping, lamination, trimming, and scoring**

One of the benefits of using tape cast ceramics for the manufacture of solid-state devices is the ability to vary the geometry of the material with relative ease. Furthermore, the technique allows the simultaneous manufacture of large numbers of devices from a single piece of tape cast material with the use of prescoring. After final sintering, the scored sections of the substrate can be separated with the application of a small amount of pressure.

Tape cast alumina was made into square or rectangular shapes using a custom, programmable 3-axis cutting machine (Velmex positioning system). The shaped tapes were then separated from their Mylar backing, stacked, and placed into a custom rig for lamination. The rig consisted of two polished, (3 inch by 3 inch) flat steel plates placed on either side of the stacked tapes with a Mylar buffer between the stack and steel. Two silicone sheets were then placed on either side of the steel plates, and the entire assembly was placed into a heated uniaxial press (Carver) as shown in Figure 8-3 and compressed at 5000 psi (80 °C) for 5 minutes. This rig was utilized to ensure uniform pressure distribution during lamination, which is necessary to prevent delamination of the tapes during subsequent handling and processing steps (Figure 8-4).

Following lamination, the alumina was trimmed and scored before further processing; these steps were also automated with the use of the custom cutting machine (Figure 8-5A). The

3 inch by 3 inch sheets of (4 to 8 layer) laminated tape were scored (taking in to consideration shrinkage of ~15% in the length and width during sintering) such that the final individual devices measured approximately 40 mm (long) by 4 mm (wide) by 0.4 mm (thick). Pressure was uniformly distributed along the scored-edges (e.g., using the straight edge of a ruler) in order to separate individual devices. This process can be automated using, for instance, the edge of the blade on custom cutting machine to apply the pressure needed to initiate fracture along the score mark.

Fiducial marks (e.g., small holes in the upper left and lower right corners) were also made in the alumina sheet. This was achieved either manually using a sharp pin and a template, or with the Velmex cutting machine where the blade had been replaced with a punch. Trimming and fiducial mark/via creation can also be done using advanced laser systems.

### **8.3.1.3 Deposition of YSZ electrolyte layer**

There are several methods for depositing an electrolyte layer. These include dip coating, spray coating, spin coating, chemical vapor deposition (CVD), and magnetron sputtering.<sup>198,205,238</sup> Initial attempts to deposit the YSZ electrolyte using spray coating were abandoned due to inhomogeneity in the film and inherent lack of repeatability due to the deposition setup. Subsequent efforts using spin coating resulted in more uniform and dense films. Therefore, this technique was further pursued as a means of electrolyte deposition in order to keep manufacturing costs low and for ease of manufacture.

A colloidal mixture consisting of 8 mol% YSZ (Tosoh), ethanol, polyvinyl buytral (PVB), and dispersant (Solsperse) was ball milled for 24 hours. Previously laminated, shaped, trimmed, and (porous) presintered (4-layer, 2 cm x 2 cm) alumina substrates were arranged (one at a time) on a custom vacuum chuck attached to the spin coater (Chemat Technologies). At the onset of the spin cycle, a digital pipette was used to deliver a specific amount of the YSZ colloidal

mixture to the top surface of the alumina. At the completion of the spin cycle, the YSZ colloidal mixture had dispersed evenly over the alumina surface.

In order to control the thickness of the YSZ film, several trials were conducted with varying number of YSZ solution applications (i.e., cycles), spin-coat speed, and spin-coat time. To prevent the slurry from seeping into the alumina pores when the vacuum was turned on, the substrate surface was first covered with ethanol. Following the spin coat deposition, the YSZ solution was allowed to dry before transferring the alumina/YSZ samples to a high temperature furnace for final sintering.

Upon initial analysis of the YSZ microstructure with SEM, a large number of surface cracks were observed. The cracks were believed to be a result of differences in shrinkage rate between the rigid substrate and electrolyte film; therefore, subsequent efforts were aimed at minimizing the surface cracks. Because the inherent shrinkage rates of the alumina and YSZ could not be known *a priori*, experiments were conducted using different presinter (alumina) and final sinter (alumina/YSZ) heat treatment conditions. Specifically, the maximum presinter temperature of the alumina and the high temperature sinter ramp rate for the alumina/YSZ were varied. The variation of these parameters modified the relative rate of grain growth in the alumina and YSZ, which is the primary cause for shrinkage during high temperature sintering.<sup>205</sup>

SEM images of these samples were collected in both secondary electron and backscatter modes using a field-emission SEM (JEOL, JSM-6335F). The micrographs were subsequently analyzed using image-processing software (ImageJ).

### **8.3.2 Multilayer Deposition with Screen Printing**

As mentioned in the introduction, until recently the fabrication of these sensors has been a manual process. This has led to inconsistencies in research between different groups and difficulty in interpretation of various data sets. Furthermore, this highlights the importance of

utilizing automated fabrication methods in fundamental research before these gas sensors can be successfully commercialized. One process step which is believed to have been the cause for a large degree of variability in results from different sensors is that of screen printing.

Previous sensor results have utilized manual screen printing.<sup>147,165</sup> There are several process parameters for this technique that are important to the quality of the final deposition. These include machine parameters such as the print pressure, print speed, print gap (i.e., the distance between the screen and substrate), and the screen separation (i.e., speed with which the section of the screen in contact with the substrate is released). Furthermore, in manual screen printing the angle of the squeegee with respect to screen cannot be consistently maintained for each user or each application of deposited material.

In an effort to ensure identical and reliable performance between sensors, batch fabrication of the devices was made possible with a fully automatic screen-printer (Horizon 03i/DEK Int'l.). This industrial machine aligns fiducial marks on the screen and substrate with the use of two high-contrast cameras to ensure accurate and repeatable deposition for multilayer devices. All processing variables (e.g., squeegee speed and pressure) are monitored and dynamically adjusted to ensure identical fabrication from batch to batch. Furthermore, the DEK keeps the squeegee at a constant 45° throughout the print stroke.

The advanced vision system is one of the key features of this automated screen-printer that is absolutely critical for commercialization and any future R&D efforts. The alignment of the screen pattern to the substrate becomes increasingly significant when, for example, a sensor design incorporates several layers (e.g., heaters, signal leads, contact pads, and sensing electrodes) or materials. This is also critical for general research purposes, which in the past

have tried to look at the influence of sensing electrode thickness by way of multiple depositions of a material on top of each other.<sup>165</sup>

The final commercialized sensors will comprise multiple features, including integrated heating elements, temperature sensors, signal leads, contact pads, vias, and sensing electrodes. In this first attempt towards commercialization, the screen designs were created in such a way as to allow a certain degree of flexibility in the final arrangement of these features. Namely, through the use of multiple screen fiducials and programming of the DEK, the patterns were able to be shifted horizontally and vertically (with respect to a single set of substrate fiducial marks) as illustrated in Figure 8-6. The patterns for the screens used in the batch fabrication of the prototype sensors are shown in Figure 8-7.  $\text{La}_2\text{CuO}_4$ , a p-type sensing electrode sensitive to  $\text{NO}_x$ , powder was mixed with a commercial binder vehicle (ESL) using the Thinky planetary centrifugal mixer.

### **8.3.3 Wire Bonding for Packaging & Reliability Testing/Calibration**

There are several issues with packaging of gas sensors which can operate at high temperatures (e.g., 200-800 °C) and in chemically harsh environments. Typical automotive gas sensors, such as oxygen (“Lambda probe”) sensors utilize thick wires brazed to the surface of sensor or attached using parallel gap welding.<sup>239</sup> As a fairly well commercialized technology, this method of wire attachment is well suited for sensors with only a few electrical leads (e.g., single sensing electrode, air-reference, and heater). However, the situation becomes increasingly complex as the number of electrical contacts increases. In this work, the preliminary sensor prototype designs have 12 electrical connections made in an area no larger than currently available tubular and planar oxygen (automotive) sensors. Due to the high wire density and automated manufacturing requirements needed to make these devices competitive, the electrical connections were made using thermosonic (thermal/ultrasonic) wire bonding.<sup>240</sup>

In many cases, these gas sensors will be used in (thermally and chemically) harsh environments, and the wrong choice of materials can result in premature device failure. Due to the corrosive nature of the testing environments for these gas sensors, only platinum and gold wire bonds and contact pads were utilized. Though little evidence is available in the literature, some researchers have shown that using gold wire bonds to platinum pads is a good way to achieve corrosion-resistant contacts up to  $\sim 600$  °C. Beyond this temperature, interdiffusion between the gold and platinum seems to weaken the bond.<sup>241</sup> While 600 °C is near the upper end of the testing temperatures for the gas sensors being developed in this work, wire bonding was attempted using Au bonding wire to both Au and Pt pads, and Pt bonding wire to both Au and Pt pads.

This work utilized a three-way convertible wire bonder (West Bond) which is capable of making ball, wedge, and deep-access bonds of common (e.g., gold) and uncommon (e.g., platinum) wire-bonding materials. The machine is capable of fully-automatic, semi-automatic, and manual operation, which allows the programming of bond loops and parameters for reliable and repeatable wire bonds. The platinum and gold bonding wire (hard temper (99.99% pure); 0.001 mil (25  $\mu\text{m}$ )) were obtained from California Fine Wire. While (45°) wedge and (90°) deep access bonds were explored, the best results were with ball-wedge bonds. The ball bond capillary was a modified tool for standard gold wires (Gaiser Tool Company) which was better at making bonds with hard materials such as platinum. Substrate and tool heating during bonding also improved Pt wire bonding.

Typical wire bonding parameters include the power (Watts, or Joules/second), bonding time, bonding force, tool temperature, and sample temperature. Any combination of these parameters represents a different way of transmitting the thermal energy, downward force, or

vibrational energy to the bond formation. Gold and platinum bonding pads were screen printed onto alumina substrates using Au paste (Englehard) and Pt paste (Haeracus). The range of bonding parameters used in this work included: ultrasonic power – 0.75-1.00 W; ultrasonic time – 35-50 ms; low bonding force (ball bond) – 35-50 g; high bonding force (wedge bond) – 60-80 g; Negative Electronic Flame Off (NEFO) current and time – 17-19 mA/3.5-4.5 ms; work holder temperature – 25-200 °C. Note that the NEFO is a parameter that determines the size of the ball bond. Also note that the loop motion was optimized to obtain ideal loop shape.

#### **8.3.4 Multisensor Setup**

Past R&D efforts have allowed testing of only a few simple devices (i.e., 1 to 2 sensors or arrays with a maximum of 11 connections at any one time). However, in order to successfully commercialize this technology dozens (e.g., 50-100) of identical devices will need to be tested simultaneously under the same conditions. Therefore, a multisensor (reliability test/calibration) setup was designed and investigated with simple computational fluid dynamics resulting in the design shown in Figure 8-8. These setups consist of stacked levels, each holding several devices which are wire bonded to wire-guides (T-shapes) that carry electrical signals from the arrays to a multichannel multimeter for recording. These wire-guides also carry applied biases (e.g., for heaters) to the devices. The setups are sealed in ceramic tubes and placed in tube furnaces for ambient temperature control. The tube inlet is attached to a gas manifold (mass flow controllers; MKS) while the outlet is vented and can be sampled using gas analysis (mass spectrometer). Each reactor can test up to 30 sensors (i.e., 6 sensors to a module; 5 modules to a reactor) and four identical reactor setups are in the process of being made and installed.

An Extrel MAX300-LG, quadrupole mass spectrometer with heated transfer line and (16 port) inlet provides the capabilities for monitoring gas effluent for calibration purposes. The gas stream is sampled from the exhaust effluent of the reactor. This gas stream can be fairly

complex (e.g., mixture of N<sub>2</sub> (m/z 28) 70 – 100 %; CO<sub>2</sub> (44) 0 – 30 %; NO (30) 0 – 2000 ppm; CO (12) 0 – 2000 ppm; O<sub>2</sub> (32) 3 – 20 %; CH<sub>4</sub> (15) 0 – 2000 ppm; NO<sub>2</sub> (46) 0 – 2000 ppm; H<sub>2</sub>O (18) 1%; NH<sub>3</sub> (17) 0 – 2000 ppm; N<sub>2</sub>O (44) 0 – 2000 ppm) and the mass spectrometer automatically calculates the gas concentration using a background gas (i.e., N<sub>2</sub>) calibration, sensitivity factor calibration for each gas, and a fragment matrix. There are ten calibration bottles permanently hooked up to the multi-port inlet of the mass spectrometer, allowing periodic (automated) re-calibration to ensure that the gas concentration measurements are accurate.

A Keithley Series 3700 Switch-Multimeter system can measure well over 400 channels with the possibility to expand indefinitely. Simultaneous testing of large numbers of sensors will allow the technology to eventually be proven in environments that simulate real combustion exhausts and other test environments. All experimental parameters were computer controlled with a custom LabVIEW program. The testing procedures have explained elsewhere.<sup>151,199,202</sup>

The (commercial) prototype sensor arrays described above have been tested using the previously utilized R&D reactor setups as a preliminary evaluation of their performance. These and other results will be discussed in the following section.

## **8.4 Results and Discussion**

### **8.4.1 Sensor Array Fabrication**

#### **8.4.1.1 Al<sub>2</sub>O<sub>3</sub>/YSZ**

As mentioned above, the final trimming step prior to presintering/final sintering was extremely important as the SEM images in Figure 8-4 illustrate; the edge of a non-trimmed four-layer laminated piece of sintered tape is compared to a trimmed substrate. The non-trimmed substrates tended to delaminate or crack during handling or subsequent screen printing. This was likely due to built-in stress from nonuniform shrinkage during sintering. Table 8-1 provides

information regarding changes in total laminate thickness with respect to the number of compression-cycles (i.e., 5 minutes at 5000 psi/80 °C) using the uniaxial press.

In terms of the effect of the spin coating parameters on the film thickness, as was expected a greater number of coating cycles resulted in a thicker film. The SEM images (both secondary emission/topographical and backscatter/compositional modes) in Figure 8-9A illustrate a representative YSZ film on the Al<sub>2</sub>O<sub>3</sub> support. The YSZ film thickness ranged from 1.5 to 3.7 μm. Furthermore, the use of a higher rotational speed and/or longer spin coating times produced a thinner film. Information regarding the YSZ film thickness dependence on spin coating parameters can be found in Table 8-2. The last two entries resulted in approximately the same number of revolutions; however, the film thickness of the sample that spun faster was almost twice as thick. These samples had two coatings and the interaction between the coats may have had something to do with this result. At higher speeds, the viscous flow behavior of the spin-coat slurry has greater control of the final film thickness than any of these parameters.

From the very beginning, the potentially major issue with the YSZ films was the presence of surface cracks as shown in Figure 8-9B. There were two concerns with the surface cracking in the YSZ. First, the cracks likely reduce the mechanical strength of the electrolyte. As they are employed at high temperatures and may experience possibly large thermal gradients (especially that which will be experienced under conditions of localized heating from integrated heaters), the structural integrity of the sensors is vital to their long term performance. Secondly, these cracks also may serve to increase the ionic resistance of the YSZ, acting as a kinetic barrier to the mobility of oxygen ions in the film. This would likely affect the response time of the sensors as discussed below.

Prior to heat treatment optimization, the cracks were larger than ~150 nm. However, the improved matching of shrinkage rates between the YSZ film and presintered Al<sub>2</sub>O<sub>3</sub> support resulted in a reduction of these cracks to below ~40 nm. An example of the improved YSZ film surface is shown in Figure 8-10. The SEM images were analyzed using the ImageJ software as shown in the inset.

Not only did the optimized conditions decrease the size of the cracks, but the number of observable cracks over the entire surface was also reduced. The YSZ film crack dependence on heat treatment can be found in Table 8-3. A number of factors determine the shrinkage rates of the support and film and thus the degree to which the YSZ surface will crack. During the presinter step of the Al<sub>2</sub>O<sub>3</sub>, the polymers were burned out and the particles began to coalesce, resulting in some densification (i.e., shrinkage). In altering the maximum temperature of this presinter step, the degree of shrinking was changed. As the growth of the YSZ particles and Al<sub>2</sub>O<sub>3</sub> grains during final sintering is strongly time dependent, the use of different furnace ramp rates changed their respective rates of grain growth. The thermal expansion of YSZ and Al<sub>2</sub>O<sub>3</sub> are similar; therefore, the closer the relative rates of grain growth between the two materials, the less stress build-up there will be in the YSZ film (i.e., fewer surface cracks).

Beyond the issue with the YSZ film, there was significant progress made in terms of pre-scoring and separating individual device-sized (e.g., 40 mm by 4 mm by 0.4 mm) pieces of alumina from larger, sintered sheets. Figure 8-5B illustrates the scored alumina before and after the individual sensor substrates were broken apart with minimal effort required. Note that before separation, the score marks were difficult to see; therefore, the main image was taken with the sample on top of a glass sheet illuminated from below.

### 8.4.1.2 Automated screen printing

Initial attempts to screen print electrode patterns (e.g., Figure 8-11A) onto sintered, laminated substrates resulted in cracking and delamination. As mentioned above, this was due to uneven pressure distribution during lamination, which created weak points in the substrates. Once this was solved, the higher quality substrates provided a good surface for screen printing. As shown in Figure 8-11A, the presence of fiducial marks (e.g., holes) on the substrate provide markers with which the automated screen printer aligns the screen before depositing the material. Here, the screen pattern in Figure 8-7A has been used to transfer  $\text{La}_2\text{CuO}_4$  to a greentape. Screen printing on greentape will likely only be used to embed such features as heating elements and temperature sensors into the device with subsequent lamination of another piece of greentape. Figure 8-11B shows the results from utilizing the extra screen fiducials to shift the screen pattern (as in Figure 8-6). The electrode pattern was also transferred to a sintered, laminated substrate as shown in Figure 8-11C).

### 8.4.2 Wire Bonding

The use of wire bonding as a means of attaching electrical connections to these sensors is critical, as the devices can have more than 12 leads in a small area (Figure 8-12A). The Au bonding wire was significantly easier to bond than the Pt bonding wire because of the relative hardness between the two materials (i.e., Vickers hardness – Au: 20-60  $\text{kgf/mm}^2$ ; Pt: 40-100  $\text{kgf/mm}^2$ ).<sup>240,242</sup> Similarly, both types of bonding wire were easier to bond to Au pads than Pt pads. However, the Pt pads were significantly easier to bond to when the substrate was heated to between 150 and 200 °C during bonding. Figures 8-12B through 8-12C show an optical image, 3D model, and height profile of the final wedge-bond of a Pt ball-wedge bond to a gold pad obtained with an optical profilometer (Keyence). These images represent a case where too much force was delivered during the second (wedge) bond. The wire bonding machine has

independent (high and low) force settings for this type of (ball-wedge) bond, and the required settings had to be fine tuned. However, the strength of the bond seemed to be sufficient as repeated pulling of the bond loop with a hook did not result in any damage.

### 8.4.3 Sensor Testing

The sensor prototypes for this preliminary commercialization work were tested in an R&D type reactor. In the data presented in Figures 8-13 through 8-17, an  $\text{Al}_2\text{O}_3/\text{YSZ}$  based device and a laminated YSZ based sensor were tested simultaneously in the same reactor. While the multisensor reactor described above was not utilized in these tests, the ability of the mass spectrometer to analyze simulated gas streams was verified and will be more than sufficient (i.e., with respect to speed and resolution) for future work.

The primary difference between the  $\text{Al}_2\text{O}_3\text{-YSZ}$  sensor and the YSZ sensor was their magnitude and speed of response. While the  $\text{Al}_2\text{O}_3\text{-YSZ}$  sensor exhibited a far greater voltage response to both NO and  $\text{NO}_2$  at lower temperatures (Figures 8-13 through 8-16), the response time to  $\text{NO}_2$  was much slower (Figure 8-14). In particular, the response to  $\text{NO}_2$  was several orders of magnitude greater for the YSZ- $\text{Al}_2\text{O}_3$  sensor (Figure 8-13). However at 575 °C, the magnitude and speed of response to NO for both sensors was comparable (Figure 8-17).

At 475 °C there were several different rates of response before the  $\text{Al}_2\text{O}_3\text{-YSZ}$  signal reached a steady-state value (Figure 8-14). This behavior occurred during the initial  $\text{NO}_2$  exposure and after the gas flow was turned off with these sharp jumps in signal occurring at roughly the same measured potential difference in each case. However, this behavior was not observed for NO exposure which is primarily believed to occur as the result of electrochemical alterations of  $\text{La}_2\text{CuO}_4$  and not the electrochemical reactions at the TPB. There is the possibility that the cracks in the YSZ film caused an increase in electrolyte resistance which thereby altered the  $\text{NO}_2$  response, which is believed to partially depend on the TPB reactions.<sup>65,68,91,243</sup>

## 8.5 Conclusions and Future Work

### 8.5.1 Multisensor Testing in New Reactors

Future work will focus on reliability and accuracy testing of the batch-fabricated gas sensor arrays in the new multisensory reactors. We will also use the on-line gas monitoring to calibrate the devices. After verifying the repeatability of the devices, complete packaging will be designed and implemented depending on the application; two examples of possible sensor packages are shown in Figure 8-18.

Using the combined gas sensor output and analytical verification from the mass spectrometer, the accuracy of the gas sensors will be able to be determined. The accuracy (in terms of a % of full scale output, FSO, from the sensor) can be quantified as shown in Equation 8-1.

$$\epsilon_a = 100 \times \frac{(X_m - X_{tv})}{X_{FSO}} \quad (8-1)$$

In Equation 8-1,  $X_m$  is the measured value (i.e., from the solid-state gas sensor) and  $X_{tv}$  is the true value (i.e., as determined by the calibrated mass spectrometer).

### 8.5.2 Further Miniaturization and New Designs

Conductor lines, bonding pads, heater elements, etc. will be deposited by screen printing or sputtering, depending on feature size. Pattern delineation for sputtered features will be accomplished with shadow masking and lift-off (photo resist mask) processes. We will also utilize a direct-write machine capable of dispensing a wide range of materials (1 to 1,000,000 cP), including ceramic/metallic inks and pastes.<sup>44</sup> The machine is capable of picoliter volume control and can print fine line widths (below 10 microns) or raster larger patterns from CAD files. Conformal printing and 3D features are also within the reach of this cutting-edge machine.

Examples of the type of rapid prototyping that is possible with this system are shown in Figure 8-19.

### **8.5.3 Expanded Materials Development for New Applications**

In order to expand the gas sensors for use in other applications such as breath analysis or chemical warfare agent detection, the materials will need to be modified or new materials will need to be developed. These materials will be designed with the knowledge gained from the differential electrode equilibria theory and two active enhancement methods discussed elsewhere.<sup>199,203</sup>

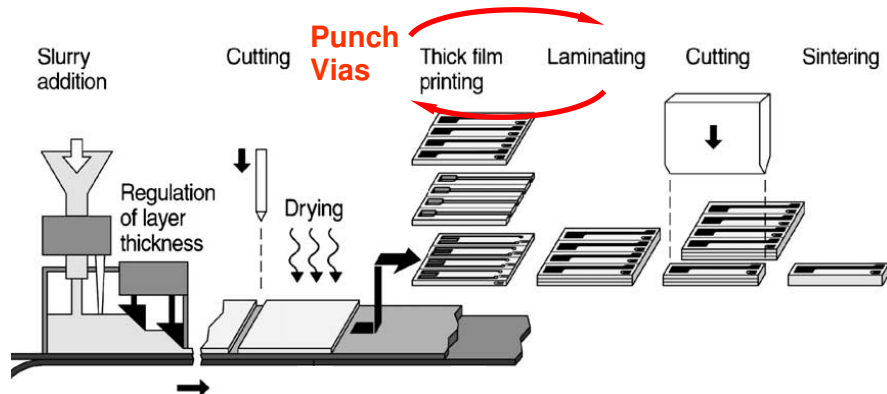


Figure 8-1. Multilayer ceramic processing for manufacture of the gas sensor arrays. This will likely consist of tape-casting; tape trimming and via-punching; laminating; screen-printing; tape scoring; sintering; device separation. Figure modified from Riegel et al.<sup>66</sup>

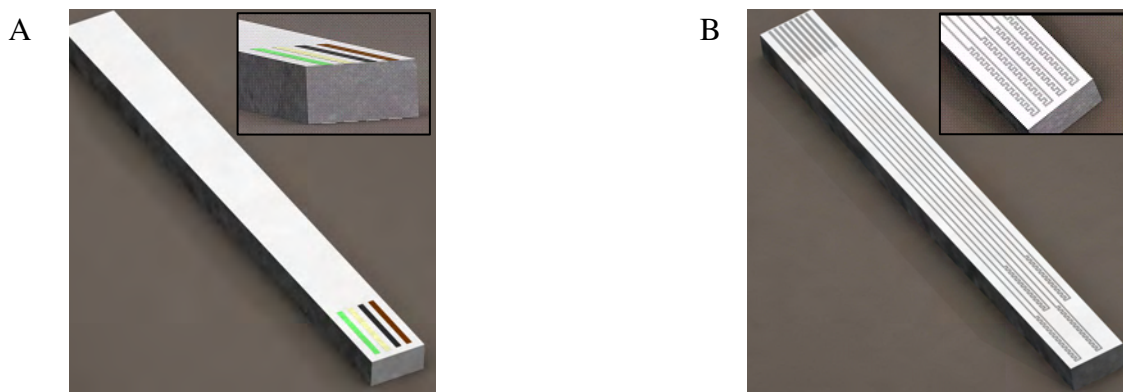


Figure 8-2. A possible configuration for the small potentiometric gas sensor array ( $<1\text{cm}^2$ ). In A) sensing electrodes are shown on the top surface of the sensor (YSZ film not shown). Temperature-control structures are shown on the device bottom in B).

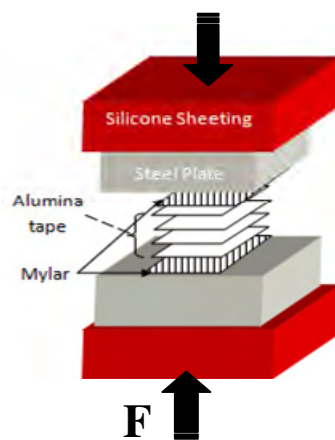


Figure 8-3. Illustration of the laminating process. In the laminating process several layers of greentape are aligned and stacked between two sheets of Mylar; these are then placed between two smooth steel plates. This assembly is loaded between two silicone sheets in a heated laminating uniaxial-press and force (F) is applied.

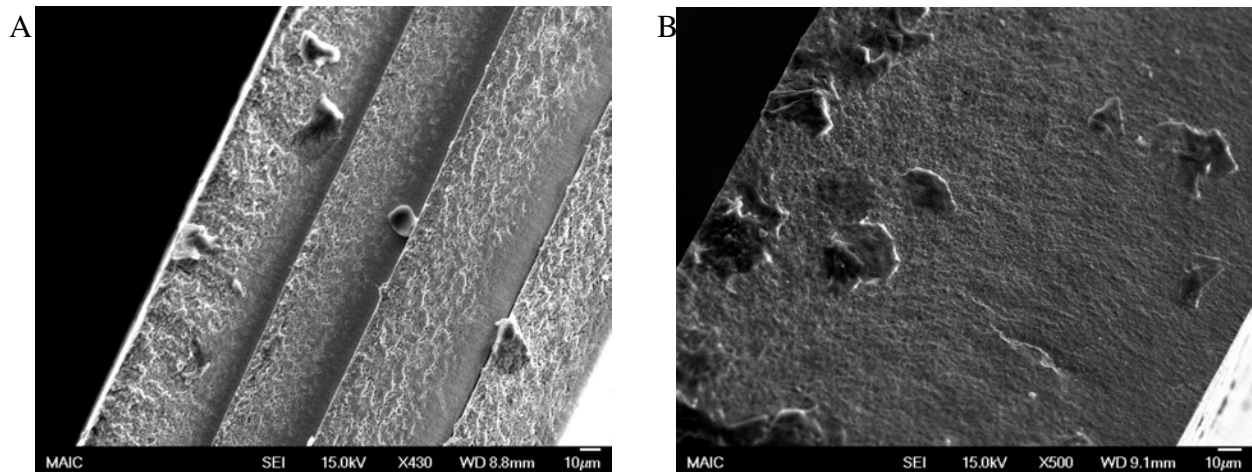


Figure 8-4. SEM micrograph of laminated tape before and after trimming. Individual layers at the edge of a (sintered) laminated substrate can be seen in A), while B) shows the smooth edge of a laminated substrate that has been trimmed before sintering. The scale bar is 10 microns.

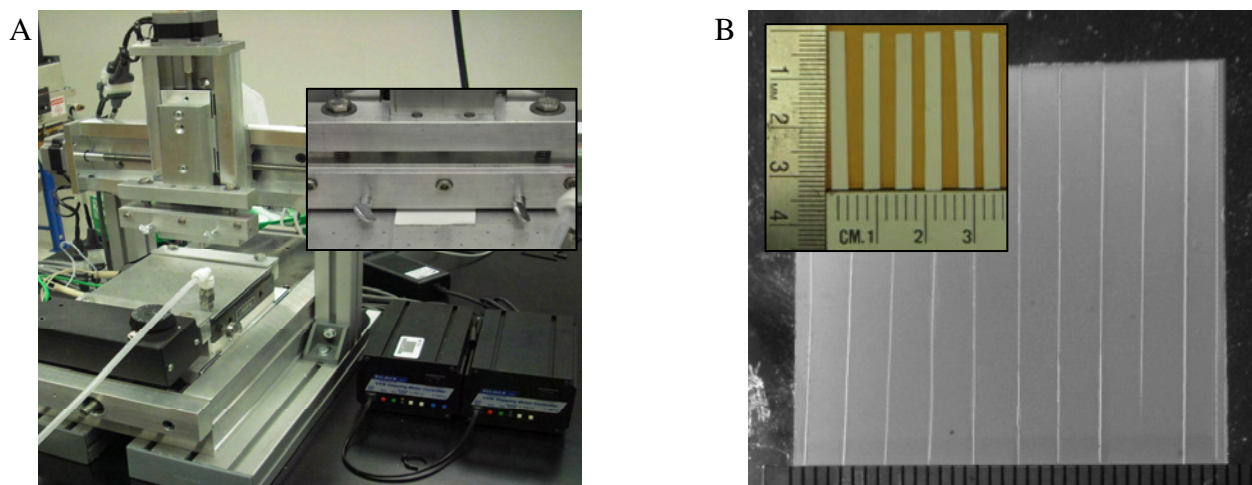


Figure 8-5. Custom three-axis cutting/punching machine and sintered/scored alumina substrates before and after device separation. A) shows the cutting/punching system with heated vacuum platen. The inset shows the cutting machine as a pre-programmed sequence of steps trims and scores a green tape. In B) the scored sections in a sintered  $\text{Al}_2\text{O}_3$  substrate can be seen; the inset illustrates the separated devices.

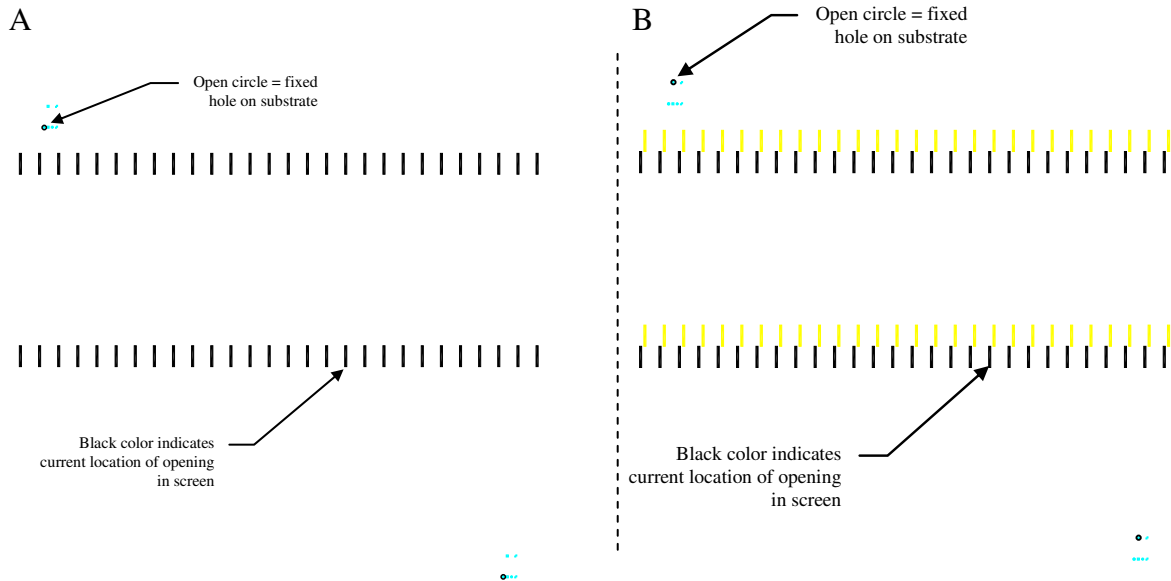


Figure 8-6. Illustration of screen designs allowing a degree of flexibility in the final sensor layout. A) and B) show how each screen has 6 fiducial shapes (top left and bottom right of each screen). In A) the substrate fiducial is aligned with the screen (bottom left) screen fiducial; screen printing leaves material deposited in the pattern of the black rectangles. In B) the machine aligns the top left screen fiducial with the same substrate fiducial, such that the pattern shifts down/left of the previous deposition.

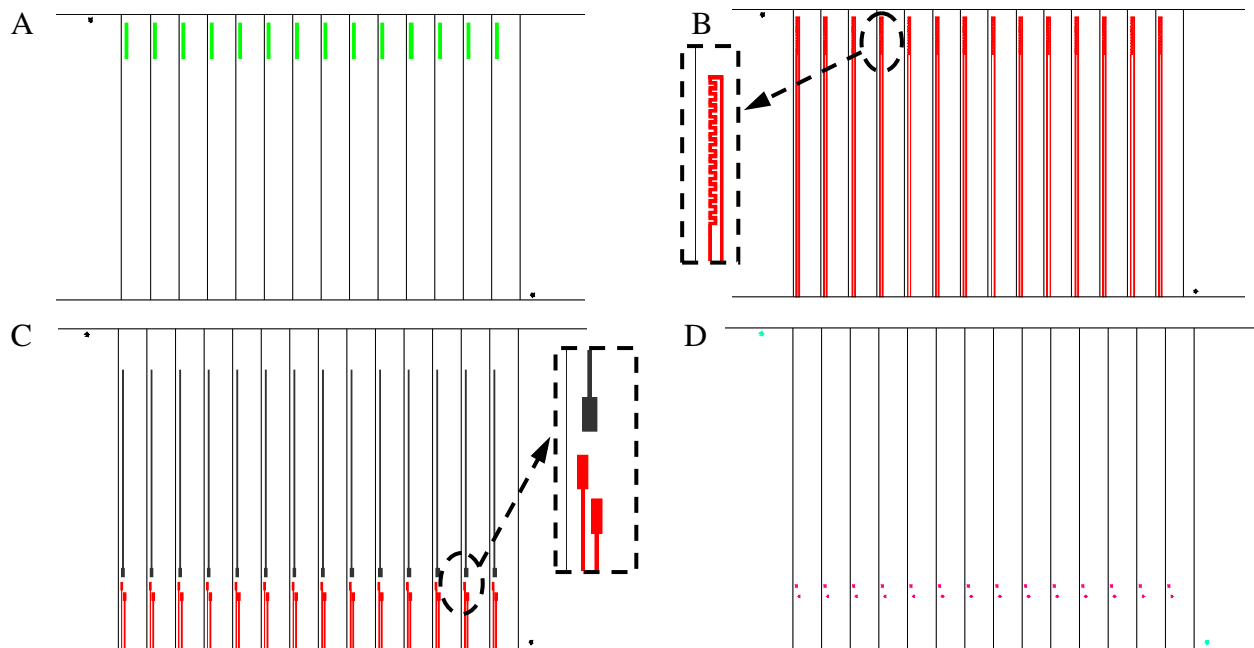


Figure 8-7. Screen printing patterns used for the batch fabrication of the gas sensors. A) shows the sensing electrodes; B) is for the heating elements/temperature sensors; C) shows the signal leads and contact pads; and D) is for the filling of vias from the backside to the front. The designs allow the use of vias or printing on the edge of the devices (i.e., across the thickness dimension) to connect heaters/temperature sensors to pads.

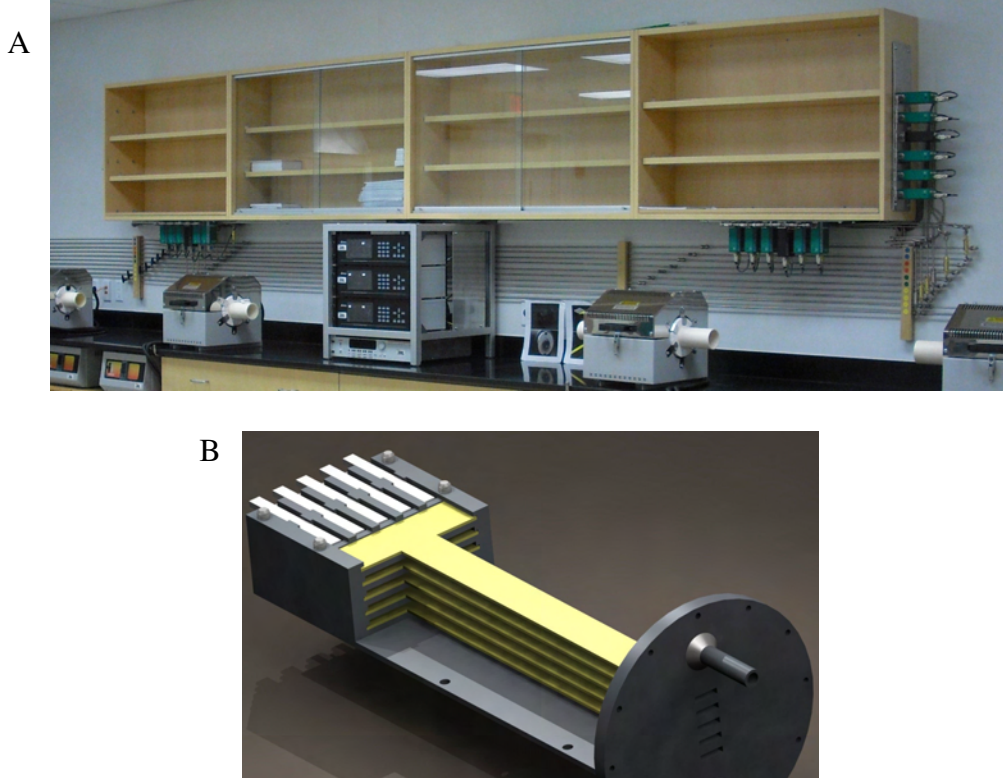


Figure 8-8. Facilities for scale-up multi-sensor testing. Reactor furnaces, gas lines, and mass flow controllers and control boxes can be seen in A). Over 400 channels can be rapidly measured with the switch-multimeter system. An illustration of one of the multisensor setups can be seen in B) with multiple stacked levels, holding several devices each. These reactor setups are sealed in the furnace reactor tubes, allowing over 100 devices to be tested simultaneously for repeatability/reliability tests.

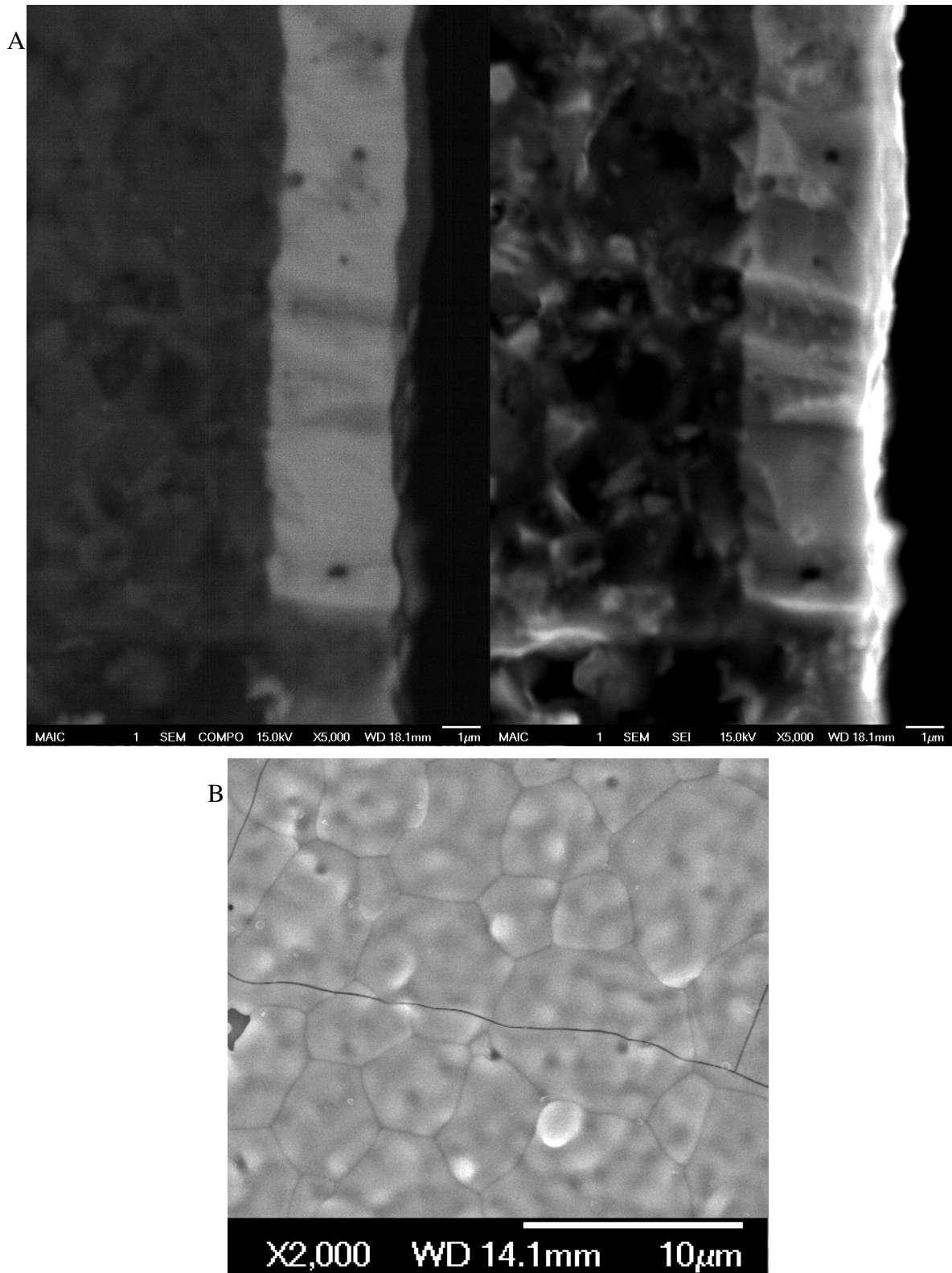


Figure 8-9. Cross-sectional and surface SEM images of a spin coated YSZ film on an Al<sub>2</sub>O<sub>3</sub> support. In A), the back-scatter and secondary electron images of the cross-section show that on top of the dense Al<sub>2</sub>O<sub>3</sub> support is a dense film with a thickness of ~2 microns (scale bar is 1 micron). The surface of the YSZ film can be seen in B).

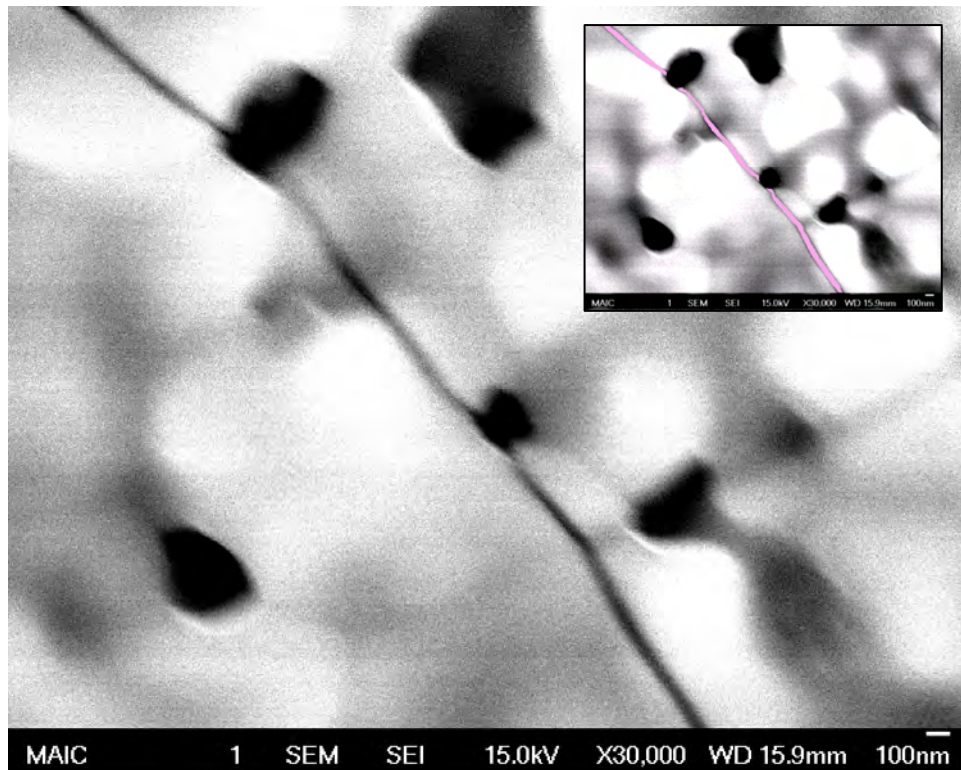


Figure 8-10. An example of a high magnification SEM micrograph showing improved YSZ films on  $\text{Al}_2\text{O}_3$  supports. The inset illustrates post-processing of the image using the ImageJ software to determine crack widths in the surface. The scale bar is 100 nm.

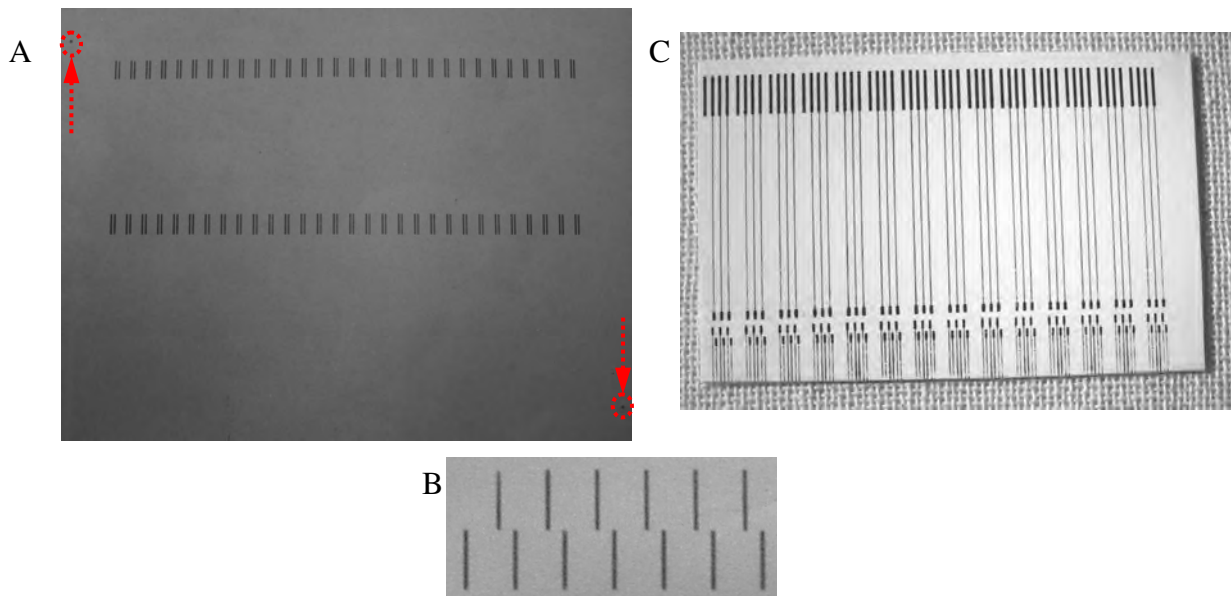


Figure 8-11. Batch-processed  $\text{La}_2\text{CuO}_4$  sensing electrodes deposited with automated DEK screen printer. In A) two rows of electrode pairs were screen printed onto a piece of green-tape. The holes indicated in the corners of the picture are fiducial marks for automated alignment purposes. Several vertically shifted electrode pairs screen printed onto green tape can be seen in B). In C) the electrodes and contact pads were screen printed onto a sintered, laminated substrate of  $\text{Al}_2\text{O}_3$  with YSZ film.

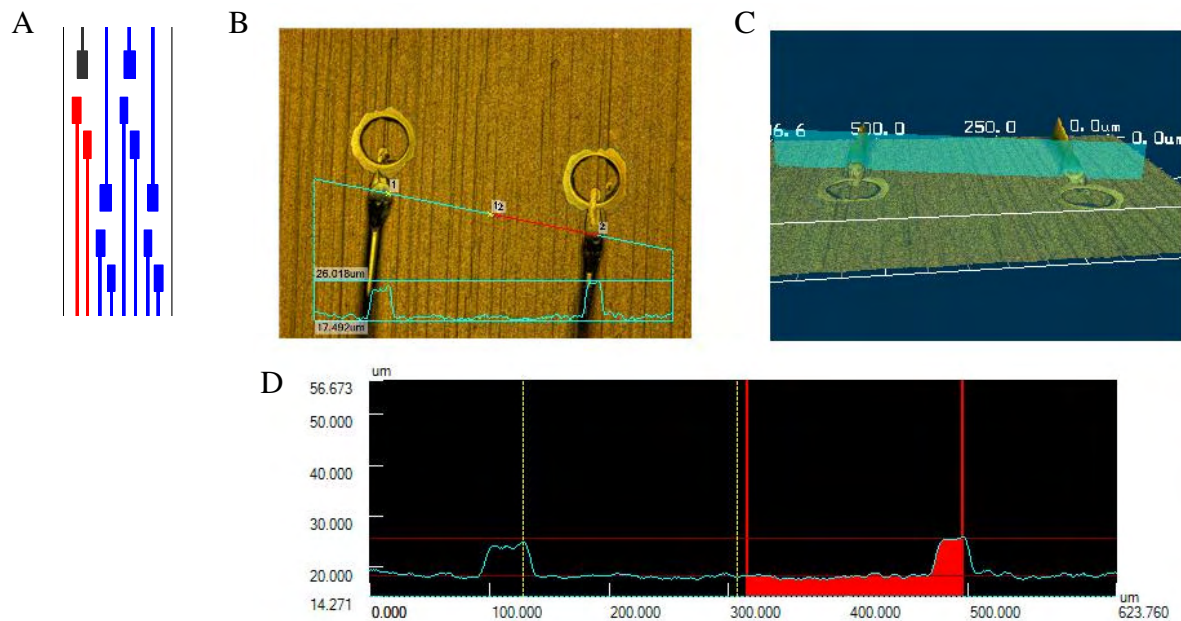


Figure 8-12. Wire bonding pads and resulting analysis of a Pt wire bonds to an Au pad.

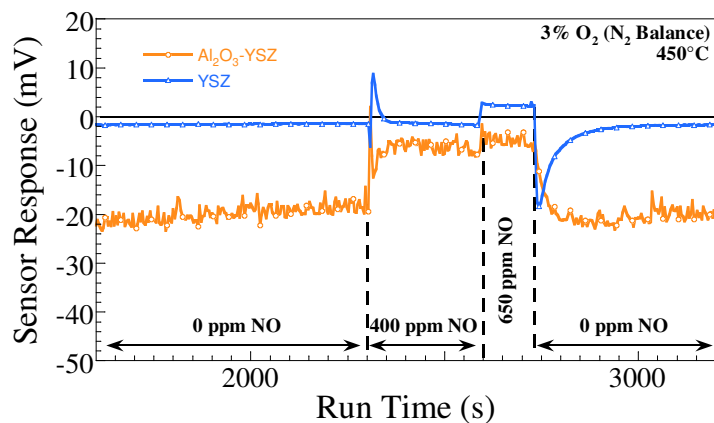


Figure 8-13. NO response of the  $\text{La}_2\text{CuO}_4$ -Pt electrode-pair on YSZ and  $\text{Al}_2\text{O}_3/\text{YSZ}$  substrates at  $450^\circ\text{C}$ . The NO concentration was varied between 0 and 650 ppm in 3%  $\text{O}_2$  ( $\text{N}_2$  balance) with a flow rate of 300 cc/min.

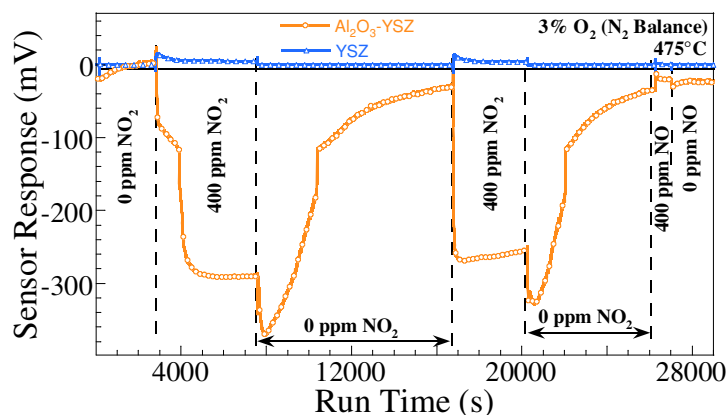


Figure 8-14.  $\text{NO}_x$  response of the  $\text{La}_2\text{CuO}_4$ -Pt electrode-pair on YSZ and  $\text{Al}_2\text{O}_3/\text{YSZ}$  substrates at 475 °C. The  $\text{NO}_x$  concentrations were varied between 0 and 400 ppm in 3%  $\text{O}_2$  ( $\text{N}_2$  balance) with a flow rate of 300 cc/min.

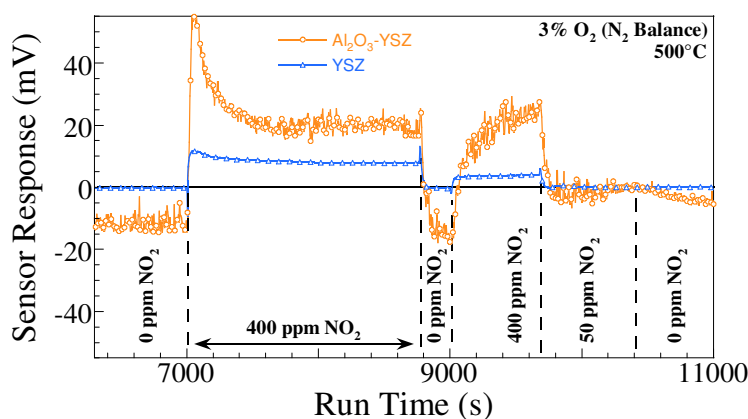


Figure 8-15.  $\text{NO}_2$  response of the  $\text{La}_2\text{CuO}_4$ -Pt electrode-pair on YSZ and  $\text{Al}_2\text{O}_3/\text{YSZ}$  substrates at 500 °C. The  $\text{NO}_2$  concentration was varied between 0 and 400 ppm in 3%  $\text{O}_2$  ( $\text{N}_2$  balance) with a flow rate of 300 cc/min.

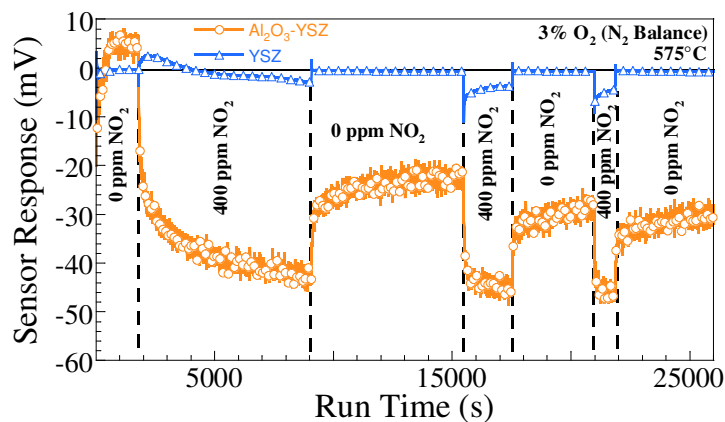


Figure 8-16.  $\text{NO}_2$  response of the  $\text{La}_2\text{CuO}_4$ -Pt electrode-pair on YSZ and  $\text{Al}_2\text{O}_3/\text{YSZ}$  substrates at 575 °C. The  $\text{NO}_2$  concentration was varied between 0 and 400 ppm in 3%  $\text{O}_2$  ( $\text{N}_2$  balance) with a flow rate of 300 cc/min.

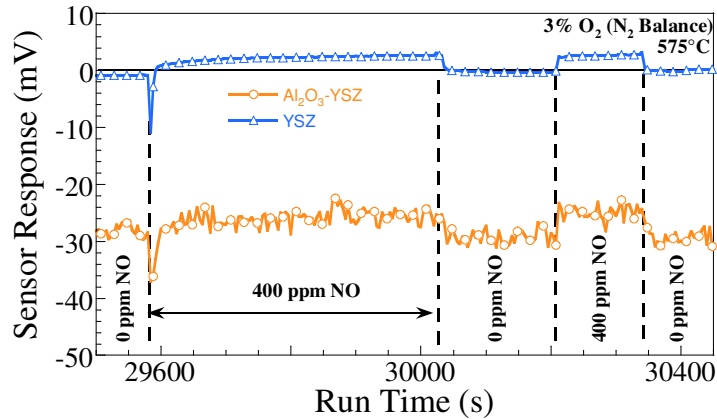


Figure 8-17. NO response of the  $\text{La}_2\text{CuO}_4\text{-Pt}$  electrode-pair on YSZ and  $\text{Al}_2\text{O}_3/\text{YSZ}$  substrates at  $575^\circ\text{C}$ . The NO concentration was varied between 0 and 400 ppm in 3%  $\text{O}_2$  ( $\text{N}_2$  balance) with a flow rate of 300 cc/min.

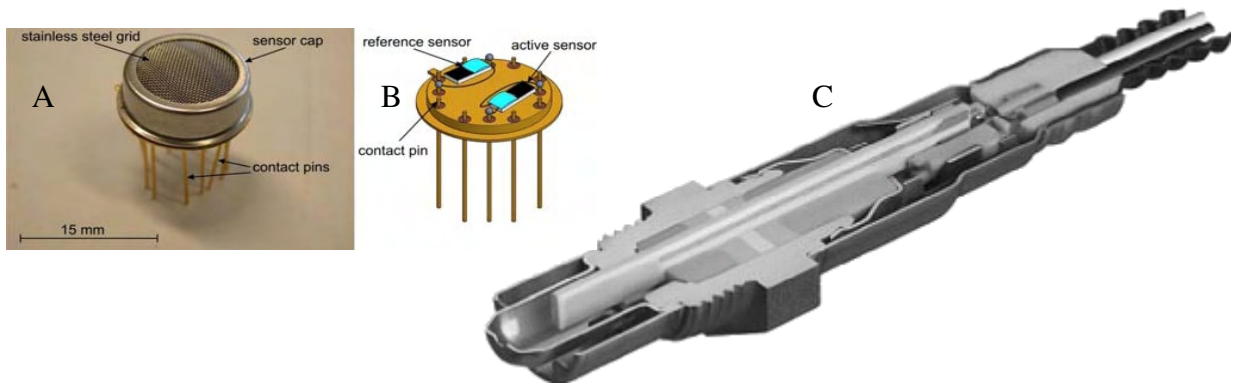


Figure 8-18. Two examples of packaging that may be used to house the advanced gas sensor technology. A) and B) show a transistor outline (TO-12) package with and without a particulate filter cap. C) shows a cutaway of a planar oxygen sensor package. Figures from Riegel et al and Näther et al.<sup>66,244</sup>

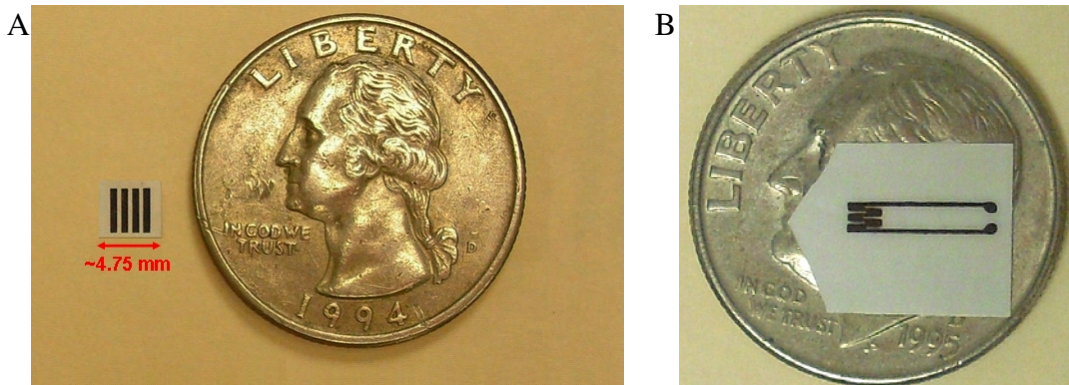


Figure 8-19. Rapid prototypes of gas sensor array features. In A) four identical  $\text{La}_2\text{CuO}_4$  sensing electrodes were deposited onto a small piece of YSZ using the nScript direct-write system. In B) a small Pt heating element was deposited onto an alumina substrate.

Table 8-1. Densification of tapes during tape lamination

Number of presses	Total 8-layer thickness (mm)	Average thickness per layer (mm)
0	1.19 mm	0.149
1	0.98 mm	0.123
2	0.96 mm	0.120

Table 8-2. Film thickness dependence on spin coating parameters

Number of coats	Deposition speed (rpm)	Deposition time (sec)	Average film thickness ( $\mu\text{m}$ )
1	1000	20	2.315
2	1000	20	3.2808
2	1000	30	1.5094
2	1500	20	2.9122

Table 8-3. YSZ film crack width dependence on heat treatment

Maximum presinter temperature ( $^{\circ}\text{C}$ )	Final sinter heating rate ( $^{\circ}\text{C}/\text{min}$ )	Average crack width (nm)
850	3	69.734
850	5	53.359
850	7	65.991
900	3	73.642

## CHAPTER 9 CONCLUSIONS

There were several objectives for this work, some of which followed as a result of work involving original objectives that did not go as planned. In all, the goal was to investigate methods for enhancing the performance of potentiometric gas sensors using sensor arrays, thermal and electric-field enhancements, surface science, and improvements in fabrication and testing procedures for R&D and commercialization purposes.

This work resulted in the creation of multifunctional gas sensor arrays through the combination of multiple sensing electrode-pairs into a single, miniature sensor device, thus allowing the detection of multiple gas species. Investigations included evaluation of crosstalk between sensing electrodes (i.e., the response of one affects another) when placed in close proximity to each other and the electrode arrangement with respect to each other and the rest of the device. Knowledge from these studies will be used to help design future devices.

The differential electrode temperature effect was investigated using two investigatory gas sensor arrays. These results demonstrated that this enhancement method can be used to improve the sensitivity and selectivity of potentiometric gas sensors. Furthermore, the investigatory devices demonstrated how more signals than electrodes can be yielded from the array because the signals are made up of the potential difference between any two sensing electrodes. From this basis, a prototype sensor array was improved through local heating of sensing electrode-pairs to different temperatures. This resulted in a device that was able to selectively detect both NO and NO<sub>2</sub>, without any interference from CO<sub>2</sub>. The small effect of CO did not change the response other than to cause a small shift, which means that with the addition of a CO selective sensing electrode pair (e.g., TiO<sub>2</sub>), the array should be able to compensate for this deviation. This is significant because then the device would be able to quantitatively detect NO, NO<sub>2</sub>, and

CO in harsh environments and with widely varying O<sub>2</sub> and humidity levels as is present in many combustion exhausts.

The concept for electric-field enhancements of a solid-state potentiometric gas sensor was a direct result of 'failed' sensor experiments involving thermal enhancements. After the initial observations and formulation of hypotheses as to why there was an electric-field effect on gas sensing performance, the objectives for this work were expanded. This resulted in an initial investigation to see the potential for using the electric field to enhance sensor performance in terms of sensitivity and selectivity. The influence of field shape, magnitude, and polarity was investigated and found to be important in determining the extent of enhancement. Through the use of an air-reference sample with concurrent mass spectrometry measurements a correlation was found between local gas concentrations coming off the sensing electrode and the sensor response. Furthermore, temperature programmed desorption (TPD) experiments revealed that an electric field localized around the sensing material can cause the shape of the TPD spectra and the peak temperature to change. This opens up the possibility of using the electric field effect to actively alter the operating temperature range of a gas sensor. Furthermore, this evidence led to the conclusion that there exists the possibility of using the electric-field enhancements with other solid-state ionic devices, such as hydrogen production membranes or solid oxide fuel cells. If the electric-field can enhance heterogeneous catalysis to the point where SOFC operating temperatures can be lowered without a decrease in performance, then this will be very significant.

A surface science analysis of the gas sensors utilized XPS, UPS, AES, and the Kelvin method to investigate changes in the chemical composition of sensing electrodes, the electronic

band structure of the materials, and changes in the work function when gases are adsorbed on the surface.

Improvements were made in terms of R&D procedures and steps towards commercialization of this gas sensor technology. This was accomplished through the development of development of procedures for automated manufacturing and testing. This also included sensor design and processing studies involving automated screen-printing, rapid-prototyping, wire bonding, test setups, and analyses programs.

In summary, this work resulted in the development of two novel methods for actively enhancing gas sensors. Two patent applications have been filed internationally and commercialization efforts are on the way. Future research will involve further improvements in manufacturing, reliability tests, and sensor enhancements. Furthermore, the electric-field enhancements will be further investigated using surface science and electroanalytical techniques to gain additional insight into the underlying mechanisms. Finally, the electric-field enhancements will be explored in other solid-state ionic devices, such as hydrogen production membranes and SOFCs.

APPENDIX A  
MORE ON THE THERMALLY MODIFIED GAS SENSOR ARRAY

**A.1 Heating Element Design**

Several initial heater designs were investigated before settling on the C-shaped heaters used in the primary investigations. Many of these patterns were difficult to make using a manual screen printer, however most were tested. It was found that the 8 mol% YSZ was not an ideal material as a support regardless of the heater pattern design. This was based on results that showed that the substrates would crack even under modest thermal stress. A comparison of the performance of each determined that the C-shaped elements were the best choice for use in the prototype arrays due to lower power requirements and less build up of stress. Note that in these initial measurements a thermal couple was placed in contact with the samples rather than using local surface temperature measurements.

The ideal Pt element microstructure was also investigated using several sintering temperatures. The ideal sintering temperature was found to be between 1000 and 1250 °C in order to get a sufficiently dense layer with good adhesion while not resulting in too low a resistance such that extremely high voltages would be necessary to heat the samples.

**A.2 Surface Temperature Measurements**

Surface temperature measurements are not easy. However, with the use of calibrated Pt RTDs, fairly accurate measurements can be made. Platinum was selected for the fabrication of heating elements and temperature sensors. Platinum is an industry standard for high-temperature resistance-temperature-devices (RTD) and as heating elements in gas sensors because of durability and chemical and thermal stability. For the initial design of a sensor array, thermal analysis can be a useful tool to determine the temperature profile of the device when heated locally. The sensing electrodes can then be spaced such that each is at the optimum temperature.

Below approximately 400 °C the resistance of Platinum has a linear dependence on temperature. However, above this temperature, further heat loss causes the linear model to deviate from experimental data, and a better model is a second order polynomial.

### **A.3 Finite Element Modeling of Thermal Distributions**

Finite Element Modeling (FEM) was performed using the Partial Differential Equation Tool in MatLAB 7.0 from Mathsoft. FEM requires entry of the device geometry (e.g., heater and substrate dimensions), boundary conditions, and material properties. Neumann boundary conditions (i.e., heat flux or (convective) heat transfer) were specified on the boundaries of the YSZ substrate. Dirichlet boundary conditions (i.e., specific temperatures) were entered for the Platinum heater. Material properties used in the analysis are listed in Table A-1.

Table A-1. Physical parameters used for thermal modeling

Density (g/cm <sup>3</sup> )	Thermal conductivity (W/(m °C))	Heat capacity (J/g °C)	Length (mm)	Width (mm)	Thickness (mm)
5.85	2.8	0.500	20	12	0.10

## APPENDIX B MORE ON THE ELECTRIC-FIELD ENHANCED GAS SENSOR

During sensor experiments utilizing a potentiometric gas sensor with heating elements, there were large sensor responses to small applied heater voltages after a crack formed in one of the heaters. The applied voltage caused changes in the potential of the sensor, and after testing the effect of the voltage gap it was proposed that there was a possibility the electric-field affected adsorption/desorption and/or chemical/electrochemical reactions taking place at the electrodes. From this initial hypothesis, the electric-field effect was further investigated with a standard planar sensor configuration, mass spectrometry, temperature programmed techniques, cyclic voltammetry, electrochemical impedance spectroscopy, photoelectron spectroscopy, and the Kelvin method.

## APPENDIX C PROGRAMMING

The Velmex gantry system used in making the custom 3-axis cutting machine had a control box (VXM Stepping Motor Controller) that allowed programming of axial movement. Using the Velmex Cosmos software and program language, the following code was written in order to automate trimming and scoring of laminated greentapes.

```
F           //Opening command for Velmex
PM-0,      //Saves program to memory slot 0
LM0,       //Loop Marker
I2M-4000,  // Raise blade 4000 motor steps
I1M-4000,  // Move blade forward 4000 steps
I2M4000,   // Lower blade 4000 steps
L5,        // Repeat loop 5 times
I2M-4000,  // Raise blade 4000 steps
R          // End program
```

## APPENDIX D ADDITIONAL INFORMATION

### D.1 Spray Coating

Prior to the decision to deposit YSZ coatings on alumina using spin coating, the use of spray coating was explored. Once the alumina substrate was prepared, a layer of YSZ had to be deposited to serve as the electrolyte for the gas sensor. A YSZ slurry was prepared by ball-milling denatured ethanol, YSZ (Tosoh Corp., 8 mol% Ytria), polyvinyl butyral (binder), and dispersant (solsperse, Lubizrol Inc.) for at least 24 hours. The substrates consisted of presintered tape-cast alumina. The slurry was fed to an air-fed spray gun, which created an aerosol that was deposited onto the alumina. During this process the alumina was heated to ~50 °C using a hotplate. The gun was positioned approximately 30 cm directly above the substrate. The coated alumina was then placed in a drying oven for 2 hours to evaporate the ethanol from the as-deposited film, and then it was then sintered at 1500 °C for 5 hours. The exact parameters of this process, such as rate of application and total amount of slurry applied, were not standardized. Therefore only qualitative remarks can be made with regard to the homogeneity of the deposition.

The coated substrates were examined using a scanning electron microscope (SEM, JEOL 6335F or JEOL 6400). The micrographs revealed that the YSZ coatings were extremely non-uniform. Furthermore, the films were relatively porous. Therefore, this method was deemed to be unsuitable for use in the gas sensor arrays.

### D.2 Pulsed Laser Deposition of $\text{La}_2\text{CuO}_4$

Following results of research from the literature, an attempt was made to make single crystal thin films of  $\text{La}_2\text{CuO}_4$  for the purpose of investigating the surface science of the material. This involved focusing a pulsed high-power laser onto a dense, pressed  $\text{La}_2\text{CuO}_4$  pellet. This

created a plume of material which deposited onto a LaO single crystal substrate which was at elevated temperatures. The XRD pattern for the  $\text{La}_2\text{CuO}_4$  thin film is shown in Figure D-1. The c-lattice parameter measured from (004) reflection is 13.141 Å.

### **D.3 Multi-Sensor Reactor Design and Modeling**

In order to ensure that the multi-sensor reactor resulted in uniform gas distribution to each of the 30 sensors being simultaneously tested (per reactor), first-order computational fluid dynamics (CFD) simulations were performed using CosmosFloworks (SolidWorks). Figure D-2 shows the preliminary results of the simulations, which indicated that the square stack of sensor modules resulted in non-uniform flow patterns near the top, bottom, and edges of the stack. This would result in variable sensor results between the sensors, which is not desirable when trying to demonstrate sensor repeatability between each sensor and different batches of fabricated sensors.

Therefore after careful analysis of the problem, quasi-hemispherical components were attached to the sides of the module stack in order to match the circular profile of the reactor tube. As the results in Figure D-3 indicate, this seems to have solved the problem as the gas distribution around the module stack is much more uniform.

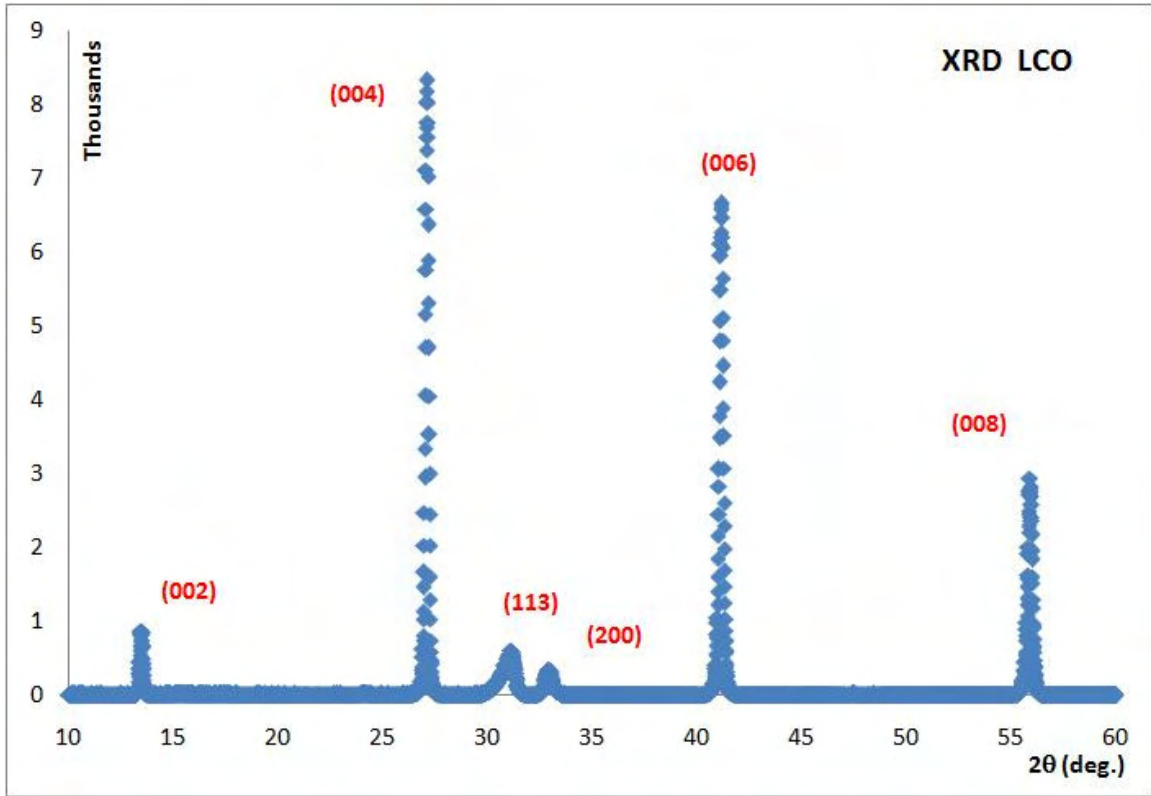


Figure D-1. XRD of the Pulsed-Laser-Deposited  $\text{La}_2\text{CuO}_4$  thin film.

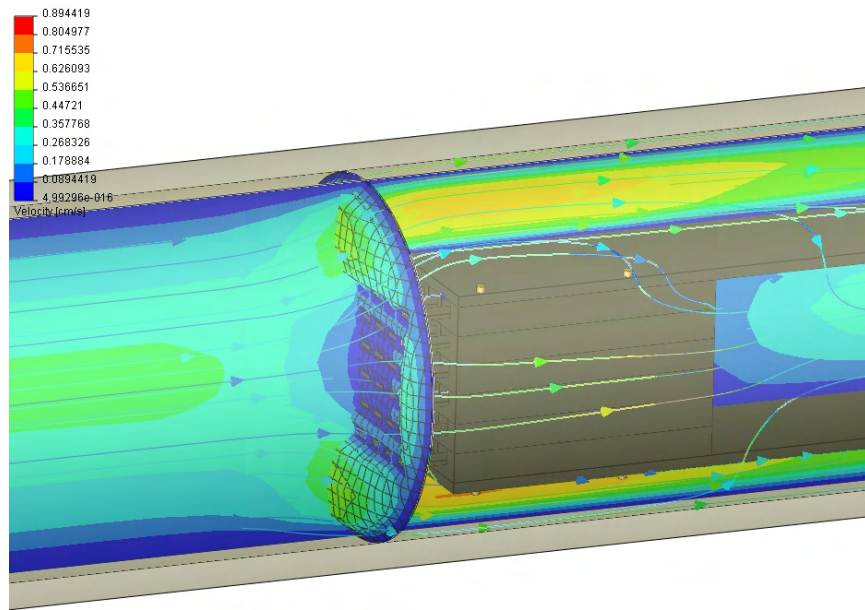


Figure D-2. CFD simulation of multi-sensor reactor before adding the side and top hemispheres.

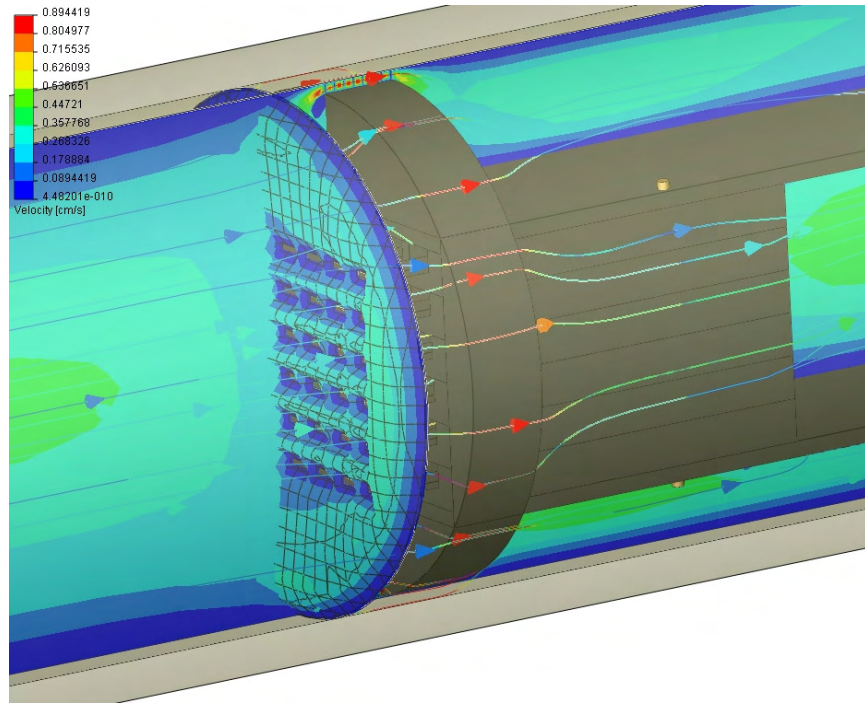


Figure D-3. CFD simulation of multi-sensor reactor after adding the side and top hemispheres.

## LIST OF REFERENCES

1. S. Akbar, P. Dutta, and C. Lee, "High-Temperature Ceramic Gas Sensors: A Review," *International Journal of Applied Ceramic Technology*, 3 [4] 302-311 (2006).
2. S. Borenstein, "Cost, Conflict and Climate: U.S. Challenges in the World Oil Market," *Center for the Study of Energy Markets (CSEM) Working Paper Series*, CSEM-WP-177R, 1-27, (2008), <http://www.ucei.berkeley.edu/PDF/csemwp177.pdf>, Last Accessed 6-22-2009.
3. L. Aguiar-Conraria and Y. Wen, "A Note On Oil Dependence and Economic Instability," *Macroeconomics Dynamics*, 12 717-723 (2008).
4. R. B. Barsky and L. Kilian, "Oil and the Macroeconomy Since the 1970s," *Journal of Economic Perspectives*, 18 [4] 115-134 (2004).
5. K. Rogoff, "Oil and the Global Economy," Working paper, Harvard University, 1-47, (2006), [www.hec.unil.ch/deep/evenements/Walras-Pareto-papers/Oil and the Global Economy.pdf](http://www.hec.unil.ch/deep/evenements/Walras-Pareto-papers/Oil%20and%20the%20Global%20Economy.pdf), Last Accessed 06-24-2009.
6. R. Earley and K. Smith, "Energy Price Impacts on the U.S. Economy," Department of Energy, 2001, Last Accessed 6-21-2009.
7. M. T. Klare, *Resource Wars: The New Landscape of Global Conflict*, Henry Holt and Company LLC, New York, 1-289, 2002.
8. R. U. Ayres, H. Turton, and T. Casten, "Energy Efficiency, Sustainability and Economic Growth," *Energy*, 32 634-648 (2007).
9. P. Glavic and R. Lukman, "Review of Sustainability Terms and Their Definitions," *Journal of Cleaner Production*, 15 1875-1885 (2007).
10. N. Hanley, P. G. McGregor, J. K. Swales, and K. Turner, "Do Increases in Energy Efficiency Improve Environmental Quality and Sustainability?," *Ecological Economics*, 68 692-709 (2009).
11. A. A. Leiserow, R. W. Kates, and T. M. Parris, "Sustainability Values, Attitudes, and Behaviors: A Review of Multinational and Global Trends," *Annual Review of Environment and Resources*, 31 413-444 (2006).
12. National Research Council (U.S.), Committee on the Effectiveness and Impact of Corporate Average Fuel Economy (CAFE) Standards, National Research Council (U.S.), Transportation Research Board, "Effectiveness and Impact of Corporate Average Fuel Economy (CAFE) Standards," Ed. by D. Brown, National Academies Press, 1-165, (2003), [http://www.nhtsa.dot.gov/Cars/rules/CAFE/docs/162944\\_web.pdf](http://www.nhtsa.dot.gov/Cars/rules/CAFE/docs/162944_web.pdf), Last Accessed 6-22-2009.
13. D. L. Fox, "Air Pollution," *Analytical Chemistry*, 69 [12] 1R-13R (1997).

14. The U.S. Environmental Protection Agency: Office of Air Quality Planning and Standards, "The Plain English Guide to the Clean Air Act," EPA-456/K-07-001, The US Environmental Protection Agency, 1-23, (2007), <http://www.epa.gov/oar/caa/peg/peg.pdf>, Last Accessed 6-22-2009.
15. U.S. Consumer Product Safety Commission, "Indoor Air Pollution: An Introduction for Health Professionals," DIANE Publishing Company, 1-27, (1996), [http://www.epa.gov/iaq/pdfs/indoor\\_air\\_pollution.pdf](http://www.epa.gov/iaq/pdfs/indoor_air_pollution.pdf), Last Accessed 6-22-2009.
16. R. E. Clement, P. W. Yang, and C. J. Koester, "Environmental Analysis," *Analytical Chemistry*, 69 [12] 251R-287R (1997).
17. U.S. Environmental Protection Agency (EPA), "EPA's 2008 Report on the Environment," EPA/600/R-07/045F, National Center for Environmental Assessment, Washington, DC, 1-1-7-3, (2008), <http://www.epa.gov/roe>, Last Accessed 6-21-2009.
18. The U.S. Environmental Protection Agency, "Automobile Emissions: An Overview," The U.S. Environmental Protection Agency: Office of Mobile Sources, EPA 400-F-92-007, The U.S. Environmental Protection Agency, 1-4, (1994), <http://www.epa.gov/otaq/consumer/05-autos.pdf>, Last Accessed 6-22-2009.
19. W. Göpel, *Micro- and Nanosensor Technology/Trends in Sensor Markets*, in *Sensors: A Comprehensive Survey*, Wiley-VCH, New York, 181-523, 1995.
20. G. Ertl, *Environmental Catalysis*, ed. G. Ertl, H. Knözinger, J. Weitkamp, Wiley-VCH, New York, 1-236, 1999.
21. K. Oskarsson, *A Planner's Guide for Selecting Clean-Coal Technologies for Power Plants*, ed. K. Oskarsson, A. Berglund, R. Deling, U. Snellman, O. Stenbäck, J. J. Fritz, World Bank Technical Paper No. 307, World Bank Publications, Washington, D.C., 1-160, 1997.
22. P. Schwartz and D. Randall, "An Abrupt Climate Change Scenario and Its Implications for United States National Security," Jet Propulsion Laboratory, Pasadena, CA, 1-22, (2003), [handle.dtic.mil/100.2/ADA469325](http://handle.dtic.mil/100.2/ADA469325), Last Accessed 6-21-2009.
23. V. Rapp, "Western Forests, Fire Risk, and Climate Change," *Science Update* [6] 1-12 (2009).
24. M. P. Harold and B. A. Ogunnaike, "Process Engineering in the Evolving Chemical Industry," *AIChE Journal*, 46 [11] 2123-2127 (2000).
25. E. C. Sivret, W. L. Peirson, and R. M. Stuetz, "Nitrous Oxide Monitoring for Nitrifying Activated Sludge Aeration Control: A Simulation Study," *Biotechnology and Bioengineering*, 101 [1] 109-118 (2008).
26. N. Müller, A. Jess, and R. Moos, "Direct detection of coke deposits on fixed bed catalysts by electrical sensors," *Sensors and Actuators B: Chemical*, corrected proof, 10.1016/j.snb.2009.03.008.

27. P. A. de Jong, J. R. Mayo, K. Golmohammadi, Y. Nakano, M. H. Lequin, H. A. W. M. Tiddens, J. Aldrich, H. O. Coxson, and D. D. Sin, "Estimation of Cancer Mortality Associated With Repetitive Computed Tomography Scanning," *American Journal of Respiratory and Critical Care Medicine*, 173 199-203 (2006).
28. B. W. Zeff and M. V. Yester, "Patient Self-Attenuation and Technologist Dose in Positron Emission Tomography," *Medical Physics*, 32 [4] 861-865 (2005).
29. D. J. Paul, "Picturing People: Non-Intrusive Imaging," *Foresight Exploiting the Electromagnetic Spectrum State of the Science Review*, Foresight Directorate, (2004), [http://www.foresight.gov.uk/electromagnetic\\_spectrum/EEMS\\_Picturing\\_People.pdf](http://www.foresight.gov.uk/electromagnetic_spectrum/EEMS_Picturing_People.pdf), Last Accessed 6-22-2009.
30. N. Docquier and S. Candel, "Combustion Control and Sensors: a Review," *Progress in Energy and Combustion Science*, 28 107-150 (2002).
31. A. M. Annaswamy and A. E. Ghoniem, "Active Control in Combustion Systems," *IEEE Control Systems Magazine*, 15 [6] 49-63 (1995).
32. E. Haile, O. Delabroy, D. Durox, F. Lacas, and S. Candel, "Combustion Enhancement by Active Control," Ch. 8 in *Flow Control*, 53<sup>rd</sup> edition, ed. W. Beiglböck, Ed., Springer-Verlag, Germany, 467-499, 1998.
33. G. A. Aluwande, "Exploitation of Advanced Control Techniques in Power Generation," *Computing & Control Engineering Journal*, 12 [2] 63-67 (2001).
34. M. G. Allen, "Diode Laser Absorption Sensors for Gas-Dynamic and Combustion Flows," *Measurement Science and Technology*, 9 545-562 (1998).
35. C. Malmborg, G. Petrina, D. Pratt, and D. Taylor, "An Introduction to Materials Handling Equipment Selection," Ed. by B. A. Peters, College-Industry Council on Material Handling Education (CICMHE), 1-39, (1998), <http://www.mhia.org/downloads/industrygroups/cicmhe/guidelines/equpguid.pdf>, Last Accessed 6-22-2009.
36. The U.S. Environmental Protection Agency: Office of Transportation and Air Quality, "Summary of EPA's Proposed Program for Low Emission Nonroad Diesel Engines and Fuel," EPA420-F-03-008, The US Environmental Protection Agency, 1-5, (2004), <http://www.epa.gov/nonroad-diesel/420f03008.pdf>, Last Accessed 6-21-2009.
37. The U.S. Environmental Protection Agency: Assessment and Standards Division, "Clean Air Nonroad Diesel Rule Summary," EPA420-F-04-029, The US Environmental Protection Agency, 1, (2004), <http://www.epa.gov/nonroad-diesel/2004fr/420f04029.pdf>, Last Accessed 6-21-2009.
38. The U.S. Department of Energy, "EIA Industry Analysis Briefs," The U.S. Department of Energy, 2004, <http://www.eia.doe.gov/emeu/mecs/iab98/index.html>, Last Accessed 6-21-2009.

39. D. J. Bamford, D. J. Cook, S. J. Sharpe, and A. D. Van Pelt, "Widely Tunable Rapid-Scanning Mid-Infrared Laser Spectrometer for Industrial Gas Process Stream Analysis," *Applied Optics*, 46 [19] 3958-3968 (2007).
40. H. Adam and J. Tulip, "Laser Gas Detection Is Now Cheap, Fast and Reliable," Boreal Laser Inc., (2004), <http://www.boreal-laser.com/docs/Laser%20Gas%20Detection.pdf>, Last Accessed 6-23-2009.
41. D. E. Williams, "Chemical Sensors and Gas Sensors for Process Control in Biotechnology," *Advances in Sensors for Biotechnology, IEE Colloquium on* 1-8 (1988).
42. S. Chauvatcharin, T. Seki, K. Fujiyama, and T. Yoshida, "On-Line Monitoring and Control of Acetone-Butanol Fermentation by Membrane-Sensor Mass Spectrometry," *Journal of Fermentation and Bioengineering*, 79 [3] 264-269 (1995).
43. S. Chauvatcharin, K. B. Konstantinov, K. Fujiyama, T. Seki, and T. Yoshida, "A Mass Spectrometry Membrane Probe and Practical Problems Associated With Its Application in Fermentation Processes," *Journal of Fermentation and Bioengineering*, 79 [5] 465-472 (1995).
44. R. Ramon, J. X. Feliu, O. Cos, J. L. Montesinos, F. X. Berthet, and F. Valero, "Improving the Monitoring of Methanol Concentration During High Cell Density Fermentation of *Pichia Pastoris*," *Biotechnology Letters*, 26 1447-1452 (2004).
45. O. Cos, R. Ramón, J. L. Montesinos, and F. Valero, "Operational Strategies, Monitoring and Control of Heterologous Protein Production in the Methylophilic Yeast *Pichia Pastoris* Under Different Promoters: A Review," *Microbial Cell Factories*, 5 [1] 17 (2006).
46. Y. Katakura, W. Zhang, G. Zhuang, T. Omasa, M. Kishimoto, Y. Goto, and K.-I. Suga, "Effect of Methanol Concentration on the Production of Human  $\beta_2$ -Glycoprotein I Domain V by a Recombinant *Pichia Pastoris*: A Simple System for the Control of Methanol Concentration Using a Semiconductor Gas Sensor," *Journal of Fermentation and Bioengineering*, 86 [5] 482-487 (1998).
47. W. Cao and Y. Duan, "Current Status of Methods and Techniques for Breath Analysis," *Critical Reviews in Analytical Chemistry*, 37 [1] 3-13 (2007).
48. M. Phillips, M. Sabas, and J. Greenberg, "Increased Pentane and Carbon Disulfide in the Breath of Patients With Schizophrenia," *Journal of Clinical Pathology*, 46 861-864 (1993).
49. W.-H. Cheng and W.-J. Lee, "Technology Development in Breath Microanalysis for Clinical Diagnosis," *The Journal of Laboratory and Clinical Medicine*, 133 [3] 218-228 (1999).
50. B. Fruhberger, N. Steriling, F. G. Grillo, S. Ma, D. Ruthven, R. J. Lad, and B. G. Frederick, "Detection and Quantification of Nitric Oxide in Human Breath Using a Semiconducting Oxide Based Chemiresistive Microsensor," *Sensors and Actuators B: Chemical*, 76 [1-3] 226-234 (2001).

51. R. M. Bowler, K. Murai, and R. H. True, "Update and Long-Term Sequelae of the Sarin Attack in the Tokyo, Japan Subway," *Chemical Health and Safety*, 8 [1] 53-55 (2001).
52. N.-J. Choi, J.-H. Kwak, Y.-T. Lim, T.-H. Bahn, K.-Y. Yun, J.-C. Kim, J.-S. Huh, and D.-D. Lee, "Classification of Chemical Warfare Agents Using Thick Film Gas Sensor Array," *Sensors and Actuators B: Chemical*, 108 298-304 (2005).
53. A. A. Tomchenko, G. P. Harmer, and B. T. Marquis, "Detection of Chemical Warfare Agents Using Nanostructured Metal Oxide Sensors," *Sensors and Actuators B: Chemical*, 108 41-55 (2005).
54. W. Göpel, *Fundamentals and General Aspects*, in *Sensors: A Comprehensive Survey*, Wiley-VCH, New York, 18-43, 1989.
55. S. Hefner, "Medical and Biological Sensors and Sensor Systems: Markets, Applications, and Competitors Worldwide," *A Kalorama Information Market Intelligence Report*, Ed. by S. Heffner, MarketResearch.com, 1-296, (2002).
56. R. F. Taylor "Chemical and biological sensors: markets and commercialization," Ch. 23 in *Handbook of Chemical and Biological Sensors*, 1<sup>st</sup> edition, ed. Schultz, J. S., Taylor, R. F., Eds., American International Distribution Corp., Bristol, 553-580, 1996.
57. N. Izu, W. Shin, N. Murayama, and S. Kanzaki, "Resistive Oxygen Gas Sensors Based on CeO<sub>2</sub> Fine Powder Prepared Using Mist Pyrolysis," *Sensors and Actuators B: Chemical*, 87 [1] 95-98 (2002).
58. J.-L. Seguin, S. Gomri, J. Guerin, and K. Aguir, "Bases of Noise Spectroscopy for Enhancing Metallic Oxide Gas Sensors Selectivity," Ch. 10 in *Science and technology of chemiresistor gas sensors*, ed. Aswal, D. K., Gupta, S. K., Eds., Nova Science Publishers, New York, 351-371, 2006.
59. A. Hassibi, R. Navid, R. W. Dutton, and T. H. Lee, "Comprehensive Study of Noise Processes in Electrode Electrolyte Interfaces," *Journal of Applied Physics*, 96 [2] 1074-1082 (2004).
60. S. Gomri, J. L. Seguin, J. Guerin, and K. Aguir, "Adsorption-Desorption Noise in Gas Sensors: Modelling Using Langmuir and Wolkenstein Models for Adsorption," *Sensors and Actuators B: Chemical*, 114 [1] 451-459 (2006).
61. R. I. Mackie, P. G. Stroot, and V. H. Varel, "Biochemical Identification and Biological Origin of Key Odor Components in Livestock Waste," *Journal of Animal Science*, 76 [5] 1331-1342 (1998).
62. J. W. Gardner, *Electronic Noses and Olfaction 2000*, in *Sensors*, ed. J. W. Gardner, K. Persaud, series ed. B. E. Jones, Insititute of Physics Publishing, Philadelphia, 1-302, 2000.
63. J. Janata, *Principles of Chemical Sensors*, in *Modern Analytical Chemistry*, series ed. D. Hercules, Plenum Press, New York, 1-312, 1989.

64. S. D. Senturia, "A Microbridge Gas Sensor," Ch. 23 in *Microsystem Design*, Kluwer Academic Publishers, Boston, 629-649, 2001.
65. E. D. Wachsman, *Selective Potentiometric Detection of NO<sub>x</sub> by Differential Electrode Equilibria*, in *Solid State Ionic Devices III, Proceedings of the Electrochemical Society*, series ed. E. D. Wachsman, K. S. Lyons, M. Carolyn, F. Garzon, M. Liu, J. Stetter, The Electrochemical Society, 215-221, 2003.
66. J. Riegel, H. Neumann, and H. M. Wiedenmann, "Exhaust Gas Sensors for Automotive Emission Control," *Solid State Ionics*, 152-153 783-800 (2002).
67. M. W. Barsoum, *Fundamentals of Ceramics*, IOP Publishing Ltd., Philadelphia, 1-505, 2003.
68. P. J. Gellings and H. J. M. Bouwmeester, *The CRC Handbook of Solid State Electrochemistry*, ed. P. J. Gellings, H. J. M. Bouwmeester, CRC Press, Florida, 1-656, 1996.
69. J. McMurry and R. Fay, *Chemistry*, 3<sup>rd</sup> edition, Prentice-Hall, New Jersey, 2001.
70. H. Girault, *Analytical and Physical Electrochemistry*, EPFL, Great Britain, 2004.
71. J. Newman and K. Thomas-Alyea, *Electrochemical Systems*, 3<sup>rd</sup> edition, Wiley-Interscience, New Jersey, 1-672, 2004.
72. J. Wang, *Analytical Electrochemistry*, 3<sup>rd</sup> edition, Wiley-VCH, New Jersey, 1-272, 2006.
73. C. M. Mari, "Non-Nernstian Solid State Gas Sensors: Operating Principles and Materials," *Ionics*, 9 (2003).
74. J. Nowotny, T. Bak, M. K. Nowotny, and C. C. Sorrell, "Charge Transfer at Oxygen/Zirconia Interface at Elevated Temperatures - Part 2: Oxidation of Zirconia," *Advances in applied ceramics*, 104 [4] 154-164 (2005).
75. F. Delannay, *Characterization of Heterogeneous Catalysts*, in *Chemical Industries*, series ed. F. Delannay, Marcel Dekker, Inc., New York, 1-401, 1984.
76. M. Baerns, *Basic Principles in Applied Catalysis*, in *Springer Series in Chemical Physics*, ed. M. Baerns, series ed. A. W. Castleman, Jr., F. P. Schäfer, J. P. Toennies, W. Zinth, Springer, Berlin, 1-542, 2004.
77. S. Brosda, C. G. Vayenas, and J. Wei, "Rules of Chemical Promotion," *Applied Catalysis B: Environmental*, 68 [3-4] 109-124 (2006).
78. C. G. Vayenas, S. Bebelis, C. Pliangos, S. Brosda, and D. Tsiplakides, *Electrochemical Activation of Catalysis: Promotion, Electrochemical Promotion, and Metal-Support Interactions*, Kluwer Academic/Plenum Publishers, New York, 1-531, 2001.

79. S. Wodiunig, V. Patsis, and C. Comninellis, "Electrochemical Promotion of RuO<sub>2</sub>-Catalysts for the Gas Phase Combustion of C<sub>2</sub>H<sub>4</sub>," *Solid State Ionics*, 136-137 813-817 (2000).
80. I. Riess and C. G. Vayenas, "Fermi Level and Potential Distribution in Solid Electrolyte Cells With and Without Ion Spillover," *Solid State Ionics*, 159 [3-4] 313-329 (2003).
81. D. Tsiplakides, S. Neophytides, and C. G. Vayenas, "Investigation of Electrochemical Promotion Using Temperature-Programmed Desorption and Work Function Measurements," *Solid State Ionics*, 136-137 839-847 (2000).
82. S. Ladas, S. Bebelis, and C. G. Vayenas, "Work Function Measurements on Catalyst Films Subject to in Situ Electrochemical Promotion," *Surface Science*, 251-252 1062-1068 (1991).
83. E. Di Bartolomeo, M. Luisa Grilli, and E. Traversa, "Sensing Mechanism of Potentiometric Gas Sensors Based on Stabilized Zirconia With Oxide Electrodes: Is It Always Mixed Potential?," *Journal of the Electrochemical Society*, 151 [5] H133-H139 (2004).
84. P. T. Moseley, "Solid State Gas Sensors," *Measurement Science and Technology*, 8 [3] 223-237 (1997).
85. A. J. Moulson and J. M. Herbert, *Electroceramics*, 2<sup>nd</sup> edition, Wiley Publishing, New Jersey, 1-498, 2003.
86. W. Göpel and K. D. Schierbaum, "SnO<sub>2</sub> Sensors: Current Status and Future Prospects," *Sensors and Actuators B: Chemical*, 26 [1-3] 1-12 (1995).
87. A. M. Azad, S. A. Akbar, S. G. Mhaisalkar, L. D. Birkefeld, and S. Goto, "Solid-State Gas Sensors: A Review," *Journal of the Electrochemical Society*, 139 [12] 3690-3704 (1992).
88. N. Barsan and U. Weimar, "Conduction Model of Metal Oxide Gas Sensors," *Journal of Electroceramics*, 7 [3] 143-167 (2001).
89. R. Pierret, *Semiconductor Device Fundamentals*, Addison-Wesley Publishing Co., Massachusetts, 1-792, 1996.
90. E. Tsagarakis and W. Weppner, "Thermodynamic and Kinetic Principles for Electrochemical Gas Sensors Based on Solid Ionic Conductors," *Materials Research Society Symposium Proceedings*, 828 (2005).
91. E. D. Wachsman and P. Jayaweera, *Selective Detection of NO<sub>x</sub> by Differential Electrode Equilibria*, in *Solid State Ionic Devices II, Proceedings of the Electrochemical Society*, series ed. E. D. Wachsman, W. Weppner, E. Traversa, M. Liu, P. Vanysek, N. Yamazoe, The Electrochemical Society, 298-304, 2001.
92. B. M. White, E. Macam, F. M. Van Assche, E. Traversa, and E. D. Wachsman, *Theoretical Framework for Predicting Solid-State Potentiometric Gas Sensor Behavior*, in

*Proceedings of the 210th Meeting of The Electrochemical Society, Vol. 3, Chemical Sensors 7-and MEMS/NEMS 7, ECS Transactions*, series ed. G. Hunder, S. Akbar, S. Bhansali, O. Brand, C. Bruckner-Lea, M. Carter, J. Davidson, E. Enikov, P. Hesketh, R. Hillman, C. Kranz, J. Li, R. Maboudian, R. Mukundan, C. Roper, S. Shoji, A. Simonian, M. Tabib-Azar, The Electrochemical Society, New Jersey, 2009.

93. B. M. White, F. M. Van Assche, E. Traversa, and E. D. Wachsman "Electrical Characterization of Semiconducting  $\text{La}_2\text{CuO}_4$  For Potentiometric Gas Sensor Applications," in *Proceedings of the Electrochemical Society, Solid State Ionic Devices IV*, series ed. E. D. Wachsman, V. Birss, F. H. Garzon, R. Mukundan, E. Traversa, Eds., The Electrochemical Society, New Jersey, 106, 2006.
94. L. Chevallier, M. Luisi Grilli, E. Di Bartolomeo, and E. Traversa, "Non-Nernstian Planar Sensors Based on YSZ With Ta (10 at.%) -Doped Nanosized Titania As a Sensing Electrode for High-Temperature Applications," *International Journal of Applied Ceramic Technology*, 3 [5] 393-400 (2006).
95. L. Chevallier, E. Di Bartolomeo, M. L. Grilli, M. Mainas, B. M. White, and E. D. Wachsman, "Non-Nernstian Planar Sensors Based on YSZ With an  $\text{Nb}_2\text{O}_5$  Electrode: Discussion on Sensing Mechanism," *Proceedings of the Electrochemical Society, Solid State Ionic Devices IV*, 1 163 (2006).
96. J. Yoo, S. Chatterjee, and E. D. Wachsman, "Sensing Properties and Selectivities of a  $\text{WO}_3/\text{YSZ}/\text{Pt}$  Potentiometric  $\text{NO}_x$  Sensor," *Sensors and Actuators B: Chemical*, 122 [2] 644-652 (2007).
97. J. Yoo, F. M. Van Assche, and E. D. Wachsman, "Temperature-Programmed Reaction and Desorption of the Sensor Elements of a  $\text{WO}_3/\text{YSZ}/\text{Pt}$  Potentiometric Sensor," *Journal of the Electrochemical Society*, 153 [6] H115-H121 (2006).
98. J. Yoo, S. Chatterjee, F. M. Van Assche, and E. D. Wachsman, "Influence of Adsorption and Catalytic Reaction on Sensing Properties of a Potentiometric  $\text{La}_2\text{CuO}_4/\text{YSZ}/\text{Pt}$  Sensor," *Journal of the Electrochemical Society*, 154 [7] J190-J195 (2007).
99. M. L. Grilli, L. Chevallier, M. L. D. Vona, S. Licoccia, and E. Di Bartolomeo, "Planar Electrochemical Sensors Based on YSZ With  $\text{WO}_3$  Electrode Prepared by Different Chemical Routes," *Sensors and Actuators B: Chemical*, 111-112 91-95 (2005).
100. J. Yoo, H. Yoon, and E. D. Wachsman, "Sensing Properties of  $\text{MO}_x/\text{YSZ}/\text{Pt}$  ( $\text{MO}_x = \text{Cr}_2\text{O}_3, \text{SnO}_2, \text{CeO}_2$ ) Potentiometric Sensor for  $\text{NO}_2$  Detection," *Journal of the Electrochemical Society*, 153 [11] H217-H221 (2006).
101. H. Kanai, J. Mizusaki, H. Tagawa, S. Hoshiyama, K. Hirano, K. Fujita, M. Tezuka, and T. Hashimoto, "Defect Chemistry of  $\text{La}_{2-x}\text{Sr}_x\text{CuO}_{4-\delta}$ : Oxygen Nonstoichiometry and Thermodynamic Stability," *Journal of Solid State Chemistry*, 131 [1] 150-159 (1997).
102. N. Kieda, S. Nishiyama, K. Shinozaki, and N. Mizutani, "Nonstoichiometry and Electrical Properties of  $\text{La}_2\text{CuO}_4$  and  $\text{La}_2(\text{Cu}, \text{Ni})\text{O}_4$ ," *Solid State Ionics*, 49 85-88 (1991).

103. A. Lappas and K. Prassides, "Layered Cuprates With the T\* Structure: Structural and Conducting Properties," *Journal of Solid State Chemistry*, 115 [2] 332-346 (1995).
104. P. G. Radaelli, J. D. Jorgensen, and A. J. Schultz, "Structure of the Superconducting La<sub>2</sub>CuO<sub>4+d</sub> Phases (d ~0.08,0.12) Prepared by Electrochemical Oxidation," *Physical Review B*, 48 [1] 499-510 (1993).
105. J. D. Jorgensen, P. Lightfoot, and P. Shiyou, "Structural Properties of the Oxide Superconductors: The Critical Role of Defects," *Superconductor Science and Technology*, 4 S11-S18 (1991).
106. P. R. Kenway, S. C. Parker, and W. C. Mackrodt, "The Calculated Structure, Stability and Composition of the Low Index Surfaces of La<sub>2</sub>CuO<sub>4</sub> and Nd<sub>2</sub>CuO<sub>4</sub>," *Surface Science*, 326 301-310 (1995).
107. M. S. Dutraive, C. Pijolat, and R. Lalauze, "Sintering, Catalytic Effects and Defect Chemistry in Polycrystalline Tin Dioxide," *Sensors and Actuators B: Chemical*, 26 [1-3] 38-44 (1995).
108. R. van de Krol and H. L. Tuller, "Electroceramics-the Role of Interfaces," *Solid State Ionics*, 150 167-169 (2002).
109. N. Barsan and U. Weimar, "Understanding the Fundamental Principles of Metal Oxide Based Gas Sensors; the Example of CO Sensing With SnO<sub>2</sub> Sensors in the Presence of Humidity," *Journal of Physics: Condensed Matter*, 15 [20] R813-R839 (2003).
110. A. Gurlo and R. Riedel, "In Situ and Operando Spectroscopy for Assessing Mechanisms of Gas Sensing," *Angewandte Chemie International Edition*, 46 [21] 3826-3848 (2007).
111. B. M. White, "Solid-State Potentiometric Sensors for Nitrogen Monoxide, Nitrogen Dioxide, and Carbon Monoxide," Ph.D. Dissertation, University of Florida, Gainesville, Florida, 18-157, 2007.
112. J. D. Jorgensen, B. Dabrowski, S. Y. Pei, D. G. Hinks, L. Soderholm, B. Morosin, J. E. Schirber, E. L. Venturini, and D. S. Ginley, "Superconducting Phase of La<sub>2</sub>CuO<sub>4+δ</sub> - A Superconducting Composition Resulting From Phase-Separation," *Physical Review B*, 38 [16] 11337-11345 (1988).
113. E. D. Wachsman, P. Jayaweera, G. Krishnan, and A. Sanjurjo, "Electrocatalytic Reduction of NO<sub>x</sub> on La<sub>1-x</sub>A<sub>x</sub>B<sub>1-y</sub>B'<sub>y</sub>O<sub>3-δ</sub>: Evidence of Electrically Enhanced Activity," *Solid State Ionics*, 136-137 775-782 (2000).
114. J. Zhu, Z. Zhao, D. Xiao, J. Li, X. Yang, and Y. Wu, "Application of Cyclic Voltammetry in Heterogeneous Catalysis: NO Decomposition and Reduction," *Electrochemistry Communications*, 7 [1] 58-61 (2005).
115. J. R. MacDonald, *Impedance Spectroscopy: Emphasizing Solid Materials and Systems*, ed. J. Ross MacDonald, Wiley, New York, 1987.

116. B. White, E. Traversa, and E. Wachsman, "Investigation of La<sub>2</sub>CuO<sub>4</sub>/YSZ/Pt Potentiometric NO<sub>x</sub> Sensors With Electrochemical Impedance Spectroscopy," *Journal of The Electrochemical Society*, 155 [1] J11-J16 (2008).
117. E. J. Abram, D. C. Sinclair, and A. R. West, "A Strategy for Analysis and Modelling of Impedance Spectroscopy Data of Electroceramics: Doped Lanthanum Gallate," *Journal of Electroceramics*, 10 [3] 165-177 (2003).
118. A. D'Amico, C. Di Natale, R. Paolesse, A. Mantini, C. Goletti, F. Davide, and G. Filosophi, "Chemical Sensing Materials Characterization by Kelvin Probe Technique," *Sensors and Actuators B: Chemical*, 70 [1] 254-262 (2000).
119. J. Nowotny, T. Bak, M. K. Nowotny, and C. C. Sorrell, "Charge Transfer at Oxygen/Zirconia Interface at Elevated Temperatures – Part 5: Reactivity Models," *Advances in applied ceramics*, 104 [4] 181-187 (2005).
120. T. Sahn, A. Gurlo, N. Barsan, U. Weimar, and L. Medler, "Fundamental Studies on SnO<sub>2</sub> by Means of Simultaneous Work Function Change and Conduction Measurements," *Thin Solid Films*, 490 [1] 43-47 (2005).
121. R. Roescu, I. Dumitriu, and A. Tomescu, "Simultaneous Evaluation of the Electrical Resistance and Work Function Changes for Chemoresistive Type Sensors," *Romanian Reports in Physics*, 56 [4] 607-612 (2004).
122. A. Tomescu and R. Roescu, "Electron Affinity Changes Induced by Gaseous Species Present in the Surrounding Atmosphere," *Journal of Optoelectronics and Advanced Materials*, 7 [3] 1529-1532 (2005).
123. N. Guillet, A. Rives, R. Lalauze, and C. Pijolat, "Study of Adsorption of Oxygen on β-Al<sub>2</sub>O<sub>3</sub> + Au and β-Al<sub>2</sub>O<sub>3</sub> + Pt - Work Function Measurements-Proposition of a Model," *Applied Surface Science*, 210 [3] 286-292 (2003).
124. H. Geistlinger, I. Eisele, B. Flietner, and R. Winter, "Dipole- and Charge Transfer Contributions to the Work Function Change of Semiconducting Thin Films: Experiment and Theory," *Sensors and Actuators B: Chemical*, 34 [1-3] 499-505 (1996).
125. J. Mizsei, "Vibrating Capacitor Method in the Development of Semiconductor Gas Sensors," *Thin Solid Films*, 490 [1] 17-21 (2005).
126. D. Briggs, *Handbook of X-Ray and Ultraviolet Photoelectron Spectroscopy*, ed. D. Briggs, Heyden & Son Ltd., Philadelphia, 1-380, 1978.
127. A. Ellis, M. Feher, and T. Wright, *Electronic and Photoelectron Spectroscopy: Fundamentals and Case Studies*, Cambridge University Press, Cambridge, 1-186, 2005.
128. J. H. D. Eland, *Photoelectron Spectroscopy*, Halsted Press (John Wiley & Sons), New York, 1-239, 1974.

129. R. E. Ballard, *Photoelectron Spectroscopy and Molecular Orbital Theory*, Halsted Press (John Wiley & Sons), New York, 1-116, 1978.
130. S. Hüfner, *Photoelectron Spectroscopy: Principles and Applications*, in *Advanced Texts in Physics*, 3<sup>rd</sup> edition, Springer, Berlin, 1-652, 2003.
131. J. W. Rabalais, *Principles of Ultraviolet Photoelectron Spectroscopy*, in *Wiley-Interscience Monographs in Chemical Physics*, series ed. J. B. Birks, S. P. McGlynn, John Wiley & Sons, New York, 1-373, 1977.
132. T. Doll, *Advanced Gas Sensing: The Electroadsorptive Effect and Related Techniques*, Kluwer Academic Publishers, Norwell, 1-200, 2003.
133. I. Eisele, T. Doll, and M. Burgmair, "Low Power Gas Detection With FET Sensors," *Sensors and Actuators B: Chemical*, 78 [1-3] 19-25 (2001).
134. T. Doll, J. Lechner, I. Eisele, K. D. Schierbaum, and W. Göpel, "Ozone Detection in the PPB Range With Work Function Sensors Operating at Room Temperature," *Sensors and Actuators B: Chemical*, 34 [1-3] 506-510 (1996).
135. Z. Fan and J. G. Lu, "Gate-Refreshable Nanowire Chemical Sensors," *Applied Physics Letters*, 86 [12] 123510-123513 (2005).
136. H. L. Tuller, "Photo-Activated Low Temperature, Micro Fuel Cell Power Source," DE-FC26-05NT42624, The U.S. Department of Energy, (2008).
137. A. Rothschild and H. L. Tuller, "Photo-induced sensitivity and selectivity of semiconductor sensors," US2006/0000259 A1, 1-5-2006.
138. N. A. Anastasijevic, "NEMCA--From Discovery to Technology," *Catalysis Today*, 146 [3-4] 308-311 (2009).
139. E. D. Wachsman, "Multifunctional (NO<sub>x</sub>/CO/O<sub>2</sub>) Solid-State Sensors for Coal Combustion Control," *Final Technical Progress Report*, DE-FC26-03-NT41614, U.S. Department of Energy, 1-72, (2007).
140. W. Göpel, G. Reinhardt, and M. Rösch, "Trends in the Development of Solid State Amperometric and Potentiometric High Temperature Sensors," *Solid State Ionics*, 136-137 519-531 (2000).
141. M. C. Carotta, G. Martinelli, L. Crema, M. Gallana, M. Merli, G. Ghiotti, and E. Traversa, "Array of Thick Film Sensors for Atmospheric Pollutant Monitoring," *Sensors and Actuators B: Chemical*, 68 [1-3] 1-8 (2000).
142. M. C. Carotta, G. Martinelli, L. Crema, C. Malagú, M. Merli, G. Ghiotti, and E. Traversa, "Nanostructured Thick-Film Gas Sensors for Atmospheric Pollutant Monitoring: Quantitative Analysis on Field Tests," *Sensors and Actuators B: Chemical*, 76 [1-3] 336-342 (2001).

143. M. L. Grilli, E. Di Bartolomeo, A. Lunardi, L. Chevallier, S. Cordiner, and E. Traversa, "Planar Non-Nernstian Electrochemical Sensors: Field Test in the Exhaust of a Spark Ignition Engine," *Sensors and Actuators B: Chemical*, 108 [1-2] 319-325 (2005).
144. E. Di Bartolomeo, M. L. Grilli, A. Nicoletta, C. Stefano, and E. Traversa, "Testing Planar Gas Sensors Based on Ytria-Stabilized Zirconia With Oxide Electrodes in the Exhaust Gases of a Spark Ignition Engine," *Sensor Letters*, 3 [1-4] 22-26 (2005).
145. F. M. Van Assche and E. D. Wachsman, "Isotopically Labeled Oxygen Studies of the NO<sub>x</sub> Exchange Behavior of La<sub>2</sub>CuO<sub>4</sub> to Determine Potentiometric Sensor Response Mechanism," *Solid State Ionics*, 179 [39] 2225-2233 (2008).
146. F. M. Van Assche, IV, J. C. Nino, and E. D. Wachsman, "Infrared and X-Ray Photoemission Spectroscopy of Adsorbates on La<sub>2</sub>CuO<sub>4</sub> to Determine Potentiometric NO<sub>x</sub> Sensor Response Mechanism," *Journal of The Electrochemical Society*, 155 [7] J198-J204 (2008).
147. B. White, S. Chatterjee, E. Macam, and E. Wachsman, "Effect of Electrode Microstructure on the Sensitivity and Response Time of Potentiometric NO<sub>x</sub> Sensors," *Journal of the American Ceramic Society*, 91 [6] 2024-2031 (2008).
148. I. Simon, N. Barson, M. Bauer, and U. Weimar, "Micromachined Metal Oxide Gas Sensors: Opportunities to Improve Sensor Performance," *Sensors and Actuators B: Chemical*, 73 1-26 (2001).
149. M. Baroncini, P. Placidi, G. C. Cardinali, and A. Scorzoni, "Thermal Characterization of a Microheater for Micromachined Gas Sensors," *Sensors and Actuators A: Physical*, 115 8-14 (2004).
150. W. Chung, J. Lim, D. Lee, N. Miura, and N. Yamazoe, "Thermal and Gas-Sensing Properties of Planar-Type Micro Gas Sensor," *Sensors and Actuators B: Chemical*, 64 118-123 (2000).
151. B. M. Blackburn, B. M. White, and E. D. Wachsman, "Multifunctional Potentiometric Gas Sensor Array With An Integrated Heater And Temperature Sensors," *Ceramic Engineering and Science Proceedings*, 28 [8] 101-108 (2008).
152. D. Gostovic, J. R. Smith, D. P. Kundinger, K. S. Jones, and E. D. Wachsman, "Three-Dimensional Reconstruction of Porous LSCF Cathodes," *Electrochemical Solid-State Letters*, 10 B214-B217 (2007).
153. M. Stoukides, "Applications of Solid Electrolytes in Heterogeneous Catalysis," *Industrial & Engineering Chemistry Research*, 27 [10] 1745-1750 (1988).
154. L. Bultel, C. Roux, E. Siebert, P. Vernoux, and F. Gaillard, "Electrochemical Characterisation of the Pt/YSZ Interface Exposed to a Reactive Gas Phase," *Solid State Ionics*, 166 [1-2] 183-189 (2004).

155. B. J. Polk, J. A. Smith, S. P. DeWeerth, Z. Zhou, J. Janata, and K. Domansky, "Design of Solid State Array for Simultaneous Potentiometric and Impedance Sensing in Gas Phase," *Electroanalysis*, 11 707-711 (1999).
156. B. T. Marquis and J. F. Vetelino, "A Semiconducting Metal Oxide Sensor Array for the Detection of NO<sub>x</sub> and NH<sub>3</sub>," *Sensors and Actuators B: Chemical*, 77 [1-2] 100-110 (2001).
157. B. M. Blackburn and E. D. Wachsman, "Multifunctional Gas Sensor Array With Improved Selectivity Through Local Thermal Modification," *ECS Transactions*, 11 [33] 141-153 (2008).
158. H. D. Wiemhöfer and W. Göpel, "Fundamentals and Principles of Potentiometric Gas Sensors Based Upon Solid Electrolytes," *Sensors and Actuators B: Chemical*, 4 [3-4] 365-372 (1991).
159. M. J. Madou and S. R. Morrison, *Chemical Sensing with Solid State Devices*, Academic Press, Inc., San Diego, 1-546, 1989.
160. H. D. Wiemhöfer, "Sensing Effects at Gas-Solid Interfaces," *Solid State Ionics*, 75 167-178 (1995).
161. T. Wolkenstein, *Electronic Processes on Semiconductor Surfaces during Chemisorption*, English edition, ed. E. M. Yankovskii, R. Morrison, Consultants Bureau, New York, 1-444, 1991.
162. G. Eranna, B. C. Joshi, D. P. Runthala, and R. P. Gupta, "Oxide Materials for Development of Integrated Gas Sensors: Comprehensive Review," *Critical Reviews in Solid State and Materials Sciences*, 29 [3] 111-188 (2004).
163. E. Di Bartolomeo, N. Kaabbuathong, M. L. Grilli, and E. Traversa, "Planar Electrochemical Sensors Based on Tape-Cast YSZ Layers and Oxide Electrodes," *Solid State Ionics*, 171 [3-4] 173-181 (2004).
164. E. R. Macam, B. White, B. M. Blackburn, L. Chevallier, E. Di Bartolomeo, E. Traversa, and E. D. Wachsman. "La<sub>2</sub>CuO<sub>4</sub> Sensing Electrode Configuration Influence on Sensitivity and Selectivity for a Multifunctional Potentiometric Gas Sensor." Unpublished Work.
165. E. R. Macam, F. M. Van Assche, J. Yoo, and E. D. Wachsman, "Optimization of La<sub>2</sub>CuO<sub>4</sub> Sensing Electrodes for a NO<sub>x</sub> Potentiometric Sensor," *ECS Transactions*, 1 [7] 121-129 (2006).
166. S.-J. Huang, A. B. Walters, and M. A. Vannice, "Adsorption and Decomposition of NO on Lanthanum Oxide," *Journal of Catalysis*, 192 [1] 29-47 (2000).
167. C. Y. Chen, E. C. Branlund, C. Bae, K. Yang, M. A. Kastner, A. Cassanho, and R. J. Birgeneau, "Comparison of Strontium-Induced and Oxygen-Induced Holes in La<sub>2</sub>CuO<sub>4</sub>," *Physical Review B*, 51 [6] 3671-3677 (1995).

168. B. Klingenberg and M. A. Vannice, "NO Adsorption and Decomposition on  $\text{La}_2\text{O}_3$  Studied by DRIFTS," *Applied Catalysis B: Environmental*, 21 [1] 19-33 (1999).
169. F. M. Van Assche, "Heterogeneous Catalytic Evaluation and Adsorption Characterization of the  $\text{La}_2\text{CuO}_4/\text{YSZ}/\text{Pt}$  Potentiometric Couple," Ph.D. Dissertation, University of Florida, Gainesville, Florida, 21-229, 2008.
170. I. Stará and V. Matolín, "The Influence of Particle Size on CO Adsorption on Pd/Alumina Model Catalysts," *Surface Science*, 313 [1-2] 99-106 (1994).
171. L. Marchetti and L. Forni, "Catalytic Combustion of Methane Over Perovskites," *Applied Catalysis B: Environmental*, 15 [3-4] 179-187 (1998).
172. J. C. Yang, J. V. Spirig, D. Karweik, J. L. Routbort, D. Singh, and P. K. Dutta, "Compact Electrochemical Bifunctional  $\text{NO}_x/\text{O}_2$  Sensor With Metal/Metal Oxide Internal Reference Electrode for High Temperature Applications," *Sensors and Actuators B: Chemical*, 131 [2] 448-454 (2008).
173. R. Mukundan, E. L. Brosha, and F. H. Garzon, *Mixed Potential Hydrocarbon Sensors Based on Yttria Stabilized Zirconia Electrolyte and Oxide Electrodes*, in *Solid State Ionic Devices III, Proceedings of the Electrochemical Society*, series ed. E. D. Wachsman, K. S. Lyons, M. Carolyn, F. Garzon, M. Liu, J. Stetter, The Electrochemical Society, New Jersey, 278-279, 2003.
174. D. E. Williams, "Semiconducting Oxides As Gas-Sensitive Resistors," *Sensors and Actuators B: Chemical*, 57 [1-3] 1-16 (1999).
175. M. Johansson, D. Loyd, and I. Lundström, "Influence of Mass Transfer on the Steady-State Response of Catalytic-Metal-Gate Gas Sensors," *Sensors and Actuators B: Chemical*, 40 [2-3] 125-133 (1997).
176. B. M. Blackburn, F. M. Van Assche, and E. D. Wachsman, "Electric-Field Effects in Solid-State Ionic Devices," *ECS Transactions*, 16 [51] 355 (2009).
177. B. M. Blackburn, M. Camaratta, and E. D. Wachsman, "Advances in Rapid Prototyping for Solid State Ionics," *ECS Transactions*, 16 [51] 367 (2009).
178. J. H. Block, H. J. Kreuzer, and L. C. Wang, "Electrostatic Field Effects in Surface Reactivity: Adsorption, Dissociation and Catalytic Reaction of Nitric Oxide," *Surface Science*, 246 [1-3] 125-134 (1991).
179. V. P. Zhdanov and B. Kasemo, "Kinetics of Electrochemical Reactions: From Single Crystals to Nm-Sized Supported Particles," *Surface Science*, 521 [1-2] L655-L661 (2002).
180. S. G. Neophytides, D. Tsiplakides, and C. G. Vayenas, "Temperature-Programmed Desorption of Oxygen From Pt Films Interfaced With  $\text{Y}_2\text{O}_3$ -Doped  $\text{ZrO}_2$ ," *Journal of Catalysis*, 178 [2] 414-428 (1998).

181. I. Riess and C. G. Vayenas, "Fermi Level and Potential Distribution in Solid Electrolyte Cells With and Without Ion Spillover," *Solid State Ionics*, 159 [3-4] 313-329 (2003).
182. Karl Hauffe, *The Application of the Theory of Semiconductors to Problems of Heterogeneous Catalysis*, in *Advances in Catalysis*, ed. Walter G. Frankenburg, Academic Press, 213-256, 1952.
183. S. R. Morrison, *The Chemical Physics of Surfaces*, 2<sup>nd</sup> Edition, Plenum Press, New York, 1-403, 1990.
184. J. Nowotny, T. Bak, and C. C. Sorrell, "Charge Transfer at Oxygen/Zirconia Interface at Elevated Temperatures: Part 10: Effect of Platinum," *Advances in Applied Ceramics: Structural, Functional & Bioceramics*, 104 [4] 214-222 (2005).
185. F. T. Ulaby, *Fundamentals of Applied Electromagnetics*, 2001 Media Edition, Prentice Hall, New Jersey, 1-433, 2001.
186. F. R. Zypman, "Off-Axis Electric Field of a Ring of Charge," *American Journal of Physics*, 74 [4] 295-300 (2006).
187. A. C. Heinricher and J. S. Rigden, "Numerical Methods and Physics Instruction," *European Journal of Physics*, 1 [4] 201-206 (1980).
188. Ejup Ganic and Tyler Hicks, *McGraw-Hill's Engineering Companion*, McGraw-Hill, New York, 3.35, 2003.
189. P. Bragieli, "Surface Reactions in an External Electrostatic Field," *Surface Science*, 266 [1-3] 35-39 (1992).
190. M. T. M. Koper and R. A. van Santen, "Electric Field Effects on CO and NO Adsorption at the Pt(111) Surface," *Journal of Electroanalytical Chemistry*, 476 [1] 64-70 (1999).
191. M. Moors, T. V. de Bocarm, and N. Kruse, "Surface Reaction Kinetics Studied With Nanoscale Lateral Resolution," *Catalysis Today*, 124 [1-2] 61-70 (2007).
192. G. Pacchioni, J. R. Lomas, and F. Illas, "Electric Field Effects in Heterogeneous Catalysis," *Journal of Molecular Catalysis A: Chemical*, 119 [1-3] 263-273 (1997).
193. A. Du, G. Z. Wei, Q. L. Hu, and Z. Xianyu, "Néel Temperature of Orthorhombic  $\text{La}_2\text{CuO}_4$ ," *Journal of Magnetism and Magnetic Materials*, 146 [1-2] 201-202 (1995).
194. C. Stassis, B. N. Harmon, T. Freltoft, G. Shirane, S. K. Sinha, K. Yamada, Y. Endoh, Y. Hidaka, and T. Murakami, "Field-Induced Magnetic Form Factor of  $\text{La}_2\text{CuO}_{4-y}$ ," *Physical Review B*, 38 [13] 9291 (1988).
195. J. Shimizu, M. Nakagawa, and Y. Oda, "The Normal State Magnetic Susceptibility of  $\text{La}_2\text{CuO}_{4+\delta}$  With Excess Oxygen," *Physica C: Superconductivity*, 388-389 263-264 (2003).

196. M. J. Weaver, "Electrostatic-Field Effects on Adsorbate Bonding and Structure at Metal Surfaces: Parallels Between Electrochemical and Vacuum Systems," *Applied Surface Science*, 67 [1-4] 147-159 (1993).
197. C. Vayenas and S. Brosda, "Electrochemical Promotion: Experiment, Rules and Mathematical Modeling," *Solid State Ionics*, 154-155 243-250 (2002).
198. S. C. Singhal and K. Kendall, *High Temperature Solid Oxide Fuel Cells: Fundamentals, Design, and Applications*, Elsevier Advanced Technology, Great Britain, 1-405, 2003.
199. B. M. Blackburn and E. D. Wachsman, "Performance of Thermally Modified, Potentiometric Gas Sensor Array in Gas Mixtures," *ECS Transactions*, 16 [51] 339 (2009).
200. B. M. Blackburn, B. M. White, and E. D. Wachsman, "Multifunctional Potentiometric Gas Sensor Array with an Integrated Heater and Temperature Sensors," in *Advances in Electronic Ceramics: Ceramic Engineering and Science Proceedings*, series ed. Clive Randall, Jonathan Salem, Dongming Zhu, Eds., 101-108, 2008.
201. B. M. Blackburn and E. D. Wachsman, "Multifunctional Potentiometric Gas Sensor Array with an Integrated Temperature Control and Temperature Sensors," International Application Number: PCT/US2008/079416, 10-9-2008.
202. B. M. Blackburn and E. D. Wachsman, "Multifunctional Gas Sensor Array with Improved Selectivity Through Local Thermal Modification," *ECS Transactions*, 11 [33] 141 (2008).
203. B. M. Blackburn, F. M. Van Assche, and E. D. Wachsman, "Electric-Field Effects in Solid-State Ionic Devices," *ECS Transactions*, 16 [51] 355 (2009).
204. B. M. Blackburn, F. M. Van Assche, and E. D. Wachsman, "Electric-Field Enhanced Performance in Catalysis and Solid-State Devices Involving Gases," International Application Number: PCT/US2008/086693, 12-12-2008.
205. D. W. Richerson, *Modern Ceramic Engineering: Properties, Processing, and Use in Design*, 3<sup>rd</sup> edition, CRC Press, Boca Raton, 1-696, 2006.
206. P. Atanassova, P. Atanassov, R. Bhatia, M. Hampden-Smith, T. Kodas, and P. Napolitano, "Direct-Write Materials and Layers for Electrochemical Power Devices," Ch. 4 in *Direct-Write Technologies for Rapid Prototyping Applications: Sensors, Electronics, and Integrated Power Sources*, ed. Pique, A., Chrisey, D. B., Eds., Academic Press, San Diego, 55-92, 2002.
207. Ju-Hyung, Y.; Han, C.; Joondong, K.; Jin-Won, S.; Dong-Hun, S.; Young-Geun, P. "Fabrication of Carbon Nanotube Sensor Device by Inkjet Printing," in *Nano/Micro Engineered and Molecular Systems, 2008 (NEMS 2008), 3rd IEEE International Conference on*, 506-509, 2008.

208. Y. B. Kim, S. J. Ahn, J. Moon, J. Kim, and H. W. Lee, "Direct-Write Fabrication of Integrated Planar Solid Oxide Fuel Cells," *Journal of Electroceramics*, 17 [2] 683-687 (2006).
209. A. Pique, *Direct-Write Technologies for Rapid Prototyping Applications: Sensors, Electronics, and Integrated Power Sources*, ed. A. Pique, D. B. Chrisey, Academic Press, San Diego, 1-726, 2002.
210. M. Heule, S. Vuillemin, and L. J. Gauckler, "Powder-Based Ceramic Meso- and Microscale Fabrication Processes," *Advanced Materials*, 15 [15] 1237-1245 (2003).
211. A. Vertanessian, A. Allen, and M. J. Mayo, "Agglomerate Formation During Drying," *Journal of Materials Research*, 18 [2] 495-506 (2003).
212. J. N. Stuecker, J. Cesarano, and D. A. Hirschfeld, "Control of the Viscous Behavior of Highly Concentrated Mullite Suspensions for Robocasting," *Journal of Materials Processing Technology*, 142 [2] 318-325 (2003).
213. J. S. Ahn, D. Pergolesi, M. A. Camaratta, H. Yoon, B. W. Lee, K. T. Lee, D. W. Jung, E. Traversa, and E. D. Wachsman, "High-Performance Bilayered Electrolyte Intermediate Temperature Solid Oxide Fuel Cells," *Electrochemistry Communications*, 11 [7] 1504-1507 (2009).
214. G. Rietveld, M. Glastra, and D. van der Marel, "Doping Dependence of the Chemical Potential in Cuprate High-Tc Superconductors I.  $\text{La}_{2-x}\text{Sr}_x\text{CuO}_4$ ," *Physica C: Superconductivity*, 241 [3-4] 257-272 (1995).
215. A. D'Amico, C. Di Natale, R. Paolesse, A. Mantini, C. Goletti, F. Davide, and G. Filosophi, "Chemical Sensing Materials Characterization by Kelvin Probe Technique," *Sensors and Actuators B: Chemical*, 70 [1-3] 254-262 (2000).
216. *KP6500 Kelvin Probe User's Manual*, McAllister Technical Services, version 4.x, 2007, [www.clanmcalister.org/download/kp6500-manual.pdf](http://www.clanmcalister.org/download/kp6500-manual.pdf), Last Accessed 09-19-2009.
217. A. Hadjadj, P. Cabarrocas, and B. Equer, "Analytical Compensation of Stray Capacitance Effect in Kelvin Probe Measurements," *Review of Scientific Instruments*, 66 [11] 5272-5276 (1995).
218. R. J. D'Arcy and N. A. Surplice, "The Effects of Stray Capacitance on the Kelvin Method for Measuring Contact Potential Difference," *Journal of Physics D: Applied Physics*, 3 [4] 482-488 (1970).
219. P. A. W. van der Heide, "Systematic x-ray photoelectron spectroscopic study of  $\text{La}_{1-x}\text{Sr}_x$ -based perovskite-type oxides," *Surface and Interface Analysis*, 33 414-425 (2002).
220. H. J. Michel, H. Leiste, K. D. Schierbaum, and J. Halbritter, "Adsorbates and Their Effects on Gas Sensing Properties of Sputtered  $\text{SnO}_2$  Films," *Applied Surface Science*, 126 [1-2] 57-64 (1998).

221. R. W. M. Kwok, *XPSPEAK*, Version 4.1, 1999, [www.uksaf.org/xpspeak41.zip](http://www.uksaf.org/xpspeak41.zip), Last Accessed 09-19-2009.
222. J. F. Moulder, W. F. Stickle, P. E. Sobol, and K. D. Bomben, *Handbook of X-ray Photoelectron Spectroscopy*, ed. J. Chastain, R. C. King, Physical Electronics, 1992.
223. D. J. Miller, M. C. Biesinger, and N. S. McIntyre, "Interactions of CO<sub>2</sub> and CO at fractional atmosphere pressures with iron and iron oxide surfaces: one possible mechanism for surface contamination?," *Surface and Interface Analysis*, 33 299-305 (2002).
224. T. Takahashi, F. Maeda, H. Katayama-Yoshida, Y. Okabe, T. Suzuki, A. Fujimori, S. Hosoya, S. Shamoto, and M. Sato, "Photoemission Study of Single-Crystalline (La<sub>1-x</sub>Sr<sub>x</sub>)<sub>2</sub>CuO<sub>4</sub>," *Physical Review B*, 37 [16] 9788 (1988).
225. M. Strongin, S. L. Qiu, J. Chen, C. L. Lin, and E. M. McCarron, "Question of Superoxide in La<sub>2</sub>CuO<sub>4+δ</sub>," *Physical Review B*, 41 [10] 7238 (1990).
226. T. Riesterer, J. G. Bednorz, K. A. Müller, and B. Reihl, "The high-T<sub>c</sub> superconductor Sr<sub>0.2</sub>La<sub>1.8</sub>CuO<sub>4</sub>: A direct and inverse-photoemission study," *Applied Physics A: Materials Science & Processing*, 44 [1] 81-82 (1987).
227. N. Nücker, J. Fink, B. Renker, D. Ewert, C. Politis, P. J. W. Weijs, and J. C. Fuggle, "Experimental electronic structure studies of La<sub>2-x</sub>Sr<sub>x</sub>CuO<sub>4</sub>," *Zeitschrift für Physik B Condensed Matter*, 67 [1] 9-14 (1987).
228. P. Steiner, J. Albers, V. Kinsinger, I. Sander, B. Siegwart, S. Hüfner, and C. Politis, "Photoemission investigation of the high temperature superconductors La<sub>2-x</sub>Sr<sub>x</sub>CuO<sub>4</sub>," *Zeitschrift für Physik B Condensed Matter*, 66 [3] 275-278 (1987).
229. P. Steiner, R. Courths, V. Kinsinger, I. Sander, B. Siegwart, and S. Hüfner, "Photoemission on High T<sub>c</sub> Superconductors," *Applied Physics A: Materials Science & Processing*, 44 [1] 75-79 (1987).
230. S. Hüfner, P. Steiner, M. Weirich, and R. Courths, "Electronic structure of (LaSr)<sub>2</sub>CuO<sub>4</sub> and (NdCe)<sub>2</sub>CuO<sub>4</sub>," *Zeitschrift für Physik B Condensed Matter*, 85 [1] 43-48 (1991).
231. M. Y. Smirnov, A. V. Kalinkin, A. A. Dubkov, E. I. Vovk, A. M. Sorokin, A. I. Nizovskii, B. Carberry, and V. I. Bukhtiyarov, "Use of the differential charging effect in XPS to determine the nature of surface compounds resulting from the interaction of a Pt/BaCO<sub>3</sub>/Al<sub>2</sub>O<sub>3</sub> model catalyst with NO<sub>x</sub>," *Kinetics and Catalysis*, 49 [6] 831-839 (2008).
232. P. J. Schmitz and R. J. Baird, "NO and NO<sub>2</sub> Adsorption on Barium Oxide: Model Study of the Trapping Stage of NO<sub>x</sub> Conversion Via Lean NO<sub>x</sub> Traps," *The Journal of Physical Chemistry B*, 106 [16] 4172-4180 (2002).
233. O. I. Klyushnikov, V. V. Sal'nikov, and N. M. Bogdanovich, "X-ray Photoelectron Spectra of La<sub>1-x</sub>Ca<sub>x</sub>Cr<sub>1-y</sub>M<sub>y</sub>O<sub>3</sub> (M = Mn, Fe, Ni, Cu) Perovskite Oxides," *Inorganic Materials*, 38 [3] 265-270 (2002).

234. L. F. Mattheiss, "Electronic Band Properties and Superconductivity in  $\text{La}_{2-y}\text{X}_y\text{CuO}_4$ ," *Physical Review Letters*, 58 [10] 1028-1031 (1987).
235. Gy. Vida, V. K. Josepovits, M. Gyor, and P. Deak, "Characterization of Tungsten Surfaces by Simultaneous Work Function and Secondary Emission Measurements," *Microscopy and Analysis*, 9 337-342 (2003).
236. R. E. Mistler and E. A. Twiname, *Tape Casting: Theory and Practice*, The American Ceramic Society, Westerville, 1-298, 2000.
237. M. Wesselmann, "Tape Casting and Pre-Formulated Water Based Binder Solutions," [www.polymerinnovations.com/presentation4101/wb4101.pdf](http://www.polymerinnovations.com/presentation4101/wb4101.pdf), 2009, Last Accessed 6-2-2009.
238. M. N. Rahaman, *Ceramic Processing and Sintering*, Marcel Dekker, New York, 1-770, 1995.
239. J. J. Fendrock and L. M. Hong, "Parallel-Gap Welding to Very-Thin Metallization for High Temperature Microelectronic Interconnects," *Components, Hybrids, and Manufacturing Technology, IEEE Transactions on*, 13 [2] 376-382 (1990).
240. G. G. Harman, *Wire Bonding in Microelectronics : Materials, Processes, Reliability, and Yield*, McGraw-Hill, New York, 1-290, 1997.
241. K. Gottfried, T. Gessner, C. Kaufmann, and T. Gessner, "Interconnect Systems in Automotive Sensors at Elevated Temperatures," Ch. 1.7 in *Advanced Microsystems for Automotive Applications*, ed. Valldorf, J., Gessner, W., Eds., Springer-Verlag, New York, 67-77, 2003.
242. S. Murali, N. Srikanth, Y. M. Wong, and C. J. Vath III, "Fundamentals of thermo-sonic copper wire bonding in microelectronics packaging," *Journal of Materials Science*, 42 [2] 615-623 (2007).
243. S. Zhuiykov and N. Miura, "Development of Zirconia-Based Potentiometric  $\text{NO}_x$  Sensors for Automotive and Energy Industries in the Early 21st Century: What Are the Prospects for Sensors?," *Sensors and Actuators B: Chemical*, 121 [2] 639-651 (2007).
244. N. Näther, H. Henkel, A. Schneider, and M. J. Schöning, "Investigation of Different Catalytically Active and Passive Materials for Realising a Hydrogen Peroxide Gas Sensor," *Physica Status Solidi A*, 206 [3], 449-454 (2009).

## BIOGRAPHICAL SKETCH

Bryan Michael Blackburn was born and raised in Tampa, Florida. From an early age a love of learning and the pursuit of knowledge were instilled in him by his family. Bryan also developed a desire to learn about the world of business from his grandfather, Irving, and father, Robert, both of whom started successful companies. Bryan attended Jesuit High School in Tampa in the late 1990s, and graduated as Salutatorian of his class in 2000. While being offered several opportunities to attend other prestigious universities across the nation, Bryan choose to attend the University of Florida and began his academic career as an Honors student studying business. After his second year, Bryan decided that if he wanted to start a technology related company that he would need to learn about engineering. Therefore, Bryan took on a dual-major in business administration and electrical engineering. Bryan was an undergraduate researcher at the Particle Engineering Research Center and in the Biophotonic Microsystems labs on campus, where he worked on creating a camera system for monitoring the rastered laser of a MEMS micromirror assembly, developing a monodisperse silica nanoparticles, and gained experience in microelectronics fabrication in a cleanroom environment. He also was team leader in a year long program called Integrated Products, Process, and Design, where Bryan and his multi-disciplinary team developed a working prototype for a magnetic field safety device for MRI facilities. Working with an industrial liaison, this gave Bryan much experience in the process of taking a product from an original concept through the initial and detailed design phases all the way to a working prototype which was tested for proof of concept. This also provided an opportunity for Bryan to utilize his business skills in developing a break-even analysis to determine if further development of the product would be worth while.

During this time Bryan was also a member of The Professional Business Fraternity, Alpha Kappa Psi, which allowed him to learn more about professionalism and to participate in

community service. Bryan was also a member on the University of Florida triathlon team and attended several national conference races.

Bryan received his Ph.D. in materials science and engineering from the University of Florida in 2009. His research interests range from the design and fabrication of electrochemical and electronic devices, with a current focus on energy production and efficiency, to the study of electron transfer during chemical reactions at the surface of such devices. Bryan is a professional engineer intern and has a master's degree in materials science and engineering and bachelor's degrees in electrical engineering and business administration, all from the University of Florida. Bryan is now focused on growing his company, which is working toward the commercialization of the gas sensors from this work and other solid-state ionic devices (e.g., solid oxide fuel cells and H<sub>2</sub> production membranes).